ANTENNA SYSTEMS FOR WIDEBAND DIRECTION FINDING AND SPECTRUM SENSING

by

JAKE ALEXANDER CAZDEN

B.A., University of Colorado, 2015

M.A., University of Colorado, 2019

A thesis submitted to the
Faculty of the Graduate School of the
University of Colorado in partial fulfillment
of the requirement for the degree of
Doctor of Philosophy
Department of Electrical, Computer, and Energy Engineering
2022

Committee Members:

Dejan S. Filipović, Chair

Mohamed A. Elmansouri

Scott Palo

Erik Lier

Gregor Lasser

Cazden, Jake Alexander (Ph.D., Electrical Engineering, Antenna Design)
Antenna Systems for Wideband Direction Finding and Spectrum Sensing
Thesis directed by Professor Dejan Filipović

ABSTRACT

Antenna systems for direction finding (DF) and spectrum sensing remain vital for engineering challenges faced in the modern day. The challenges of both civilian and defense beamforming and sensing require wideband antennas and passive components that can meet rigourous requirements in all regions of the spectrum. To achieve wideband sensing, antenna systems for wideband DF can be split into two categories, wide absolute bandwidth sensing at mm-wave frequencies, and wide relative bandwidth sensing at lower microwave frequencies. The challenges posed by each category of design require different approaches to achieve high performance. In mm-wave frequencies, the primary challenge is posed by the large impact of small mechanical features, and the need to carefully control pattern shape over >30GHz bandwidths. At lower microwave frequencies, the challenge is rather due to the difficulty of establishing wideband, ripple-free beam shape over >3:1 bandwidths. Typical means of performing DF at high frequencies allow for poorly controlled pattern shape that limits performance, while at low frequencies typically allow low efficiencies, low gain, and strong pattern ripple, reducing accuracy and system range. Meeting more rigourous goals requires establishing analytical means of evaluating antennas for DF, and applying careful pattern and mode control to enable wideband operation.

A theoretical framework is developed through the analysis of direction finding with two squinted antennas with identical cosine, sinc, or gaussian ideal radiation patterns. The proposed framework allowing for the direct modelling of a wide variety of realistic antenna beam shapes for DF, and shows a fundamental link, and tradeoff, between three parameters of interest: system field of view (FOV), minimum gain inside the FOV, and minimum direction finding function (DFF) slope. The interaction of these parameters is controlled by antenna beam shape and the pointing angle off from system boresight. Utilizing this framework, realistic system goals can be established, antennas can be better evaluated to meet those goals, and antenna design can be guided for good DF operation. This analysis is validated and guides the design of three antennas. A cylindrical curved aperture horn for wide absolute bandwidth sensing at W-band, a miniaturized dual polarized TEM horn for wide relative bandwidth sensing at microwave frequencies, and a log periodic dipole array for wide relative bandwidth sensing at microwave frequencies.

The cylindrical curved aperture horn is designed to achieve a high degree of pattern control over frequency, enabling near frequency independent direction finding operation. The curved aperture horn is manufactured in single horn, 40° FOV 2-element array, 40° FOV 8-element array, and 360° FOV sensor configurations, and shows good agreement with simulation.

The dual polarized TEM horn is developed from basics, and miniaturized using spherical modes engineering to combine the basic TEM horn with a collocated loop and bowtie antenna located within the footprint of the TEM horn. These added features excite low-order TE and TM spherical modes coherently to extend low-frequency performance. The miniaturized design is recessed into an absorbing cavity to effect good pattern shape over a >5:1 bandwidth. High efficiency, dual polarization, and low dispersion are obtained, alongside good spectrum sensing and DF operation. Manufactured results show good agreement of pattern shape and validate the design process, but are impacted by the poor agreement of modeled and actual absorber losses and permittivity.

A low profile LPDA antenna is designed for operation with consistent gain and match over a >5:1 bandwidth. The development is guided by design for 3D printing, allowing for a high level of fabrication integration of complex structural features difficult to replicate with traditional machining, including a tapered line matching network integrated into the LPDA boom. The performance impact of variable growth rate, miniaturization strategies, and other features are discussed, and the feasibility of monolithic manufacture with 3D printing is reviewed. Additionally, the design is extended in simulation to dual polarization.

Finally, the support of these and future designs through Ka-band through 3D printing of coaxial components is studied in depth, and a family of components is constructed. The performance of modern DMLS and SLA processes is investigated for self-supporting, low-loss coaxial line manufacture. A High Q resonator is designed to investigate the impact of DMLS and SLA roughness. Wideband bandpass filters and diplexer devices are demonstrated, and incorporate a novel coaxial cross-junction geometry to compensate for parasitic loading. Manufactured devices achieve a high degree of miniaturization, and good agreement with simulation.

DEDICATION

To my parents, who have supported me throughout my long schooling. And To William, whose love and support have sustained me through tough times.

ACKNOWLEDGEMENTS

I would like to thank my advisor, Prof. Dejan Filipović for his support, his wisdom, and his patience over the past 6 years. He has given me an appreciation for the rigours of our discipline, and I will always be grateful to have worked with him. I also want to thank in particular Dr. Mohamed Elmansouri, whose attention to detail and guidance has been invaluable in tackling challenging problems throughout my time as a graduate student, Ljubodrag Bosković, without whose skill few of my designs would be realized, and Dr. Muhannad Al-Tarifi, who taught me how to take antenna measurements.

I would like to thank the members of my committee, Prof. Scott Palo, Prof. Gregor Lasser, Dr. Erik Lier, and Dr. Kris Merkel, for their time, their commentary on my work, and the chance to join them as a peer.

I would like to thank the S2 corporation, BAE systems, and Lockheed Martin for the funding that has enabled the many stages of this research.

I would like to thank all the alumni, present students, and associates of the antenna research group, and the broader CU RF group for their friendship and assistance over many years, especially: Dr. Ehab Etellisi, Dr. David Garrido, Dr. Saurabh Sanghai, Dr Sara Manafi, Dr Riley Pack, Dr. Elie Tianang, Dr. Prathap Prasannakumar, Dr. Aman Samaiyar, Dr. Conrad Andrews, Dr Carlos Mulero Hernandez, Liliana Rodriguez, Selena Leitner, Merarys A. Caquias Olivera, Theodore Prince, Dong-Chan Son, Gaeron Friedrichs, Songyi Yen, Amy Robinson, and many others. Your friendship has made this group into a family I will cherish throughout my life.

And most importantly, I would not have come this far without the support and love of my family, who have always supported me, even when they haven’t known what I was talking about, my boyfriend william, without whose support I may not have finished, and my best friends, Vivian Becks, Chandler Black, and Emily Eisenberg, who have helped to make me who I am today.

CONTENTS

LIST OF TABLES

LIST OF FIGURES

CHAPTER 1

INTRODUCTION

1.1 Background

Radio direction finding remains a vital part of the engineering landscape. It is also among the oldest disciplines of radio frequency engineering. Passive direction finding techniques evolved alongside radar and other technologies primarily beginning in the 1920s [1], with one of the earliest patents for direction finding using an array being published in 1919, describing the use of the sum and difference signals of four monopoles for direction finding. [2] There are many applications of passive radio direction finding, including classical radio navigation, spectrum use enforcement, electronic support measures, and in more recent years supporting active communications beamforming [3]. These applications have sustained the growth of radio direction finding as a field of active study for many decades.

Antennas used for direction finding (DF) have evolved dramatically over the past 100 years. The pursuit of wider bandwidths has introduced the use of frequency independent antennas like planar spiral antennas [1, 4], conical spiral antennas [5, 6], and sinuous antennas [7]. While pursuit of higher frequencies has embraced the use of horn antennas [1, 8] and Vivaldi antennas [9], among others. The techniques for DF have also evolved, and broadly speaking can be grouped into a few categories. Amplitude only direction finding (AODF) is the analysis of the received power of signals incident on an antenna system of two or more antennas, mapping the ratio of the received power to a function of angle of arrival (AoA) called the direction finding function (DFF). Reaching back to the earliest works like that seen in [2], this is a simple, fast method requiring only simple receiver architectures, but requires careful design of antenna beams to ensure reliability. Interferometric or phase based techniques, or combined phase and amplitude techniques, make use of the time delay between antennas to identify the AoA. These systems can improve accuracy through the use of large distances between antennas, but can be limited by ambiguities based on the frequency and the distance between receivers [1, 6]. As digital technology has developed, so too have digital systems that can make use of multi-snapshot techniques like the MUSIC algorithm, or other superresolution processing algorithms [10-12]. These techniques can be highly accurate, but require additional time and processing requirements. In recent years, new techniques have also been brought into being utilizing machine learning to great effect [13], and have done so using variations on the original Adcock antenna [2].

In spite of perceived limitations of amplitude only direction finding in the face of more modern techniques, AODF remains essential to many systems, as it has capabilities for extremely wideband operation, extremely rapid signal resolution, and relatively low cost. In particular, the development of wideband and ultrawideband recievers has refocused attention on achieving high quality AODF over bandwidths as wide as 40GHz [14]. Pursuit of this goal is a nontrivial task, and requires examining AODF goals at different frequencies in different contexts. At lower microwave frequencies, up to approximately K-Ka band, wideband antennas can be expected to cover wide relative bandwidths, greater than 3:1 operation. While this is a feasible goal, covering many common bands of operation, it becomes infeasible when examining bands like W-band and above, where a 3:1 bandwidth would be prohibitive, covering possibly hundreds of GHz in bandwidth. When examining mm-wave operation, a designation of wideband design can be reconsidered, to examine absolute bandwidths greater than ~30GHz. As will be discussed, to achieve wideband AODF at microwave or mm-wave bands, the selection and design of antennas has many impacts on the final capabilities of the receiver systems systems they supply.

Beyond questions of the approach to design for modern receiver systems for AODF and spectrum sensing, another critical question for the design of future RF systems is how best to feed the antennas in use. Modern, complicated commercial and defense systems require increasingly complex RF components to deal with increasingly strict electrical requirements. In recent years, increases in cost of machining, rapid development cycles, and other factors have driven widespread examination of additive manufacturing as a tool for design, prototyping, and possible future mass production. The full monolithic integration of 3D printed microwave passive systems and antennas is a goal that has only become feasible in recent years, waveguide components in particular have seen successful monolithic systems for a few years [15, 16]. In coaxial technology, successful monolithic integration of antennas and passive components has seen only very recent success [17], and capabilities of this technology remain largely unexplored.

1.2 Motivation

1.2.1 Wideband Amplitude Only Direction Finding

The theory of direction finding put forward in the literature takes pains to detail the analysis of existing antennas for their system accuracy as AODF antennas [1, 6, 19-22]. Starting from existing systems, and in limited analyses from theoretical beam shapes similar to those discussed later [1, 6, 19, 20], the works discuss the impact of parameter variation with respect to the change to the DFF slope (a measure of the system noise invariance discussed later), the induced system error by pointing accuracy and antenna gain imbalance [1, 6, 20, 21], the impact of thermal noise and SNR [1, 6], changing beamwidth [1, 21], and elevation impacts [22]. The analyses put forward provide detailed analytical examinations of the vast majority of sources of error. However, what these analyses neglect to discuss are a variety of very practical considerations. When designing an AODF system, these sources neglect to discuss features like the realistic performance limits of a system, in terms of features like detection range, angular coverage, and the desired accuracy of the DFF. In particular, the theory lacks a detailed explaination of how to systematically analyze new antennas for DF operation, how the selection of an antenna archetype, and the subsequent design of that antenna, impact the expected system level performance. For example, while planar spiral antennas are one clear and popular means of achieving wideband operation in microwave frequencies [1, 19], they lock in the particular frequency independent beam characteristics that a DF system can utilize. One alternate example of a wideband architecture to achieve >3:1 BW would be dual ridged horns like [18]. While the literature can describe whether this specific antenna is good for DF, it is unclear what antenna level design goals should be pursued to achieve specific system-level requirements. This provides an opportunity for a rigourous analysis of mathematical beam functions, their behaviors for DF, and the link between antenna parameters like gain and beamwidth, and DF system parameters like angular coverage and DFF slope.

1.2.2 Wide Absolute Bandwidth AODF and Spectrum Sensing

Important features for direction finding in any band are to obtain near frequency independent behaviors in the shape of a radiation pattern, to exhibit bilateral or circular symmetry, to have consistent monotonic behavior off boresight, and for the radiation pattern to be free of tight spacial rippling [1, 6]. There are a variety of antenna types that can satisfy some or all of these design goals, at varying frequency ranges. These include planar log-periodic antennas [23], Log-periodic dipole arrays (LPDA) [23, 24], spiral antennas [25], corrugated horns [26, 27], ridged horns [28], polyrod antennas [29-31], and sectoral horns [8, 32], to name a few. At lower frequency ranges, LPDAs, planar log-periodic antennas and spiral antennas are all commonly used for DF, however manufacturing them at high frequencies often requires micromachining methods [23-25]. These micromachined antennas feature large exterior support structures which can result in scattering and pattern ripple. The result of this pattern ripple is commonly to exclude micromachined frequency independent antennas. Of the remaining antennas, the antenna family with the greatest utility for DF at these frequencies will be aperture antennas, due to the ability to control gain and beamwidth. Pattern ripple is still a concern for these designs, due to the small wavelengths and fine build details that can degrade operation, however for carefully constructed DMLS or split block designs, this source of error can be minimized. However, horn antennas commonly do not satisfy the goal of having nearly frequency independent behaviors in their radiation pattern. As such, there is a need in the literature to examine the impact of tightly pattern controlled horn antennas at W-band. While some of the sources listed [8, 27, 28, 32] do pursue some pattern control through minimizing beamwidth variation, they still exhibit not only >10°

10dB beamwidth variation, but subtler pattern shape variations that are more challenging to control. This is still sufficient to result in substantially varying DFF behavior. Achieving extremely consistent behavior over frequency at mm-wave frequencies is a substantial challenge.

1.2.3 Wide relative bandwidth antennas for AODF and spectrum sensing

While in mm-wave frequencies, wide absolute bandwidth requires careful control of device dimensions and construction, at microwave frequencies, the challenges of direction finding are of a different nature. In addition to wide bandwidth, desirable characteristics are dual polarized spectrum sensing with DF capabilities in both planes, low dispersion for good fidelity of received signals, and low profile. Operating over wide relative bandwidths brings in the additional design problem that in parts of the operating band, the antenna will be electrically much larger than in other bands. Not only can this be a significant issue for retaining reasonably self-consistent behavior over frequency, but the higher order spherical modes that can be generated by an electrically large antenna can result in substantial pattern rippling if they are not carefully controlled [33-35]. These higher order modes can be generated by both the primary radiating body of the antenna, as well as near field and scattering interactions with support structures and other objects. Construction of frequency independent antennas is substantially more feasible by conventional means at these frequencies, and they make up a significant number of spectrum sensing and DF devices [4, 33, 34] due to their multiple possible polarizations and extremely wide achievable bandwidths. However, limited design choices are available to achieve dual polarized operation, and as is clear in [33] the rippling in frequency independent patterns can be a substantial issue. In addition, as will be shown in chapters 2 and 4 and in the appendix, overall low gain of planar frequency independent antennas results in low DF accuracy (low DFF slope). Other drawbacks to these frequency independent antenna architectures are their nominal low efficiency due to bidirectional radiation and absorbing cavity integration, and their dispersive operation. One alternate means of achieving wideband, dual polarized, low dispersion signals is the quad-ridge horn, either with or without antenna walls [35, 36]. These horn antennas have numerous extremely attractive features, including low dispersion and the potential for consistent 10dB beamwidth, however their high gain can be detrimental for good direction finding angular coverage, and their size and weight can be substantial. In addition, there is limited capability to miniaturize these horns. From all this, it can be seen that there is a potential for creating a novel, dual polarized, low profile spectrum sensor with low dispersion, consistently high efficiency, and good beam shape over frequency for DF. Achieving these features is nontrivial.

1.2.4 Additive Manufacturing of Coaxial Components

As requirements for antennas such as those suggested here become more stringent, the proper feeding of complex antennas will by necessity involve careful construction of matching networks and other passive microwave devices. With the growth of 3D printed devices, it is essential to look into the literature to examine how to extend the utility and manufacturability of these devices to wide bandwidths and numerous frequency bands, as well as to investigate the practical behaviors of devices created with varying additive techniques such as SLA and DMLS. Over the past few years, the growth of 3D printed waveguide devices in particular has been substantial [15, 37-45]. However, these devices are largely narrowband, and the waveguide construction is not conducive to all antenna types. While the construction of waveguide components seems highly feasible with additive manufacturing, increasing attention is being paid to the construction of coaxial components [17, 45-52]. These devices show substantial promise for development of low loss, low dispersion, high quality components, which can also be rapidly prototyped at extremely low cost. Extending the work in [17, 52], to wider bandwidths, and developing a family of air-filled low loss coaxial components can substantially progress the state of the art for the additive manufacture of microwave passive feed chain devices. Of particular interest are the possibilities for development of components which are structurally impossible to create by traditional methods, taking full advantage of 3D printing to achieve complex internal geometry and dense structural packing schemes.

1.2.5 Antenna Systems for Wideband Direction Finding and Spectrum Sensing

The contention of this work is that the challenges posed by the development of wideband direction finding and spectrum sensing antennas are tractable. Nearly frequency independent AODF and spectrum sensing can be achieved through tight pattern control over a wide absolute instantaneous bandwidth, with high accuracy and gain at mm-wave frequencies, and wide relative bandwidth AODF and spectrum sensing are achievable through mode and pattern control with dual polarization and high efficiencies. Further, 3D printing technologies can be leveraged to support wideband, strict antenna requirements and develop diplexers and other devices that are wideband and low loss, while achieving substantial internal complexity and miniaturization.

1.3 Thesis Objectives

This thesis presents a variety methods by which wideband spectrum sensing and direction finding can be achieved, focusing on the differing contexts for high performance over wide absolute bandwidth operation at mm-wave frequencies, and wide relative bandwidth operation at microwave frequencies, as well as the development of a family of coaxial components in additive manufacturing. This is achieved through the construction of an analytical direction finding theory using realistic mathematical radiation patterns to model direction finding behaviors, and the resulting interactions between three critical parameters: system detection coverage or field of view (FOV), system detection range as described through minimum gain within the FOV, and system noise tolerance, as described by the direction finding function slope. The analytical theory demonstrates the fundamental tradeoff between these three parameters, and shows that there are concrete limits on the available performance from AODF systems of any design.

The insights gained from this analytical framework are utilized to develop a curved aperture horn antenna operating over W-band, achieving wide absolute bandwidth AODF operation in mm-wave frequencies, and validating the analytical framework. The design makes use of novel means of minimizing antenna beam variation over frequency and achieves extremely low variation and nearly frequency independent direction finding operation. The extention of the curved aperture horn to W-band operation also revisits an antenna that has seen little use in the literature, and provides concrete parametric information not found in the literature on the proper construction of the curved aperture horn.

Wide relative bandwidth spectrum sensing and direction finding are achieved at lower microwave frequencies through the extention of the spherical mode miniaturized TEM horn to dual polarization, and the improvement of the spherical mode miniaturization technique through the addition of new current paths to the TEM horn. The miniaturized TEM horn is utilized for direction finding by being recessed into a cavity backing, and meets the additional goals of low dispersion and higher efficiency than the commonly competing frequency independent antennas, without substantially increasing size or weight. A novel balun for the feeding of a dual polarized TEM horn is developed. Additional wide relative bandwidth spectrum sensing is achieved through the development of a compact LPDA with an integrated impedance transforming feed designed for additive manufacture.

Further, this work presents the development of a family of coaxial components, including coaxial through lines with self-supporting inner conductors, Ka band resonators, and filter and diplexer devices with wide contiguous passbands, low loss, and significant structural complexity both internally and in external minaturization that cannot be replicated with traditional machining. In support of this, this work also presents a novel coaxial cross-junction with geometric compensation for circuit parasitics.

1.4 Thesis Organization

This thesis is organized into chapters as follows:

- Chapter 2 describes a framework for the analysis of antennas for AODF operation. It presents three mathematical beam patterns to describe a variety of antennas, and links parameters describing their shape to the three critical system level parameters for AODF through the additional factor of mechanical beam squint. The use of this framework is demonstrated for an existing spiral antenna from the literature, and suggestions are given as to what constitutes a good design for an AODF antenna. Also presented is a framework to minimize the radiation pattern variation over frequency.
- Chapter 3 examines the design of a curved aperture horn antenna at W-band. The parametric space describing the design of the curved aperture horn is analyzed in light of the radiation pattern variation framework, the average system gain, and the AODF theory put forward in chapter 2. The design of the individual element is then extended to a family of array configurations for DF, including a pair of 2-element arrays, a pair of 8-element arrays, and a 360^{o} detection capable DF system. Measured results are presented for all components, comparing favourably with simulation, and good DF operation is demonstrated. The ability to use the AODF framework to guide design is shown, and its limitations are discussed with respect to the nonidealities of realistic antennas.
- Chapter 4 presents the design and miniaturization of a novel dual polarized TEM horn. The TEM horn is analyzed in isolation to provide design guidelines for more traditional fabrications, and the spherical mode miniaturization technique is applied to combine the TEM horn with a correctly phased loop antenna and bowtie antenna, to reduce the turn-on frequency substantially. The TEM horn is then integrated into an absorbing cavity to improve radiation pattern shape for DF. A novel balun is developed to feed the TEM horn with two coaxial inputs and simplify the beamforming required for feeding of the TEM

horn. Measured results are presented, showing correlation of radiation patterns and DF performance. Inaccuracies of absorber models utilized in the antenna tuning are discussed.

- Chapter 5 presents the design of a dual polarized LPDA. The design features extremely low spacing factor to achieve small size. The characteristics of the LPDA are contrasted with that of the classical LPDA literature. Integration of an impedance transforming feed is discussed and implemented. Further miniaturization strategies from the literature are discussed, both to achieve shorter antenna length, as well as to alter the self-similarity characteristics to achieve greater high frequency gain. A second polarization is added to the LPDA, and individual means of tuning each polarization are discussed. The single polarization device is manufactured, and measured results compare favourably with simulation. Wide-angle but low-accuracy DF operation is observed.
- Chapter 6 presents the design and fabrication of a family of 3D printed coaxial devices. The first devices discussed are coaxial through-line devices intended for mechanical support of inner conductors and very wide bandwidths. Manufacturing of the device is presented in DMLS, and fabrication errors are discussed, leading to good agreement of the measured parameters with simulation. Following this a high Q_0 resonator is designed for operation at 30GHz, the device is printed in both DMLS and SLA processes, and the differences between the process results are discussed. Third to be designed is a set of standalone bandpass filter devices, which are designed for both DMLS and SLA fabrication. Multiple devices fabricated show good agreement with simulation. The optimization of the novel coaxial cross-junction is presented, and utilized to reduce paracitic loading within the bandpass filters. Finally, three diplexer devices are presented, one with a planar configuration, and two variations achieving different levels of miniaturization. The measured results of all three diplexers are presented, showing agreement with simulation.

- Chapter 7 provides a summary of the work and the contributions to the scientific community. Possibilities for future extention of the subjects presented are outlined.

CHAPTER 2

THEORY OF DIRECTION FINDING ANTENNA DESIGN

2.1 Introduction

Direction finding is a consistent and historically prominent application of antennas, whether for active radar techniques, or passive signal interception [1]. As digital technology has developed, so too has direction finding been driven to utilize computationally expensive but highly accurate processing strategies like MUSIC and bayesian estimation methods. [10-12]. These techniques are highly accurate, but often require large numbers of samples and digital post-processing, inevitably slowing down their implementation. Even with the widespread use of these digital techniques, amplitude only direction finding (AODF) remains popular for its rapid resolution of signals and typically low cost of implementation [6]. For AODF operation, a minimum of two beams from the antenna front-end is required, and the angle of arrival (AoA) is determined by comparing the voltage/power magnitudes processed by each receiver channel [1, 6, 19]. These can be formed by a planar array with a beamformer, or by using physically squinted antennas [1, 9, 21]. The latter configuration is preferred for wide instantaneous bandwidth operation since it can reduce beam variations with frequency due to the associated beam shape and pointing dispersion [6, 9, 21]. This allows for separate design of antenna elements with the focus on their pattern stability with frequency [9, 21]. A simplified diagram illustrating a 2-antenna AODF system can be seen in Fig. 2.1, showing two adjacent antennas, squinted by an angle α off from the system boresight. Fig. 2.1 also illustrates the field beam patterns $F(\theta \pm \alpha)$, and the positions of two critical system level requirements that will be discussed, the field of view (FOV) and minimum gain in the field of view, G_{min}.

For a typical two-antenna AODF system, identical antennas squinted off each other along the scanning plane are ideally used [6]. Unambiguous direction finding (DF) is feasible by

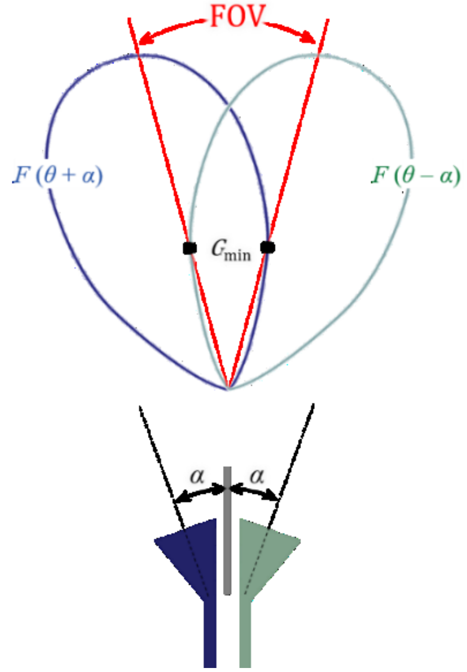

Fig. 2.1. Idealized diagram of a 2-antenna AODF system, illustrating patterns for left and right antennas, each squinted off from boresight by the angle α.

correlating the AoA with the ratio between signals received by each antenna. Assuming symmetry around boresight, the direction-finding function (DFF) can be written as

$$\mathrm{DFF\ [linear]} = \frac{|\mathrm{F}(\theta-\alpha)|}{|\mathrm{F}(\theta+\alpha)|} \tag{2.1}$$

where α is the squint angle off boresight, and F is the field pattern. In dB scale, DFF is expressed as

$$\mathrm{DFF\ [dB]} = 20\log_{10}\frac{|\mathrm{F}(\theta-\alpha)|}{|\mathrm{F}(\theta+\alpha)|} = \mathrm{G}(\theta-\alpha)-\mathrm{G}(\theta+\alpha) \tag{2.2}$$

where G is the gain pattern of the standalone antenna in dB. Three antenna DFF functions can be used [53], however, limited accuracy near boresight is seen. Utilizing the DFF as stated above gives rise to the DFF slope (also called error slope [20]), which is a convenient metric for judging system performance in terms of sensitivity to magnitude errors. This is simply the first derivative of the DFF, and can be considered to be a system level requirement for the design of a DF front-end. The higher the DFF slope, the more resilient the direction estimates will be to a decrease in signal-to-noise ratio (SNR) [6]. Within a specific field of view (FOV), increasing the DFF slope comes at the expense of reducing the minimum gain, which affects receiver's sensitivity and thus DF range. Alternatively, increasing a specific DFF slope without reducing the minimum gain means that the FOV has to be reduced. It is apparent that these performance aspects are of conflicting nature. This chapter provides a guideline for evaluating antenna suitability to achieve specific AODF operating goals. Moreover, an approach to directly connect system level requirements to antenna requirements is demonstrated. Accordingly, a suitable tradeoff is defined to provide guidance prior to design of an antenna front end.

While AODF may be commonly considered to be outdated compared with multi-sample correlation techniques, modern ultrawideband, low latency receivers [54, 55] have brought AODF and thus carefully designed antennas into a new limelight. Wideband AODF performance is best facilitated by consistent radiation patterns over frequency . Analysis of wideband antenna systems inclusive of design of antenna elements with smooth or constant beamwidth patterns is reported in the literature [32, 56, 57]. There are a variety of antennas which can achieve good pattern control for this purpose including pyramidal log periodics [57], spirals [4], pin-wall ridged horns, polyrods [30], cylindrical [27] and rectangular [58] corrugated horns, and sectoral horns [56, 59], to name a few.

The literature often details the analysis of existing antennas for AODF accuracy [1, 6, 19-22]. Starting from an existing system, the works discuss impact of parameter variation with respect to change to the DFF slope, induced system error by pointing accuracy and antenna gain imbalance [1, 6, 20, 21], thermal noise and SNR [1, 6], changing beamwidth [1, 21], or elevation impacts [22]. Other works examine the means of refining existing antenna systems to achieve pattern smoothness or constant beamwidth for DF operation [32, 56, 57]. In [32], pattern control is achieved with 10dB beamwidth and the non-standard metric of 'pattern concavity beamwidth' is defined, as will be discussed later. In [56] and [57] pattern control is achieved through 3dB beamwidth. By contrast, this work expands the direction finding theory by taking common functions used to represent radiation patterns [1, 60] and linking their parameters directly to system level requirements of DFF slope, system FOV, and minimum gain. The framework presented works for both system design, and for evaluation of individual antennas for DF suitability. For practical demonstration, chapter 3 examines the use of a W-band curved aperture horn to achieve a high level of radiation pattern control by using a fitness function taking into account pattern behavior at multiple points, rather than solely at a particular beamwidth.

This chapter is organized as follows: in Section 2.2, the design constraints of a DF system are approached analytically, focusing on the system requirements: the FOV, the DFF slope within the FOV, and the minimum gain within the FOV. These requirements are related to each other theoretically for any antenna beam. The developed formulas assume idealized beam functions, enabling researchers to find the combination of required beam and squint angle to achieve desired DF performance. Section 2.3 shows an example of the application of the framework to an existing spiral design in the literature to illustrate the impact of wide bandwidth in a typical DF antenna and to illustrate the design and analysis process. Section 2.4 presents a multi-point method of pattern control which will be utilized in chapter 3. Section 2.5 concludes, and discusses possible areas for future expansion of this analysis.

2.2 Analytical Approach

2.2.1 System Level Metrics

To analyze the two-channel AODF system theoretically, the following assumptions are made. First, the DF aperture consists of two identical antennas, one for each channel. They are squinted in the scanning plane, symmetrically around the symmetry axis. Second, the radiation pattern of a standalone antenna is evenly symmetric with the main lobe directed towards antennas' boresight directions ($\theta = -\alpha$ and $\theta = +\alpha$). This makes the DF front end (i.e. with squinted antennas) evenly symmetric around system's boresight ($\theta = 0$). Finally, all losses including polarization mismatch are assumed to be equal in both channels, which yields an AoA estimation based on antenna gain patterns solely. This is a reasonable assumption in practical systems if linearly polarized antennas are utilized, and symmetrical design and fabrication of all subsystems is ensured. Since imperfections are unavoidable in practice, high accuracy systems call for high DFF slope (error slope).

The AODF system requirements are specified with minimum gain, $\mathrm{G_{min}}$, and minimum DFF slope, $\mathrm{SLOPE_{min}}$, maintained within a desired FOV. Satisfying these performance parameters, if achievable, depends on the antenna pattern $\mathrm{F}(\theta)$ as well as the squint angle α. The minimum gain requirement is

$$\left|\mathrm{F}\left(\frac{-\mathrm{FOV}}{2}-\alpha\right)\right|^2=\left|\mathrm{F}\left(\frac{\mathrm{FOV}}{2}+\alpha\right)\right|^2 \geq \mathrm{G_{min}}\ [\text{linear}] \tag{2.3}$$

whereas the minimum DFF slope requirement is

$$\frac{\partial}{\partial\theta}\left|\frac{\mathrm{F}(\theta-\alpha)}{\mathrm{F}(\theta+\alpha)}\right|_{\theta=\left[-\frac{\mathrm{FOV}}{2},\frac{\mathrm{FOV}}{2}\right]} \geq \mathrm{SLOPE_{min}}\ \ [/^\circ] \tag{2.4}$$

in dB scale, the relations (2.3) and (2.4) can be re-written as

$$\mathrm{G}\left(\frac{\mathrm{FOV}}{2}+\alpha\right) \geq \mathrm{G_{min}}\ [\mathrm{dBi}] \tag{2.5}$$

$$\frac{\partial}{\partial\theta}\left|\mathrm{G}(\theta-\alpha)-\mathrm{G}(\theta+\alpha)\right|_{\theta=\left[-\frac{\mathrm{FOV}}{2},\frac{\mathrm{FOV}}{2}\right]} \geq \mathrm{SLOPE_{min}}\ [\mathrm{dB}/^\circ] \tag{2.6}$$

where $\mathrm{G}=20\log_{10}|\mathrm{F}|$ is the gain pattern in dBi. These two relations are contradictory in terms of not being able to satisfy higher $\mathrm{G_{min}}$ (over a specific FOV) without sacrificing a lower $\mathrm{SLOPE_{min}}$, and vice versa. Alternatively, both aspects can be improved together if a required FOV is reduced. To better understand this, a thorough investigation with idealized radiation patterns is conducted next.

2.2.2 Cosine Beam Analysis

A cosine pattern function is often used to model an antenna beam [60]. To obtain beam variations and control directivity the cosine function is raised to a positive power number n. Thus, a non-squinted beam pattern of a lossless antenna is

$$\mathrm{F}(\theta) = \mathrm{A}\cos^{\mathrm{n}}(\theta) \tag{2.7}$$

and, hence, the gain pattern can be written as

$$\mathrm{G}(\theta) = \mathrm{D}_0 + 20\ \mathrm{n}\ \log_{10}\cos\theta \tag{2.8}$$

where $\mathrm{D}_0 = 20\ \log_{10}\mathrm{A}$ is the directivity in dB. For convenience during the following analysis, the pattern in the non-scanning principal cut (i.e., perpendicular to the scanning plane) is assumed to be $\mathrm{A}\cos^{0.5}(\theta)$. The need to have a wider beam in the perpendicular cut without sidelobes is often desired in practical systems and is therefore utilized here.

Two cosine beams are squinted to obtain the mathematical model of the AODF system that ties FOV, DFF slope, and antenna minimum gain (receiver sensitivity). Squinted patterns are substituted in relations (2.5) and (2.6) to yield

$$\mathrm{D}_0 + 20\ \mathrm{n}\ \log_{10}\cos\left(\frac{\mathrm{FOV}}{2} + \alpha\right) \geq \mathrm{G}_{\mathrm{min}} \tag{2.9}$$

$$\frac{\partial}{\partial\theta}\left\{20\ \mathrm{n}\ \log_{10}\frac{\cos(\theta-\alpha)}{\cos(\theta+\alpha)}\right\} \geq \mathrm{SLOPE}_{\mathrm{min}} \tag{2.10}$$

Relation (2.10) can be further simplified by only ensuring that the minimum of the left-hand side is higher than $\mathrm{SLOPE}_{\mathrm{min}}$. Following double differentiations to determine minima, it is proven that the minimum DFF slope occurs at $\theta = 0$, which leads to a simplified version of the relation as

$$\frac{-40\ \mathrm{n}}{\ln 10}\,\frac{\sin(-\alpha)}{\cos(-\alpha)} \geq \mathrm{SLOPE}_{\mathrm{min}} \tag{2.11}$$

When designing an AODF front-end for a specific $\mathrm{G}_{\mathrm{min}}$ and $\mathrm{SLOPE}_{\mathrm{min}}$ over a required FOV, the only design parameters that can be controlled are the antenna pattern n and the squint angle α. Therefore, the evaluation of DF performance requirements in terms of α and n that satisfy (2.9) and (2.11) is needed. Initially, α is made the subject in both relations as

$$\alpha \leq \cos^{-1}\left[10^{\frac{\mathrm{G}_{\mathrm{min}}-\mathrm{D}_0}{20\mathrm{n}}}\right] - \frac{\mathrm{FOV}}{2} \tag{2.12}$$

$$\alpha \geq \tan^{-1}\left[\frac{3.3\ \mathrm{SLOPE_{min}}}{\mathrm{n}}\right] \tag{2.13}$$

Then α is sketched against n for a specific set of DF performance parameters ($\mathrm{G_{min}}$, $\mathrm{SLOPE_{min}}$, and FOV). Relations are represented as regions of satisfaction, which means that satisfying both relations occurs only if there is an overlapping region. In this case, choosing a point (α and n) within that overlapping region should satisfy both relations and, hence, all preset DF performance parameters.

A demonstration of this analysis methodology is shown in Fig. 2.2. The required DF performance parameters are $\mathrm{G_{min}} = -12$ dBi, $\mathrm{SLOPE_{min}} = 0.5$ dB/°, and FOV $= \pm 20°$. Relation (2.12) is satisfied at any point below the solid line, whereas relation (2.13) is satisfied at any point above the dotted line. All points within the overlap region between these two lines represent antenna patterns (related to n) and squint angles (α) that meet all required DF performance parameters. On the other hand, (α,n) pair outside this region will not lead to satisfaction of all requirements. This is evident in Fig. 2.3, which shows the patterns and DFF functions of the AODF

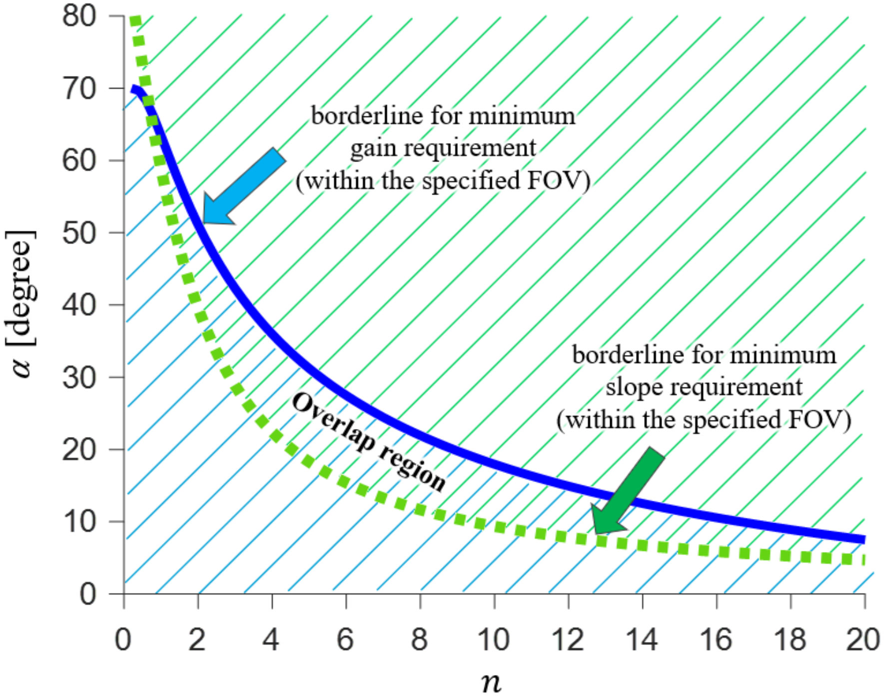

Fig. 2.2. Regions of satisfaction for relations (2.12) and (2.13). DF performance requirements are $\mathrm{G_{min}} = -12$ dBi, $\mathrm{SLOPE_{min}} = 0.5$ dB/°, and FOV $= \pm 20°$. All points (n,α) within the overlap region satisfies these requirements.

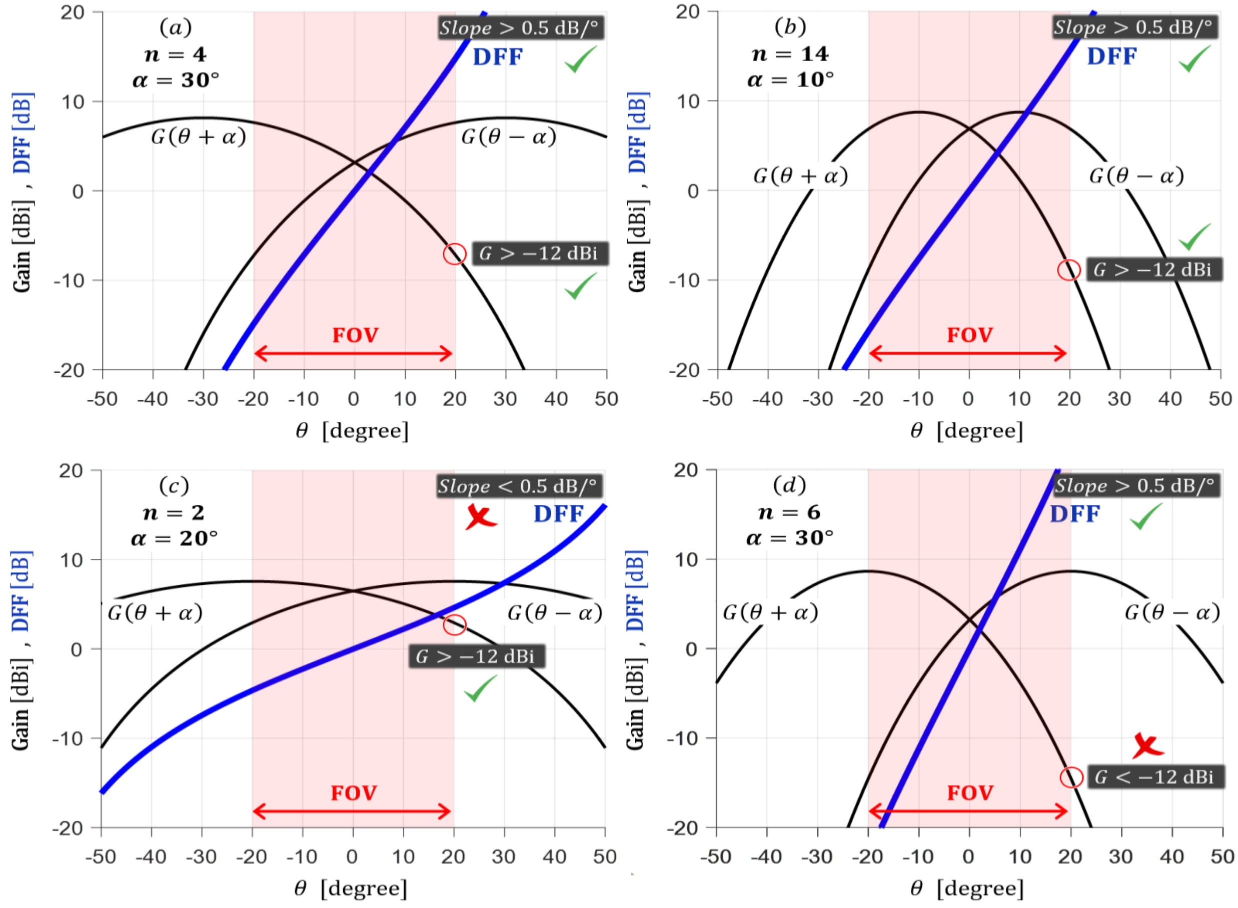

Fig. 2.3. Radiation patterns and corresponding DFF curves using four different design parameter sets of n and α. Two sets (a and b) are chosen to within the overlap region in Fig. 2. The other sets (c and d) are not chosen within the overlap region. Required performance parameters are $G_{\min} = -12$ dBi, $SLOPE_{\min} = 0.5$ dB/° , and FOV $= \pm 20°$.

assuming several design parameters (α and n).

Let us now assume that a better DF performance is required such as higher $G_{\min}$, a higher $SLOPE_{\min}$, a wider FOV, or any combination of these improvements. Interestingly, any of these improvements causes the overlap region to shrink or even disappear, forcing the designer into limited choices or none. Fig. 2.4 illustrates this behavior. Each case shows the reduction in the region of satisfaction resulting from increased performance goals, in all cases, the overlap region shrinks, indicating a more challenging antenna design, if feasible.

The 10-dB beamwidth is examined and found to be a legitimate, practical, replacement of the parameter n. Consequently, it is possible to draw the regions of satisfaction (such as in Fig.

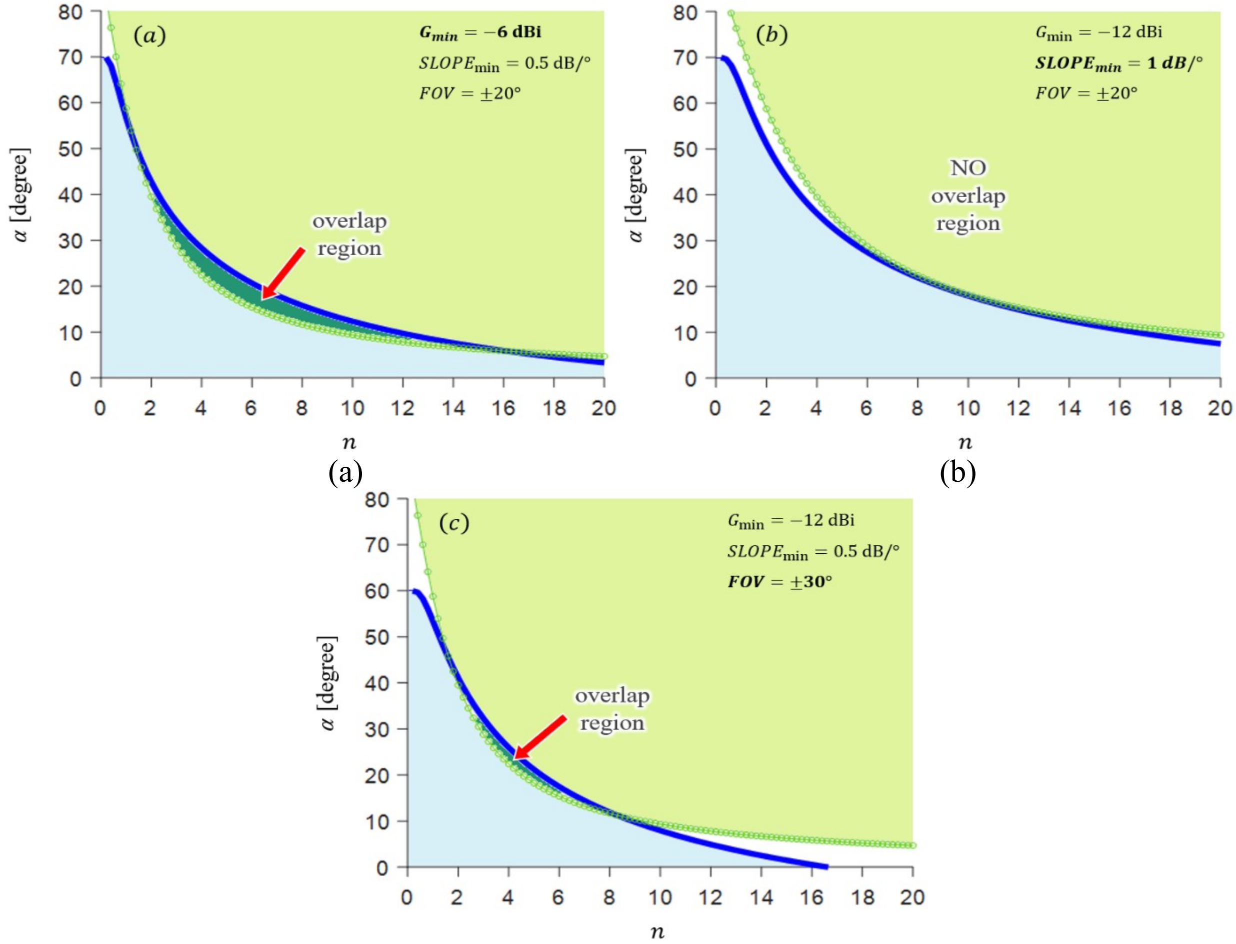

(a) (b)

(c)

Fig. 2.4. Regions of satisfaction for relations (12) and (13) based on three sets of DF performance parameters: (a) $G_{min} = -6$ dBi, $SLOPE_{min} = 0.5$ dB/°, and FOV = ±20°, (b) $G_{min} = -12$ dBi, $SLOPE_{min} = 1$ dB/°, and FOV = ±20°, and (c) $G_{min} = -12$ dBi, $SLOPE_{min} = 0.5$ dB/°, and FOV = ±30°.

2.2) by substituting the x-axis n values with their equivalent 10-dB beamwidth values. The 10-dB beamwidth (denoted as Beamwidth) of the theoretical cosine pattern defined in (2.7) can be expressed as

$$\text{Beamwidth} = 2\cos^{-1}\left[10^{\frac{-1}{2n}}\right]. \qquad (2.14)$$

Accordingly, the relations that define regions of DF performance satisfaction are the same as those in (2.12) and (2.13) but with n replaced as

$$n = \left[2\log_{10}\sec\left(\frac{\text{Beamwidth}}{2}\right)\right]^{-1}. \qquad (2.15)$$

Fig. 2.5 shows a replication of the chart in Fig. 2.2 but with the x axis being the 10-dB beamwidth instead of n. The same DF performance parameters are used here ($\mathrm{G_{min}} = -12\ \mathrm{dBi}$, $\mathrm{SLOPE_{min}} = 0.5\ \mathrm{dB}/°$, and $\mathrm{FOV} = \pm 20°$). The antenna design set ($\alpha = 30°, \mathrm{n} = 4$), which satisfies all performance requirements, is now ($\alpha = 30°, \mathrm{Beamwidth} = 83°$). From the viewpoint of standalone-antenna design, obtaining the required 10-dB beamwidth encapsulates a great deal of the desired pattern information, assuming that the overall shape of the pattern is cosine-like. Such assumption is adequate in simple design cases where a narrow frequency bandwidth is targeted, which induces less challenge on achieving the required ‘cosine’ pattern. However, in systems with wideband operation, antenna pattern may be expected to vary significantly, and the presumption that all patterns resemble cosine shapes is questionable. Therefore, the above proposed theoretical analysis should expand to examine a variety of patterns.

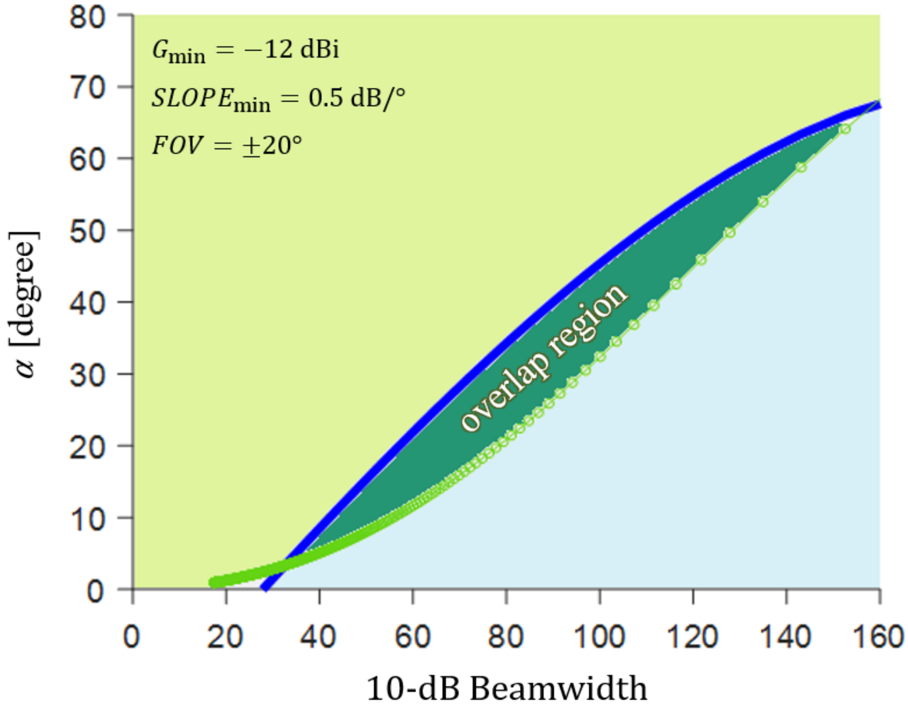

Fig. 2.5. Regions of satisfaction for relations (2.12) and (2.13) with n replaced by the 10-dB beamwidth per equations (2.14) and (2.15). DF performance requirements are $\mathrm{G_{min}}$ = -12dBi, $\mathrm{Slope_{min}}$ = 0.5 dB/°, and FOV = ±20°. This figure is equivalent to that in Fig. 2.2; however, the x-axis has a parameter of greater utility for visualizing the antenna far-field.

2.2.3 Other Pattern Functions

Variations of the cosine pattern itself can be obtained by merely adding a control parameter to the argument; i.e.,

$$F(\theta) = A\cos^{n}(k\theta), \tag{2.16}$$

where k is positive real number. Note that this holds for the main beam, within $|\theta| < \frac{\pi}{2k}$, and that $F(\theta)$ is held to be 0 outside of the main beam. In the previous subsection, k is set to one, but selecting a non-unity value of k is expected to slightly change the overall beam shape, especially at high elevation angles. Fig. 2.6 shows the normalized antenna patterns for the cosine pattern with various k values but same 10-dB beamwidth (arbitrarily 80° for the sake of illustration). The effect of varying k does not look significant, but in fact a closer look to the slope of the patterns reveals quite some difference. This is explored next.

By following the same analysis procedure from the previous subsection, relations for satisfying DF performance requirements can be derived as

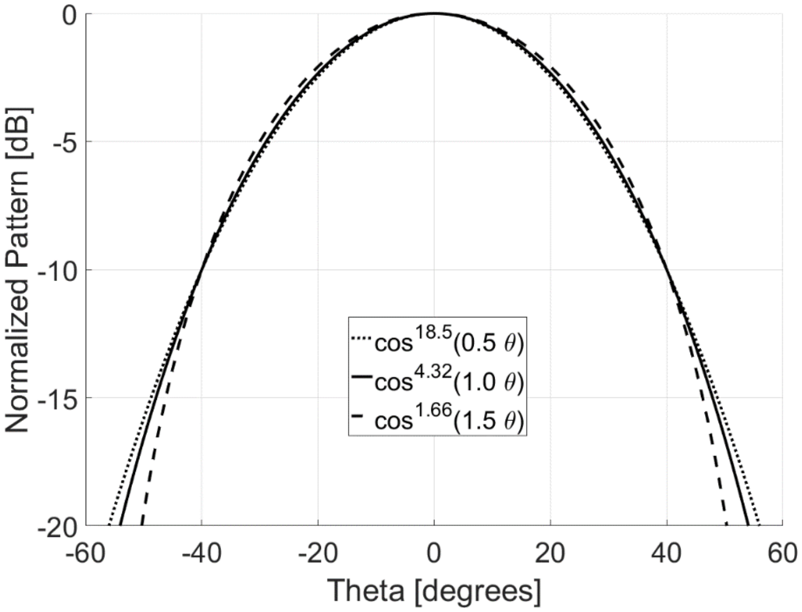

Fig. 2.6. Normalized radiation patterns of the cosine function in (2.16) with various k values (0.5, 1, and 1.5) but the same 10-dB beamwidth of 80°. The power number n is adjusted in each case to maintain equal 10dB beamwidth for all.

$$\alpha \leq \frac{1}{k}\cos^{-1}\left[10^{\frac{G_{min}-D_0}{20n}}\right]-\frac{FOV}{2}\text{, and} \tag{2.17}$$

$$\alpha \geq \frac{1}{k}\tan^{-1}\left[\frac{3.3\ SLOPE_{min}}{nk}\right]\text{,} \tag{2.18}$$

where

$$n=\left[2\log_{10}\sec\left(\frac{\text{Beamwidth}}{2/k}\right)\right]^{-1}\text{.} \tag{2.19}$$

Fig. 2.7 shows the chart of α vs 10-dB beamwidth illustrating borderlines of satisfaction conditions in relations (2.16) and (2.18) for various k values. The same DF performance parameters are used here ($G_{min} = -12$ dBi, $SLOPE_{min} = 0.5$ dB/°, and FOV = ±20°). It is seen that the region of satisfaction does vary with k. Although it might appear minimal, the practical beam shape does not often follow a specific theoretical pattern, especially for wideband operations. Therefore, it is favorable to select the design point (i.e., α and beamwidth) located within a broad range of overlap regions regardless of k. From the chart in Fig. 2.8, many design points belonging to $10° \leq \alpha \leq 30°$ and $50° \leq$ Beamwidth $\leq 90°$ can be chosen within all satisfaction regions.

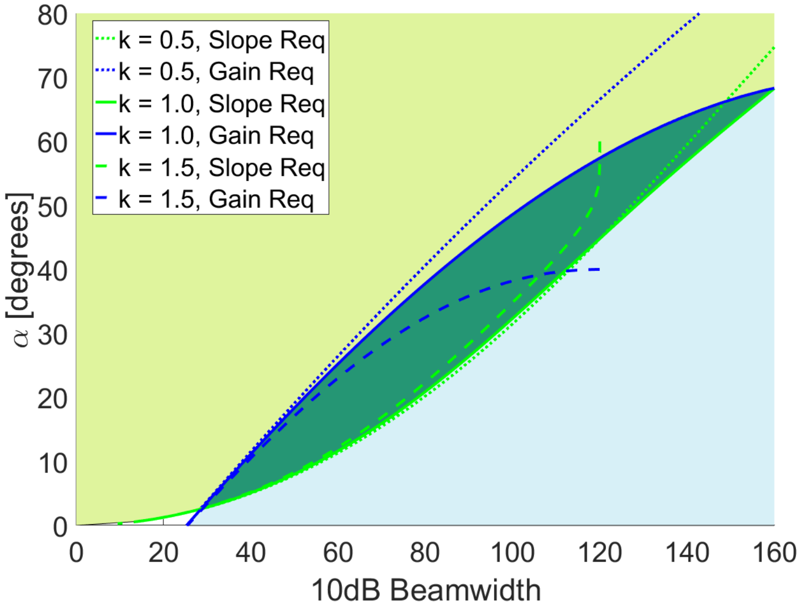

Fig. 2.7. Regions of satisfaction for (2.17), (2.18), with n replaced with 10-dB beamwidth per (2.19). Three values of k are assumed (0.5, 1, and 1.5). Required DF performance parameters are G_{min} = -12dBi, $Slope_{min}$ = 0.5 dB/°, and FOV = ±20°.

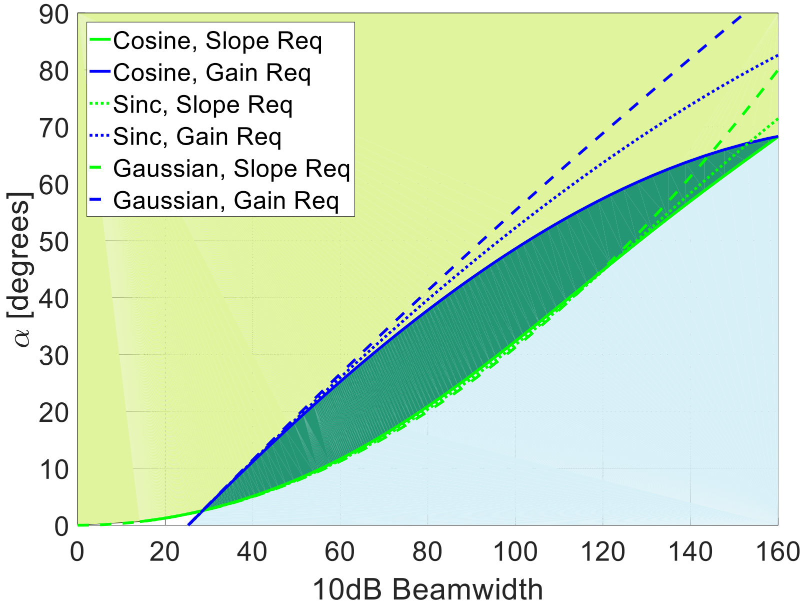

Fig. 2.8. Regions of satisfaction for variety of pattern functions, assuming required DF performance parameters of G_{min} = -12dBi, $Slope_{min}$ = 0.5dB/°, and FOV = ±20°. E-plane 3dB beamwidth held constant at 60°

To demonstrate the applicability of this analysis to other pattern shapes, Sinc and Gaussian patterns are considered next, i.e:

- For Sinc patterns

$$F(\theta) = \mathrm{sinc}^n(k\theta) = \left(\frac{\sin(k\theta)}{k\theta}\right)^n \tag{2.20}$$

$$\mathrm{sinc}\left(k\left(\frac{FOV}{2}+\alpha\right)\right) \geq 10^{\frac{G_{min}-D_0}{20n}} \tag{2.21}$$

$$\frac{1}{k\alpha} - \cot(k\alpha) \geq \frac{3.3\ SLOPE_{min}}{kn} \tag{2.22}$$

- For Gaussian patterns

$$F(\theta) = \exp(-n\,\theta^2) \tag{2.23}$$

$$\alpha \leq \sqrt{\frac{D_0 - G_{min}}{8.7\ n}} - \frac{FOV}{2} \tag{2.24}$$

$$\alpha \geq \frac{SLOPE_{min}}{34.7\ n} \tag{2.25}$$

For sinc patterns, the function F(θ) is utilized for the main beam, $|\theta| < \frac{\pi}{k}$, and 0 elsewhere. For each of these relations, the 10-dB beamwidth can be calculated, then a chart of α vs 10-dB beamwidth can be plotted. Fig. 2.8 shows the borderlines of satisfaction conditions for variety of functions with the same DF parameters as before ($G_{\text{min}} = -12\ \text{dBi}$, $\text{SLOPE}_{\text{min}} = 0.5\ \text{dB}/°$, and $\text{FOV} = \pm 20°$).

2.2.4 Strategy for Wideband Operation

Targeting DF system design for wideband operation adds an inevitable challenge due to pattern variations. Ideally, the goal is to design the antenna pattern to be stable in maximum gain, 10-dB beamwidth, and smoothness, up to high elevation angles. However, in reality, all these parameters do vary to some extent when frequency is varied over ~1.5:1 bandwidth or more. To alleviate the delicacy of such challenge, it is helpful to start the design knowing the allowed range of acceptable performance parameter. For example, it would be reasonable if the 10-dB beamwidth can vary by 20° instead of 5°. To maximize such allowance, a suitable squint angle must be selected first.

It is established that the squint angle α does not change much with frequency because it is fixed physically and antenna is well balanced. Once α is set, the range of allowed 10-dB beamwidths is set as well. This range can be approximated by referring to Fig. 2.7 and Fig. 2.8 and measuring allowed horizontal movement for a specific α under varying shape parameters and funcitons. For example, if α is set to 30°, in Fig. 2.7, to satisfy the range of shape parameters examined, beamwidth variations from 74° to 95° are acceptable without violating all DF performance requirements specified for this figure. In other words, the standalone antenna should be designed so that the radiation pattern is controlled in terms of smoothness within a 10-dB beamwidth of not less than 65° and not more than 95°. It can also be seen that depending on the expected range of shape parameters in a designed antenna, it may be more applicable to select a squint near 20° rather than 30° for the widest range of allowed beamwidths. In later chapters, the squint angle is set to 30°, thus setting the design focus on controlling the pattern stability in terms of beamwidth and smoothness.

2.3 Example of Framework Applicability

To illustrate the utility and use of this framework as a design tool, a hypothetical antenna can be examined as an example. Similar to that in [57], the example used here is a simulated ring-loaded archimedian spiral antenna designed with DF operation in mind. Taking a representative radiation pattern from the design, a variety of similar theoretical patterns can be calculated. These are found by minimizing difference between the idealized beam pattern and the simulated full-wave patterns over a particular angular sweep. In this case, the beam pattern differences are minimized over ±75º. As can be seen in Fig. 2.9(a), this results in some variance between the three pattern shape models, as expected. The three patterns have somewhat different beamwidths, and subtly different behaviors throughout the beam shape. The cosine pattern concentrates more energy towards boresight, starting higher than the archimedian spiral, but with behavior tapering off faster once approaching the horizon. The gaussian beam is the reverse, with more energy being distributed throughout the pattern. Starting off with a faster roll-off than the archimedian pattern, before visibly widening. The sinc pattern operates similarly, but the behavior near horizon more closely matches the simulated spiral behavior.

From this the range of squint angles over which the design can be expected to operate can be calculated. This can be seen in Fig. 2.9(b), with the 10dB beamwidth of the pattern highlighted with

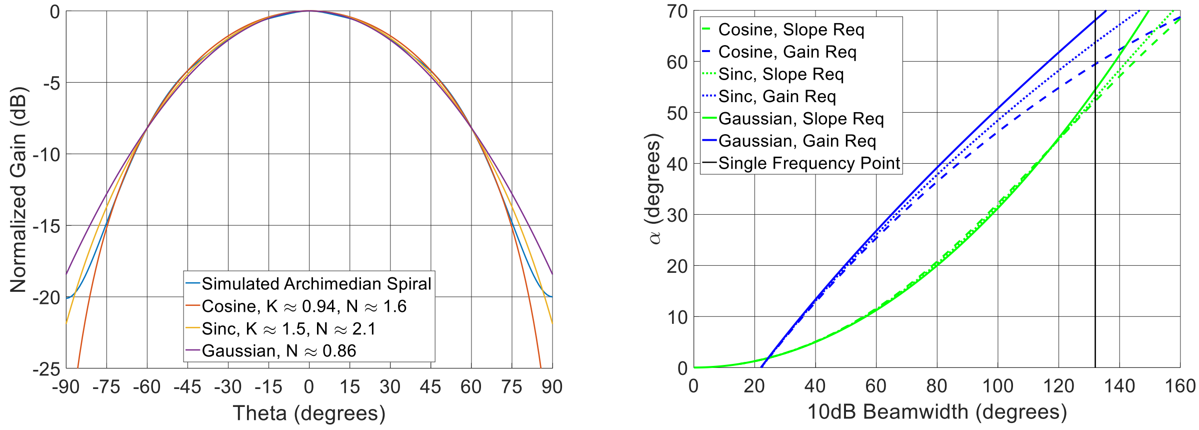

(a) (b)

Fig. 2.9. Simulated single frequency archimedian spiral antenna pattern, plotted with near matches to ideal patterns (a) and detoted single-frequency pattern plotted against cosine, sinc, and gaussian DF models (b).

the black line. For this calculation, Bi-directional, rotationally symmetric patterns (as with a spiral antenna in free space) were assumed. As can be seen, this pattern can be expected to satisfy both requirements for a range of angles over approximately 51-67° of squint. Noticeably however, the three different pattern approximations yield slightly different behavior. Most of this difference is seen in the gain requirement, as the pattern roll-off of each numerical pattern occurs at different rates, with the gaussian beam being widest and the cosine beam being narrowest. This results in nearly 10° of difference between the estimated requirements. The slope variation is less extreme, with the variation being only approximately 2° for the pattern in question. The actual simulated pattern meets the requirements for a range of squint values between 52-61°, a bound slightly tighter than the sinc beam analysis.

The complexities of the true simulated or measured pattern of an antenna are not fully captured by this model. In particular, the model does a poor job of capturing the impact of pattern spacial rippling and the impact of sidelobes or non-monotonic behaviors far from boresight. This is, for practical purposes, captured by the nonstandard metric of 'pattern concavity beamwidth', introduced in [55]. The pattern concavity beamwidth is the range of angles over which the second derivative of the radiation pattern – in dB – remains below some small limiting value. Listed anecdotally in [55] as <0.02 dB/degree^2. The pattern concavity beamwidth describes the range over which the theory put forward here holds accurately. The concavity beamwidth of this example spiral is ≈160°, meeting the <0.02 dB/degree^2 bound for frequencies between 5-20 GHz, and meeting a looser bound of <0.05 dB/degree^2 from 20-25 GHz. For best DF operation, the range over which an antenna should maintain pattern concavity beamwidth is as shown in (2.26). It is worth noting that if the boresight of the antenna is outside of the system FOV, there will be a range of angles near the antenna boresight where concavity is not strictly required. Similarly, if the antenna patterns are allowed to be asymmetrical, there may only be an angular range of equal width to the FOV where good concavity must be maintained. These features of the concavity beamwidth may potentially be of use in the design of synthesized beams from array sources.

$$Concavity\ Beamwidth \geq 2 \cdot \left(\alpha + \frac{FOV}{2}\right) \tag{2.26}$$

Specifically, while the ideal patterns should operate between approximately 51-67° squint, they would require pattern concavity beamwidth of ~142-174°. As the concavity beamwidth is only ~160°, in practice the design only operates as desired below ~60° squint, getting both the DFF slope and FOV as required. While higher squint values could allow for better slopes the FOV is limited by the change in concavity. With a 160° concavity beamwidth and 60° squint, the point where the pattern deviates from theory is in the vicinity of ±20°, in the DFF slope, this can be clearly seen as the point when the DFF slope transitions from steadily increasing in the FOV, to steadily decreasing.

From this example, the guidelines for a requirements-oriented design begin to take shape. This design has certain limitations that should be overcome in an ideal DF oriented antenna design. In particular, while the mathematical theory and real operation are highly similar for this antenna, it can be seen that for such a low directivity design, achieving high slope is challenging, and while the system may still operate above a gain cutoff, neither receivers beam will be pointed near to boresight due to high squint. The sensor FOV is far from the individual antennas peak directivity, and as such not only is this inefficient, but this leaves a system more susceptible to reception of spurious signals and reflections. Meanwhile if this analysis were applied to a highly directive antnenna, it can be reasoned that higher slope values would be possible, but the gain fall-off, or positioning of sidelobes, would limit the usable FOV.

It is clear from the theory that better performance can be obtained for designs which operate with moderate, consistent gain, showing beamwidths in the range of 60-100° in the detection plane, with a squint of 20-40°. An antenna system with this characteristic has the widest range of possible squint angles, and would be tolerant of variation. This centered range of squints and beamwidths provides the largest window wherein an antenna could operate fulfilling all requirements. This is of particular importance when one considers antennas with wide bandwidths. For a spiral design, this is less significant due to their frequency independent nature, leading to their wide use in DF operations [6]. Continuing the example from before, in [57] the spiral in question operates over an extremely wide bandwidth. In simulation, the design put forth varies only between 127-133° 10dB beamwidth between 6 and 25GHz. Using the sinc-beam with n and k shape factors as a good match to the spiral operation, as you move across the simulated bandwidth, the best k value used to simulate the radiation pattern changes between approximately 1.7-1.98. The radiation pattern cuts over frequency, and the slope and gain requirement inequalities for k = 1.7, 1.98, are plotted in Fig. 2.10(a), and Fig 2.10(b), respectively. The highlighted region in Fig. 2.10(b) shows the variation in 10dB beamwidth over frequency for the simulated archimedian spiral. As seen, the highlighted band can theoretically satisfy the requirements for all different beam shapes with any squint value between approximately 53-60°. Plotted in Fig. 2.10(c) and Fig. 2.10(d) is the DF behavior for a 58° squint, meeting the requirements of 0.5 dB/degree

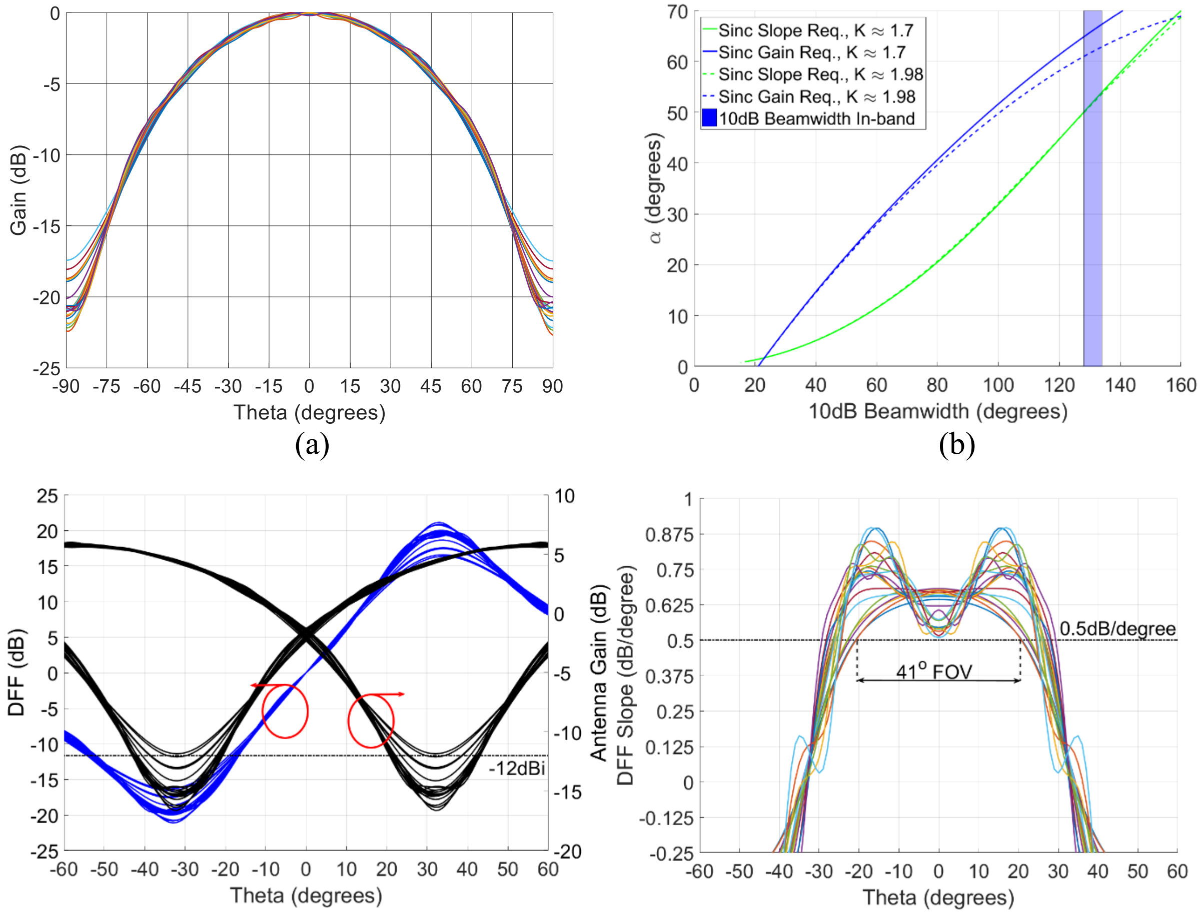

(a) (b)

(c) (d)

Fig. 2.10. (a) Simulated 6-25 GHz pattern cuts in 1 GHz steps for a ring-loaded archimedian spiral. (b) slope and gain requirements with minimum and maximum shape factor, and archimedian spiral 10dB beamwidth over frequency highlighted. (c) squinted antenna patterns (black) and DFF (blue) at 58° squint. (d) DFF slope for 58° squint, showing 41° FOV with slope > 0.5dB/degree.

DFF slope and >-12dBi gain in the 40° FOV. Worth noting is that these extreme squint values bring the antenna close to the boundaries of it's pattern concavity beamwidth, as seen in the behavior of the DFF slope past approximately ±20°.

2.4 Pattern Control Methodology

From the gain and slope requirements, the desired radiation patterns produced by a variety of antennas can be considered. This facilitates analysis of their behavior in an AODF system. A natural extension of this investigation is in extending the bandwidth. Within this framework, as seen when the beam continues to narrow (presumably as frequency increases), the minimum gain within a specified FOV requirement may fail. Conversely, if the beam widens, or pattern nulls intrude within the desired FOV, the minimum slope requirement will not be met. To maintain wideband behavior, these modes of failure must be addressed. Two possible, low-complexity approaches are controlling the directivity through arraying and improving the radiation pattern control of a single element. Arraying is feasible for systems which have single-plane detection, or when detecting azimuth and elevation with separate front-ends. By arraying the elements perpendicular to the plane of detection, the directivity can be manipulated substantially without significantly affecting detection plane pattern shape. This will be discussed further in Chapter 3. However, improving the allowed band using the gain requirement is still limited by the pattern concavity beamwidth [32], nulls in the pattern, and deviation from idealized beam shapes. Therefore, controlling the shape of the beam is critical for wideband DF operation. Not only does pattern control make wideband operation easier to accomplish, but with modern systems requiring minimal processing times, consistent pattern shape over frequency offers the possibility of AoA estimation without wasting processing time on frequency determination. If all DFF calculations are the same across the band of interest, estimations with low error can be achieved in a very short time.

To that end, approaches seen in literature for pattern control can be revisited. In many cases, pattern control is achieved through parametric optimization of the antenna's geometry, predominantly tuning to minimize variation in the 10dB or 3dB beamwidth [32, 35, 56, 57, 61, 62] or beam level at a particular angle [61]. In [32, 62] pattern control is achieved by maximizing the pattern concavity beamwidth. While these works are all successful for their application, a higher degree of pattern control is desired herein, to attempt to obtain nearly frequency independent DF operation from an antenna that is not necessarily frequency independent by nature. Minimizing the variation only of one control point like 10dB beamwidth or 45° gain, neglects to control the pattern shape far from that point.

Thus, a metric for pattern control is developed to work over multiple points [63]. The function is shown below in (2.27). The metric S measures the total change in the radiation pattern slope at a particular point in theta, and allows for a generalized average of this change over selected points of interest in a pattern.

$$S = \frac{1}{N}\sum_{\theta_1}^{\theta_N}\int_{f_{min}}^{f_{max}}\left|\frac{\partial}{\partial f}\frac{\partial}{\partial \theta}\frac{G(\theta, f)}{\max\left[\frac{\partial}{\partial \theta}G(\theta, f)\right]}\right|\partial f \tag{2.27}$$

$$\theta_i = 10°, 20°, 30°, 40°, 50°; N = 5$$

In (2.27), the function G represents the 2D linear gain pattern in the detection plane, that is to say some particular presupposed ϕ-cut, fully described by θ and f, with the assumption that $\theta = 0°$ at the pattern boresight. The function G is normalized by the term $max[\partial/\partial\theta\ G(\theta, f)]$ such that the maximum radiation pattern slope seen is set to 1. This allows for patterns of substantially different beamwidth and gain to be compared without biasing towards low-gain, wide beam antennas which otherwise result in lower values of S due to shallower slope. The partial derivatives are taken over θ and f, to obtain a function of the change over frequency of the radiation pattern slope. By then taking the absolute value and integrating over the frequency band of interest, we arrive at a function in θ representing the total change (over the band of interest) of the radiation pattern slope at each point in θ. By then taking an average over this change at critical points, a single valued, minimizable metric describing the variation of a radiation pattern is found. This calculation can be performed for each geometry of a parametric sweep or optimization, allowing for the minimization of the change in the radiation pattern slope over frequency, to effect pattern control over selected theta points of interest. This could also be taken further, changing the summation to an integral over theta, but this was not deemed necessary, due to the risk of 'over-averaging' the pattern shape. Instead, knowing that the direction finding theory suggests the widest range of usable beams fall near a squint angle of 30°, a sampling of theta points representing a ±20° FOV about 30° is utilized.

Worth noting, though not examined in substantial depth, is the possibility of using a family of similar metrics. Specifically, rather than focusing on the beam slope, the focus could be placed on the beam level, taking instead the formulation in (2.28) for minimizing change in beam level, or the formulation in (2.29), minimizing difference between an obtained antenna pattern, and some hypothetical desired pattern. Due to the critical nature of the DFF slope, and the vulnerability of good DF performance to subtle pattern rippling that may not be captured in (2.28), the metric S utilized for the design work in chapter 3 is (2.27). (2.29) is also rejected for use in the design work in chapter 3, as it is not a-priori clear what beam shapes can be reasonably expected from the antenna family in use.

$$S_2 = \frac{1}{N}\sum_{\theta_1}^{\theta_N} \int_{f_{min}}^{f_{max}} \left| \frac{\partial}{\partial f} \frac{G(\theta, f)}{\max[G(\theta, f)]} \right| \partial f \tag{2.28}$$

$$\theta_i = 10°, 20°, 30°, 40°, 50°; N = 5$$

$$S_3 = \frac{1}{N}\sum_{\theta_1}^{\theta_N} \int_{f_{min}}^{f_{max}} \left| \frac{\partial}{\partial f} \left(\frac{G(\theta, f)}{\max[G(\theta, f)]} - G_{desired}(\theta, f) \right) \right| \partial f \tag{2.29}$$

$$\theta_i = 10°, 20°, 30°, 40°, 50°; N = 5$$

2.5 Conclusion

This chapter presents the characterization of three of the most common families of hypothetical beam shapes for system requirements oriented direction finding. The shape parameters of the idealized beams are linked directly to physical system squint, and to realistic system requirements, the DFF slope and minimum gain in the field of view, that impose limits on system error and maximum range. Manipulation of the system requirements with these ideal patterns is shown to impose fundamental tradeoffs on the FOV, the minimum gain in the FOV, and the DFF slope, requiring a system to either be designed for moderate performance in all three categories, or accept a loss in at least one metric, in exchange for a substantial gain in another. In addition, the impact of realistic radiation patterns disagreement with idealized patterns is discussed through the lens of the pattern concavity beamwidth. An example is presented, illustrating the use of these DF metrics, and examining how they apply to wideband systems. Finally, a brief discussion is put forward of methods to achieve pattern control for DF over specific angular regions of an antenna beam. These sections provide a novel guideline on the future design of AODF antennas, and provide concrete theoretical grounding to guide design. Future work in this analysis must examine in greater detail the impact of two sources of error in the analysis. First, the limitations posed by the 'pattern concavity beamwidth.' This metric, while useful on a practical level, does not provide the precision in analysis that may be desired. Future extentions of this framework should include compound functions, i.e. additional terms in the expression representing the antenna beam, such that the cosine, sinc, and gaussian beam are augmented to more accurately display a noise floor or backlobe of a pattern. As it stands, the functions of the main beam decay to 0 outside of the main beam, resulting in negative concavity throughout the dB gain pattern. Additional terms to represent accurately the behavior of antennas outside their main beam may allow for a more concrete analysis of the DFF slope, giving a tighter bound to acceptable squint angles. The second extention to the analysis is also through the use of additional terms in the main beam expression, however to express the impact of high spatial frequency rippling in the antenna pattern, as often results from system integration in the presence of scattering structures, or wideband antennas radiating many modes in a less than controlled manner. Limits on the acceptable magnitude or frequency of this rippling could provide further design information to future AODF works.

CHAPTER 3

MM-WAVE SPECTRUM SENSING AND DIRECTION FINDING

3.1 Introduction

Direction finding and spectrum sensing technologies over wide bandwidths have become an essential tool for both military and civilian applications. In particular, decoy and detection applications increasingly require ultra-wide bandwidth operation, and 5G networks are projected to operate over numerous different operating bands, and feature technologies like active beamforming. To support these technologies, direction finding over wide and ultra-wide bandwidths is an essential tool. Naturally, direction finding front end antennas have pushed into both increasingly high frequencies, and increasingly wide and ultrawide bandwidths to match the demand for these technologies [21]. Receivers have been developed that can allow for up to 40GHz instantaneous bandwidth spectrum sensing. [14, 54, 55, 64-68]. These systems enable and motivate the design of antenna front-ends to meet these extremely wide bandwidths. The design of new systems to meet new requirements necessitates splitting desired bandwidths into manageable sub-bands, or utilizing frequency independent antennas with sufficient size and feed region detail [6]. Even when using frequency independent antennas, the high and low frequency limits of manufacturing methods will necessitate splitting antenna front ends into smaller operating groups as higher frequencies are reached, and different manufacturing regimes are entered. Near V and W-band in particular, common frequency independent direction finding and spectrum sensing antenna designs like spiral antennas and log-periodic antennas [6] run into prohibitive size and integration requirements due to tight tolerances and millimeter wavelengths. To account for this, direction finding designs at W-band typically make use of techniques like slotline feeds to tapered slot antennas [21] and waveguide fed horn antenans [8]. Some critical features for direction finding, as noted in the previous chapter, are to obtain near frequency independent behavior in the normalized radiation pattern of an antenna, and antenna patterns that exhibit bilateral symmetry over the detection plane, and have smooth, monotonic behavior off boresight [6]. To achieve wide absolute bandwidth operation for DF at W-band, There are a variety of antenna types that may fit these design goals. These include planar log periodic antennas [23], Log-periodic Dipole arrays [23, 24], spirals [25], corrugated horns [26, 27], ridged horns [28], polyrods [29-31], and sectoral horns [8, 32], to name a few.

To achieve operation over the W-band, this chapter will focus on a purely azimuth-only direction finding front end with linearly polarized radiators. One design that can achieve these direction finding goals, and particularly designing for DF system invariance over frequency, is a carefully designed horn antenna. Specifically, a curved-aperture rectangular horn, as described by Dewey and Hill [61, 67]. With this design, stable patterns over a wide band are achieved through consistant phase of the aperture fields across a cylindrical aperture, and limited interference from higher order modes [61]. Non-cylindrical apertures have been investigated to a limited extent but show beam splitting not conducive for DF [68]. The curved aperture horn antenna has seen little use in the open literature, [30, 59, 61, 67, 68], and as such there is limited practical information available to utilize in designing such a horn for use at W-band. The design shown in [61] utilizes first a transition from coaxial feed to double ridged waveguide, followed by an exponential taper to rectangular waveguide, with a deliberate discontinuity to excite a TE_{30} mode, phased to reduce the TE_{30} mode generated by the waveguide to horn transition, thus reducing 45° beam level variation and extending the frequency range of an existing curved aperture horn, the dimensions of which are not discussed clearly in [61]. The design discussed in [67] utilizes an angularly wider horn than the horn in [61], consisting essentially of an exponential upper and lower horn wall taper, swept through a 180° space, fed from the center by a coaxial feed with a rear matching cavity. The fields from the symmetrical coaxial feed are expected to spread out in a primarily symmetrical manner. However, neither approach is appropriate for the design of such a system at W-band. While coax can be, and is manufactured into the W-band range, the associated connectorization tolerances and required chain of transitions and connectors to build and feed an appropriate system are prohibitive. In addition, use of a coaxial feed in this manner would significantly reduce integration capabilities of such horns, preventing good integration into an array or other multi-beam system. Feeding horns directly with WR-10 waveguide enables reliable integration strategies and ensures repeatability.

Due to the infeasibility of a coaxial feed, and the challenging nature of machining a thin mode controlling iris or a dual ridge waveguide system to operate over the band of interest, these features are removed from the design presented in this chapter. Instead, horn geometry is investigated to maintain wide absolute bandwidth operation with a high degree of self-similiarity over frequency. Utilizing the slope metric described in chapter 2, the horn antenna is evaluated for a wide range of geometric parameters, and a design is arrived at showing high self-similarity over frequency in the H-plane. Following this, the system is examined in the context of a linear array construction, to effect higher gain without damaging DF performance, and separately in the context of a circular array, to effect a full 360° DF system. Measured performance is found to be in good agreement with simulation. Fig. 3.1 shows the family of components to be discussed.

Fig. 3.1. Family of demonstrated curved aperture horn antennas. Left to right from top: single element (CNC and DMLS), 2 element array (DMLS), 8 element array (CNC) and circular array (CNC) configurations.

This chapter is organized as follows: Section 3.2 discusses the design of the curved aperture horn element, and examines the behavior of a range of geometries in terms of gain and pattern consistency over frequency. Section 3.3 examines the simulated DF performance of the system, and how to extend the minimum gain in the FOV by arraying without altering the DFF. Section 3.4 shows measured results for all systems, and discusses system level performance.

3.2 Design of a Curved Aperture Horn Antenna

The curved aperture horn has limited design information available through the open literature. As such, studies of the practical design must be carried out. The ideal case of the aperture described would be a cylindrical arc in free space described by three parameters. The radius of the arc 'L_{Horn},' The E-plane aperture width 'B_{Ap},' and the H-plane angular width 'W_{Ang}.' These parameters can be seen labeled in Fig. 3.2(a). In the case of a low frequency horn, this aperture could be constructed, as with a standard pyramidal horn, using relatively thin conducting walls, as is done in [61]. However, for a design operating at W-band, with any significant quantity of

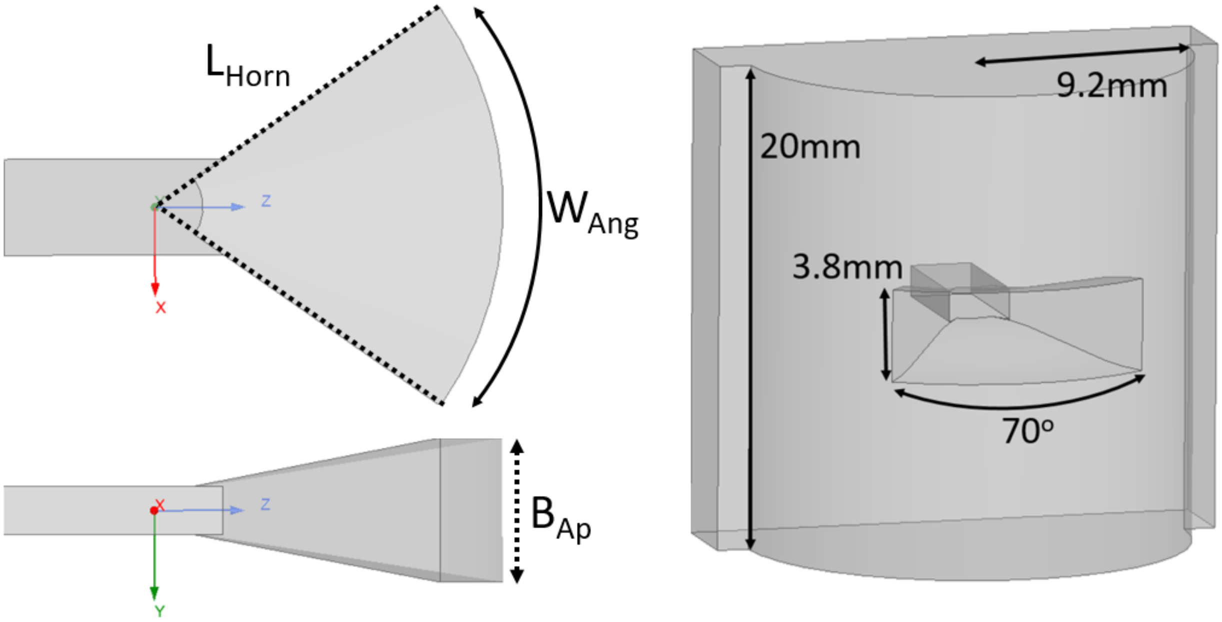

(a) (b)

Fig. 3.2. Illustration of idealized horn with critical parameters labeled (a) and illustration of final design for single W-band horn (b).

waveguide feeding, the ‘free space’ construction of a system is impractical. Instead, the designs pursued here look at cutting away material from a solid structure, with a continuous surface of radius L_{horn} forming a cylindrical block into which the horn is built. Additionally, the greatest departure from the ‘idealized’ horn design of Fig. 3.2(a) is the flat plate visible behind the curved surface in Fig. 3.2(b). This flat plate is the minimum dimension to allow integration of a WR10 waveguide flange located behind the horn. This has an impact on the final construced design, however is not included in the parametric studies of the horn geometry to be discussed. In the case of small values of L_{Horn}, the impact of this flange is expected to be nontrivial as it would form a large rear groundplane relatively close behind the horn aperture, however in the final design, the flange section does not protrude much beyond the cylindrical block, and does not have a substantial impact on the radiated fields.

The theory put forward in [68] describes a limited approximation of the curved aperture horn antenna, and puts forward formulations for the far field patterns of narrow angular width sectoral curved aperture horns under the assumption that there is no reflection from the aperture, and that the horn only supports the primary TE mode. These assumptions are not found to be supported by the full-wave simulations outside of an extremely narrow region of geometries, as can be seen in the appendix. As a result, design information for the curved aperture horn must be found through simulation. To that end, not knowing a-priori the pattern shape of a well-designed curved aperture horn, the slope metric described in chapter 2 is developed to minimize radiation pattern change over frequency, without enforcing a beam shape that may be unrealistic. To fully evaluate the pattern behavior, two metrics are utilized, the slope metric described in chapter 2, and the average boresight gain. Average change in beamwidth is also examined, but does not provide significant additional information. A collection of parametric studies is undertaken over the three parameters previously described, and over the additional structural parameter of the taper style between the waveguide E-plane height b and B_{Ap}. Three taper styles are investigated: linear, exponential, and sinusoidal tapers. Marginally superior performance in terms of pattern variability is found for the sinusoidal tapering of the upper and lower walls. The parametric study of the three primary geometric parameters is conducted over first a broad, sparse parametric space spanning horn radial length of 2-30mm, E-plane aperture width of 2-10mm, and 60-180° angular width. Poor performance for particularly large horns leads this to be refined to a narrower, more thouroughly investigated span covering 2-9mm (0.5-2.25λ at 75 GHz) L_{Horn}, 2-5mm (0.5-1.25λ at 75 GHz) B_{Ap}, and 60-180° W_{Ang}. Fig. 3.3 shows four plots, Fig. 3.3(a) and Fig. 3.3(b) show an overview of the 3D design space, with (a) showing the average slope change metric, in units of degrees^{-1}, and (b) showing the average boresight gain over frequency in dB. Fig. 3.3(c) shows a detail plot of the average slope change, foused on the plane through E-plane aperture width of 4mm. Finally, Fig. 3.3(d) shows a detail plot of the average boresight gain, through the same plane.

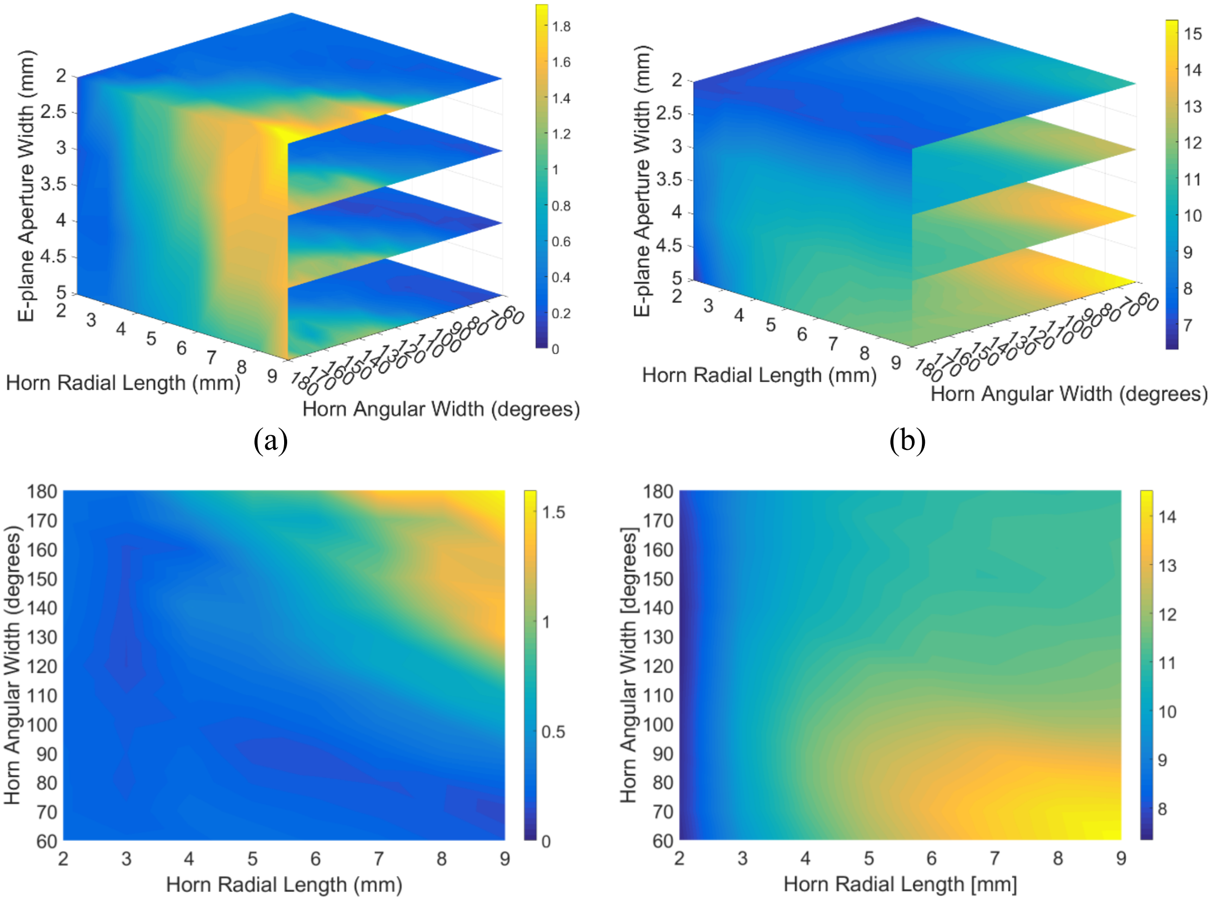

(a) (b)

(c) (d)

Fig. 3.3. Visualizations of the 3D parametric space with respect to the average slope change metric S (a), and average gain (b). Detail views of the plane at B_{Ap} = 4mm, showing average slope change (c) and average gain (d).

What these design plots show is a region of poor behavior (high values of S) for long, angularly wide horns, with reasonable behavior for a broad range of antennas throughout the design space. This makes intuitive sense, as the abrupt transition from the WR-10 guided mode to an effectively radial parallel plate transmission region is not conducive to a good match between modes. The best (i.e. lowest average slope change) performance is concentrated in a relatively narrow band geometric parameters, forming a curved path near the diagonal of the parametric space, stretching between 2mm length horns with 180° angular width, down to 9mm length horns with 60° angular width. Examining the average boresight gain behavior, we see that the region of poor behavior in the average slope change corresponds to a region of moderate to low gain, even for relatively large apertures. The region of the highest gain corresponds well to an area of relatively narrow angular width, long horn designs, which also shows notably consistent radiation patterns over frequency. Parametric sweeps with finer granularity in that high gain, low variation region arrive at a design which satisfies both low variation and high gain. The parameters for the design seen in Fig. 3.2(b), with angular width 70°, E-plane aperture width 3.8mm, and horn radial length 9.2mm. Fig. 3.4(a) shows the simulated normalized linear-gain H-plane behavior in 1GHz steps from 75-110 GHz, and Fig. 3.4(b) shows the un-normalized H-plane behavior in dB. Fig. 3.4(c) shows E-plane dB gain, not controlled for pattern shape. As is plain to see, the overall shape of the H-plane is extremely consistent over the band of interest, as desired. E-plane demosntrates primarily broad beam front, with side-lobes appearing after 90 GHz. Boresight gain varies from 12.8-15 GHz over the band of interest, with aperture efficiency of 46-60%, using the flat projection of the aperture viewed at boresight. 10dB beamwidth varies from 58.8-62.5°. Simulated $|S_{11}|$ is better than -15 dB across the band.

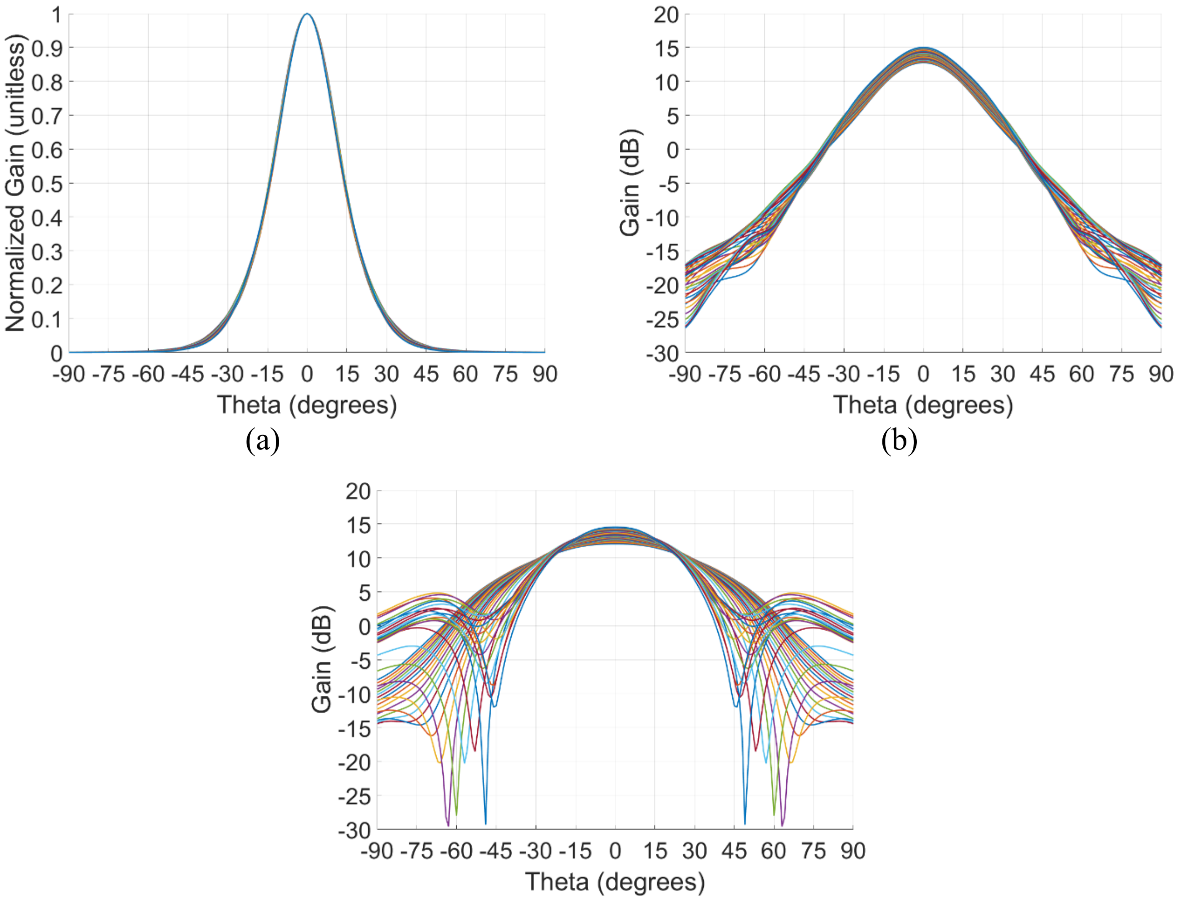

(a) (b)

(c)

Fig. 3.4. Plots of H-plane gain from a single curved aperture horn antenna as (a) normalized linear gain and (b) standard dB gain. And plot of E-plane gain in dB (c). All plots contain 36 curves, in 1GHz steps from 75-110 GHz.

3.3 Simulated Direction Finding and Arraying

3.3.1 Direction Finding with Curved Aperture Horns

Relating this system back to the design principles for good DF operation, we can find a good match to the H-plane behavior for cosine pattern shape parameters k = 0.5, n ≈30. This operating point can be plotted on the squint vs 10dB beamwidth graphs introduced in chapter 2, seen as the red indicator in Fig. 3.5. The DF system parameters utilized throughout chapter 2 as example parameters, 0.5 dB/degree DFF slope, -12dBi minimum gain, and 40° FOV, are here taken to be the system level requirements to be met with this design. As can be seen in Fig. 3.5,

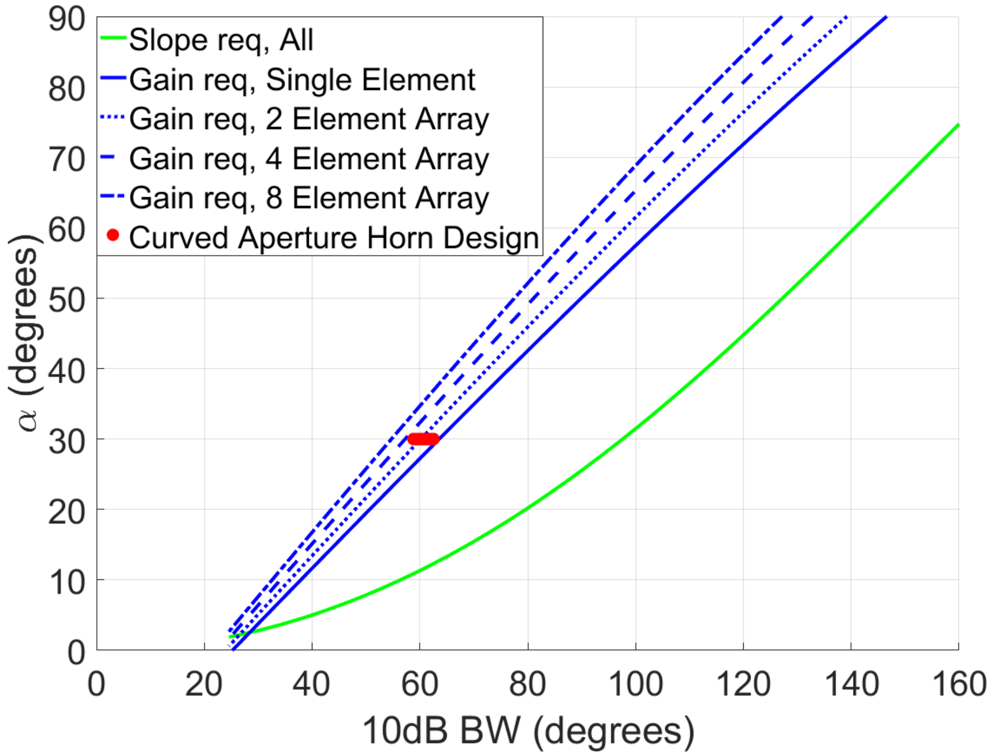

Fig. 3.5. Plot of curved aperture horn squint angle vs 10dB beamwidth. Red indicated location is the 10dB beamwidth of the curved aperture horn over frequency, indicated at 30° squint.

there is a wide range of angles, approximately 12-27° according to the theory, over which these requirements should be met for this design, however, as noted in chapter 2, there is some inaccuracy to that range, related to the pattern concavity beamwidth.

The theoretical analysis must be taken in conjuction with a detailed discussion of the concavity beamwidth, which for this deisgn is 80° for concavity less than 0.02 dB/degree^2, meaning the maximum squint possible maintaining good agreement with theory for a 40° FOV is, according to [32], approximiately 20°. Clearly, while the operating squint angle could be adjusted down to 20° to obtain the desired behavior, it is desirable to both be able to operate the system in a full 360° DF configuration, and to obtain the greatest possible DFF slope (via the maximum permissable squint), to minimize error. To obtain a full 360° DF system built as a circular array, the primary squint angles we should concern ourselves with are those used to construct a 6 or 8 element circular array, namely squint of 30° or 22.5°. Under ideal circumstances, to maintain high DFF slope over the entire FOV measured between antenna boresights, for these two squints a pattern concavity beamwidth of 90° and 120° should be maintained respectively for full boresight-to-boresight FOV, or 85° and 100° concavity beamwidth for the more limited 40° FOV. Clearly, the design in question does not meet the pattern concavity beamwidths put forward in [32]. However, when the DFF is plotted for 22.5° and 30° squint, as can be seen in Fig. 3.6, the patterns still display greater than 0.5 dB/degree slope over the FOV of interest. Re-examining the recommendation put forward in [32] of 0.02 dB/degree^2 as the limit for pattern concavity beamwidth, we can see that this bound appears too strict. The actual limit, at least for 0.5dB/degree DFF slope operation, appears closer to approximately 0.05 dB/degree^2, over which the design put forward here has a pattern concavity beamwidth of 100°, in line with what is expected to be necessary for 40° FOV with high slope. What is worth noting in both of these squint cases is the capabilities for full 360° operation. In the case of a hypothetical 8 element circular array, it can be seen that for a 22.5° squint, this design maintains high DFF slope out to approximately 22.5°, equal to the squint angle. Due to this, the system can be replicated about the 8 element circular array, and maintain high accuracy over the entire 360° detection area. For a hypothetical 6-element array with 30° squint, it can be seen that while the DFF slope does not remain above 0.5dB/degree out to ±30°, it does remain above 0. The range over which the slope is nonzero represents the full possible range over which detection can be performed, referred to as the ‘unambiguous FOV’. In cases where the SNR is of lesser concern, or if fewer recievers are desired, this system can be

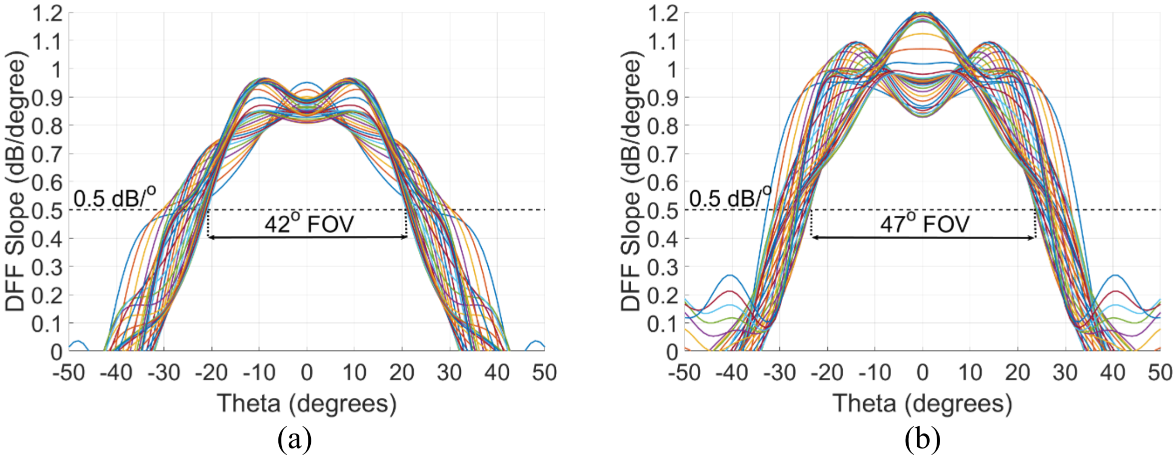

(a) (b)

Fig. 3.6. Plots of simulated DFF slope for (a) 22.5° squint, and (b) 30° squint, individual traces are 1GHz steps from 75-110 GHz, dashed line demarcates 0.5dB/degree DFF requirement.

utilized to perform 360° DF, and will still maintain high slope over large portions of the overall detection area. Additionally, the unambiguous FOV can be linked to the pattern concavity beamwidth. As previously mentioned, the required concavity beamwidth to cover a squint of 30°, and a FOV of 60°, is 120°. Over this range, the pattern concavity beamwidth of the curved aperture horn remains below 0.08 dB/degree^2. As such, it is the recommendation of this thesis to revise the limits put forward in [32] to match. That to achieve a high-slope DFF in a certain FOV, the pattern concavity beamwidth be examined limited to less than 0.05 dB/degree^2, rather than 0.02 dB/degree^2, and for an unambiguous (i.e. 0 slope minimum) FOV, the pattern concavity beamwidth be limited to less than 0.08 dB/degree^2.

3.3.2 Arraying, Feed Design, and Direction Finding

Putting aside the nuances of the pattern concavity relationship to the FOV, it is desired for this particular system to achieve the highest DFF slope possible within 40° FOV. As such, 30° is selected for the squint angle for system integration. As can be seen from Fig. 3.5, this places the device slightly beyond the boundary of the gain requirement. In cases of detection over both azimuth and elevation, this would not be permissable, however for this system operating over a single detection plane, E-plane arraying may be exploited to raise the gain without damaging the H-plane DF operation. The theoretical impact of this arraying can be seen in the different gain requirement curves shown in Fig. 3.5. As an initial test of system operation, the design is extended to an E-plane linear array of 2 elements, before being extended to a full 8 elements. Due to the 3.8mm E-plane aperture width, grating lobes cannot be avoided in the E-plane radiation pattern, however they do not have a significant impact on overall system performance as a single-plane DF sensor. Utilizing the slope change metric, studies of the spacing of the horn apertures are undertaken. The spacing of the apertures is made as tight as possible, while maintaining low pattern variation and manufacturability. The final value for the center to center separation is 4.2mm, a 0.4mm thickness E-plane wall separating the individual apertures. To feed the adjacent elements, internal waveguide 3dB splitters are implemented, studies are undertaken with a primary focus on the maximum $|S_{11}|$ within the band of interest. Given a fixed 4.2mm aperture separation, splitter geometry is parametrically analyzed with splitter length as the primary parameter, with splitter output bend radius as a fraction of splitter length as a secondary parameter. Successive sections are analyzed independantly. Splitter geometries are found to show superior performance for length and output bend radius such that the angle between splitter arms is near 40-50°. Splitter section maximum $|S_{11}|$ plots can be seen in Fig. 3.7. The waveguide inputs are placed on the rear of the antenna system, such that two adjacent standard W-band waveguide flanges can be connected flush to the system. An internal 30° H-plane bend with radius 5.5mm prior to the splitter network

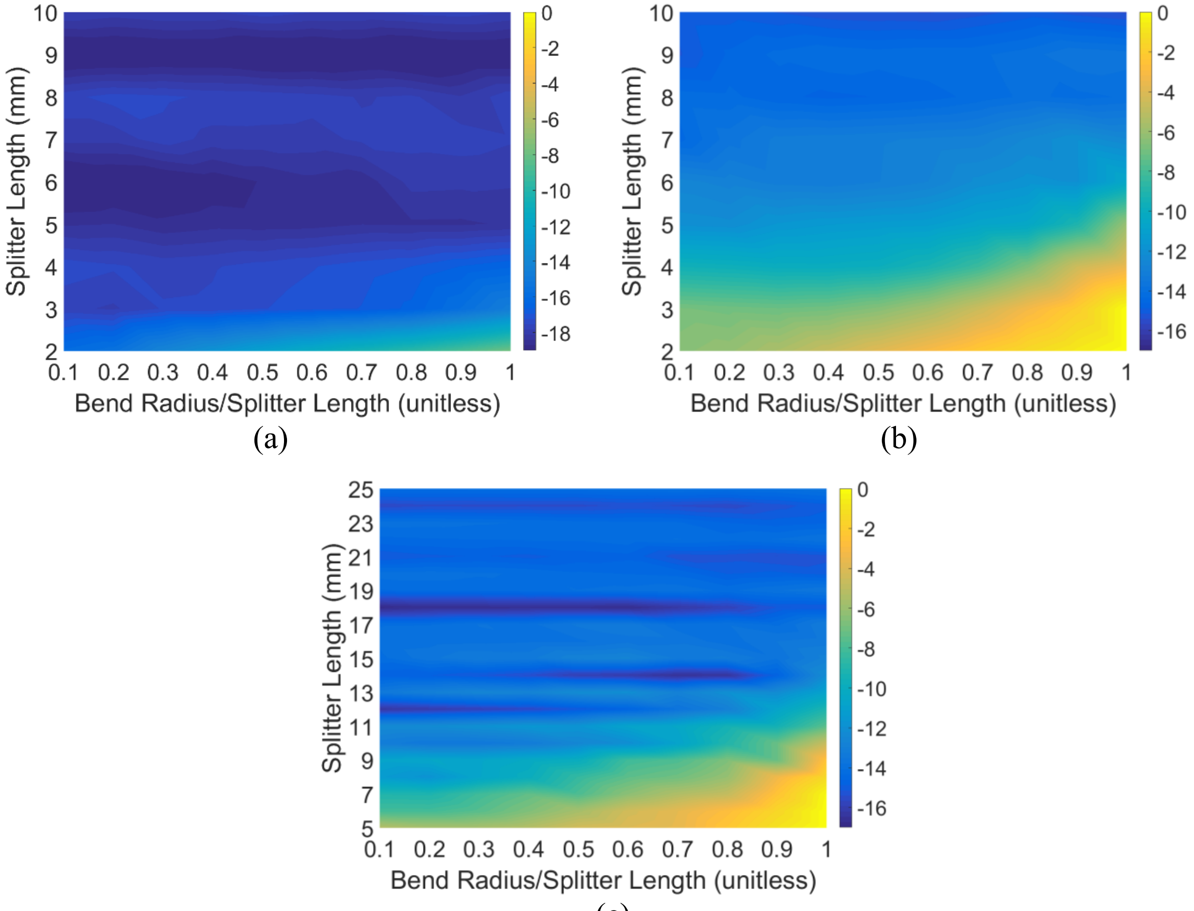

(a) (b)

(c)

Fig. 3.7. Maximum $|S_{11}|$ for successive splitter sections, plotted against splitter horizontal length, and radius of splitter output bend. (a) Section 1, showing $|S_{11}|$ between -7.8 and -19.46 dB, (b) section 2, showing values between 0 and -15.5 dB, and (c) section 3, showing values between 0 and -16.8 dB.

mechanically squints the two arrays. The illustration for the 2-element array design, and a schematic for the final 8-element array design can be seen in Fig. 3.8(a) and Fig. 3.8(b), respectively. Visible within the illustrated 8-element corporate feed are 3 splitters, labeled section 1, section 2, and section 3. The splitter visible in the design of the 2 element array utilizes the same dimensions as that of the section 1 splitter for the 8-element array. All dimensions for the waveguide feed structure and the critical array dimensions are listed in Table 3.1.

Design of the squinted DF front-end antennas results in additional critical geometry choices. Primarily, the profile of the space between the antenna cylindrical surfaces. Studies of the correct center mechanical structure examine a variety of different overall profiles. One notable design that is found to be detrimental is the natural structure used for squinting rectangular aperture horns, like that seen in [32], extending a flat conducting sheet to either side of the half-cylinder forming the horns, such that the overall structure is construced from a triangular block with cylindrical protrusions. The extended ground plane structure is found to negatively impact the radiation patterns significantly, and better agreement with the single element case is instead found for placing a flat sheet filling the space between the horn cylinders. This geometry can be seen in Fig. 3.8(a). Simulated H-plane remains consistent near beam boresight, however significant pattern spacial rippling becomes highly apparent near 50° from antenna boresight. Overall performance

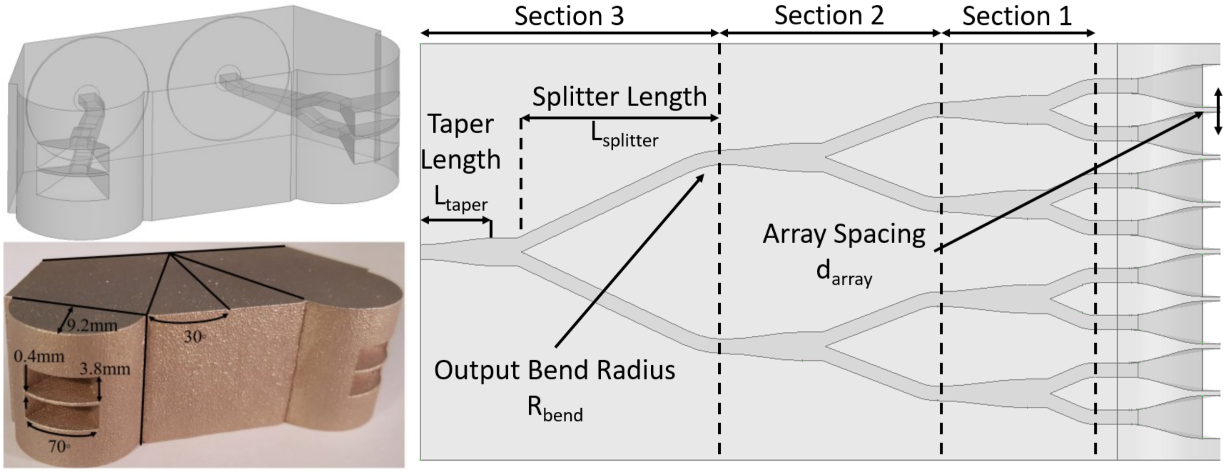

(a) (b)

Fig. 3.8. Illustration of 2-element array and picture of DMLS 3D printed implementation (a), and illustration of corporate feed with critical elements labeled (b).

TABLE 3.1. DIMENSIONS OF 8-ELEMENT ARRAY DESIGN

	Splitter Section Dimensions		
	Section 1	**Section 2**	**Section 3**
L_{Taper}	8mm	7mm	7mm
$L_{Splitter}$	4mm	10mm	18mm
R_{Bend}	2.8mm	4mm	7.2mm
	Common Dimensions		
R_{Input}	5.5mm		
L_{Horn}	9.2mm		
$B_{Aperture}$	3.8mm		
$W_{Angular}$	70°		
d_{Array}	4.2mm		

of DF remains tolerable, with the 0.5 dB/degree FOV achieving to 51.4° in simulation. Minimum gain in the FOV for this system is -5.4dBi, 6.6dB above the -12 dBi limit. The simulated system performance for the 2-element array is plotted in Fig. 3.9. Notably, due to the wider beam shape than the cosine beam approximation used in Fig. 3.5, the minimum gain is above -12dBi even for the single aperture case, however the demonstration of the arraying technique remains important to demonstrate both the ability to maintain DF capabilities with E-plane arraying, and to improve the overall detection range of the final constructed system.

3.3.3 High Gain Array and 360° System

With both the single-aperture, and a design for a proof of concept system in place, the final design work extends to two systems. One extending the design to even higher system gain using an 8-element E-plane array, and one extending the design to a 360° capable set of single horns. Due to the length of the 8-element array corporate feed network, the system is substantially larger than the design seen in Fig. 3.8. To save on system weight, and further improve agreement with

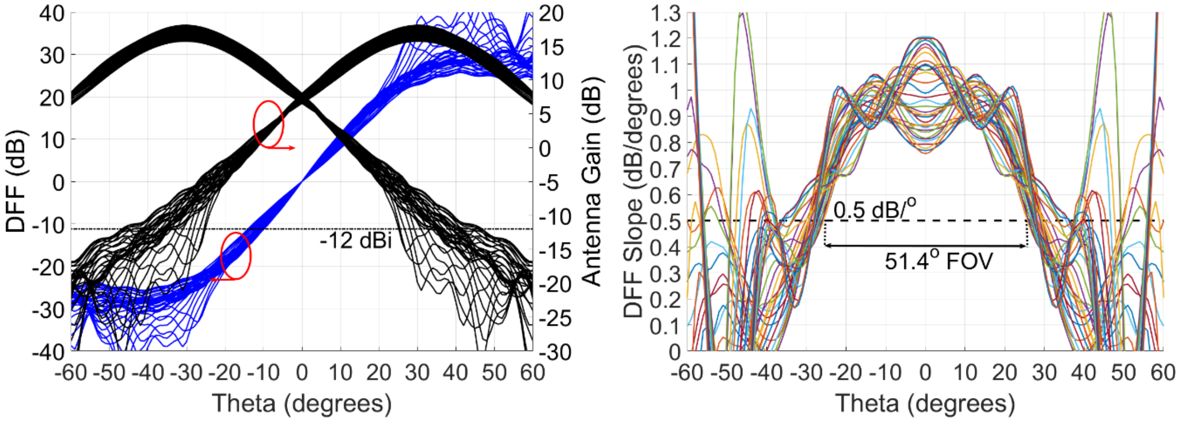

(a) (b)

Fig. 3.9. (a) 2-element array system simulated patterns (black) and DFF (blue) with -12dBi marker, and (b) 2-element array system simulated DFF slope, with FOV of high DFF slope indicated. Individual traces are 1GHz steps from 75-110 GHz.

free-space operation, the large flat region located bewteen the horn cylinders is cut away. Various profiles for the intervening space including various parabolic and cylindrical profiles are investigated. Best performance is found for the removal of material forming a cylindrical section, centered between the horn apertures. This model can be seen in the lower left of Fig. 3.1. Simulated and measured performance are shown for this model in section 3.4. As remarked previously, due to the wide unambiguous FOV for the system, the design is capable of operation in a 360° DF array of 6 elements, however will lose some DFF slope, and thus some accuracy, near each antenna boresight. This system is also constructed, utilizing the same exterior profile for each element as the 8-element array, such that the system could be extended to an 8-element E-plane array without altering the system footprint. This system can be seen in the lower right of Fig. 3.1. The simulated and measured system behavior is reported in section 3.4.

3.4. Manufacturing and Measured Results

3.4.1 Single Horn Manufacture in DMLS and SLA

The manufacture and design of the full 8-element array and 360° DF system are performed in stages to demonstrate the validity of the simulations and theory behind the design, and to demonstrate what manufacturing technique would be most suited to the final system constructions of the 8-element array and the 360° array. The first pieces to be manufactured are two copies of the single curved aperture horn, seen as the upper left two items in Fig. 3.1. The two pieces are manufactured in different methodologies to examine their different characteristics. One piece is manufactured in a traditional split-block approach from aluminum, with the other manufactured from DMLS aluminum through a commercial prototyping company. The split block piece is manufactured with the split thorugh the H-plane of the system, rather than the preferred E-plane split, due to mill tooling limitations. As a result, currents flowing across the H-plane boundary are disrupted. Assembly of the CNC horn with a combination of screws and silver epoxy improve behavior, but do not fully resolve disagreement with simulation. Simulated and measured VSWR for the CNC and DMLS single-horn construction are plotted in Fig. 3.10(a). The CNC manufactured piece demonstrates two additional resonance behaviors not present in the DMLS and simulated piece, likely due to currents flowing across the cut in the structure. The DMLS manufactured piece shows significantly good agreement with both magnitude of match and location of resonances. Overall VSWR for all pieces remains good below 1.5. Fig. 3.10(b) shows normalized H-plane linear gain radiation patterns, with simulations on the left half of the plot, and measured results on the right half of the plot for qualitative comparison.

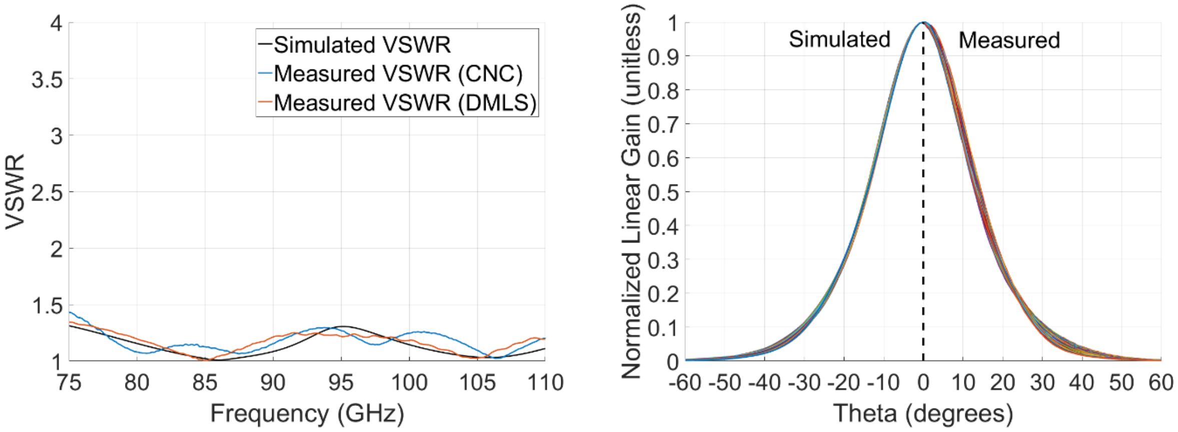

(a) (b)

Fig. 3.10. (a) Simulated (black trace) and measured VSWR performance for the CNC (blue) and DMLS (red) single curved aperture horn. (b) Simulated vs measured H-plane linear gain, in 1 GHz steps from 75-110 GHz.

3.4.2 2-Element Array System Measurements

The success of the single-horn manufacture in DMLS prompts the construction of the proof of concept 2-element array in the same DMLS aluminum process. The primary test being conducted is to examine the capabilities of the DMLS process to accurately reproduce the splitter geometry at W-band, and particularly the sharp 45-50° edge separating the upper and lower branches of each splitter. This edge is challenging for the DMLS process to reproduce accurately at this frequency due to the surface roughness and tendency of the sintered powder to form stray nodules which are electrically significant. The additional resonances and reflections caused by these discrepancies can have a substantial impact. The results of this can be seen in Fig. 3.11(a),

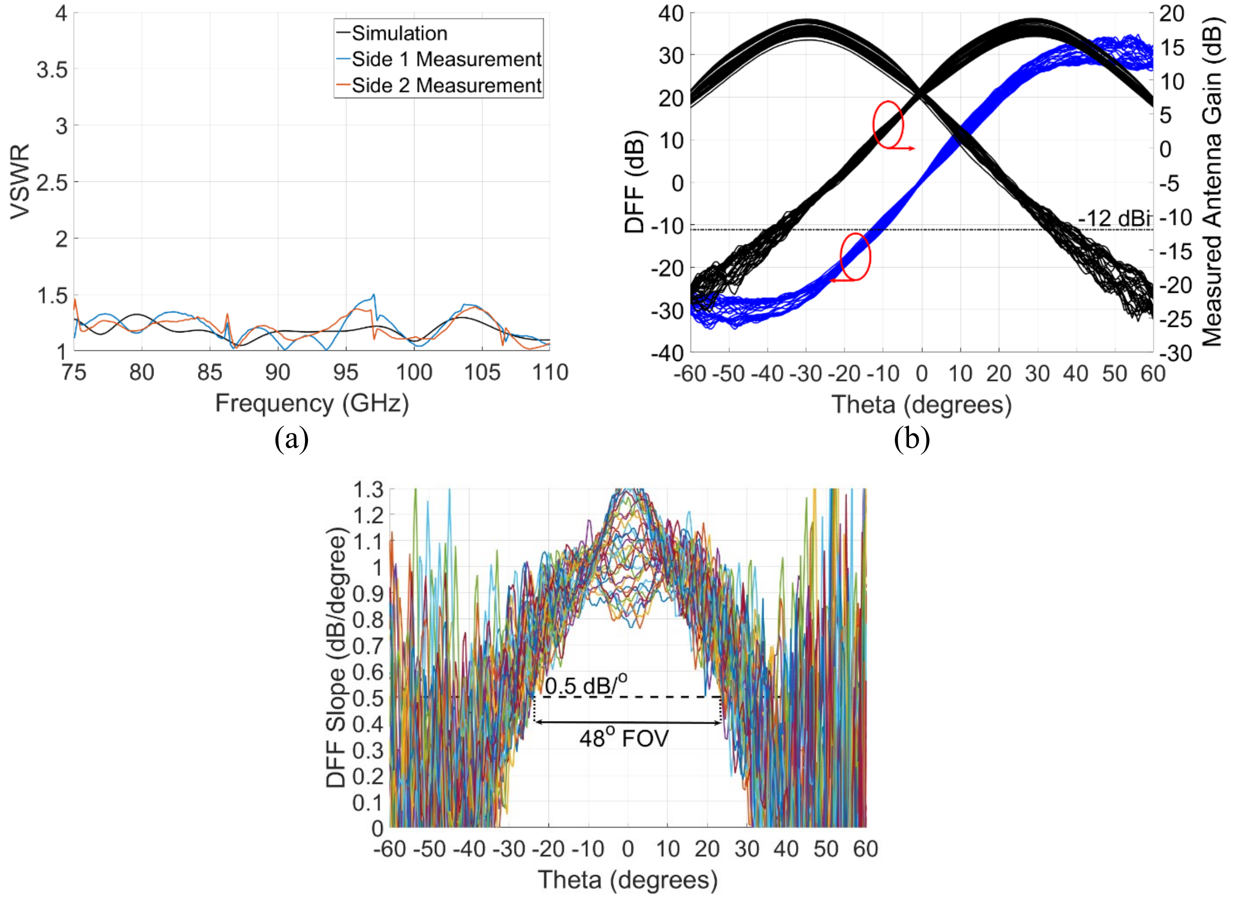

(a)

(b)

(c)

Fig. 3.11. (a) Simulated (black trace) and measured VSWR performance for side 1 (blue) and side 2 (red) of the DMLS printed two-element array design. (b) Measured gain performance and DFF for 2-element array system, traces show 1GHz setps from 75-110 GHz. (c) Measured DFF slope for 2-element array system, traces show 1GHz steps from 75-110 GHz.

showing the difference between the resulting match of the simulated and measured 2-element array. As can be seen, while the VSWR remains below 1.5, there are additional resonances and narrowband behaviors not present in simulation due to internal defects. Fig. 3.11(b) shows the measured DF and patterns. DMLS construction has a nontrivial impact on manufacturing repeatability. Measured gain between the two sides shows an average difference of 0.24 dB between the left and right antennas. This results in a small but noticable shift in the position of the DFF, as described in [20]. Due to arraying, there is an average measured increase of ~2.6 dB of gain overall, this brings the FOV minimum gain to -5.35 dB. Fig. 3.11(c) shows measured DFF slope. Desired 40° FOV maintains high DFF slope greater than 0.5dB/degree, and unambiguous FOV remains wider than 60°

3.4.3 8-Element Array System Measurements

Successful E-plane arraying of the DF antenna element informs the mechanical design for the 8-element array system. Due to sensitivity of repeated equal-power splitters to DMLS fabrication, the fabrication of the 8-element array is undertaken with a combination of techniques. Manufacture of the bulk of the splitter and horn array is undertaken with a single E-plane split, as shown in Fig. 3.12(a). However, to assemble the entire system, a 30° input bend in the H-plane is

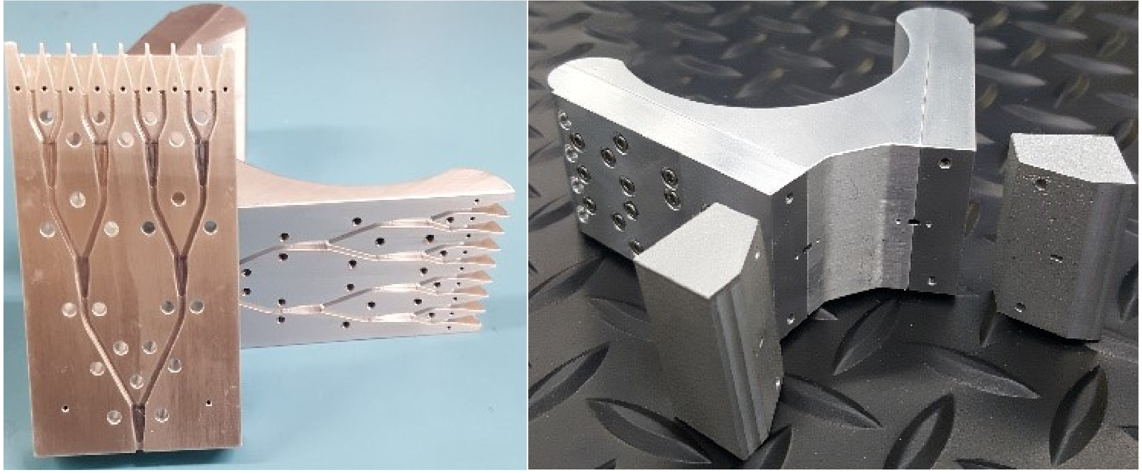
(a) (b)

Fig. 3.12. Views of mid-assembly 8 element array system, showing (a) array feed geometry detail, and (b) DMLS input pieces prior to surface flattening and assembly.

required. The curved surface involved in machining an E-plane split through the H-plane bend is challenging to achieve to the accuracy required. Instead, input waveguide flange and connector bend pieces are separately DMLS 3D-printed. The machined components can be seen in Fig. 3.12(b). Clearly evident in Fig. 3.12 is the removed circular section of metal from between the horn apertures. Measured and simulated match and DF performance are plotted in Fig. 3.13. As can be seen from examining the plotted gain patterns and DFF in Fig. 3.13(a) and Fig. 3.13(b), DFF remains a consistent, linear function in the FOV despite the electrically larger system it now comprises. Reflections from the opposing arm are minimal and do not significantly corrupt the patterns. Some gain difference is present between the two channels; however the most substantial difference is below the band of iterest, between approximately 70-72 GHz. The gain requirement of -12dBi in the FOV is thoroughly satisfied, with the left and right antnenas higher than the gain minimum in the FOV by 13.5dB and 13.8dB, respectively. The measured data compares favourably with simulation. Fig. 3.13(c) and Fig. 3.13(d) show the measured and simulated DFF slope. This design achieves the desired 40° FOV. Also of note is the unambiguous FOV, which remains greater than the 60° angle between the antennas. As a result, a full 360° system can be constructed. The VSWR plotted in Fig. 3.13(e) shows reasonable agreement between simulated and measured performances. While some resonances are shifted, the overall level of the match tracks well with simulation. Differences between the right and left channels and the simulated data are expected to be primarily due to the differences between the 3D printed input bends. These pieces, shown in Fig. 3.12(b) require further machining to smooth the mating faces due to external warping, and it is expected that the dimensional distortion is not limited to the exterior faces. overall match remains below 1.5 VSWR for the majority of the band, with an average value of 1.3.

As mentioned, one primary use of these designs is in enabling nearly frequency invariant high speed detection schemes for AODF. As a basic metric for the performance of this system under that paradigm, the minimum error (in the absence of noise) of estimated angle of arrival based on a single linear fit to the average DFF can be calculated. This represents the baseline error

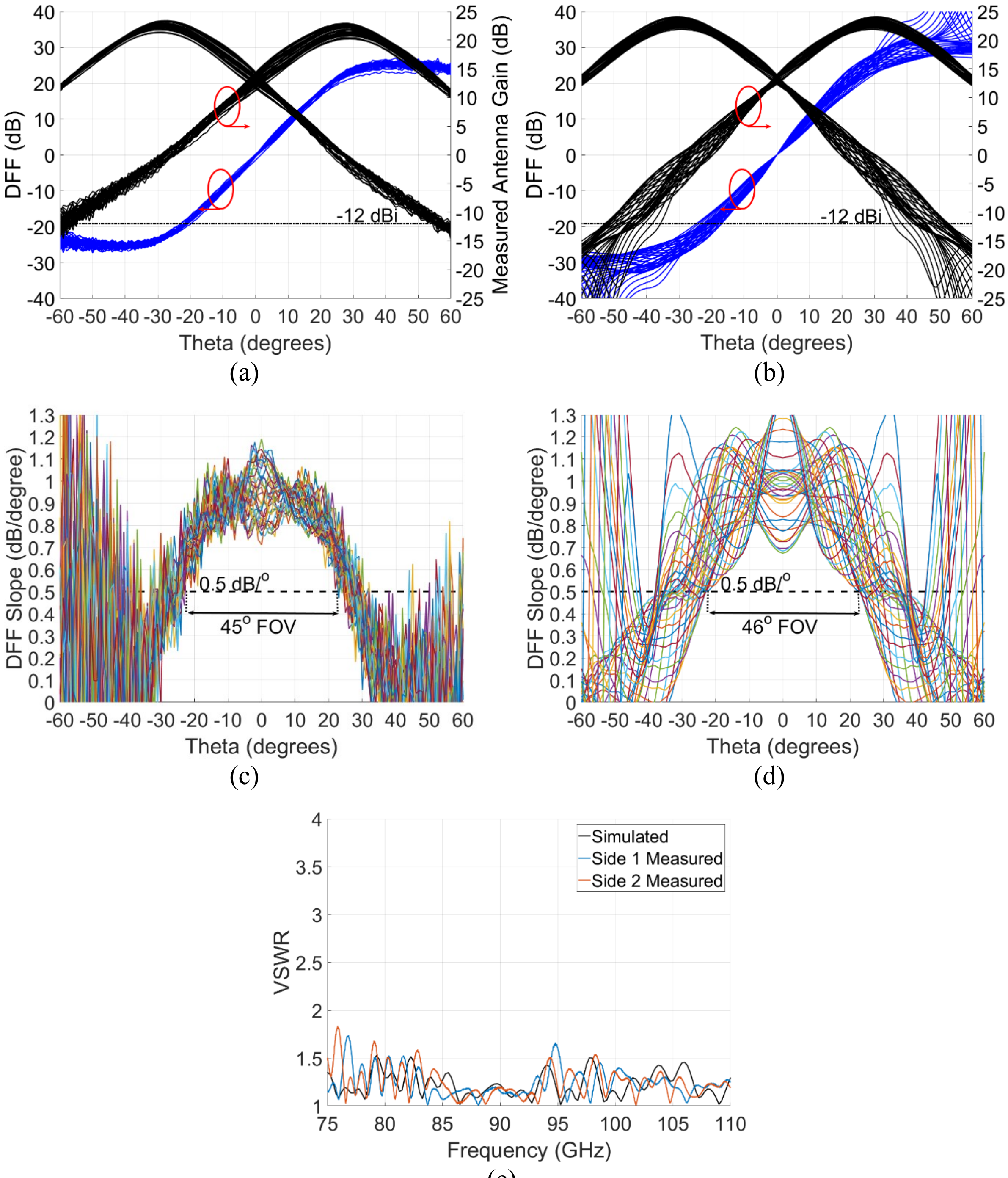

(e)

Fig. 3.13. Measured and simulated results for 8-element array system. (a) Measured radiation patterns (black) and DFF (blue). (b) Simulated radiation patterns (black) and DFF (blue). (c) Measured DFF slope. (d) Simulated DFF slope. (e) Measured (blue, red) and simulated (black) VSWR. (a)-(d) consist of traces in 1GHz steps from 75-110 GHz.

incurred in a system which discards frequency information in favour of rapid detection. i.e. utilizing a single linear function of the received power ratio to approximate the true DFF. Fig. 3.14 shows the error with respect to the true angle of arrival. Within the 0.5dB/degree FOV, low minimum error (<2°) can be maintained due to the good linearity of the DFF. However, as the operation is extended, and the unambiguous FOV limits are approached, the error increases to 5°. Obviously, by utilizing a more nuanced estimator than a linear fit, or that does not discard frequency information, this minimum error can be reduced drastically.

3.4.4 360° Detection System

Finally, the design introduced to enable 360° AODF can be seen in the lower right of Fig. 3.1. The system consists of the same exterior footprint of the 8-element array, replicated about a central axis to form six antennas. Each antenna is constructed in two pieces, split down the E-plane, then assembled into wedges and screwed down onto a shared mounting plate and waveguide

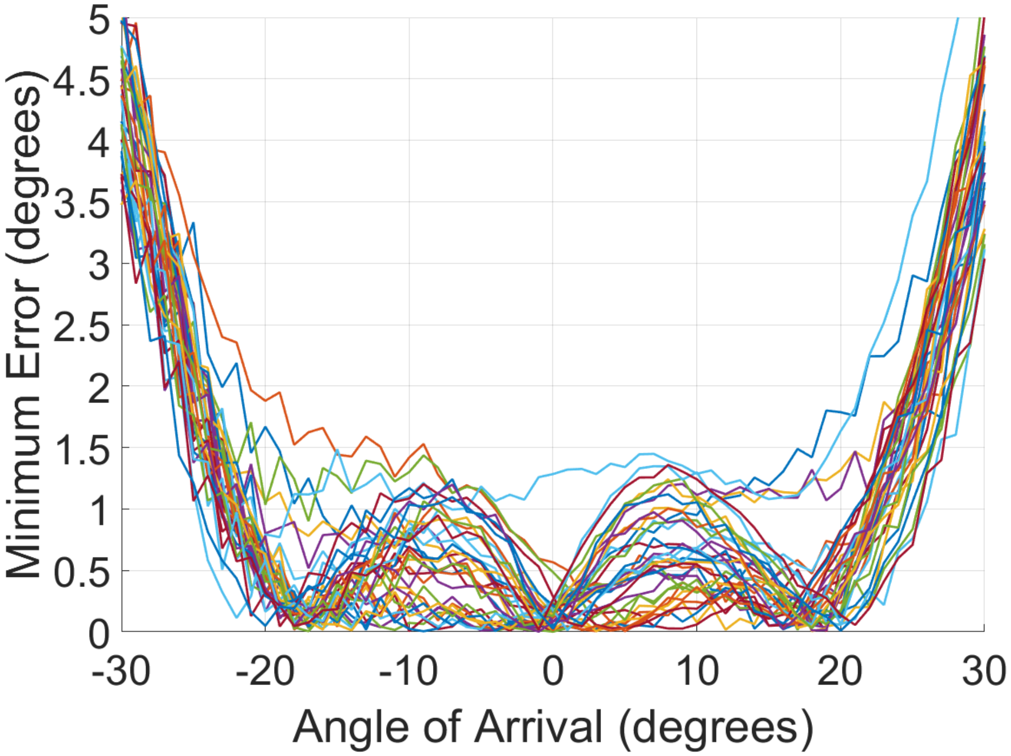

Fig. 3.14. Minimum error in the FOV, based on a linear fit to the average DFF. Individual traces are 1GHz steps from 75-110 GHz.

flange. Taken as adjacent pairs, they form six DF subsystems. For the sake of cost, the individual antennas are not implemented as 8-element arrays, but only as a single horn per arm. However, due to matching the size required for the 8-element array, this system could be built to achieve higher levels of gain if desired. Behavior for the 360^{o} system is plotted in Fig. 3.15. As can be seen from Fig. 3.15(a)-Fig. 3.15(d), measured and simulated performance remains in good agreement for radiation patterns, DFF, and DFF slope. There is some disagreement in the match, likely caused by the force of the waveguide mounting screws forcing a small gap between the waveguide flange and the body of the horn.

3.5 Conclusions

This chapter presents the design and fabrication of a family of high DFF slope direction finding front end antennas. The design process illustrates the utility of the AODF theory presented in chapter 2, and illustrates the power of pattern control as a method of achieving wide bandwidth DF operation in mm-wave frequencies. The horns designed cover a wide absolute bandwidth of >75-110 Ghz with high gain, high DFF slope operation, achieving better than 0.5dB/degree slope and better than 0dBi minimum gain across a FOV of 40^{o}. The antennas are designed for tight H-plane pattern control, and achieve <3.8^{o} 10dB beamwidth variation over 75-110 GHz. Multiple configurations of the curved aperture horn are manufactured by numerous techniques, and good agreement with simulation is obtained. This design also adaptats the little used curved aperture horn to operation at W-band, and supplies design parametric studies that are lacking from the literature. This chapter illustrates the methodology of achieving high-gain, pattern controlled DF and spectrum sensing at mm-wave frequencies.

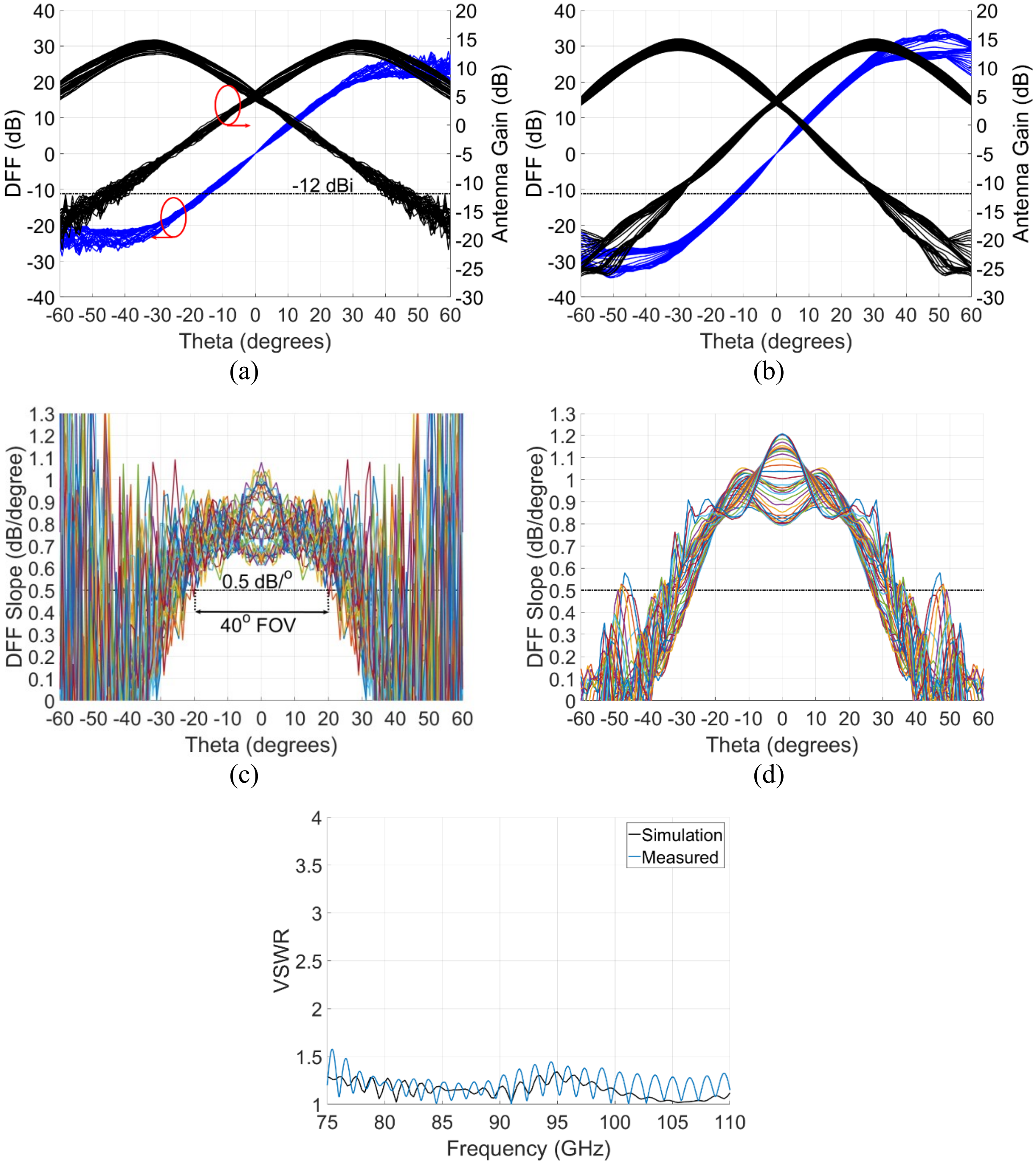

(a) (b) (c) (d) (e)

Fig. 3.15. Measured and simulated results for 360° DF system. (a) Measured radiation patterns (black) and DFF (blue). (b) Simulated radiation patterns (black) and DFF (blue). (c) Measured DFF slope. (d) Simulated DFF slope. (e) Measured (blue) and simulated (black) VSWR. (a)-(d) consist of traces in 1GHz steps from 75-110 GHz.

CHAPTER 4

MICROWAVE SPECTRUM SENSING AND DIRECTION FINDING

4.1 Introduction

Enabling spectrum sensing and direction finding at microwave frequencies requires the flexibility to fulfil multiple competing design goals. It is desirable to achieve wide relative bandwidth, low-profile, dual polarization, and high efficiency within a single aperture. Systems that fulfil most of these goals in the L-K band range frequently make use of frequency independent antennas [1, 69], often taking the format of multi-arm sinuous [7, 34, 70] or MAW spirals [71-75]. However, these antennas are generally limited to <50% efficiency by their bidirectional nature. While some systems achieve higher efficiency, this is generally either in narrow frequency bands [76] or makes use of large dielectric loading [77], though this comes at a cost in system weight. Other wideband sensors, like log periodic dipole arrays [69] , conical spirals [78], and pyramidal log periodic antennas [79], are more challenging to manufacture, and significantly larger. Achieving wideband single aperture dual polarized performance puts forward an opportunity to redesign a naturally broadband, unidirectional, low dispersion structure, the TEM horn, to achieve single aperture dual polarization with naturally high efficiency.

The TEM horn is a well known and popular wideband radiating element, developed since the mid 70s [80, 81]. They generally have benefits of simple, low-cost construction, and see use in a variety of areas, most commonly ground penetrating [82] and other sensing [83] applications. The basic horn has a variety of design studies that are well established in the literature [81, 84]. Modern design for the TEM horn focuses on adapting it for reduced size through a variety of methods. Early miniaturizations began with resistive terminations of the aperture [85, 86] forming a loop terminating behind the antenna. This reduces reflected energy from the antenna aperture, and the loop structure allows for the low frequency behaviors of the formed loop antenna and the TEM horn to be constructed in phase to direct low-frequency radiation forward [85-87]. Further advancements in this area have focused on modifications to the loop section, including removing resitive terminations [88] and modifying the geometry of the rear loop [89], and the addition of current paths forming additional electric monopoles [90]. Further study of the accurate phasing of TE and TM spherical modes [87, 91, 92] enabled the addition of an included bowtie antenna, phased correctly for forwards radiation with the low frequency compensation loop by addition of a capacitive slot, altering the phase of the currents flowing onto the loop from the TEM horn. However, the TEM horn has the drawback of lacking dual polarized radiation. Some examples of dual polarized TEM horn arrays exist in the literature [93], however they utilize adjacent, orthogonal TEM horns to achieve dual polarization. Constructing a shared aperture, dual polarized TEM horn must be achieved by utilizing a 4-conductor system, with opposing conductors excited in pairs as TEM horns. Due to utilizing 4 conductors, the familiar wideband means of exciting TEM horns [94] are no longer applicable. The most comparable feed systems will be seen in designs like the quad-ridge cylindrical horn [35] or double ridge transitions seen in some TEM horns [95].

The literature holds no clear sources for this design. As such, this thesis analyzes the dual polarized TEM horn in isolation and offers guidelines for is construction. The basic TEM horn can be seen in Fig. 4.1 (a). Following this, the design is miniaturized, and simulated results for the miniaturized design and baseline case are compared, demonstrating successful miniaturization.

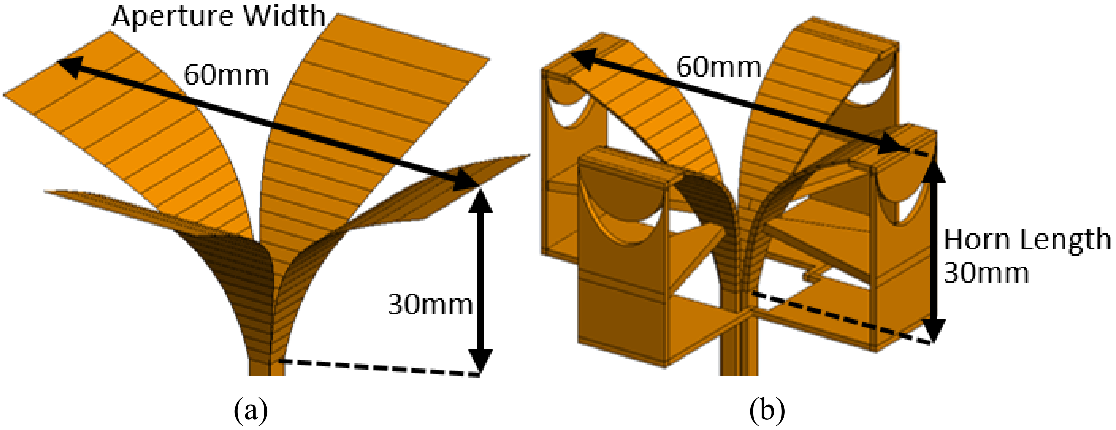

(a) (b)

Fig. 4.1. Dual-polarized TEM horn (a), and miniaturized combined TEM horn, loop antenna (b).

Building on the miniaturized design, the patterns are improved for spectrum sensing and direction finding by the addition of a cavity backing. Finally, the design is completed with the design of a quad-ridge feed. The designs of the cavity backed TEM horn, with and without the quad-ridge feed are shown in Fig. 4.2 and Fig. 4.3. The designs are fabricated and measured. Measured match performance shows reasonable agreement with expectation for the bundle-fed device, and explainable errors due to arm positioning for balun fed device. Measured directivity shows good agreement in both level and pattern shape, however gain is found to be lower than expectation. The source of error is greater than expected power losses in the absorber. Potential for re-optimization with more accurately characterized absorbers is also discussed.

This chapter is organized as follows: Section 4.2 discusses the design of a dual-polarized, miniaturized TEM horn, from the initial design of a baseline horn to the use of spherical modes engineering to reduce the overall horn footprint. Section 4.3 discusses cavity integration and the removal of narrowband effects that degrade overall performance. Section 4.4 investigates the design and integration of a dual-polarized integrated balun feed. Finally, Section 4.5 reports the fabrication and measurements of the bundle fed and balun fed systems, and analyzes their results.

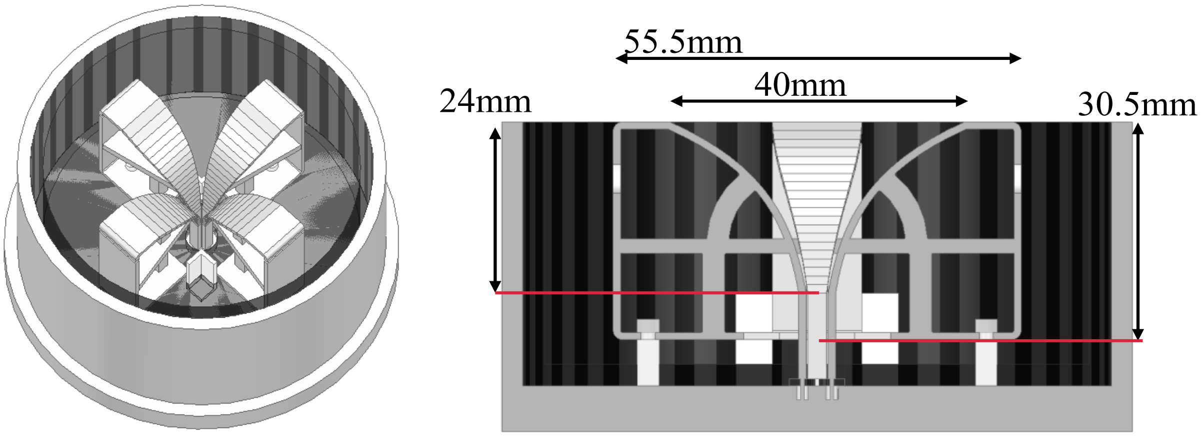

Fig. 4.2 Simulation model of bundle-fed cavity-backed dual-polarized TEM horn, with some relevant dimensions indicated.

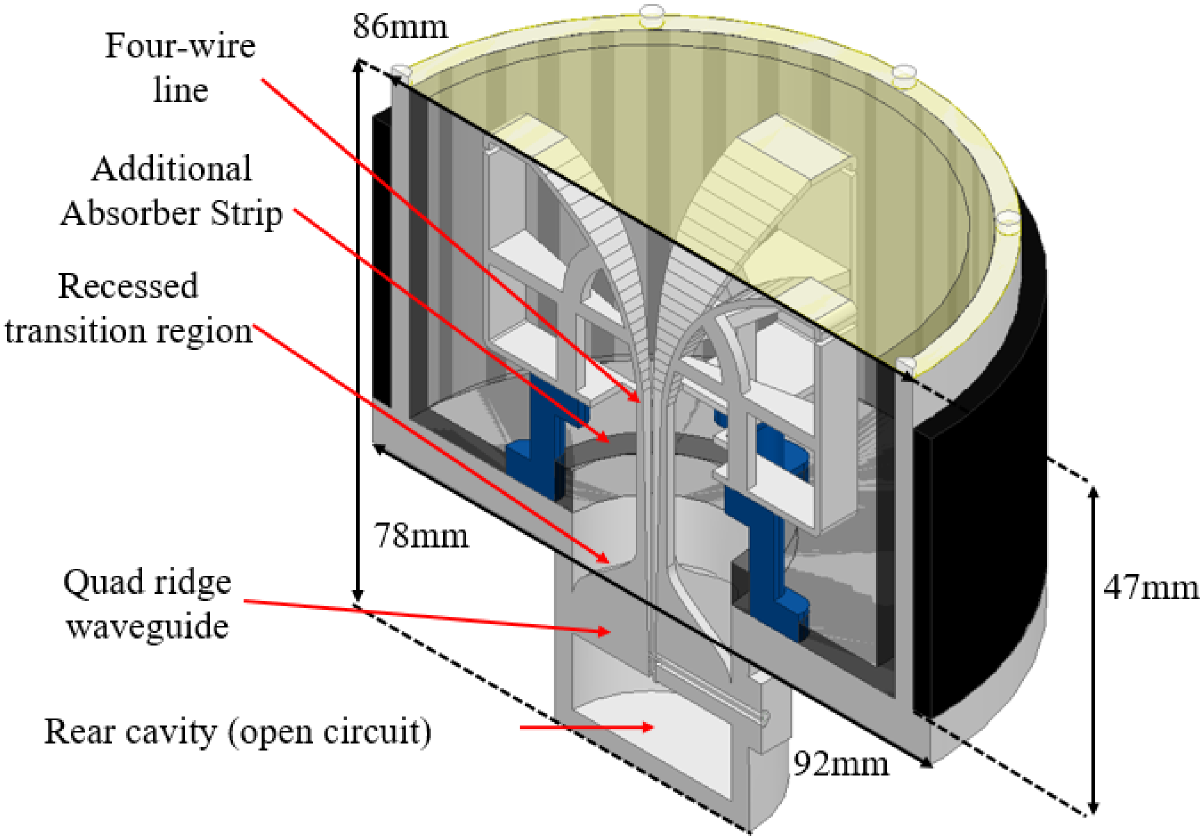

Fig. 4.3. Simulation model of quad-ridge feed cavity-backed dual-polarized TEM horn, with some relevant dimensions indicated.

4.2 Miniaturized TEM Horn Radiating Element

4.2.1 Design of a Dual-Polarized TEM Horn

Basic studies are needed to obtain a full view of standard operation of the dual-pol TEM horn, as there are not design guidelines for adapting the 2-conductor design to a 4-conductor design; TEM horns commonly utilize tapered baluns [71], however for this work that is infeasible and the antenna is considered as if fed with a coaxial bundle feed. This design follows the style of modern horns [71] and utilizes an impedance taper from the line impedance to free space rather than maintaining constant characteristic impedance while physically tapering the horn sides to achieve an appropriate ~λ/2 aperture size [96]. In [97], it is shown that better match for a standard TEM horn can be obtained for aperture impedance lower than free space, even as low as 120Ω.

For a similar study to determine a guideline for dual-pol TEM horns, the characteristic impedance of the input four-wire line must first be determined. Two wire parallel plate transmission lines have analytical formulas [98] for their characterisitic impedance; however, no such fomulas exist for the four wire line proposed here, therefore the characteristic impedance curve must be obtained through simulation. A four wire transmission line constructed from PEC sheets is simulated for varying line width and distance utilizing Ansys HFSS, and fit to a polynomial curve for design purposes. The characteristic impedance of the four wire system can be seen in Fig. 4.4, where it is calculated with thin conducting sheets. The inset figure however is an example figure with thick conductive sheets, to illustrate better the field behaviors in the expected system.

It is possible to create an exponential impedance taper from line impedance (here chosen as 100Ω with D=3mm, W=2.57mm, as if fed by a bundle of 50Ω ‘086’ coaxial cables), to an arbitrary higher impedance with the characteristic impedance now known. An exponential impedance taper is simulated using a basic model of a dual-pol TEM horn with equal aperture width and horn length, shown in Fig 4.1 (a). The best match and gain operation occur for aperture

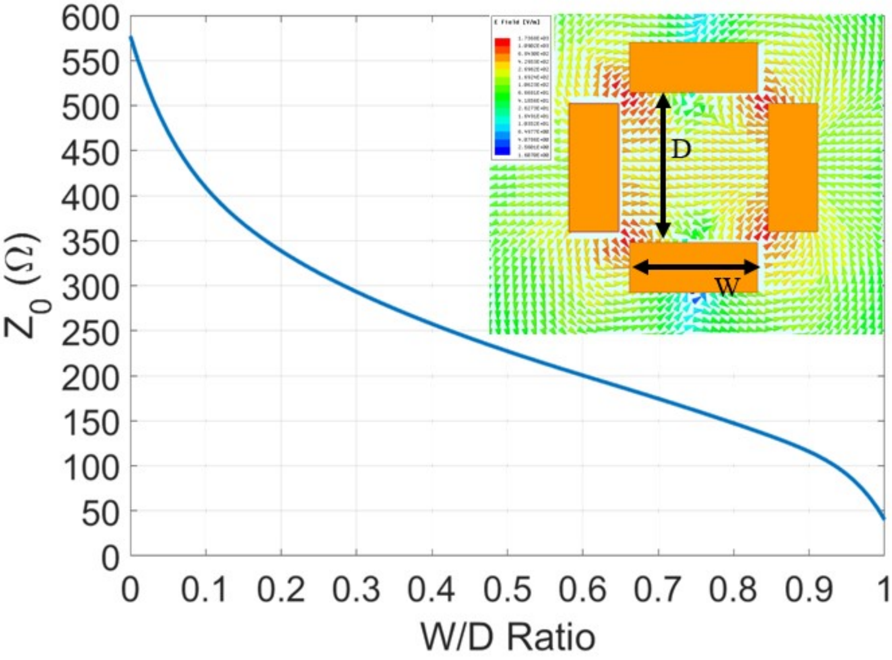

Fig. 4.4. Characteristic impedance of 4-wire line as a function of W/D ratio, calculated with thin sheets. Inset figure shows thick conductor model with W and D labeled.

impedances in the range of 240-300Ω as seen in Fig. 4.5.

The impact of the other two primary parameters, aperture width (W) and horn length (L), on the antenna performance is also studied. Using an aperture impedance of 270Ω, the aperture width and horn length are varied with permutations of 60, 90, and 120mm in both dimensions. Fig. 4.6 shows the impedance match and gain operation in these 9 cases. As seen, as the horns length to width ratio reduces, the turn-on with respect to match becomes sharper. However, the shorter horns show significant deviation from good directional gain performance, as they begin to resemble bowtie antennas, limiting the usable gain bandwidth. It can be seen from the figure that the turn-on point with respect to impedance match occurs for approximately an aperture width of λ/2.4 (illustrated with vertical dashed lines). For the longer horns, it can be seen that this turn-on point only corresponds to a significant inflection point in the match, and not to the point where $|S_{11}|$ drops to below -10dB.

4.2.2 TEM Horn Miniaturization

With impedance and size guidelines in mind, a dual-polarized TEM horn can be designed. However, the antenna is relatively large if good gain and impedance match are required at lower

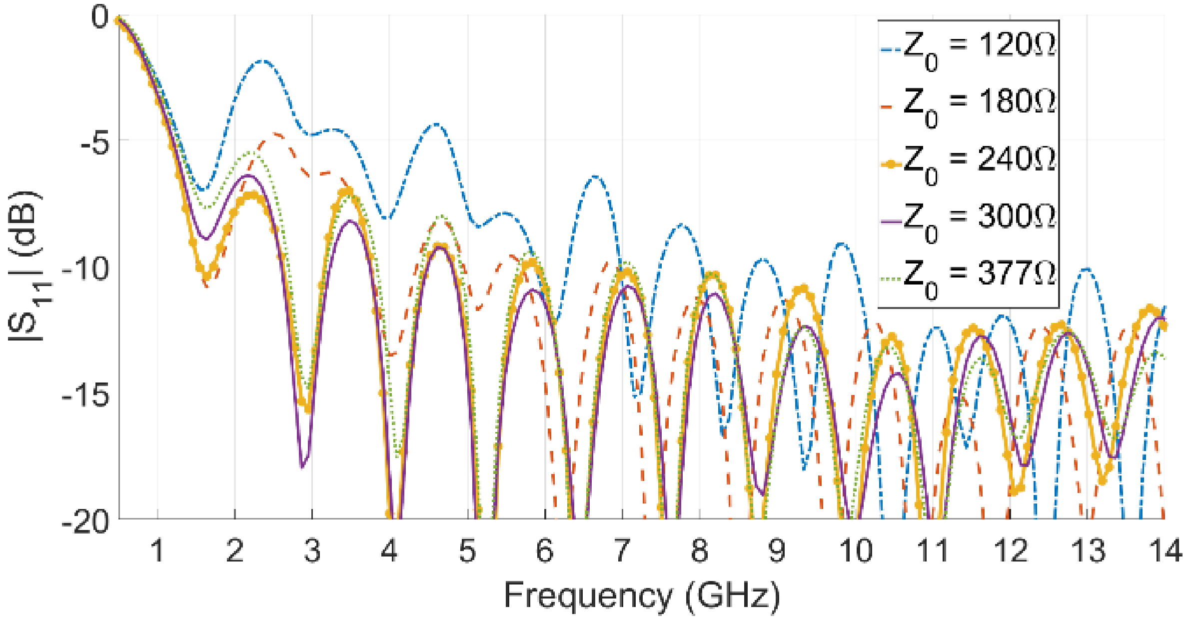

Fig. 4.5. $|S_{11}|$ for varying aperture impedances from 120-377Ω

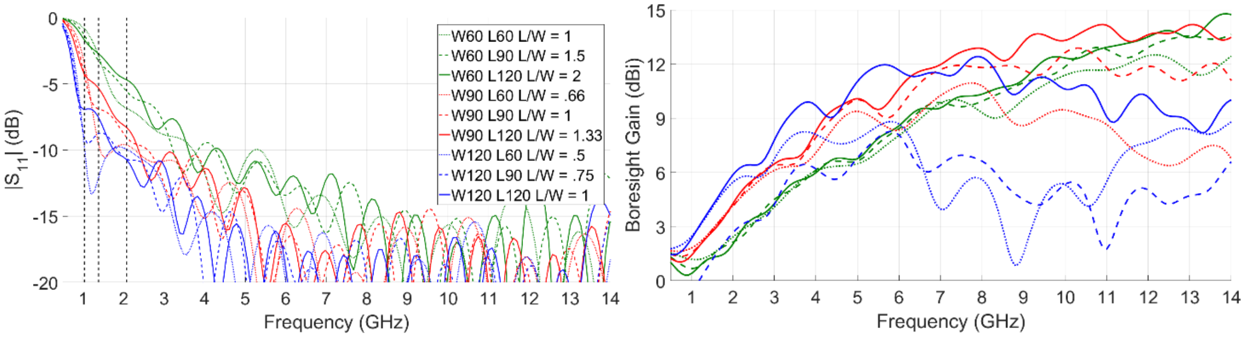

(a) (b)

Fig. 4.6. $|S_{11}|$ (a) and boresight gain (b) vs frequency, for 60mm, 90mm, and 120mm aperture horns.

frequencies; to mitigate this issue, the combined TEM horn and loop antenna design approach in [92] is considered. The baseline antenna for comparison with this design has an aperture width of 60mm and axial length of 30mm resulting in a nominal turn-on of around 2GHz, however the baseline case does not reach a consistent match until past 5.75GHz. Utilizing the combined antenna technique [92], the fundamental TE and TM, spherical modes can be excited and engineered to obtain a lower turn-on frequency and improved gain performance. This is done through the addition of a combined square loop section, 60mm wide and 30mm long, phased properly through the addition of capacitive slots, and additional bowtie-shaped plates, as depicted in Fig. 4.1(b). The dual polarized TEM horn, in it's original state, emits power primarily in the TM modes, with <20% power being emitted in TE modes. Addition of the loop section with capacitive phasing slot pulls power at low frequencies into the TE modes at turnon, with the loop section primarily powering TE_{11} and TE_{-11}, and fields bridging the capacitive gap contributing to both the TE_{11} modes and the TE_{12} modes, while maintaining close to 180° phase difference between TE and TM modes. Addition of the bowtie section extends the frequency range over which power enters into the TE_{11} and TE_{-11} modes over the first few GHz of operation by adding an additional current path to the main loop antenna, and also pulls power into the TM_{12} modes while preventing some power leakage into the TE_{12} and TE_{-12} modes, which do not appear to sum as cleanly with the TM modes shortly after turnon. Mode phase and power for the basic radiating element from Fig. 4.1(b) are shown in Fig. 4.7, with further plots of these effects located in the appendix. The obtained turn-on

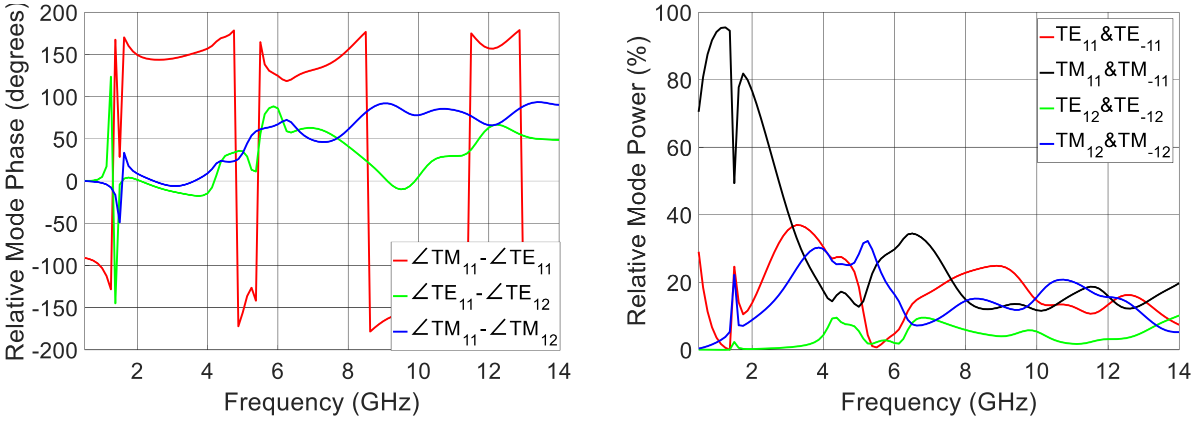

(a) (b)

Fig. 4.7. Relative mode phase (a) and power (b) for the radiating element shown in Fig. 4.1(b). TE and TM modes are out of phase with one another over turn on region, with power shared between TE_{11} modes and TM_{11} and TM_{12} modes. Limited power is put into the TE_{12} modes.

frequency with this design is 1.46 GHz as shown in Fig. 4.8(a). The boresight gain is also plotted in Fig. 4.8(b) along with that of the baseline TEM horn. As can be seen, the miniaturization technique provides a sharp improvement in impedance match and gain at the low frequency end over a similarly sized horn.

Good behavior is obtained for a radiating element design with a 50mm wide, 30mm long horn. This fits within the previously found loop and bowtie section, keeping the overall size of 6cm × 6cm × 3cm (λ/3.4 × λ/3.4 × λ/6.8) the same. Obtained bandwidth for the final design is 1.55 GHz up to 13 GHz where there is a large drop in gain for both the final design and baseline horn.

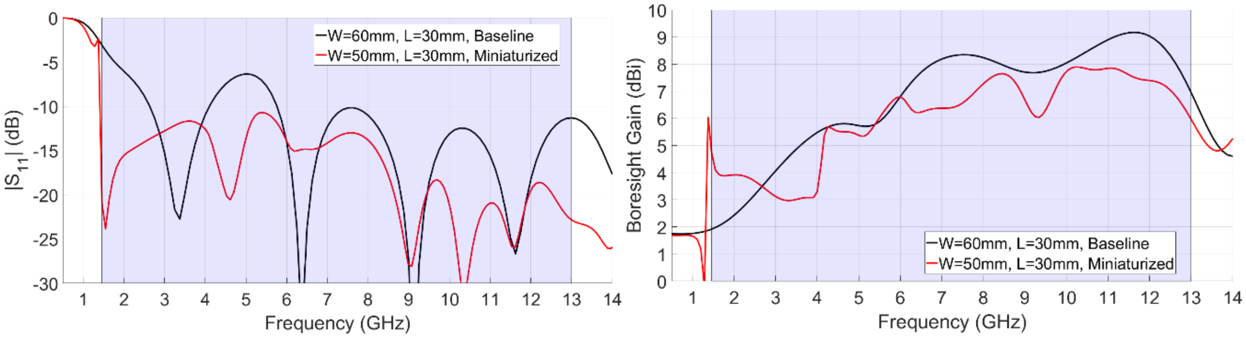

(a) (b)

Fig. 4.8. Comparison of $|S_{11}|$ (a) and boresight gain (b) between final design and baseline case. Cross-pol for both is below -35 dBi throughout the band. Miniaturized case includes small groundplane.

The miniaturized design shows significant improvement over the baseline horn in terms of usable bandwidth. Unusual gain behavior near 4 GHz is partially due to the transition between radiating from the horn and bowtie sections, to radiating from the horn primarily, but is exacerbated by the presense of a small groundplane in the model, and shows smoother operation simulated in isolation.

4.3 Cavity Backed Dual Polarized Miniaturized TEM Horn

4.3.1 Cavity Integration

To utilize the dual-pol TEM horn for spectrum sensing and direction finding, it is important to consider not only whether the device has good boresight gain characteristics, but also to consider the radiation pattern shape. Fig. 4.9 plots the pattern shape at 1GHz steps through the 2-13 GHz band. As can be seen, after 6GHz, the pattern shape shifts abruptly in the E-plane, after which

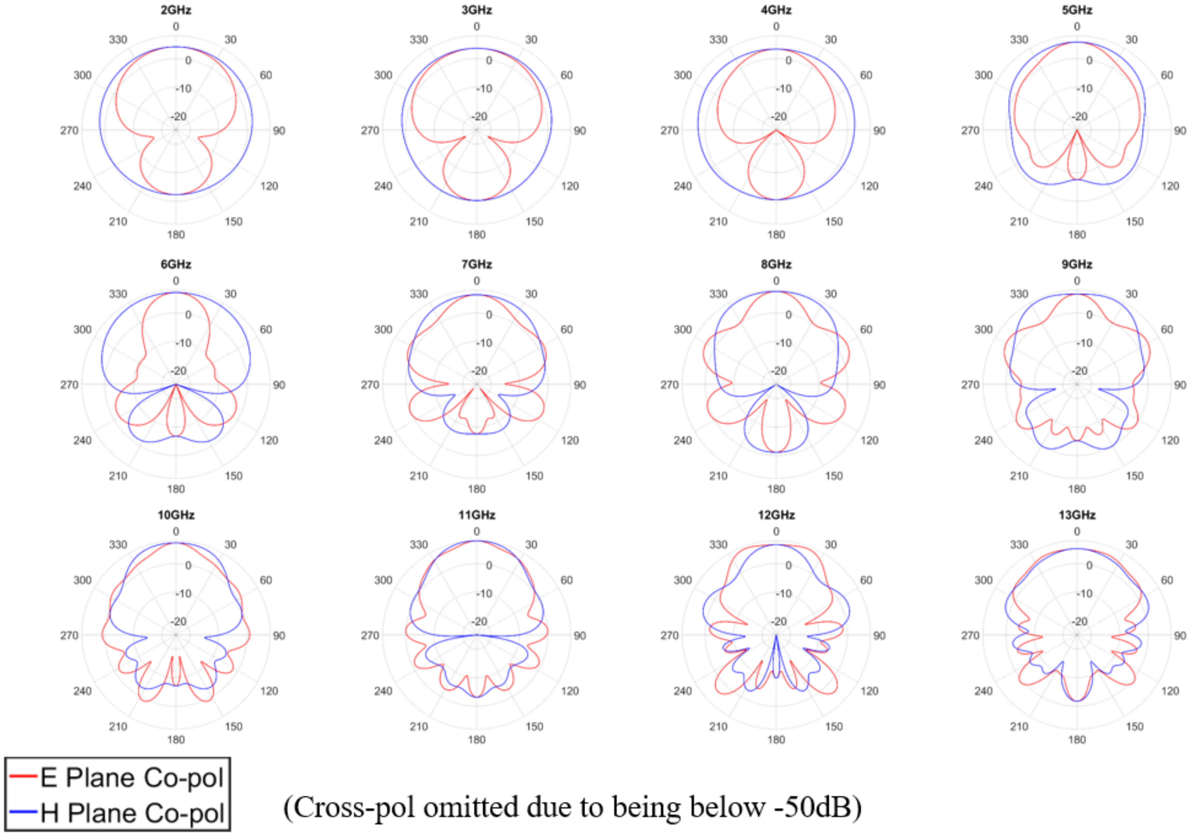

(Cross-pol omitted due to being below -50dB)

Fig. 4.9. Pattern cuts in E and H-plane principle planes for single excited pair of TEM horn arms, in configuration with small ground plane.

point the E-plane radiation pattern shows distinct sidelobes which are undesirable for DF and spectrum sensing operation. Prior work [83], [99], [100], [101] has shown that the behavior of radiating elements can be improved for sensing applications and DF by recessing the radiating element into a cavity. Using the same 60mm wide structure shown in Fig. 4.1, the boresight gain after placement into an 80mm wide conducting cavity can be seen in Fig. 4.10. Cavities narrower than 80mm reduce low-frequency gain substantially, while negatively impacting match, and wider cavities improve low frequency match and gain, but lose high frequency gain, and result in H-plane beam widening and higher power in sidelobes. The 80mm cavity diameter is selected as a compromise to ensure steadily increasing gain in the band of interest. As plotted in Fig. 4.10, recession of the radiating body into a fully conductive cylindrical cavity results in substantial increase in gain, but shows nontrivial drops due to resonant behaviors near 3.5 and 5 GHz, and additional variability at higher frequencies. Addition of absorber lining, as seen in [83], [100] reduces radiation efficiency of the system, but removes substantial cavity resonances and enables primarily linearly increasing gain operation. Proper selection of absorber is critical to performance. Best performance is found in simulation for Eccosorb FGM-125, with cavity depth between 10-15mm below the TEM horn loop section. Alternate absorbers are investigated and surface current absorbers like Eccosorb FGM-125 and Eccosorb GDS show superior match and consistent

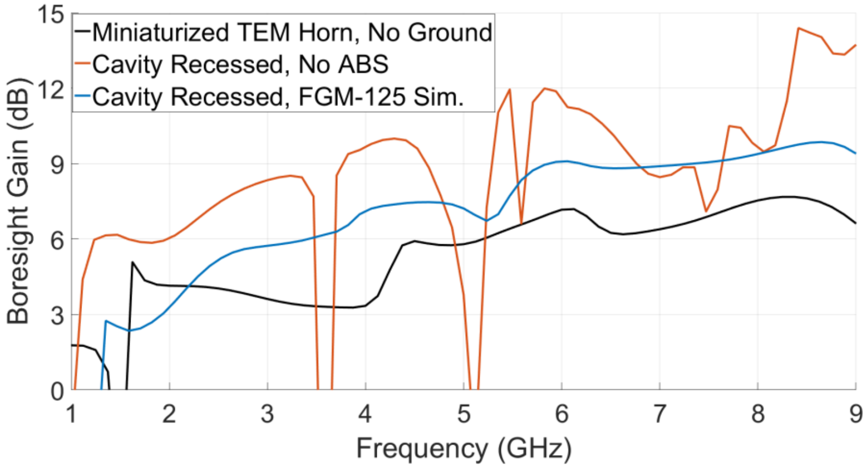

Fig. 4.10. Boresight gain for miniaturized TEM horn in free space, miniaturized TEM horn recessed into purely conducting cavity, and miniaturized tem horn recessed into simulated FGM-125 absorber lined cavity

efficiency. The combination of 13.5mm cavity depth below the loop section (total cavity depth 43.5mm) and use of FGM-125 absorber over other absorbers like Eccosorb LS and MAST MF absorbers demonstrates good radiation efficiency across the majority of the band of interest with the exception of a notable drop near 5.25 GHz, investigated in greater depth in the next section. The match, eficiency, and gain of the cavity recessed horn without further radiating element modifications can be seen in Fig. 4.11. The unmodified radiating element benefits from insertion into a cavity with improved radiation patterns, exhibiting primiarily steadily increasing gain, reasonable efficiency primarily >60%, and good match over most of the band. Nevertheless, certain elements of undesirable performance must be investigated. These are the cause of poor match below 2.5 GHz, and narrowband effects visible near 5.25 GHz.

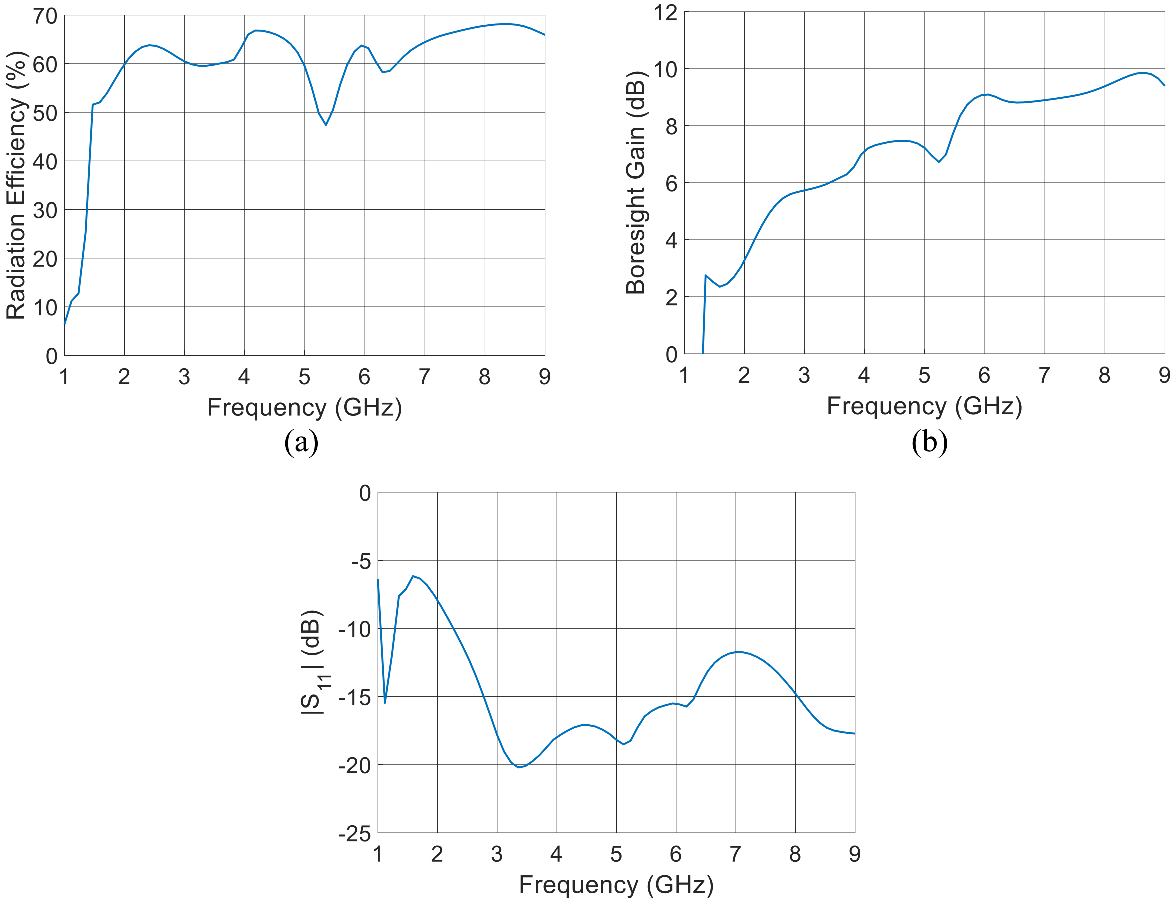

(a)

(b)

(c)

Fig. 4.11. Radiation efficiency (a), boresight gain (b), and differential $|S_{11}|$ (c) for 40mm deep cavity with simulated FGM-125 backing and unmodified radiating element.

4.3.2 Cavity TEM Horn Tuning and Narrowband Effects

The unmodified cavity backed TEM horn shows many desirable characteristics as a spectrum sensing antenna. Addition of the absorber lining results in mostly higher than 60% efficiency, creates primarily steadily increasing gain, and good match over a large bandwidth. It will be shown that this antenna demonstrates good pattern shape for unambiguous DF. However, narrowband effects dominate at certain frequencies that can be improved. Primarily these are the low frequency match behavior, and the narrowband drop in gain and efficiency near the middle of the band.

Here we first investigate the narrowband 5.25 GHz effects. From the far field patterns of the standalone radiating element from Fig. 4.9, it is obvious that at 6GHz, the antenna is no longer radiating purely in the endfire mode, with large rear lobes occurring near ±120° from boresight. Similarly Fig. 4.7(b) shows that power is pulled from the TE_{11} and TE_{-11} modes over the same band. Investigating the fields on the antenna, it can be seen that a large electric field is being generated across the 'lower' loop formed by the bowtie antenna and the outer loop antenna. These fields are illustrated in Fig. 4.12. These effects can be successfully mitigated by providing two new current paths, located directly through the center of the high field strength to either side of the

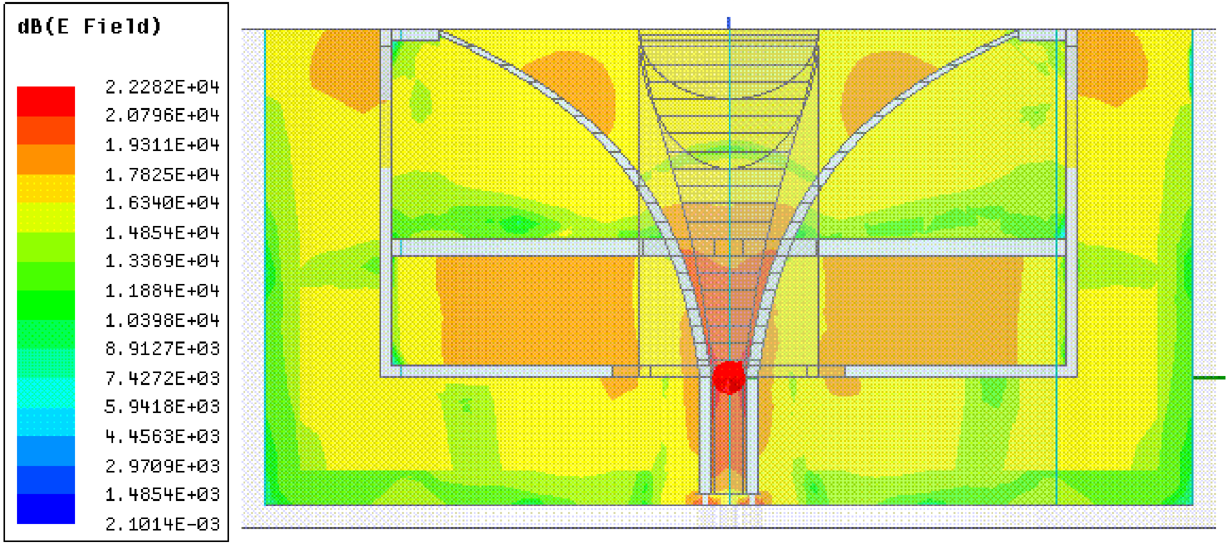

Fig. 4.12. Illustration of simulated E-field strength within the simulated TEM horn cavity. Regions of high field strength can be seen located vertically between the base of the outer loop antenna and the bowtie antenna plates.

antenna centerline. These ‘shorting posts’ have the effect of creating an additional higher frequency loop section, pulling energy back into the TE_{11} and TE_{12} modes from the TM_{11}, TM_{12}, and TM_{13} modes, and improve the linearity of the mode phasing at these frequencies. However, the shorting posts induce a higher frequency narrowband behavior near 6.75 GHz, which behaves in a similar manner, with gain and efficiency dropping over a narrow frequency span. Similarly, the higher frequency drop in gain and efficiency is caused by high strength E-fields present now in the ‘upper’ loop, formed by the the TEM horn arms and the bowtie antenna. This issue can also be solved by the addition of a current path located directly across the point of highest field strength. The progressive impact of the added current paths on mode behavior can be seen in the appendix. Resulting boresight gain behavior and efficiency are plotted in Fig. 4.13. the modifications to include upper and lower shorting posts bring overall efficiency above 57% from turn-on to 2GHz, above 63% from 2-3.8GHz, and above 65% thereafter. The narrowband drop in gain is also resolved, and gain is increasing after 2GHz. These improvements to gain and efficiency do not impact the low-frequency match issues.

Resolution of those issues is best accomplished through further modification of the central TEM horn. In keeping with the original finding of superior match for shorter horns, a modified central horn of 40mm aperture width, 24mm horn length achieves superior match behavior, and

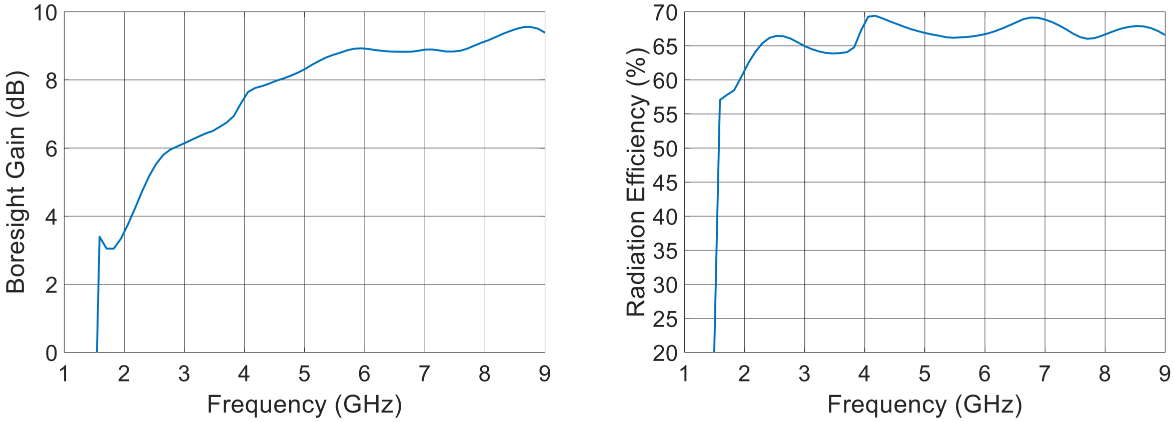

(a) (b)

Fig. 4.13. Boresight Gain (a) and Radiation Efficiency (b) for a cavity backed TEM horn with upper and lower ‘shorting posts’

has minimal impact on mid band operation. The loop is also adjusted from 60mm aperture width, 30mm depth, to 55.5mm length, 30.5mm depth. This reduction in length results in further distance to the cavity walls, and superior $|S_{11}|$ performance. Fig. 4.14 plots the change in match from the initial TEM horn model to the modified model.

One additional narrowband effect occurs in the manufacturing of the capacitive slot, and is visible in Fig. 4.13(a) and 4.13(b) as a small, sharp change to the gain and efficiency at 3.9 GHz. The initial design of the radiating element utilizes an elliptically shaped slot, similar to that put forward in [97]. The elliptical slot relies upon extremely high precision in manufacturing the sharp edges of the elliptical slot to maintain the appropriate capacitive coupling. For realistic manufacture, by manufacturing necessity the sharp ends of the elliptical slot are either blunted, moving the ‘arms’ of the slot away from the top of the TEM horn, or they are thickened, while maintaining close to the same position. (See Fig. 4.15). In either case, the infinitesimal slot width at the edge of the slot is widened, and capacitive coupling simulated by the close proximity of the ‘arms’ of the capacitive slot to its upper wall is reduced. This results in these ‘arms’ exhibiting a stronger resonant behavior, and showing high current strength along the capacitive slot edges at that frequency. Superior performance is obtained by replacing the capacitive slot by a linear slot.

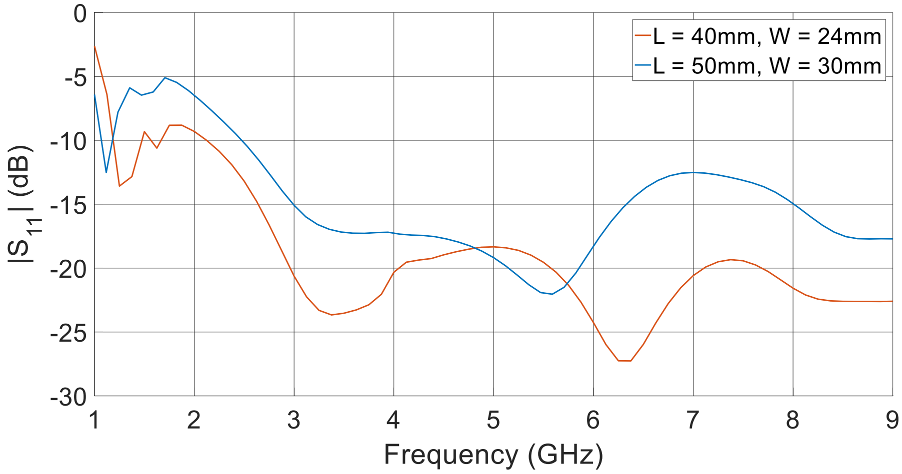

Fig. 4.14. Comparison of $|S_{11}|$ for cavity recessed TEM horn models. Red curve shows original model with L_{Horn}=30mm, L_{Loop} = 30mm, $W_{Aperture}$ = 50mm, W_{Loop} = 60mm, and blue curve shows modified model with L_{Horn} = 24mm, L_{Loop} = 30.5mm, $W_{Aperture}$ = 40mm, W_{Loop} = 55.5mm.

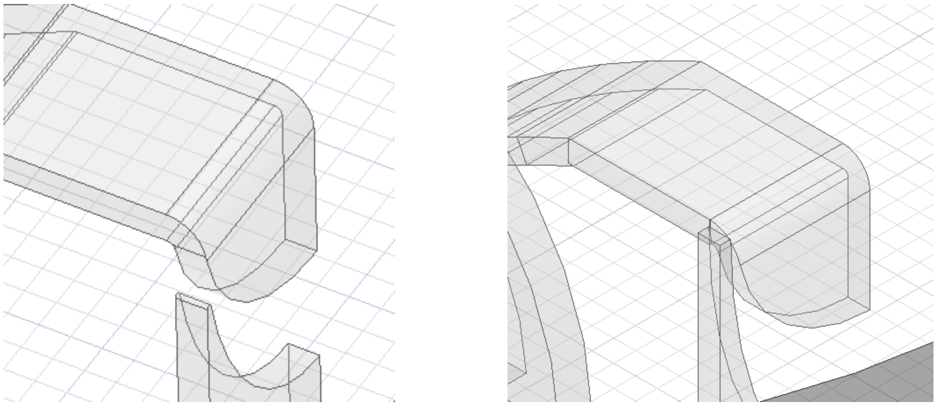

(a) (b)

Fig. 4.15. Illustration of alternate manufacturable capacitive slots. (a) blunt elliptical slot arm, and (b) extended elliptical slot arm

This can be seen by comparing Fig. 4.1(b) with Fig. 4.2, and Fig. 4.3, which both show the linear slot. The impact of the linear slot is substantial, with wider, low capacitance slots having substantially reduced gain and efficiency at turn on, or shifting the turn-on position. Similar behavior to the original elliptical slot is found for a slot width of 0.75mm, located 1mm below the top of the loop. The linear slot has, as a secondary effect, the impact of reducing the power pushed into the TE_{12} modes, the excitation of which appears linked to the fields generated across the elliptical capacitive gap, and improved linearity of phasing between turn-on modes. The altered mode power and phasing can be seen in Fig. 4.16. Comparing with Fig. 4.7, the modified radiating element has increased power in the TM_{11} modes, with remaining power primarily banlanced between TE_{11} and TM_{12} modes. Phasing of the TE to TM modes is more consistent, close to 150°

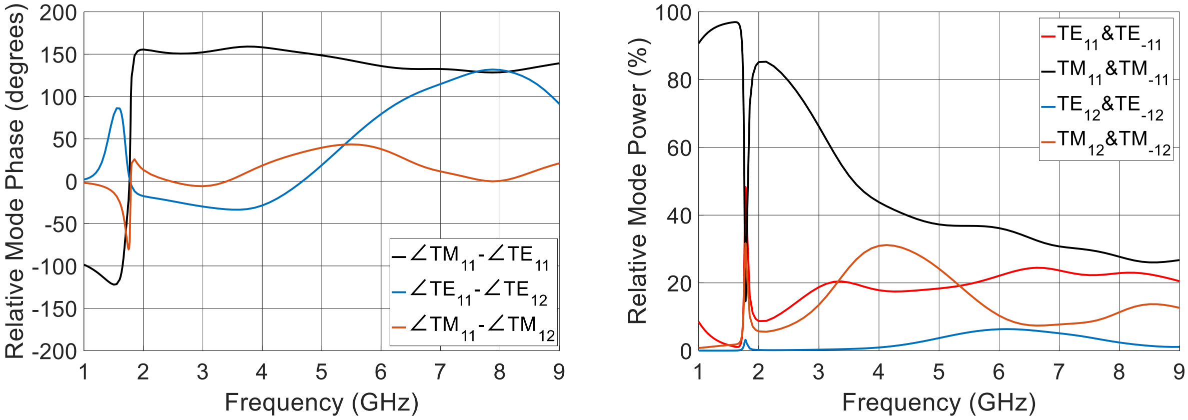

(a) (b)

Fig. 4.16. Mode relative phasing (a) and power (b) for radiating element with linear slot and two shorting posts

difference from 1.85-6 GHz.

The resulting design, seen in Fig. 4.2, shows far superior performance to the initial cavity integration. The performance of the design including shorting posts, modified TEM horn size, and linear capacitive slots is plotted in Fig. 4.17. The design demonstrates good match in the region of interest, 1.67-8.525 GHz, below -9.7dBfrom 1.8-2GHz, and below -10dB otherwise. Boresight gain is 2.8-9dB, with steadily increasing gain until 6 GHz. Efficiency is above 55% across the entire band, and above 65% after 3.3GHz. The overall impact on the radiation patterns in the E-plane and H-plane, and on simulated DF operation can be seen in Fig. 4.18, which plots the gain patterns and simulated DFF slope (for 30° squint angle) in steps of 0.125 GHz from 1.625 to 8.625 GHz. As can be seen, the cavity recessed design does not support high DFF slope, but can sustain

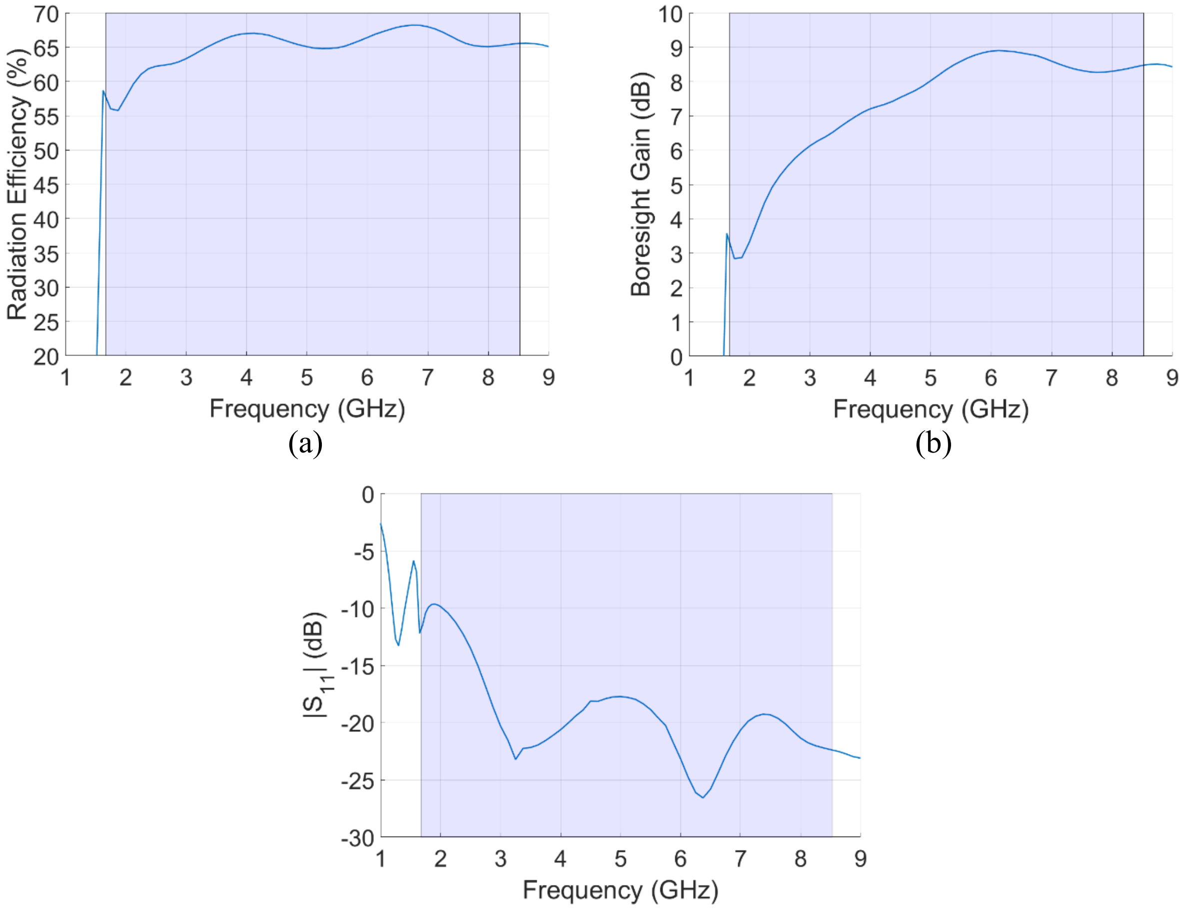

(a) (b)

(c)

Fig. 4.17. Radiation efficiency (a), boresight gain (b), and differential $|S_{11}|$ (c) for improved cavity recessed TEM horn. Band of interest is highlighted in blue.

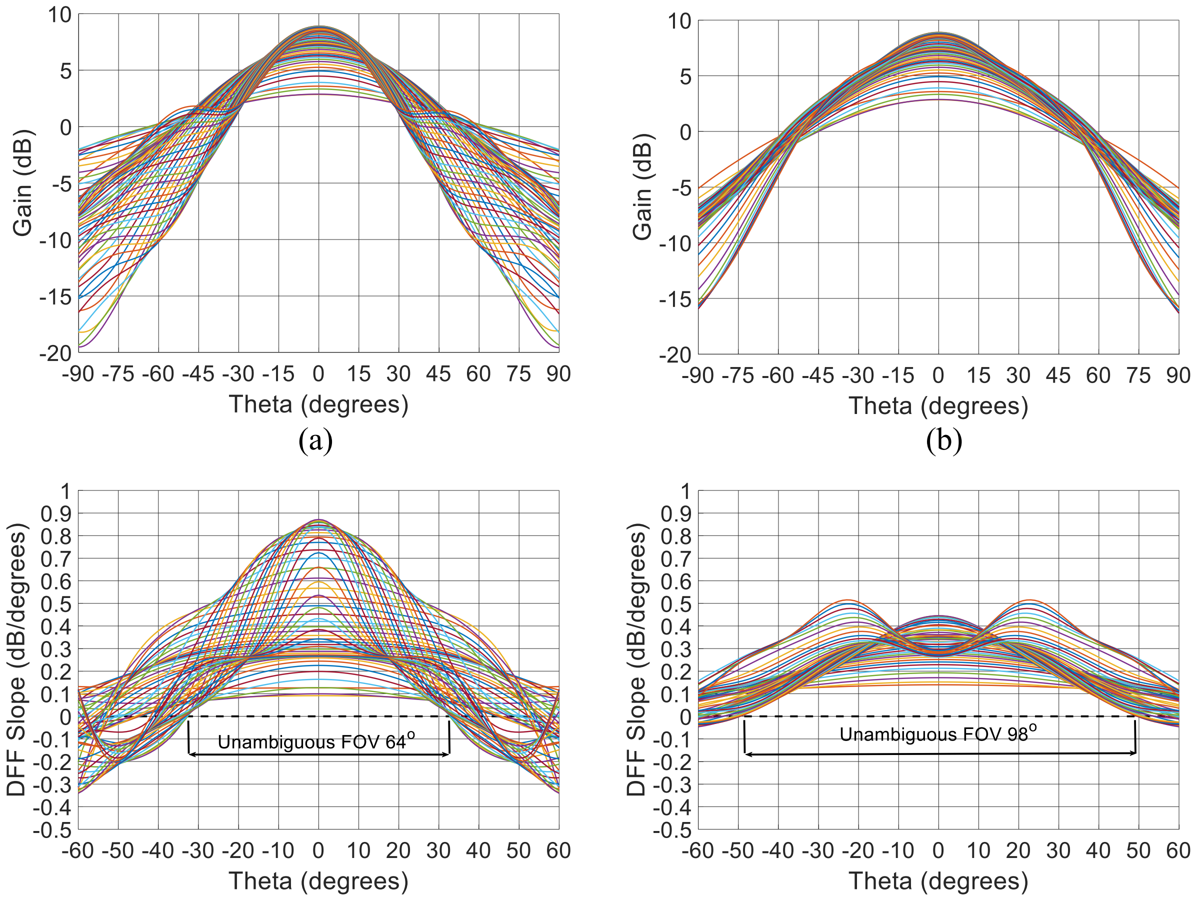

(a) (b)

(c) (d)

Fig. 4.18. E-plane (a) and H-plane (b) gain patterns, plotted in 0.125 GHz steps from 1.625-8.625 GHz, and E-plane (c) and H-plane (d) DFF slope behaviors, with unambiguous FOV marked.

sufficient DF performance in both the E-plane and H-plane to enable full coverage. Worth noting are the E-plane sidelobes developing off the main beam. The side lobes do not result in an ambiguity in the DFF slope within the band of interest. The sidelobe becomes clearly defined with it's own peak only past 8.25 GHz, with the pattern flattening near 36°, and the peak of the sidelobe occurring between 40 and 45°, less than twice the squint angle of 30 degrees. As a result, the peak of the sidelobe occurs wholly within one side of the main beam of the adjacent sensor, such that the ambiguity is removed, though slope is reduced in that area at high frequencies. As dictated by the occurrence of 0 slope in the radiation pattern, the squint cannot exceed 36°, at which point an ambiguity is created at the center of the antennas, and cannot be reduced below approximately

22.5° below which the sidelobe is positioned to create an ambiguity under the center of the adjacent antenna's main beam, reducing the unambiguous FOV.

4.4 Feed Integration and Impact

The design as presented in the previous section is fed with a bundle of four coaxial lines. With appropriate signals fed to each arm, the antenna can be made to operate in either linear polarization, or can be fed to achieve circular polarization in LHCP or RHCP. Generating the appropriate signals is often done by either a fixed configuration using a selection of hardware hybrids, which can be expensive for a greater than 5:1 bandwidth, and limits the utility of the design, or it can be fed with 4 independent receivers which can generate signals in the correct phasing. The four independent receivers is clearly the more flexible configuration, however the substantial cost of four recevers may be undesirable. In addition, a four-receiver configuration has capabilities, like the excitation of only a single arm, that are unnecessary. To remedy this, the design must be extended to allow for two-port feeding of the structure, with each port exciting two opposing arms of the TEM horn with correct phasing. In typical wideband TEM horns, this is achieved with a microstrip-like tapered balun, as in [71], or a zipper balun, similar to [83]. With four conductors, there is no way to build a similar design to the zipper balun. As such, inspiration for the balun design is taken from the design of quad-ridge horn antennas, either with [35] or without [36] sidewalls. In each case, two coaxial feeds are introduced to a tightly spaced quad-ridge cylindrical waveguide, feeding perpendicular modes. To effect a wideband transition, the feeds are placed as closely as possible to a wideband open circuit, formed as a rear cavity where the ridges are not present, or are pulled much further towards the outer walls of the cylindrical guide. A similar principle is applied in this case, as can be seen in Fig. 4.3 and 4.19(c). the important features to the operation of the quad-ridge waveguide to four wire line transition can be seen labeled as 'rear cavity,' 'quad-ridge waveguide,' 'recessed transition region,' and 'four wire line.' The basic geometry of the four wire line and transition region can be seen in Fig. 4.19(a) and

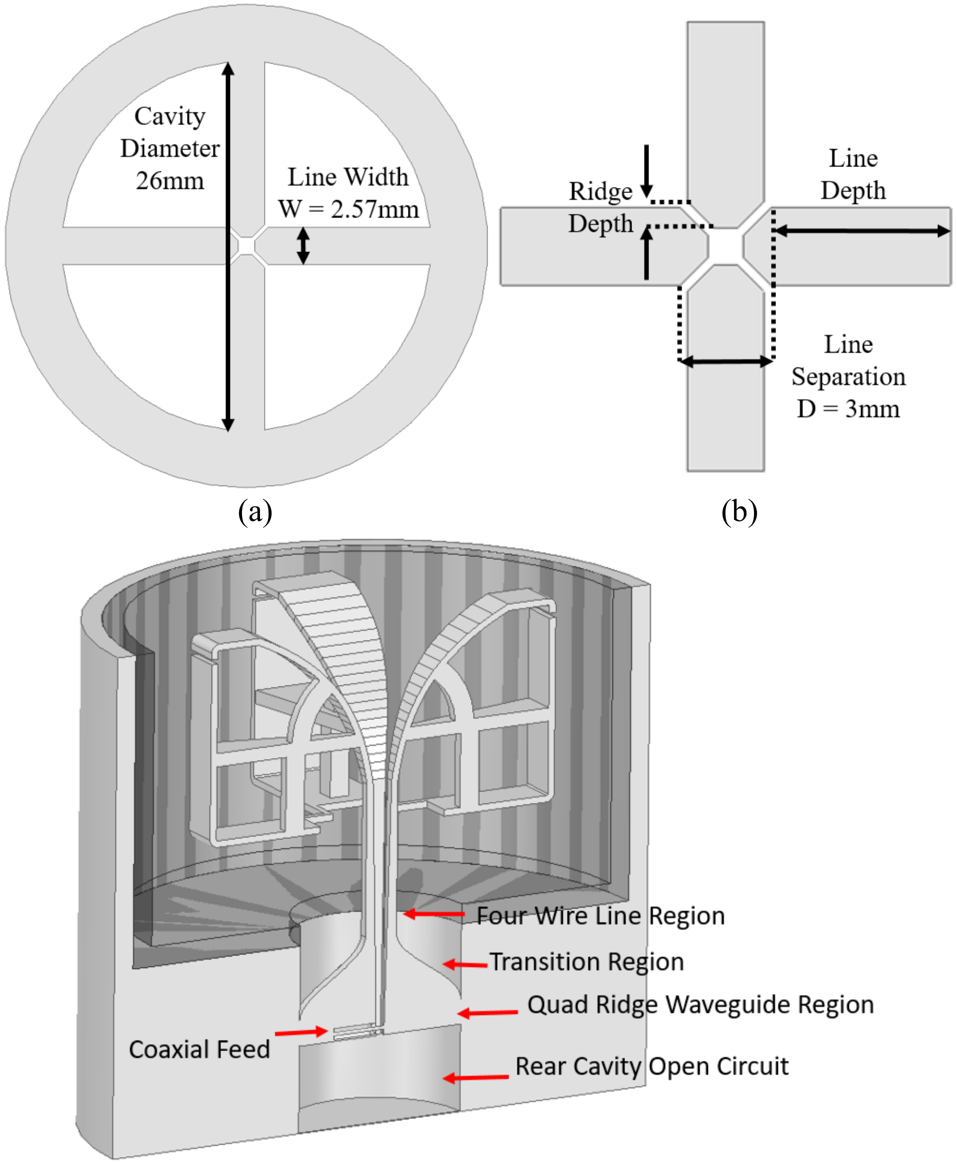

Fig. 4.19. Diagram of transition region geometry, showing fully quad-ridge waveguide geometry (a) and detail of fully separated 4-wire transition geometry (b). final design cutaway view (c)

(b). Line width W and line separation D are kept constant to align with TEM horn feed geometry. An additional 45° tapered 'ridge' is added for additional control of characteristic impedance. Cavity diameter is selected at 26mm to position first mode turn-on near 1.65GHz. While this does allow for higher order cavity modes to exist after 6GHz, the modes in question are of a significantly different character to the fundamental modes, and in practice power is not significantly coupled into the alternate modes [102]. Impedance for the basic structure varies over frequency, with higher impedance seen just after turn-on. Over the band of interest, the impedance varies from ~100-50 Ω over 2-8.525 GHz. After the four lines are disconnected from the cavity walls, impedance of the TEM mode can be manipulated to vary from 25-85Ω, while the four lines are within the 'shield' of the cavity wall. Impedance of the TEM modes over line depth and ridge depth can be seen in Fig. 4.20, for both the case of the lines existing within the cavity and in free space. The ridge length is utilized to select for 50Ω impedance at 5GHz for both the geometry of the quad-ridge waveguide where the coaxial line is inserted, as well as 50Ω impedance at the mouth of the feed cavity where the unshielded four wire line begins. The impedance profile between those points is not however necessarily a linear behavior. In particular, the mode present in the TEM analysis of the 'shielded' four-wire line, is very different in nature from the TE_{11} mode present in the quad ridge waveguide impedance analysis, whose E-field tapers to 0 near the exterior cavity wall. In addition, the extremely short distance over which the quad ridge waveguide and shielded four-wire line exist does not support a well formed TE_{11} mode in the quad ridge region or a well formed TEM mode in the rapid transition to the unshielded four-wire line. As such greater focus is given to parametrically selecting for geometries that reduce radiation from the overall transition region, and for good impedance match in a simulation consisting of the isolated balun structure in an infinite ground environment, when connected to a matched 100Ω load at an appropriate distance from the

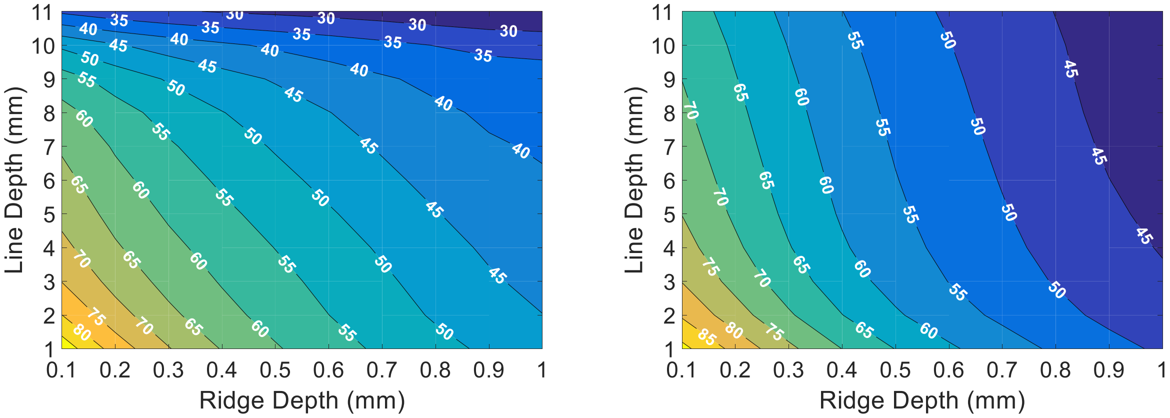

(a) (b)

Fig. 4.20. (a) impedance of the shielded four-wire transition line, plotted over line depth and ridge depth, and (b) impedance of the unshielded four-wire transmission line, plotted over line depth and ridge depth

transition area. After the mouth of the feed cavity, the impedance behavior of the four wire line is more accurately simulated with TEM behaviors, and Z_0 is tapered from 50-100Ω utilizing the ridge.

As can be seen in Fig. 4.19, the quad-ridge to four-wire-line transition is located entirely within the feed cavity. This accomplishes both good match below -12dB and low radiation from the transition region below -17.5dB in the isolated simulation. The isolated performance and simulation setup can be seen in Fig. 4.21. The rear cavity depth of 13mm, transition region length of 15mm, and transition region shape (sinusoidal change of line depth). Are all selected parametrically for low radiation and good match. Integration of the balun into the TEM horn design causes an additional narrow-band effect, notably a sharp drop in gain at high frequencies. This is found to be caused by strong fields occurring between the base of the TEM horn loop, and the fields on the edge of the feed cavity. Moving these elements apart by increasing main cavity depth from 43.5mm to 53.5mm dulls this effect substantially without reducing efficiency, and the effect can be further mitigated by the addition of a second layer of FGM-125, forming an annular ring located around the feed cavity, as indicated by ‘additional absorber strip’ in Fig. 4.3. The impact of the additional absorber strip can be seen in Fig. 4.22, comparing the S parameters and boresight gain before and after addition of the absorber strip.

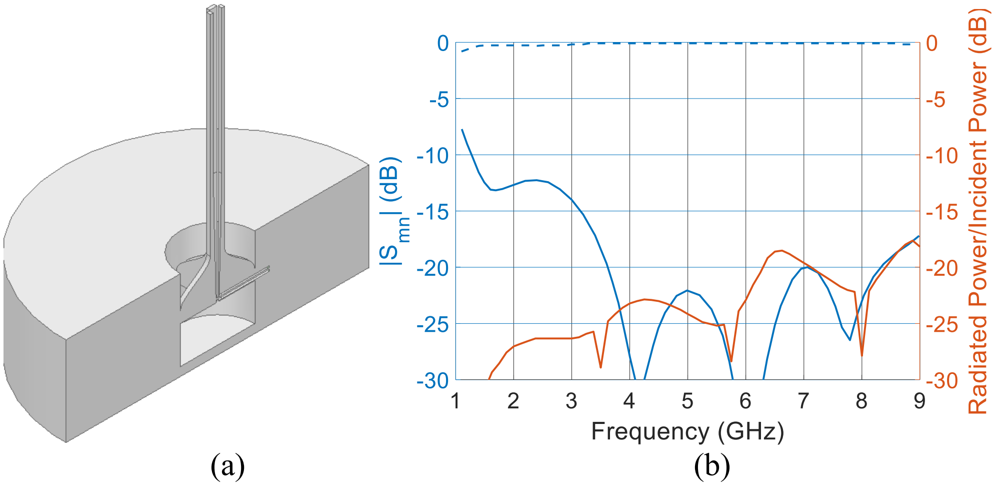

(a) (b)

Fig. 4.21. (a) simulation setup of infinite ground plane quad-ridge waveguide to four-wire-line transition and (b) isolated S-parameters and radiated power from the transition region.

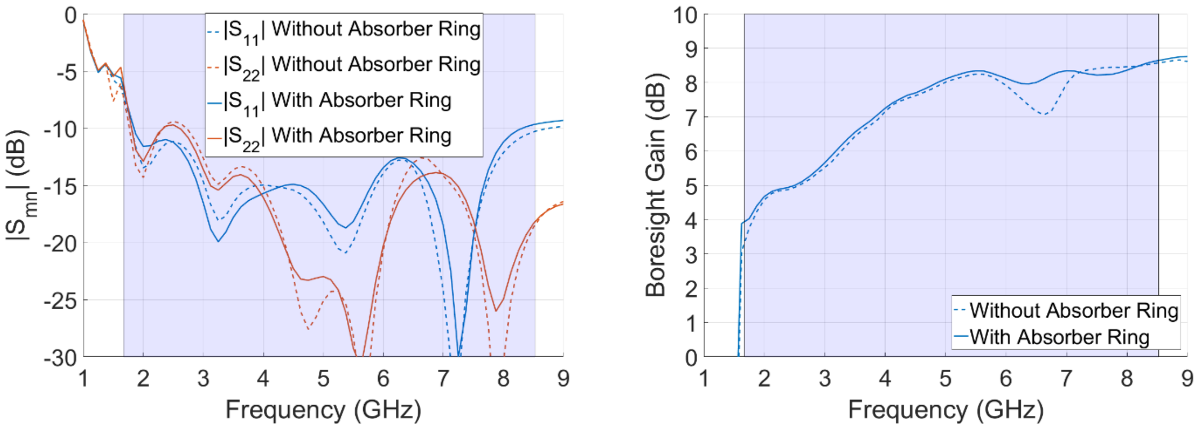

(a) (b)

Fig. 4.22. (a) S parameter behavior for channels 1 and 2, with and without additional absorber ring showing little change (b) boresight gain with and without absorber ring, showing improvement to 6.5GHz gain drop

4.5 Manufacturing and Measurements

4.5.1 Bundle-Fed TEM Horn Antenna

The bundle fed TEM Horn Antenna is manufactured from aluminum and brass machined pieces, along with lengths of 086 semi-rigid coaxial cable, Eccosorb FGM-125 absorber, FDM 3D printed standoffs and cable supports, and a small teflon spacer. The individual TEM horn arms (consisting of 1 horn arm and its associated bowtie antenna piece and mode control shorting posts) are manufactured by a combination of electrical discharge machining (EDM) and CNC milling techniques, as is the combined loop section. The bowtie section of each arm is machined to contain two screw holes to secure the arm to the loop section, as well as an additional screw hole in the base of the lower shorting post, and a small sliding fit hole in the base of the 4-wire line to enable final integration into the coax feeds. As seen in Fig. 4.23, the assembly consists of first securing the individual arm pieces to the loop, and preparing the feed structure by soldering 4 semi-rigid 086 coaxial cables into a machined brass mounting puck. The mounting puck is then secured into the larger groundplane, and a teflon spacer is brought down over the protruding coax inner conductors, both to allow alignment, and to ensure correct vertical positioning of the feed arms over the coax. Four FDM 3D printed struts are positioned with one under each loop section, to

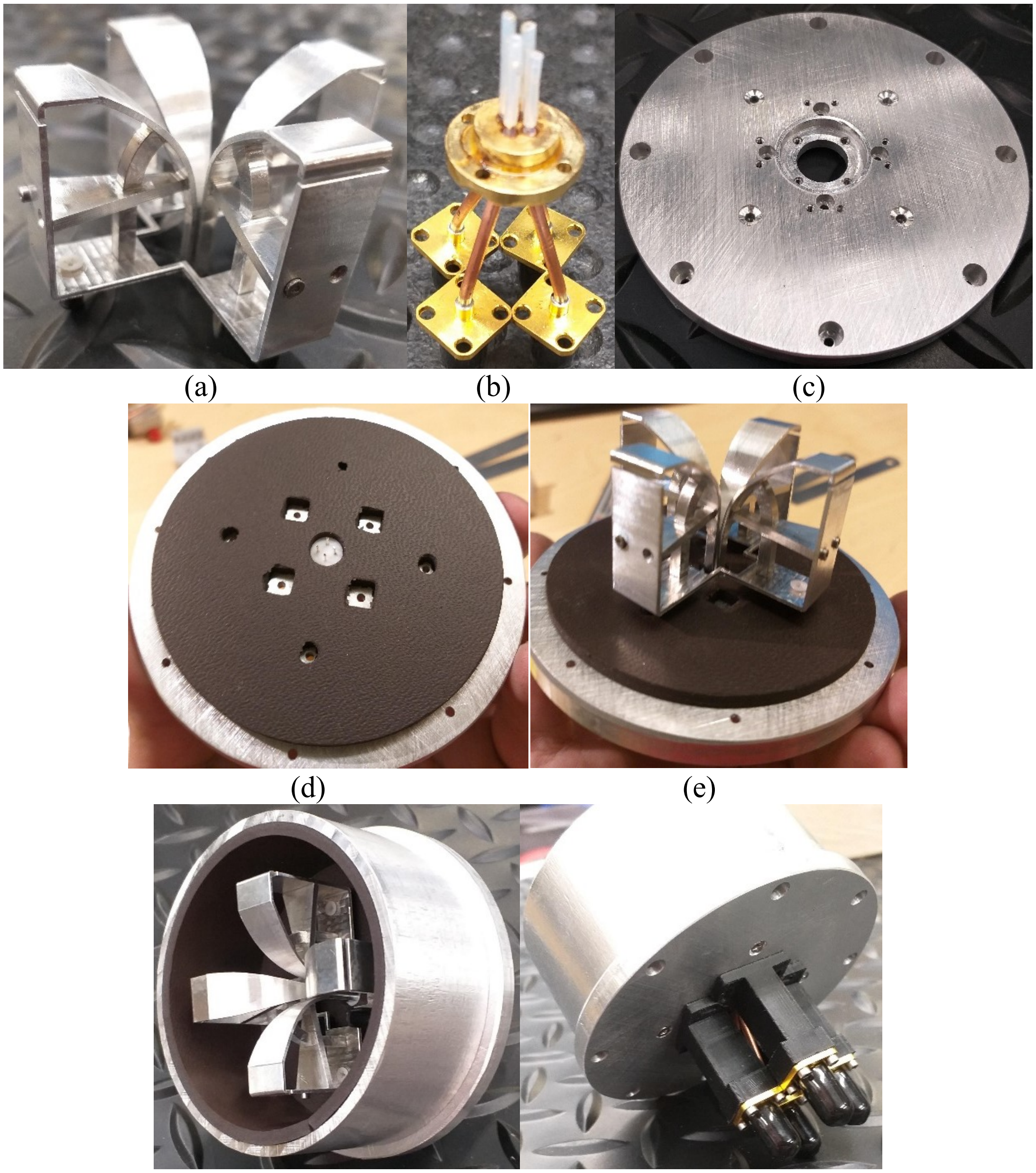

(a) (b) (c)

(d) (e)

(f) (g)

Fig. 4.23. Steps of manufacture, read sequentially left to right, top to bottom. Assembly of main radiating element from individual arms (a). Integration and soldering of cable feeds into brass mounting structure (b). Preparation of ground plane (c) and integration of brass mounting structure and absorber layer (d). Integration of ground plane structure with 3D printed standoffs and radiating element (e). Integration of cavity wall and absorber lining (f). And finally addition of 3D printed cable supports (g).

secure the TEM horn assembly to the groundplane. Nylon screws are used from each side to secure the TEM horn assembly and groundplane together. Following this, the cavity wall and absorber are brought down around the exterior and secured to the groundplane with 8 mounting screws.

Finally, the 3D printed cable supports are placed over the cables, and screwed into both the groundplane and the SMA connectors to secure their positioning and prevent damage and unnecessary bending of the cabling.

Measurements of the device are carried out using a differential vector network analyzer to obtain S-parameters from the bundle feed device. A comparison of the measured differential S parameters can be seen in Fig. 4.24. As shown, we see good match below -10dB across the majority of the band of interest, though the exact turn-on is shifted to ~1.8GHz. Agreement with the original simulations are not as close as desired. This is understood to be due to disagreement between the available model for FGM-125 utilized to tune the antenna, and the true parameters of the FGM-125 absorber, exhibiting both somewhat different permittivity, and greater losses. Efforts to model these differences demonstrate improved agreement, as can be seen in the greater agreement of the yellow and purple curves in Fig. 4.24, showing simulation with altered absorber characteristics,

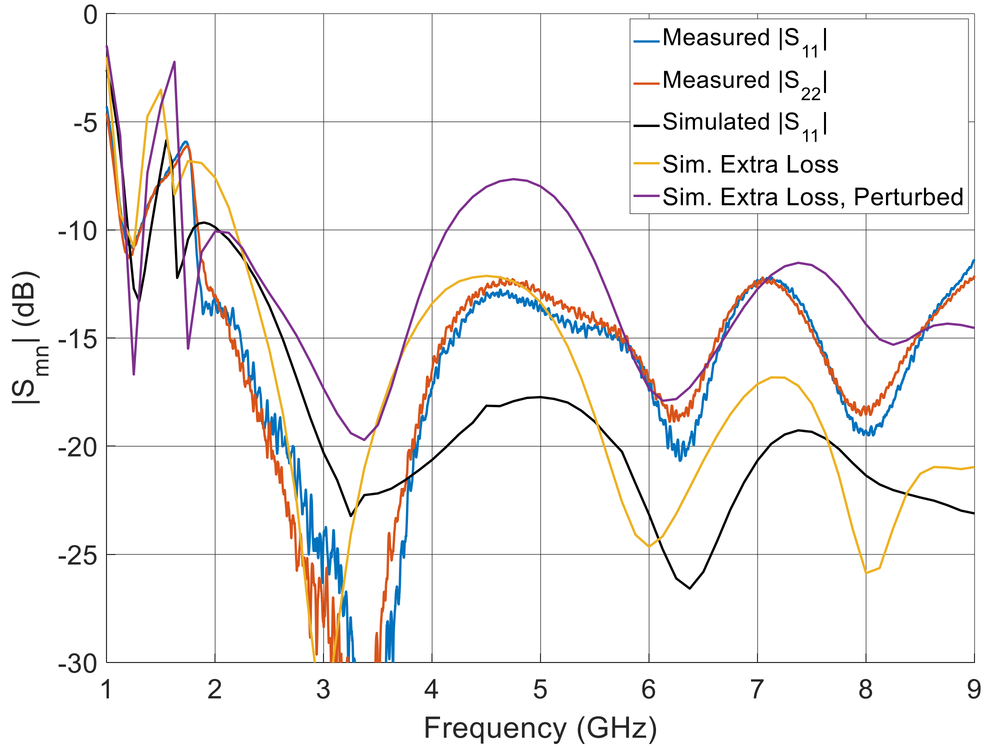

Fig. 4.24. Comparison of original simulated $|S_{11}|$ (black) vs measured $|S_{11}|$ and $|S_{22}|$ (blue, red), alongside simulation with modified absorber model (yellow), and modified absorber and arm position perturbation (purple)

and simulation with both altered absorber charactersitics, and efforts to more accurately represent the TEM horn arm positioning. Some aspects of the measured performance remain further from agreement than desired. In particular, the source of error related to the positioning of the TEM horn arms. The match performance of the design is highly sensitive to the arms being tilted inwards or outwards from the center, angular twisting around the feed point axis, and inwards or outwards translation from the center of the horn. All three failure mechanisms are related to the exact thickness of the teflon spacer at the feed point, the length and positioning of the 3D printed standoffs, and the manufactured accuracy and rigidity of the loop section. Error on the order of 100um in positioning, 1° in of inwards tilt, and 0.5° angular twist about the feed point demonstrate reasonable agreement with measured results. The single fixturing point of the 3D printed standoffs is insufficient to allow greater accuracy of positioning, and obtaining sufficient accuracy in the positioning and tilt of the four TEM horn arms to the high accuracies required for fully accurate modeling requires measurement instrumentation that is not available. Future work on this antenna will utilize adjustable positioning mechanisms located horizontally, allowing for the performance to be retuned. However, the change in match does little to alter the overall directivity of the system. As can be seen in Fig. 4.25 and Fig. 4.26, the measured boresight directivity shows close agreement with the freespace mechanical simulation, and radiation patterns show good agreement with simulation. What is worth noting however is the reduced gain vs simulations, also plotted in Fig. 4.25, alongside a simulation assuming greater losses than the original simulated model of the FGM-125 contained. In the original absorber model used, losses are simulated as purely magnetic loss. Based on measurements of the material permeability and magnetic loss tangent. As can be seen, simulated additional losses on the order of 0.02-0.04 electrical loss tangent, and perturbation of permittivity from uniformly $\epsilon_r = 7$ to varying in frequency from 11 to 10 brings much closer agreement between measured and simulated results. Effective efficiency remains higher than 40% in spite of additional losses in the measured system. Simulatiuon and measurement of radiation efficiency is plotted in Fig. 4.27, alongside simulations with perturbed absorber paramters.

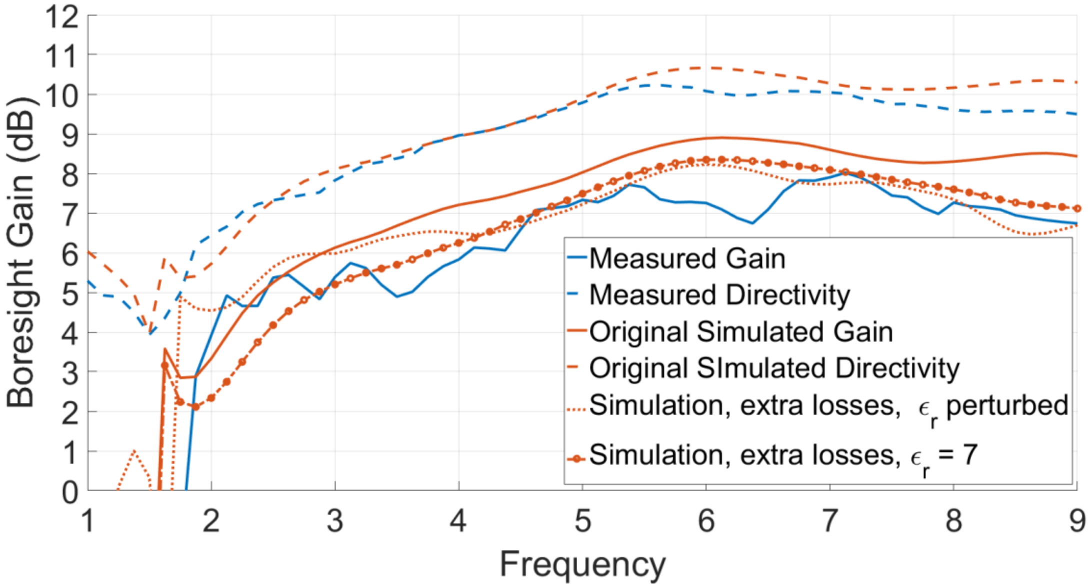

Fig. 4.25. Comparison of measured and simulated boresight directivity and gain, alongside simulations with additional absorber parameter perturbations.

Additional designs in this area will necessitate greater scrutiny of absorber models in use for tuning to achieve higher measured efficiency. Alternate models for this system utilizing different absorber models indicate that possible efficiencies higher than 65% across the band may be achievable with limited modifications. Resulting DFF from measured patterns shows good performance and agreement with simulation, with E-plane unambiguous FOV of 61° and H-plane FOV of 61.5°, as plotted in Fig. 4.28.

4.5.2 Integrated Balun TEM horn Antenna

The integrated-balun TEM horn antenna is manufactured from aluminum with a combination of EDM machining and CNC milling techniques. The mechanical design consists of four unique arm components, which include the TEM horn arm and its associated bowtie antenna, shorting posts, feed line, and a quarter section of the feed cavity wall, one main cavity wall piece, one main cavity ground piece, and one rear-cavity ground piece. The design also utilizes four FDM printed standoff pieces to support the TEM horn arms and two custom built coaxial flange pieces, built from brass and partially stripped 086 coaxial cable. The TEM horn arms are assembled in a

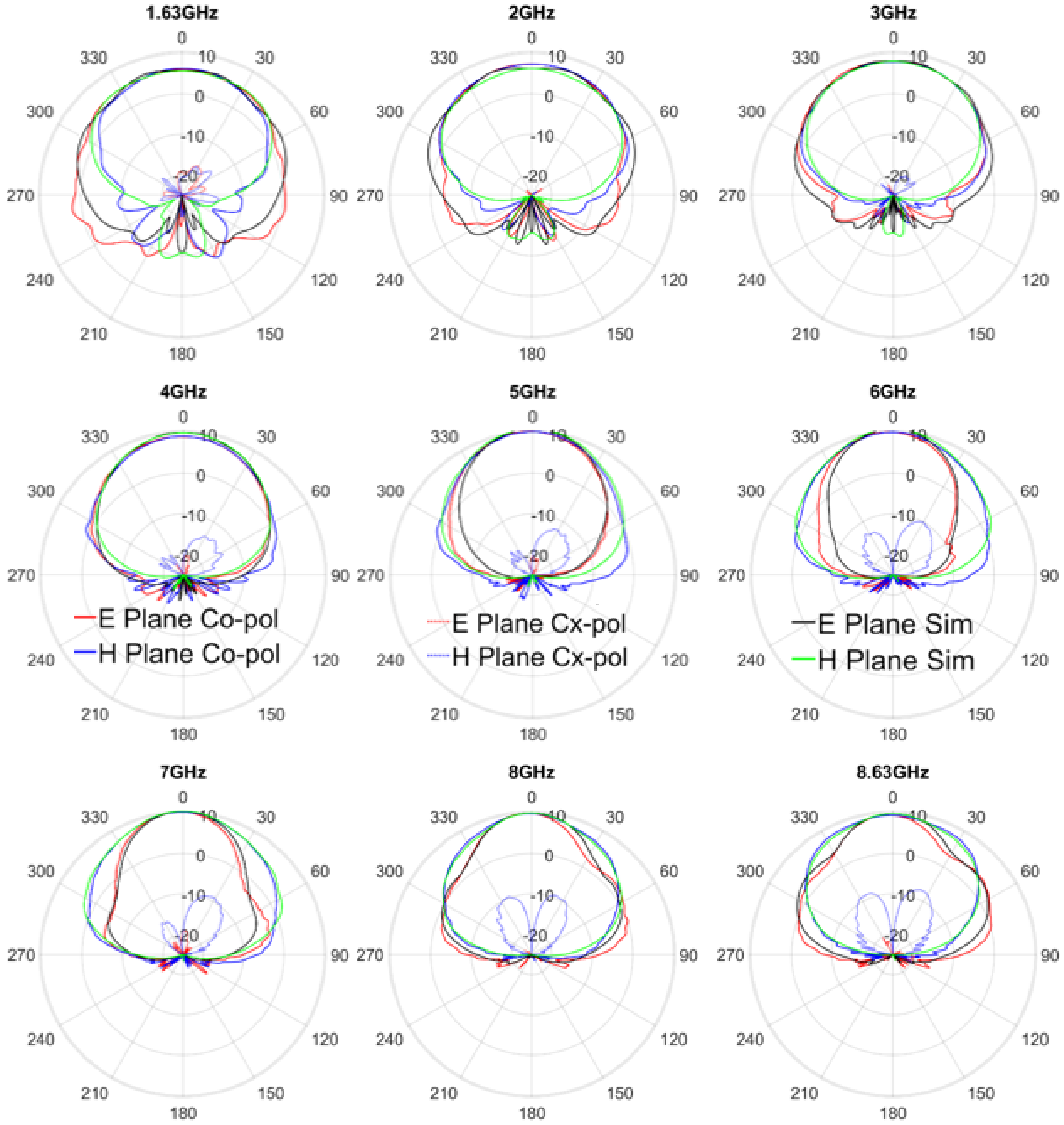

Fig. 4.26. Comparison of measured and simulated E-plane and H-plane Pattern cuts for bundle fed cavity backed miniaturized TEM horn antenna.

similar fashion to the assembly of the bundle fed TEM horn. Assembly pictures can be seen in Fig. 4.29. The constructed integrated balun TEM horn shows similar mechanical issues to those seen in the bundle feed device, in particular, the manufactured standoffs cause mechanical stress which tilts the four arms of the TEM horn inwards. Measured results can be seen compared with original

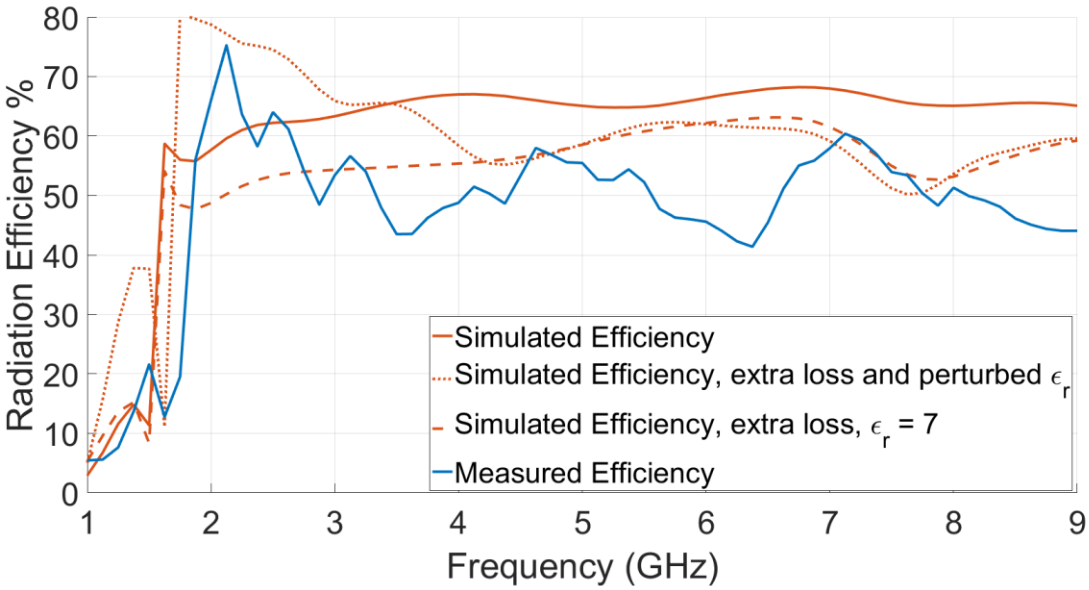

Fig. 4.27. Comparison of measured and simulated radiation efficiency alongside simulations with additional absorber parameter perturbations

simulation, and simulation accounting for some mechanical differences, in Fig. 4.30. Measured results compare favourably with simulations that account for change to the ideal geometry.

4.6 Performance Comparison

Table 4.1 shows a comparison between competing antenna architectures in the open literature, focused on designs with dual-linear polarization. As can be seen from the table, the design put forward here is competitive with, or smaller than most competing antenna designs [34, 76, 103-105], being less than 0.44 λ diameter at the turn-on, and 0.22λ deep for the bundle fed device, and achieves higher gain than existing sinuous antenna designs excluding lens loaded devices like [77]. The device shows simulated performance with higher efficiency than competing cavity backed sinuous devices, again excluding [77], and remains competitive with their performance in measurement. The device shows higher gain and comparable or better efficiency than competing cavity backed sinuous antennas, with the exception of [77] which features a large dielectric lens. Quad ridge horn devices [35, 36], achieve higher efficiencies, gain, and bandwidths, however they are much larger and their pattern shape is unsuitable for DF operation. LPDA devices

Table 4.1. Comparison to Existing Literature

Source	Type	Gain (dB) (Measured)	Efficiency % (Measured)	BW	Size (λ_{low}) diam. x depth
[108]	Conical Sinuous	5.3-7.5	-	2.5:1	0.66 x 1
[103]	Cavity backed sinuous	4-6	<50	2.5:1	0.49 x 0.8
[104]	Cavity backed sinuous	-	<50	9:1	-
[34]	Cavity backed sinuous	5	<50	5:1	0.42 x 0.34
[105]	Free space sinuous	5	-	4:1	0.28x 0.28
[106]	LPDA	6-8	~100	18 : 1	0.63 x 0.87
[107]	LPDA	6-9	90-100	5.4 : 1	0.46 x 0.44
[77]	Cavity backed Lens-loaded sinuous	3.9-12	60-80	4.2 : 1	0.41 x 0.41
[36]	Quad ridge horn	6-16	~100	8 : 1	1.40 x 1.47
[35]	Quad ridge horn	10-14	~100	6 : 1	1.14 x 1.09
[76]	Free space sinuous	2.5-5.5	-	12 : 1	0.48 x 0.18
This	TEM	3 - 8	41-75	5.4 : 1	0.44 x 0.22

[106, 107] can achieve wider bandwidth for the device and higher efficiency, however are generally much larger, particularly for higher gain devices. Conical sinuous antennas like [108] achieve comparable gain, however are again generally much larger devices. [108] does not list a measured efficiency, and achieves front to back ratio of approximately 10dB. [103, 104], and [34] do not directly list measured efficiency, and are presumed less than 50% due to absorbing cavity and gain in expected ranges. [76] and [105] are measured without cavities, and thus efficiency results are removed. Also worth noting is the expected dispersive behaviors exhibited by sinuous antennas, which exhibit substantial group delay, particularly at the low end of their frequency band. Comparisons of simulated performance with a comparable sinuous antenna are shown in the appendix.

4.7 Conclusion

A dual-linear polarized TEM horn structure is proposed, and the design in investigated from the basics of the TEM horn, through its miniaturization, integration into a cavity, and the development of a convenient feeding mechanism. The miniaturized TEM horn antenna is designed to cover 1.67-8.525 GHz with good match and rapid gain turn-on. Integration into a cavity, and

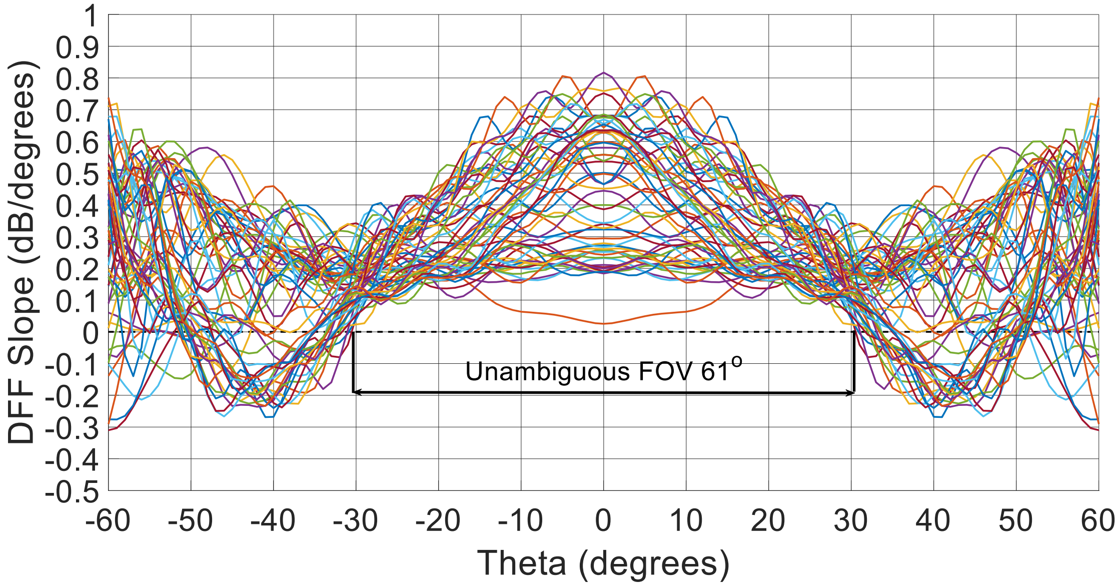

(a)

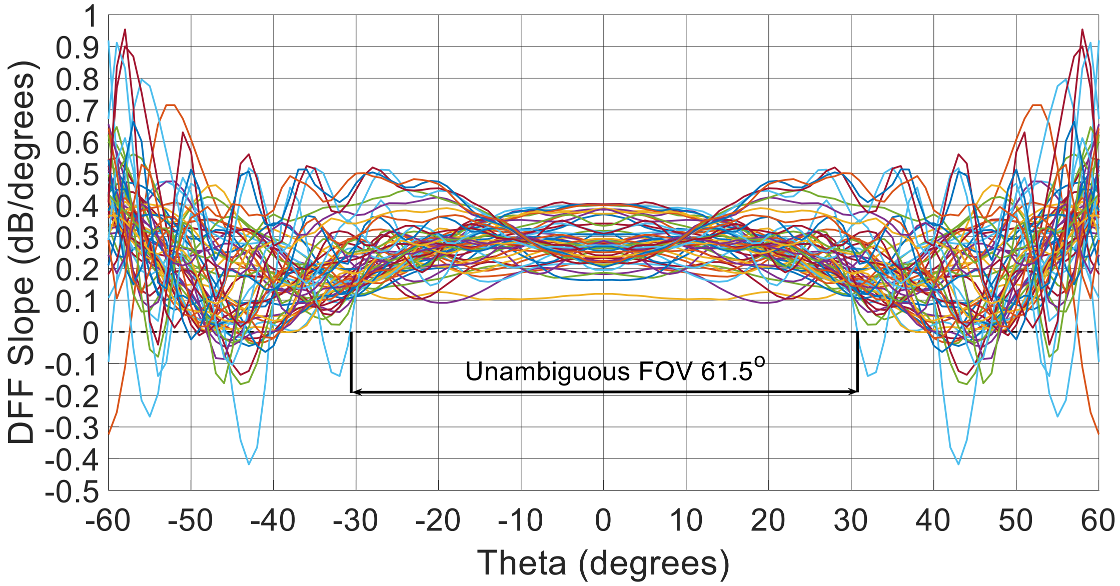

(b)

Fig. 4.28. Measured DFF slope performance of bundle-fed cavity backed miniaturized TEM horn antenna. (a) E-plane DFF slope and (b) H-plane DFF slope. 0.125 GHz steps from 1.625-8.625 GHz

careful examination of cavity fields and antenna spherical modes allows for the removal of many narrow band effects, resulting in an antenna with smoothly increasing gain performance after a sharp turn on, high efficiency relative to antennas of competitive size and use case of greater than 60% across the majority of the band, and good match <-10dB. Addition of a novel feed structure

(a)

(b) (c)

Fig. 4.29. (a) TEM horn arm pieces, main cavity wall, and loop section, manufactured by Protolabs. (b) Assembled TEM horn base view, and (c) assembled TEM horn top view

allows for convenient feeding of individual polarizations without the use of a hybrid. Measured performance shows robust radiation characteristics, with good agreement seen for measured radiation patterns across the band of interest. Measured S parameters show tolerable agreement with simulation, however are very sensitive to the exact positioning of the arms of the TEM horn antenna, limiting the match across the full band. The demonstrated device shows good direction finding performance over a wide relative bandwidth at microwave frequencies, demonstrating a successful alternate method from the common planar cavity backed antennas to achieve wideband direction finding.

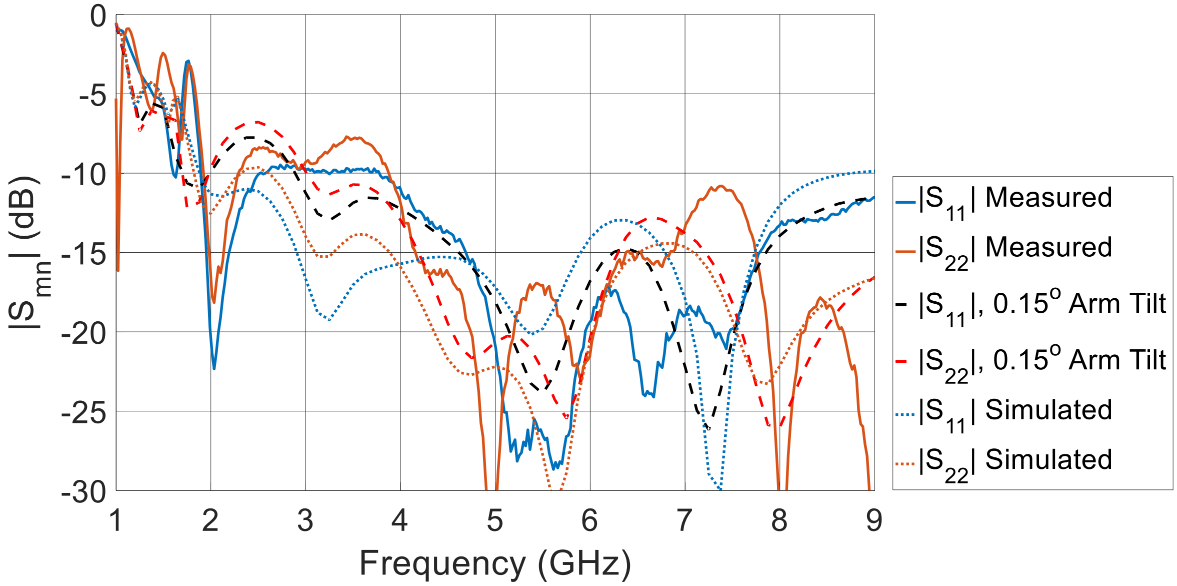

Fig. 4.30. Measured $|S_{11}|$ and $|S_{22}|$ (solid lines, blue and orange) for integrated balun TEM horn antenna, compared with original simulations (dotted, blue and orange) and simulations with arms tilted inwards (dashed, black and red).

CHAPTER 5

FURTHER DESIGNS IN MICROWAVE SPECTRUM SENSING AND DIRECTION FINDING

5.1 Introduction

Further designs to achieve wideband spectrum sensing and direction finding are possible at microwave frequencies. As noted in chapter 4, there are a variety of antenna designs that can achieve specific goals of wide or ultrawide bandwidths for sensing applications and for direction of arrival (DOA), time of arrival (TOA), and frequency of arrival (FOA) applications. Antennas for these tasks often require reduced size, polarization diversity, and low cost. To achieve these ends, the log-periodic dipole array (LPDA) is an often considered topology. It is quasi-frequency independent, limited only by its size for low frequency operation, and the ability to manufacture it's feed for high frequency operation [60, 109]. Its major defining works were put forward by DuHamel et al [110, 111] in 1957 and 1958, and R Carrel in 1961 [109]. While some modern examples of LPDAs, particularly for commercial applications, still are designed from fixed diameter piping, and can achieve very wide low frequency bandwidths [112, 113], modern designs for LPDA antennas majorly focus on substrate printed configurations [106, 114-128]. Due to fine control of boom and element dimensions on the order of 10mils or smaller for common manufacturing companies, individual dipole elements can be printed up to very high frequencies which would be prohibitively small for alternate manufacturing methods. With modern manufacturing techniques, however, one area which has not been investigated with LPDA design is working with 3D printing. In particular, designing monolithic or near monolithic antennas which can be printed with stereolithography (SLA) for high layer accuracy, and copper plated for minimal cost. In this chapter the modern state of 3D printing for the construction of LPDA is examined and a design is put forward which operates in the band from 1.67 to 8.525 GHz. While in its final design it is not feasible to cheaply 3D print the design with sufficient stability to survive plating at this time, the use of 3D printing as a guiding principle allows for inclusion of matching sections not replicated for LPDAs elsewhere in the literature, free control of characteristic impedance and structure shape, and detailed design not available in either classic designs with metal piping or design using substrate printed antennas. This chapter first reviews the basics of LPDA design put forward in [109], then examines the details of design for single polarized and dual polarized designs of LPDA with integrated impedance transformers. A method of miniaturizing the LPDA in its length, and the impact of variable growth rates are investigated. Lastly final results are displayed, measurement and manufacturing are discussed and compared with existing literature.

5.2 Design

5.2.1 Design of the Basic LPDA

The basic design for the LPDA was investigated thoroughly by R. Carrel in his thesis [109], and consists of a few key parameters that are well known. From [60, 109] the longest element is chosen to be $l_n \approx \lambda_{max}/2$, where λ_{max} is the wavelength at the lowest frequency of interest. Along with this, for each element, are a variety of associated, related parameters, namely element diameter d_n, feed spacing S_n, and position R_n. Relating each of the elements in an ideal system is the geometric ratio τ, typically between 0.7 and 0.95, governing the relationship between each subsequent value of the aforementioned as in (5.1).

$$\tau = \frac{l_n}{l_{n+1}} = \frac{d_n}{d_{n+1}} = \frac{S_n}{S_{n+1}} = \frac{R_n}{R_{n+1}} \tag{5.1}$$

Working in conjunction with this is the spacing factor σ, which governs the overall length of the antenna and the relative position of each element, defined equivalently by either the element spacing or the apex half-angle α in (5.2) [109],[60].

$$\sigma = \frac{R_{n+1} - R_n}{2l_{n+1}} = \frac{1-\tau}{4\ tan\,\alpha} \tag{5.2}$$

The last necessary value for the basic design are the number of elements, or equivalently the length of the shortest element, thereby determining the upper limit of the operating range. In [60, 109], we see the empirical equations put forward for B_a, the bandwidth of the active region, B_s the bandwidth as designed, and N, the number of elements, as below in (5.3) and (5.4).

$$B_S = BB_a = B[1.1 + 7.7(1-\tau)^2 \cot\alpha] \tag{5.3}$$

$$N = 1 + \frac{\ln B_s}{\ln\frac{1}{\tau}} \tag{5.4}$$

Where B is the desired bandwidth of the antenna. In this chapter, the band of interest is 1.67 – 8.525 GHz, as in chapter 4. Pursuing low profile, but a very consistent gain for use as a spectrum sensor, the designs examined in the process of this chapter use a high value of $\tau = 0.95$ and a low value of $\sigma = 0.05$. (5.4) above would suggest 35 elements, with the shortest element being half a wavelength at ~10 GHz. However, with a naïve design it is not until the shortest element is $\lambda/2$ at ~15.6 GHz with 44 elements that consistent gain and match is achieved at the upper end of the band, an increase of B_a from ~1.1 to ~1.8. Similarly, for the final design of this chapter, the recommended number of elements would be 14 elements, while the observed minimum for consistent gain and match is 16 elements, an increase of B_a from ~1.1 to ~1.6. This is suspected to be the result of extremely tight spacing between elements causing greater mutual loading and extending the usual band of operation.

Due to the difficulty of manufacturing the high frequency segment of LPDA antennas and the necessity of feeding the design from the tip, many LPDAs do not precisely follow the design principles dictated by the equations above. In larger, low frequency systems, the element feed-gap spacing and the element radius are often left constant due to the simplicity of utilizing standard sizes of metal round stock for elements and constant boom spacing [112, 113]. In higher frequency printed systems, the thickness of the boom is again frequently left constant due to dyson balun feeds and to maintain a constant boom impedance, as the substrate width does not change [106, 114-125]. Some designs feature a boom which does not change in size for the majority of its length, but tapers to a matching patch near the feed point [126], [127].

5.2.2 Design for 3D Printing

The design in this chapter is intended to leverage manufacturing techniques that have become more feasible for small detail in recent years, namely of 3D printing and electroplating. This allows greater flexibility of design choices, and greater control of the geometry of fine features. In the initial design work, two primary options are investigated: a standard design with round elements and a round profile two-wire boom, and a design with rectangular elements and a boom consisting of rectangular parallel strips. The rectangular boom is investigated due to allowing both greater freedom of placement for the elements, and allowing for tighter spacing of booms in a dual polarized configuration. However, the design of the rectangular LDPA offers poorer pattern shape, with a greater amount of rippling, which severely degrades amplitude based DOA sensing. Further, with the dipole elements consisting of thin sheets, manufacturing with an SLA process is judged to have a greater risk of warping. As such, the final design abandons rectangular elements in favor of the more robust, and simpler, round profile elements.

The final design consists of 16 elements, and can be seen in Fig. 5.1 and Fig. 5.2. The overall dimensions are 8cm base to feed, 8.4cm wide at the lowest frequency dipole, with a base that is 4.2cm in diameter. The geometric ratio $\tau = 0.868$, with a spacing factor $\sigma = 0.05$. The final value of τ is selected after beginning with 0.95, initially chosen to maintain high gain and highly self-similar frequency behavior. Working from an initial 44 elements to obtain sufficient

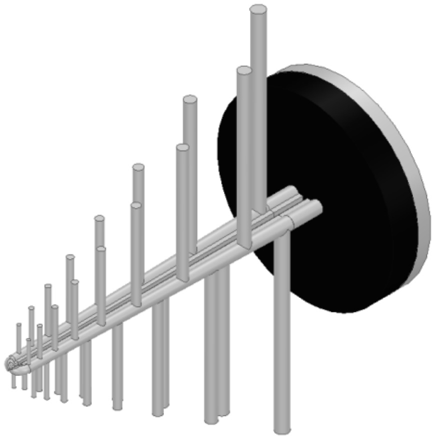

Fig. 5.1. Linearly polarized LPDA isometric view.

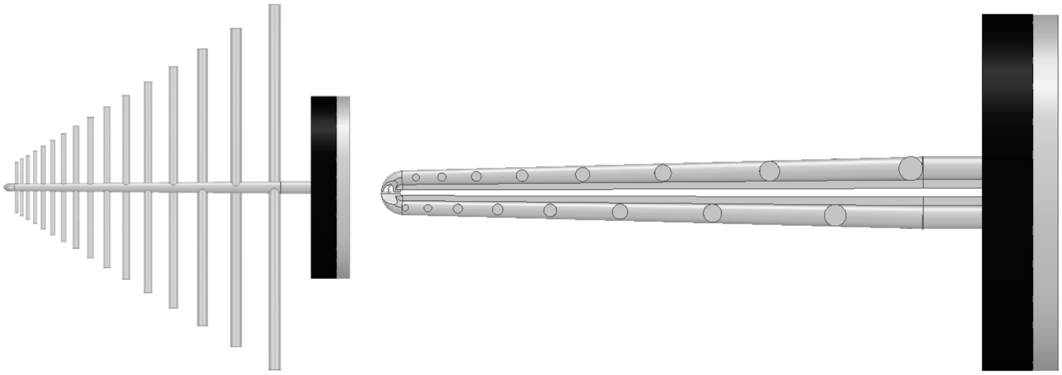

Fig. 5.2. Linearly polarized LPDA detail views.

bandwidth, the final value is chosen to keep the same minimum and maximum element length with 16 elements, keeping flat gain over frequency, and significantly reducing the size of the antenna. Fewer than 16 elements are judged to have too great a gain variability, and more than 16 are judged to have too little increase in performance to be worth the larger size. The spacing factor is kept very low at 0.05 to maintain as low a profile as possible, despite the overall reduction in gain compared to optimal designs [109]. A sampling of the sweeps of τ and number of elements are reproduced below in Fig. 5.3, showing the gain simulations from models from 12 to 17 elements.

The smallest element is chosen to be 11.6mm long, and 0.75mm in diameter, while the longest is 82mm long, and 2.8mm in diameter. The diameter of the smallest element is selected as

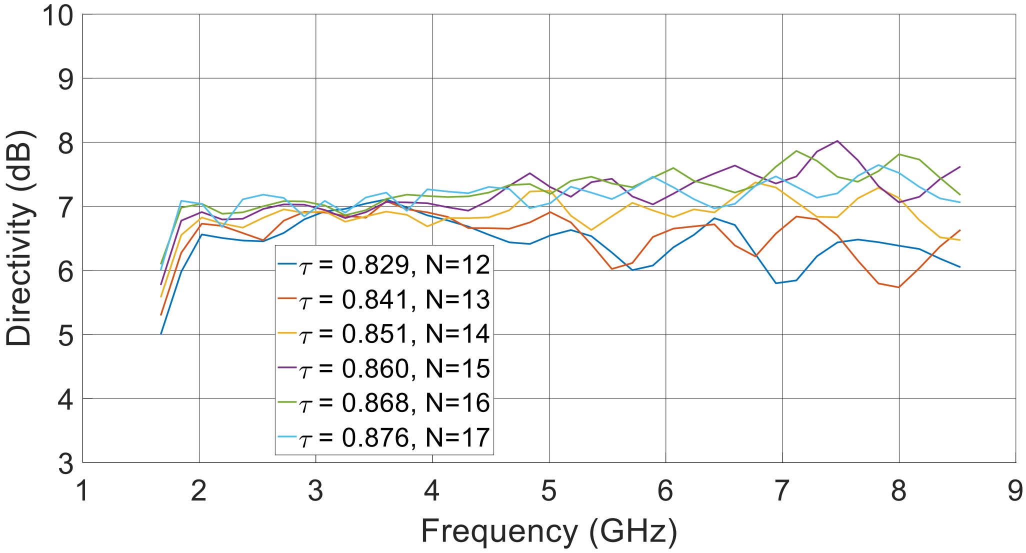

Fig. 5.3. Simulated directivity from antennas with differing N and τ to maintain the same bandwidth.

the minimum thickness of element that can be reliably printed in the DMLS and SLA processes. Fixing the smallest element results in the necessity of introducing a second value of geometric constant, $\tau_r = 0.915$, dictating the progression of the radius. This is, in part, essential to maintaining the match of the antenna, as the coaxial taper used for the feed can only match to a limited range of impedances without expanding the diameter of the boom further, and the largest element diameter (and thus the minimum diameter at the largest point of the boom) directly effects the required ratio of boom characteristic impedance to feed point impedance [109]. Thus, ensuring that the booms and elements remain a reasonable diameter by limiting their growth is essential.

A thin 047 semi-rigid cable (1.2mm diameter) is used for the feed, running up the center of the hollow boom. The boom tapers from 2.8mm to 1.75mm, with the boom spacing tapering equivalently to maintain constant characteristic impedance from 5.7mm to 3.55mm. The taper allows for the boom, and the element separation, at the feed to remain less than $\lambda/4$ side to side at the highest frequency of interest. The booms feature a capacitive fin running down the interior side, to lower the characteristic impedance from 160Ω to 107Ω. The booms curve inwards at the end to finish with parallel faces. The width of that feed region is 0.2mm. The sides of this curved feed region are tapered inwards, as can be seen in Fig. 5.4. The angle of that taper is chosen to be

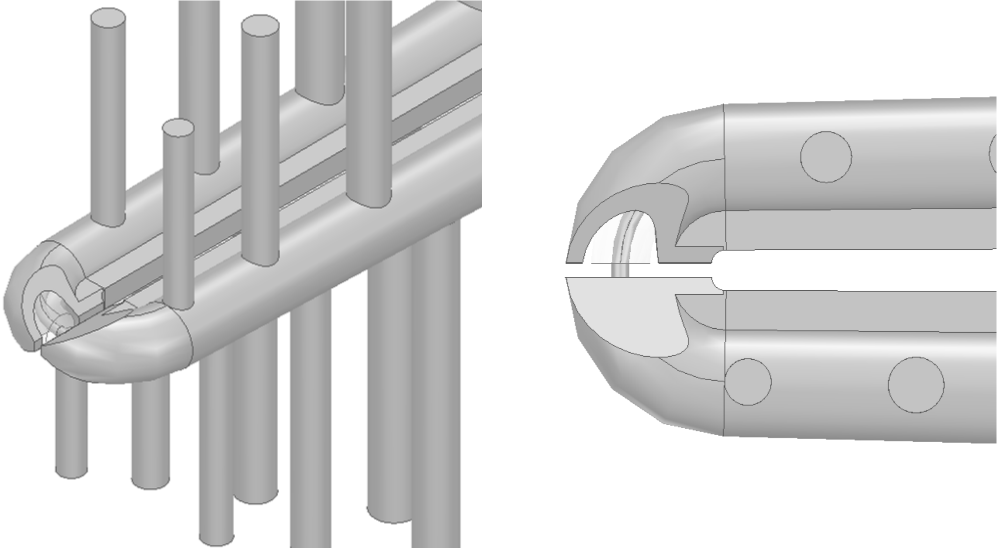

Fig. 5.4. Detail of feed region, showing angled feed taper, and capacitive plate loading of two wire boom.

30° to minimize additional capacitive loading of the feed-point, and to ease access for soldering. The coaxial feed is internally tapered, with the shield of the inserted coax removed to effect a linearly tapered line λ/4 long at the start of the band. The line tapers from 50 Ω to 68 Ω, a final coax outer diameter of 1.2mm. This dictates the minimum diameter of the feed boom as 1.75mm. As the thinnest reliable printed wall is approximately 0.25mm thick. The capacitive loading of the boom and the final impedance of the internal taper are determined iteratively, focusing on maintaining consistent radiation characteristics and consistent feed-point impedance despite varying dipole impedance as the ratio of l_n/d_n changes. The final value also agrees nicely with the graphs relating feed-point impedance and boom characteristic impedance in [109]. The distance to the ground plane is selected as a balance between minimal impact on the radiation patterns, while keeping low profile, as 13mm. The absorber chosen is MAST MF-22 series, at 6.35mm thick.

5.2.3 Design for Dual Polarization

The primary design of this chapter can be extended to dual polarization as can be seen in the geometry in Fig. 5.5. The major differences between this model and the linearly polarized model rely on the altered impedance characteristics of the 4 conductor boom. Due to the addition

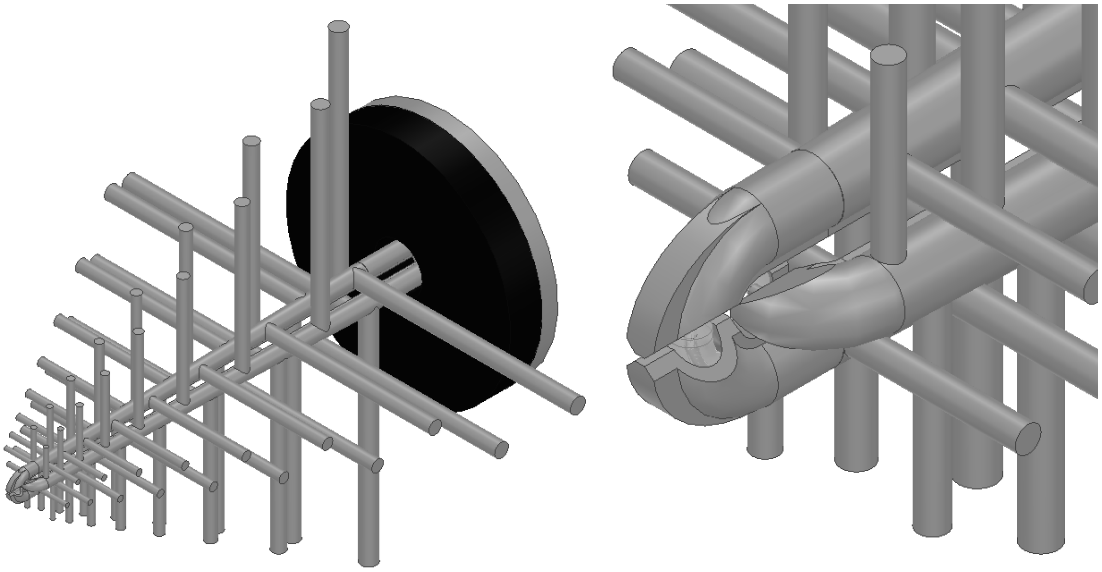

Fig. 5.5. Dual polarized LPDA isometric view, and detail of feed geometry.

of the two new booms, the two orthogonal excitations of the transmission line have a reduced characteristic impedance due to the altered field mode, as seen in Fig. 5.6. Due to the different geometry of the two feeds, the average feed-point impedance seen at each port is different. In the absence of a matching network, the impedance of the two ports differ by approximately 16%. To ensure that matching is achievable with the coaxial tapering available, the capacitive loading of the booms is used to bring the overall boom impedance down to 113Ω. This has the effect of bringing the feed-point resistance in each port down to values which can be separately matched using the same method of tapered coaxial matching sections. Due to additional inductive loading on the second ‘outer’ polarization feed preventing good match with the tapered line alone, additional capacitive loading is added at the feed-point. The taper angle of the outer feed is reduced from 60 to 45 degrees, maintaining access for soldering by hand while increasing the capacitive load on the outer feed. This is insufficient in itself to cancel the inductive load. To further compensate, a capacitive fin is added to the exterior of the boom, and swept parametrically until

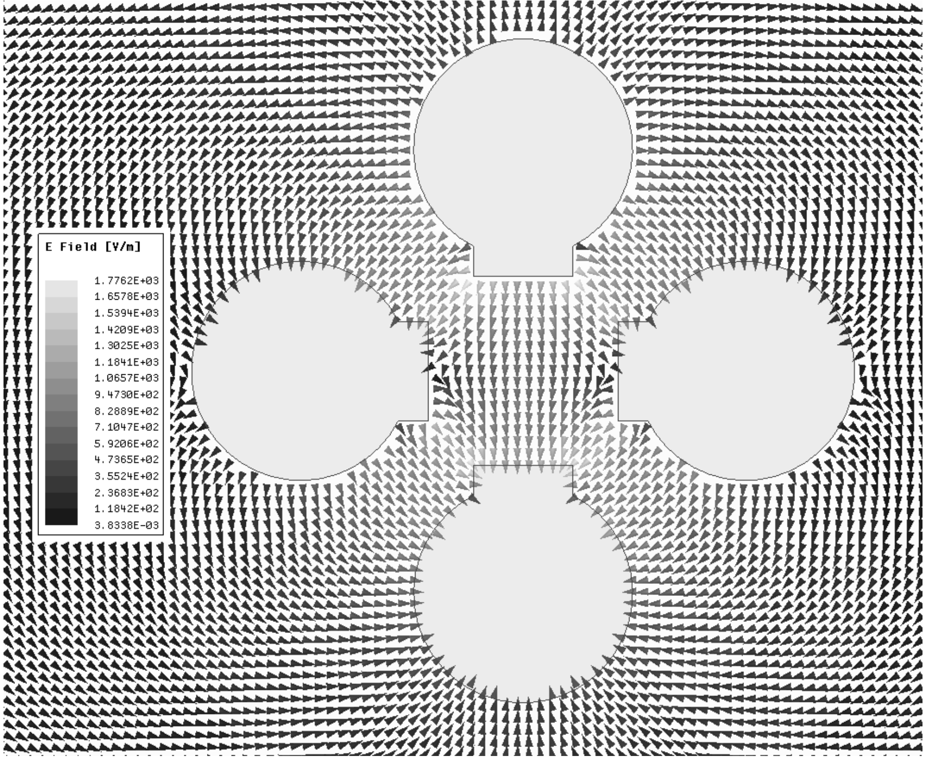

Fig. 5.6. Detail of boom electric field, top and bottom terminals are differentially excited, left and right terminals are unexcited. Simulated in ANSYS HFSS [130].

the match is brought to acceptable levels. The resistive feed point impedance of each polarization is then separately matched to 50Ω using different taper geometries as necessary.

An alternate strategy investigated for the design of the dual polarized LPDA is the use of a tapered value of τ. This is done by replacing the single value of τ as follows in (5.5).

$$l_n = l_0\tau^n \rightarrow l_n = l_0(mn+b)^n \tag{5.5}$$

Utilizing a tapered value of τ, one can increase the directivity of the higher frequency region of the antenna without changing its form factor. By fixing the value of l_0 when n=0 and l_{max} when $n=n_{max}$, the overall length of the antenna is preserved. It is then only necessary to select the length relationship of the final two dipole elements (length ratio denoted herein as τ_{15}) to uniquely determine the slope and starting value of the τ taper. It is quickly noted in simulations that the performance of the antenna in the case when element position R_n is also governed by a tapered τ value the performance of the antenna is greatly degraded. However, maintaining the same positioning from the original design, while changing the element lengths according to the tapered τ, allows for a significantly improved match and for increased high frequency directivity. One evident drawback to this method of design is the appearance of narrowband dropouts in directivity. These effects can be seen in Fig. 5.7, showing the directivity for a variety of tapered models, and

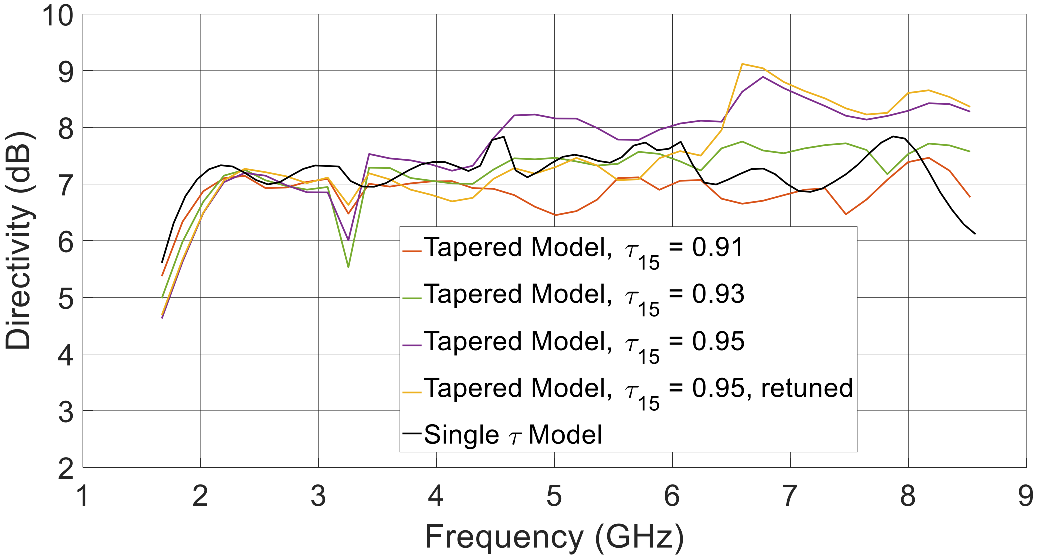

Fig. 5.7. Directivity of dual polarized models with tapered τ, showing drop in directivity at 3.25 GHz in tapered models.

Fig. 5.8, showing the effect on the match. Additionally, it shows the behavior of a model which was retuned to remove the gain dip at 3.25 GHz. As τ_{15} increases, the directivity drop near 3.25 GHz becomes more severe, and high frequency directivity is increased. Tno account for the presence of the 3.25GHz drop in directivity, a retuned model was created from the τ_{15}=0.95 model. To achieve this, the currents are examined throughout the band, and it is found that the expected elements with near resonant lengths at 3.25 GHz are not resonating, and instead the power at 3.25 GHz carries through and radiates off of the groundplane as a backlobe in the radiation pattern. To correct this, various adjustments to element lengths are attempted, in the final working version the closest element to resonance at 3.25 GHz, and the surrounding two elements, are replaced with their closest equivalent in length from the model with τ_{15}=0.90, which does not show a significant drop in gain. The two elements surrounding those are also adjusted to a length halfway between their prescribed length and the length of similar elements from the τ_{15}=0.90 model. In so doing, the directivity drop at 3.25 GHz is reduced by ~0.6dB (roughly 1dB better than the worst version of this dip seen in the τ_{15}=0.93 model). This does however introduce an additional drop of similar depth at 4.1 GHz. The net result of this is to bring the majority of the operating band back to within a variation of approximately 0.5dB from nominal. Higher frequency directivity increase is made a

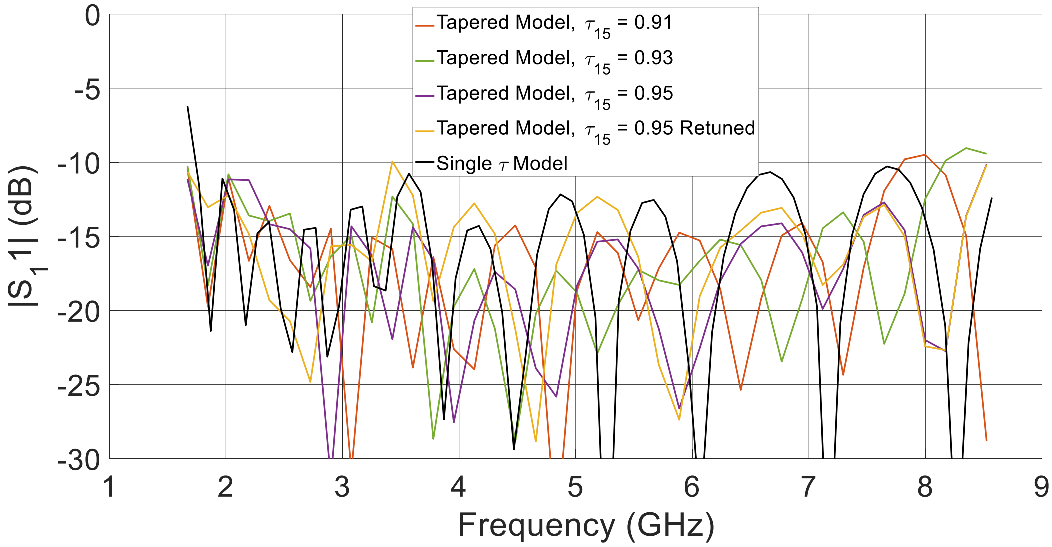

Figure 5.8. $|S_{11}|$ from tapered τ models. Match is improved over the majority of the band by tapered models, τ_{15}=0.95 model shows particular improvement at high frequencies.

sharper transition occurring after the adjusted elements operating band, as compared to the original τ_{15}=0.95 model, wherein the increasing directivity over frequency is more gradual.

5.2.4 Miniaturization Strategies

Specific efforts are made to miniaturize the LP antenna, with particular focus on miniaturization along its length. One work in particular shows great promise through the use of dual resonant elements to reduce the number of elements, and thereby reduce τ. In [128] they discuss a 40% reduction in size achieved due to this approach. They compare as a baseline case their 25 element dual band model with a differently designed model containing 40 elements, with different τ and σ. Following this approach, initial work is performed based on designs with a high τ of 0.95 and N=44. While significant reductions in size seem to be achieved via this approach, baseline comparisons without dual band elements show little difference in behavior between the dual band design and designs with only regular dipole elements in the match, but in some cases the dual band performance is worse than standard designs in terms of directivity, with greater variability and deeper narrowband drops in gain. An example of such a design can be seen in Fig. 5.9. Performance comparison of three versions of this antenna, for 14 and 16 elements are seen here in Fig. 5.10 and Fig. 5.11, alongside the performance of models with the same design parameters but with only regular dipole elements.

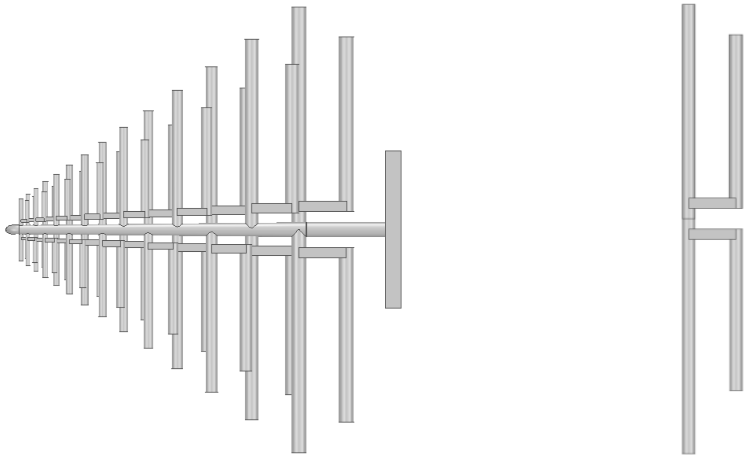

Fig. 5.9. Example of dual band element LPDA and side view of individual element.

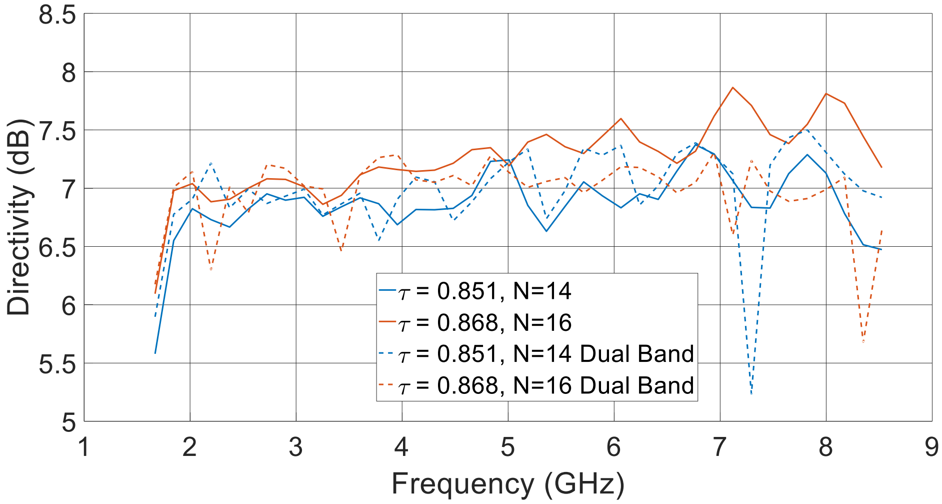

Fig 5.10. Directivity of dual band and baseline designs. Narrowband drops in gain and inferior performance are more prevalent in dual band design (black) than baseline case (gray).

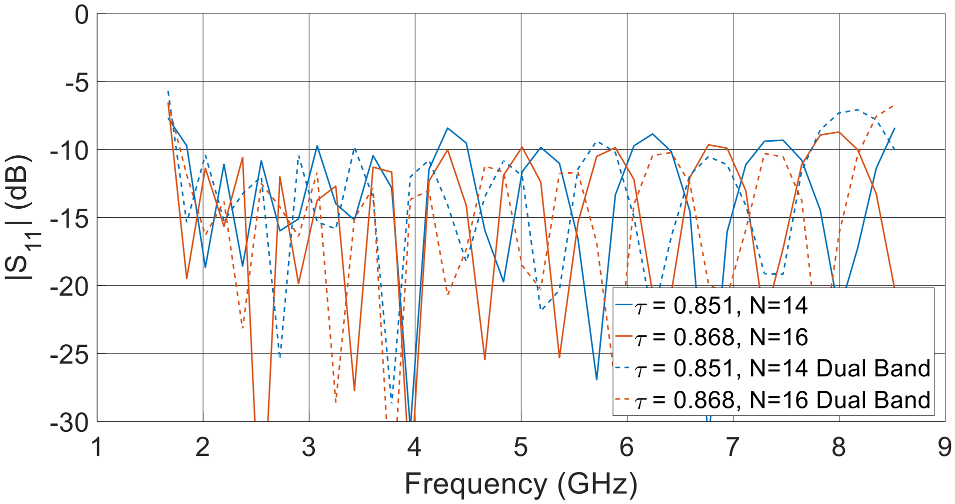

Figure 5.11. Match of compared standard and dual band LPDA configurations, no significant differences in level are observed

5.3 Manufacturing and Performance

The single pol LPDA antenna proposed is designed as a FOA sensor and amplitude based DOA sensor to operate over a larger than 5:1 bandwidth, from 1.67 to 8.525 GHz. To that end, it is desired to have minimal gain variation in that band, and be able to sustain a positive direction finding function (DFF) slope [6]. Simulations of the antenna are carried out in ANSYS HFSS. The simulated geometry can be seen in Fig. 5.1 and Fig. 5.2. Manufacturing is initially attempted with

SLA 3D printing, one example of a printed LP segment with print scaffolding can be seen in Fig. 5.12. While printing is successful in creating the exterior geometry, printing the hollow boom in a split block configuration to enable plating does not have the necessary rigidity to withstand the plating process. As a result, the final manufacturing of the design is undertaken with subtractive machining, by milling the design from brass. Due to the delicate features involved this is substantially more challenging, as the high cutting forces can damage the design. Minimum wall thickness in the milled design is 0.25mm thick. DMLS printing is also attempted however insertion of the coax results in shorting to the line wall due to sharp stray printed structures within the hollow section.

The final manufactured design can be seen in Fig. 5.13, along with a view of the two halves of the hollow boom prior to soldering. Certain manufacturing defects in the final build can be attributed to this approach of manufacturing. Among them, various elements are manufactured shorter than desired or with too thin a radius, clipped due to the tool pulling into the material. Though it cannot be discerned from the pictures below, the tip of the feed point is also clipped on one side, and bent out of position on the other. Further, measurement of the spacing of the design shows that the booms are both shifted closer to one another by approximately 0.1mm, as well as

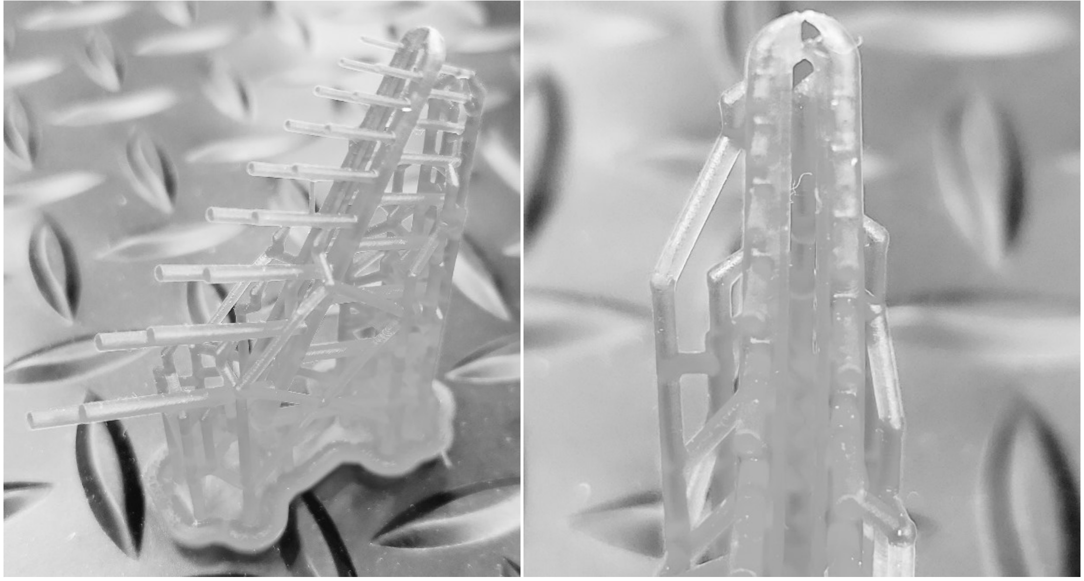

Fig. 5.12. Early test of 3D printing. Dipole elements and coaxial taper have good definition.

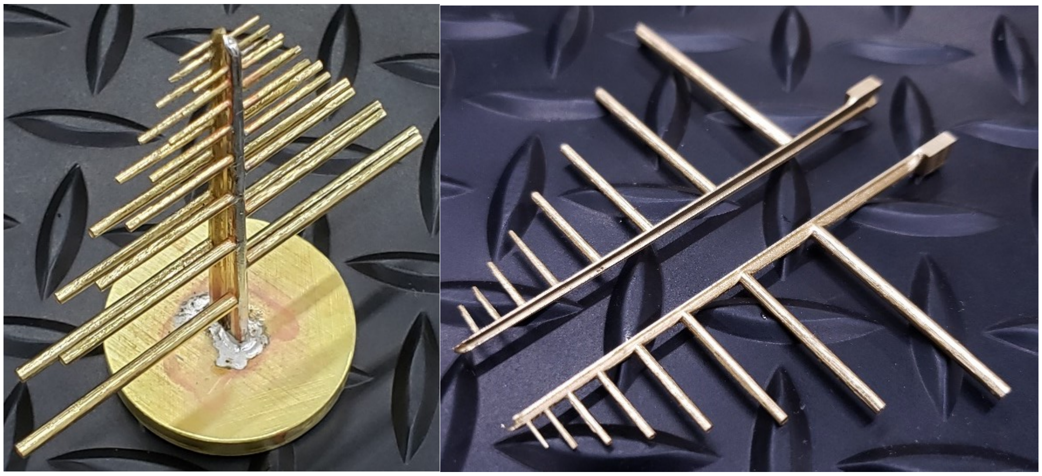

Fig. 5.13. View of design milled from brass, and view of milled hollow boom.

being tilted slightly out of position, misaligning the tip of each boom by 0.4mm. In final simulations of the measured setup these inaccuracies, and defects caused by soldering, are investigated and modeled as closely as possible.

In Fig. 5.14, the simulated and measured VSWR can be seen. Close modeling of the antenna exterior geometry, including varying element size and position for resonant elements, overall coax feed taper diameter, along with modeling of losses due to surface roughness, do not explain degraded match near 3.8 GHz, so mismatch is likely caused by solder leaked into the interior surface of the coaxial taper in a way that cannot be measured without destroying the constructed design. Even with the single point degradation, measured VSWR shows good match within the band, and even slightly higher in frequency than expected.

Fig. 5.15 shows the original measurement setup within the anechoic chamber. The antenna is mounted on a larger PLA support structure with additional MF-22 absorber, feeding cables and mounting standoffs to chamber positioner are further covered in absorber. Measured directivity can be seen in Fig. 5.16, alongside the original simulated directivity, and a simulation seen in Fig. 5.17(a), containing an accurate model of the measurement setup, along with measured inaccuracies in manufacturing and soldering, and estimated effects of surface roughness on conductivity.

The largest contributing factor to the difference between the measurement setup and original simulations exists in the placement of absorber in the test. Additional absorber placement

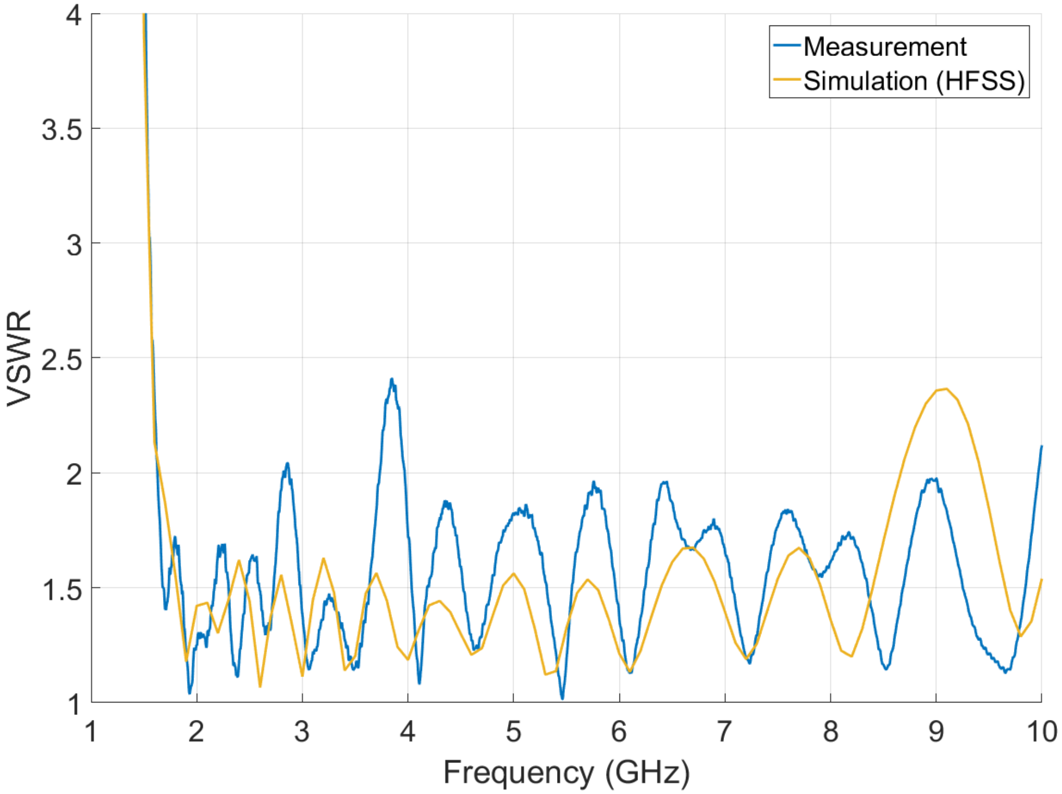

Fig. 5.14. Simulated and measured VSWR.

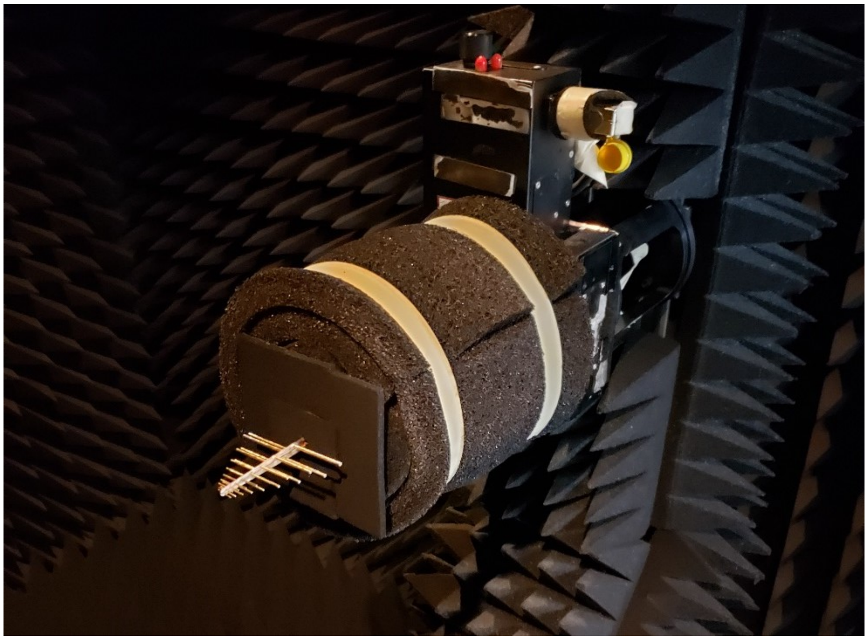

Fig 5.15. LPDA mounted in anechoic chamber.

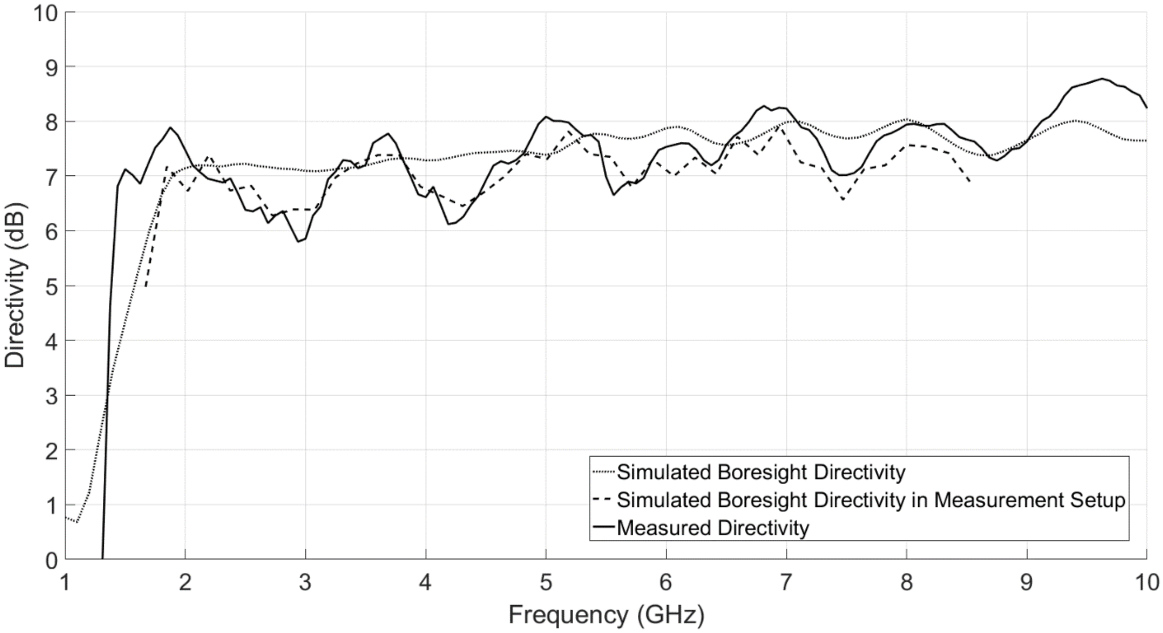

Fig. 5.16. Simulated and measured directivity, showing good agreement after accounting for absorber placement and manufacturing inaccuracies.

in the antenna near field results in significantly greater variability over frequency than initially expected. Further simulations and measurement in the absence of larger sections of absorber confirm that the antenna is more sensitive than anticipated to absorptive materials in the near field.

Simulation of additional measurements with a reduced absorber setup can be seen in Fig. 5.18, showing good agreement (within 0.5dB) of the original simulations and the simulation from Fig. 5.17(b). Simulation of printed PLA support structure (visible as larger black disk attached below the antenna ground in Fig 5.17(b), and not visible in the image in figure 17(a) is done as isotropic, utilizing data from [129]. In spite of build inaccuracies, cross polarization remains low, staying below -12dB within the band, and below -15dB in the majority of the band, as can be seen in Fig. 5.19. Measured radiation pattern shape also agrees with simulations well, as can be seen in a sampling of measured plots in Fig. 5.20. While not manufactured, simulated VSWR and directivity for the dual polarized LPDA from Fig. 5.4 can be seen in Fig. 5.21 and Fig. 5.22, respectively, alongside the simulated performance from the single pol case, and the behavior with an adjusted variable tau design. As can be seen, the match is greatly improved in the tapered tau

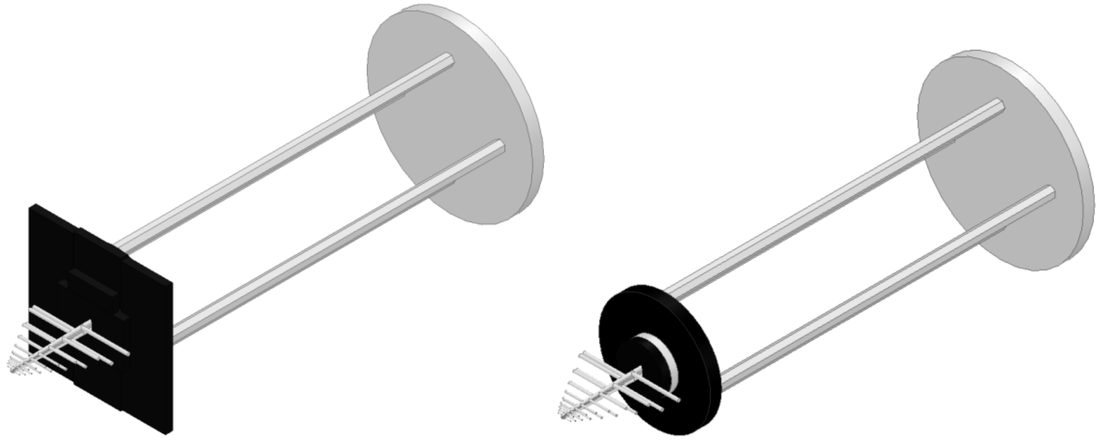

(a) (b)

Fig. 5.17. Simulation of original measured setup (a) and of measurement setup testing absorber interactions (b). Absorber covering supporting struts was found to have minimal impact. The majority of the impact is from additional MF-22 absorber. (larger square backing in (a)).

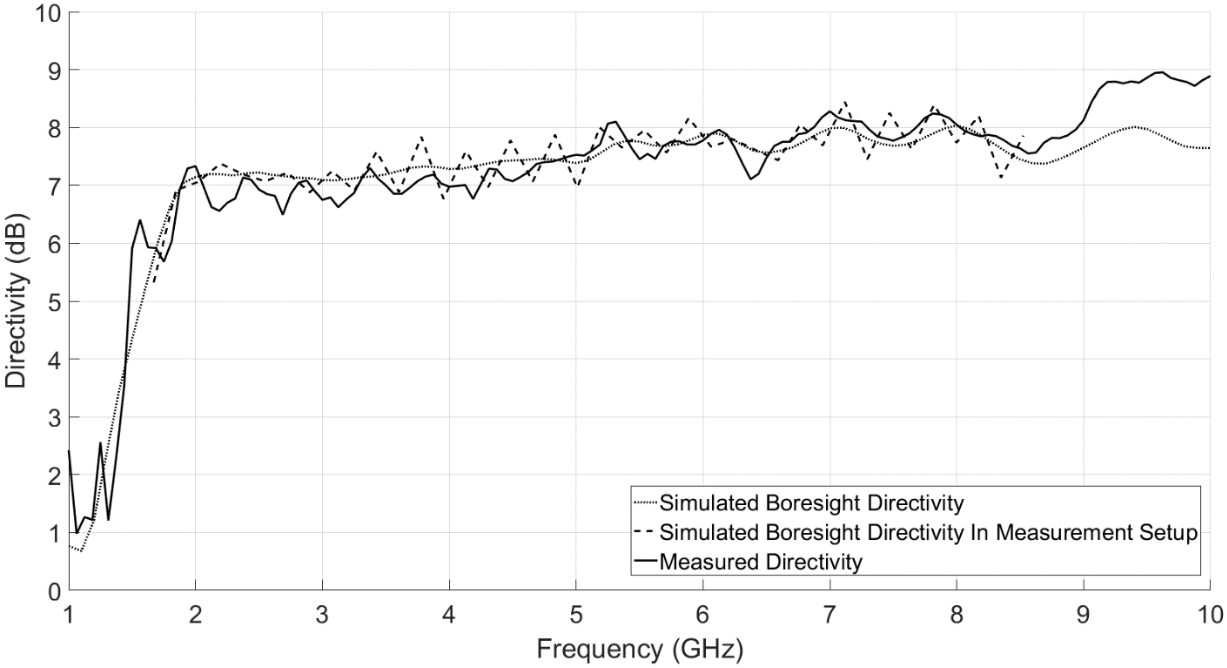

Figure 5.18. Measured and simulated directivity with only small absorber puck on ground plane. (Fig. 5.17(b)).

case. The further impact of the tapered tau model can be seen in the higher gain at high frequency, as expected from higher tau in the high frequency active region. Low frequency behavior is dominated by interaction with absorber and reduced tau, despite longer elements resonating down to lower frequencies. Drops in directivity at individual points near 3.25 and 4 GHz are the result

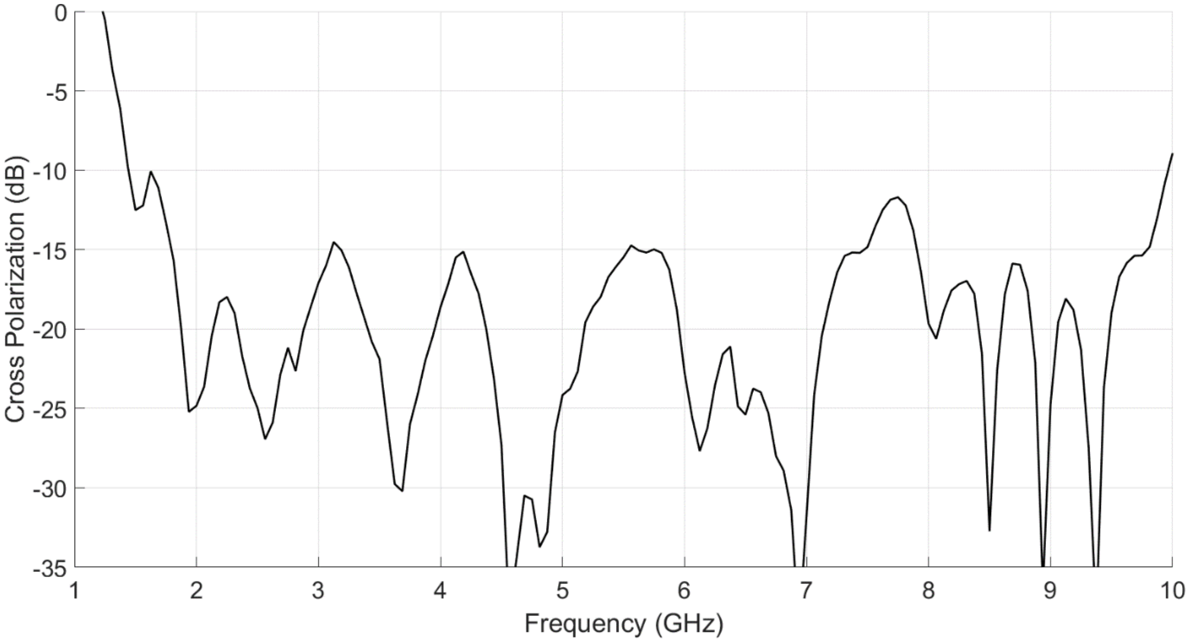

Figure 5.19. Measured cross-polarization over the band of interest.

of increased back lobes at those frequencies. Without retuning individual elements, 3.25 GHz directivity drop is ~0.6dB lower, and 4.1GHz dip is not present.

While the LPDA put forward is primarily intended for spectrum sensing applications, it is also functional as a direction finding sensor in both planes. care was taken throughout the design process to ensure that the design in question maintains unambiguous FOV for E and H-plane direction finding, for both the single pol, and dual pol designs. Low overall gain and wide beamwidth, as primarily selected for a broad beam-front directional spectrum sensor, limits the available DFF slope, however achieves wide unambiguous FOV operation. Fig. 5.23 plots the simulated and measured DF performance for the single pol case, and Fig. 5.24 plots the simulated E and H-plane DF performance for the dual pol case, and the circular pol DF performance.

5.4. Performance Comparison

Table 5.1 shows a comparison between LPDAs in the existing literature and the design put forward in this work. Relevant metrics for comparison shown are average gain, bandwidth, and mid-band electrical size, along with whether or not the design is dual polarized, and whether it was constructed and measured. As has been noted previously, [114-128] are all fabricated as PCB

Table 5.1. Comparison to Existing Literature

Source	Gain	BW	Dual Pol?	Size (λ_{mid})	Built?
[114]	7.1	1.6:1		1.48 x 0.55	
[115]	6	2.9:1		0.88 x 0.44	X
[116]	5.5	1.9:1		0.82 x 0.70	
[117]	6.6	2.25:1		0.88 x 0.24	
[118]	7	3.4:1		0.88 x 0.59	X
[119]	4.4	4:1		0.38 x 0.28	X
[120]	7.8	4.5:1		0.77 x 0.45	
[121]	4.2	5.5:1		0.51 x 0.35	X
[122]	7	4.5:1		0.75 x 0.51	
[123]	6.2	1.28:1		0.42 x 0.49	X
[124]	7.3	1.6:1		1.10 x 0.53	X
[125]	5	3.42:1		0.94 x 0.59	X
[126]	5.2	12.5:1		0.48 x 0.37	X
[106]	6.7	18:1*	X	0.63 x 0.87	X
[127]	8.1	9:1		1.20 x 0.53	X
[128]	4	20:1		0.36 x 0.43	X
This	7.3	5.4:1		0.46 x 0.44	X
This	7	5.4:1	X	0.46 x 0.44	

printed traces. The majority of work prior to the last few years shows inferior gain, bandwidth, and longer length, [114, 115, 117, 118, 122, 124, 125]. The majority of these are classical designs consisting of a single boom width, often fed from the tip with a coaxial cable, though in [118, 125] fed with microstrip from the back. Most are designed with loading or line meandering intended to miniaturize width. Designs in [116, 119, 123], while smaller in length, are of a substantially reduced bandwidth relative to this work, and of substantially lower gain. [120] shows comparable gain, however the design is substantially larger. The work in [121] shows substantially lower gain, without having a significantly reduced length, although over similar bandwidth. Further, none of the designs mentioned so far can be made dual polarized. The designs really worth investigating are [106, 126-128]. With [126-128] showing wide bandwidths, and [127] showing significant gain. They are each, however, significantly larger than the design proposed, and were not designed for miniaturization of any kind. These designs also are not made for dual polarization, and their design framework could not support it. Only one printed design capable of achieving similar performance to the dual polarized antenna proposed herein was found in the literature in [106]. However, the

E-Plane Directivity at 1.67GHz

E-Plane Directivity at 2.02GHz

E-Plane Directivity at 2.55GHz

E-Plane Directivity at 3.08GHz

E-Plane Directivity at 3.43GHz

E-Plane Directivity at 4.13GHz

E-Plane Directivity at 4.48GHz

E-Plane Directivity at 5.01GHz

E-Plane Directivity at 5.54GHz

E-Plane Directivity at 6.06GHz

E-Plane Directivity at 6.59GHz

E-Plane Directivity at 7.12GHz

E-Plane Directivity at 7.47GHz

E-Plane Directivity at 8.17GHz

E-Plane Directivity at 8.53GHz

Fig. 5.20. Measured (solid) and simulated (dashed) co-pol and cross-pol patterns.

match of the antenna proposed in [106] is quite poor, with the two polarizations substantially differing. In all this, it can be seen that designing for modern manufacturing capabilities for LPDA antennas offers significant improvements in design, particularly with respect to integration of improved matching structures allowing rear side feeding without additional matching like that needed in [126, 128].

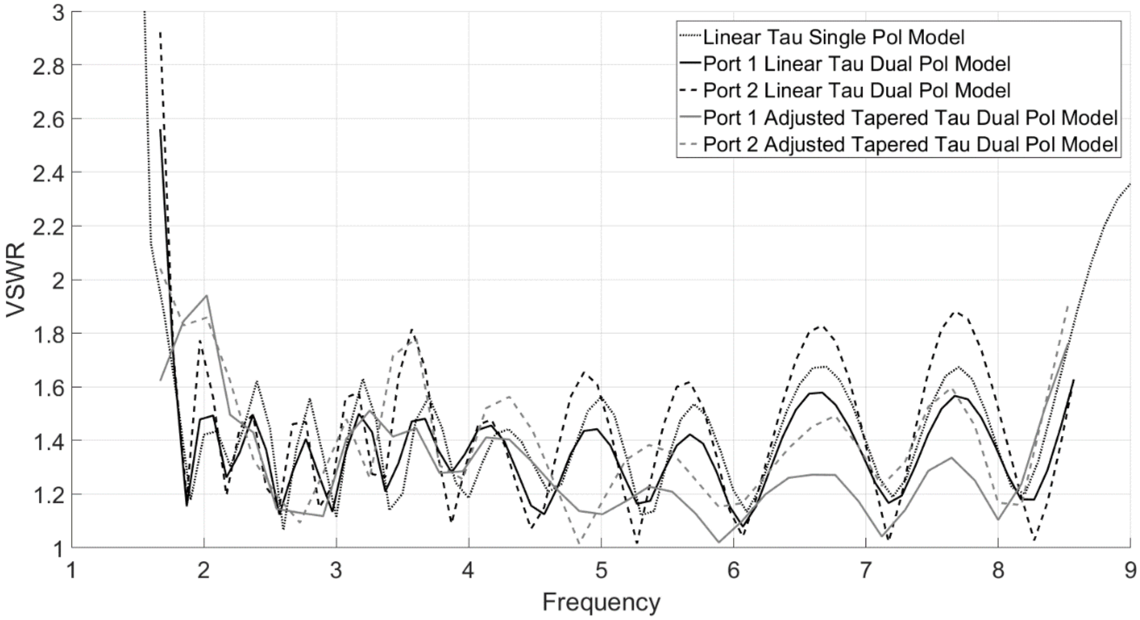

Fig. 5.21. Simulated VSWR for dual pol LPDA as compared with single pol LPDA.

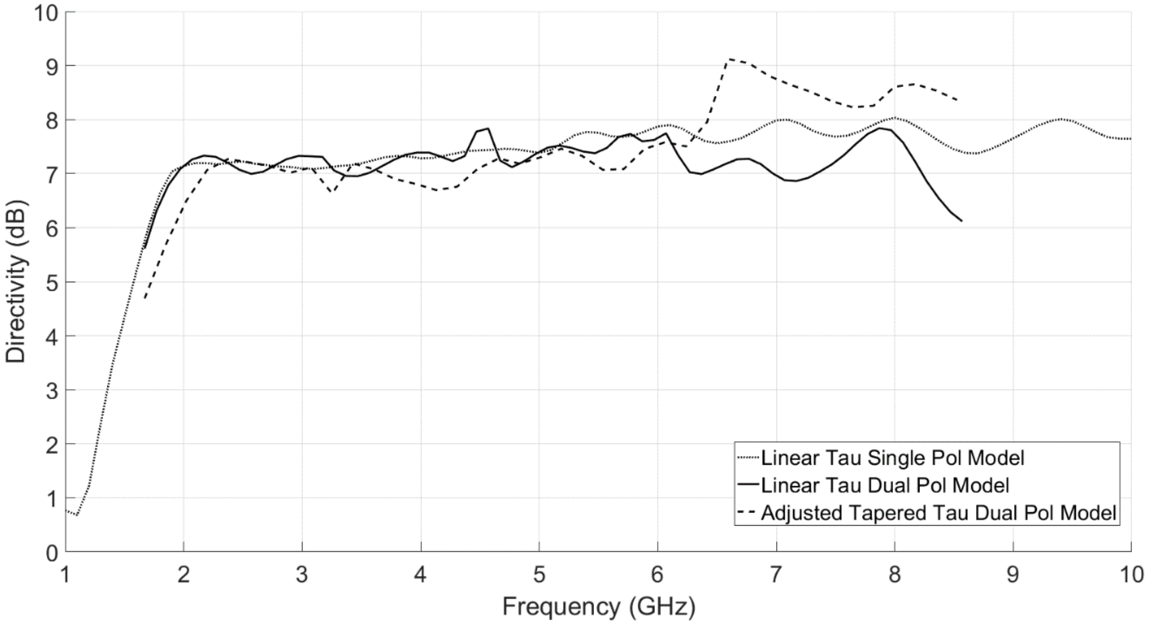

Fig. 5.22. Simulated Directivity for dual pol LPDA as compared with single pol LPDA.

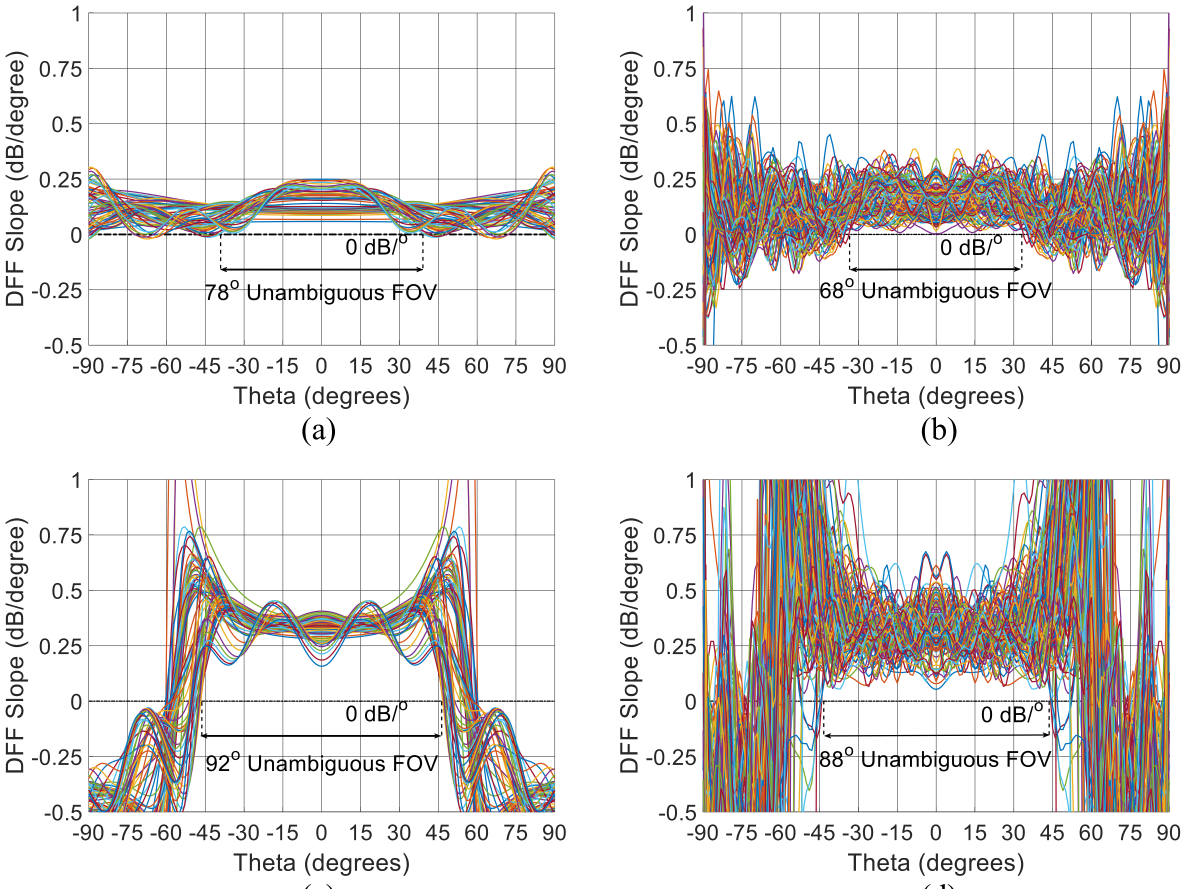

(a) (b)

(c) (d)

Fig. 5.23. Simulated and measured DFF for single pol LPDA. (a) simulated H-plane DFF slope, (b) measured H-plane DFF slope, (c) simulated E-plane DFF slope, (d) measured E-plane DFF slope.

5.5 Conclusions

This chapter has presented the design procedure and measured results of a compact LPDA developed for operation between 1.67 and 8.525 GHz. Design for additive manufacturing allows for convenient integration of matching networks, and allows for a work to take advantage of loading structures not available to printed LPDAs to gain significant control of match without sacrificing gain. While materials available at this time for cost effective 3D printing do not allow for sufficient rigidity to survive construction, enhancement of 3D printing technology will likely allow for further developments of dual polarized LPDA antennas of extremely high bandwidth, while taking advantage of methods like top loading and meandered lines, already widely known

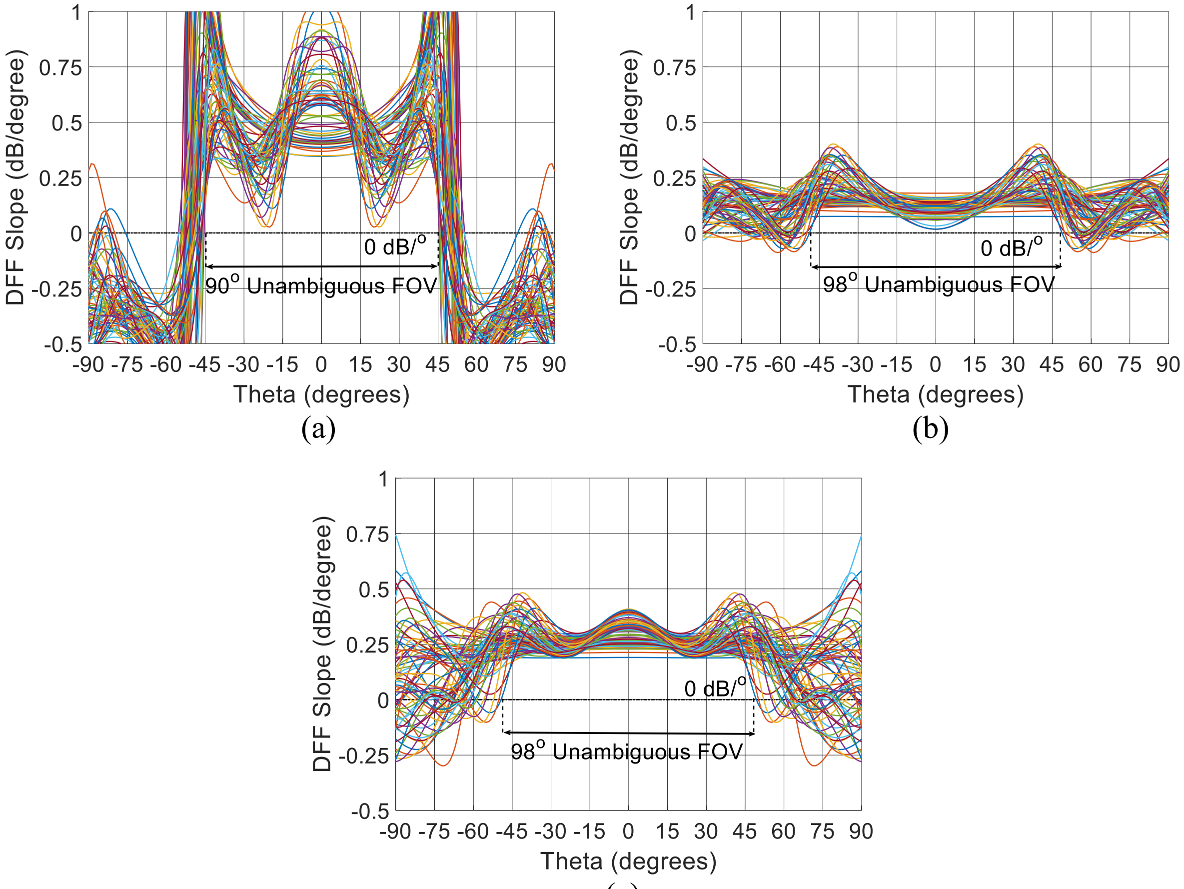

(a)

(b)

(c)

Fig.5.24. Simulated (a) E-plane DFF slope, (b) H-plane DFF slope, and (c) LHCP DFF slope for dual pol LPDA system.

for reducing width and length of LPDA antennas in printed form. The design approaches taken herein provide a starting point to further the realization of 3D printed antenna structures with integrated matching. Future work includes the fabrication of the dual polarized model included herein, along with further exploration of miniaturization techniques as they can be applied to dual polarized 3D printed LPDAs, and greater exploration of the application of DMLS printing techniques to this work.

CHAPTER 6

C-KA BAND 3D PRINTING OF COAXIAL COMPONENTS

6.1 Introduction

Modern commercial and defense systems require increasingly complex RF components to deal with increasingly strict electrical requirements. In addition, high complexity is often desired alongside low weight, small form factor, low loss, and low cost. While the use of traditional manufacture methods like split block fabrication and assembly methods remains common for accuracy and ease of access to internal components [37, 45, 46], increasingly manufacturing is moving towards monolithic designs with reduced integration complexity and post-processing [28, 38-40, 131]. Monolithic designs have been greatly enabled by both micromachining approaches [23, 24, 131-133], and additive manufacturing (AM) approaches like direct metal laser sintering (DMLS) and stereolithography (SLA) [28, 37-41, 45-48, 134, 135]. While previously micromachining was the dominant alternative to traditional machining, steadily improving accuracy of these AM methods has led to their adoption across the RF spectrum, including up to millimeter wave frequencies in V and W-band, and above [28, 136]. AM technologies have been used for both standalone antenna configurations [134, 136] and fully integrated subsystems [135]. While this has seen significant implementation for waveguide-based systems [39-41], it has seen significantly less use for monolithic self-supported coaxial line-based systems. Other monolithically printed components using coaxial inputs frequently rely upon inserted pre-fabricated coaxial probes or cables [38]. The drawback of this monolithic approach is the challenge of maintaining manufacturing accuracy on internal components, both from a standpoint of avoiding distortion, and allowing for un-cured or un-sintered material to be released properly from internal areas, all without internal supporting structures which cannot be removed.

DMLS manufacturing is commonly utilized for antenna systems [28, 134-136], however its high cost and high surface roughness continue to reduce its widespread adoption. SLA manufacturing can achieve high flexibility and low weight with relative ease, even with commercially available, desktop systems like the Form 3 printer [137]. Copper plating of SLA printed devices is popular [37-43, 45, 46] for its increasingly good accuracy, and its low surface roughness.

To support spectrum sensing and direction finding antennas across the spectrum, a family of fully monolithic 3D printed, coaxial-based components must be made available to meet a variety of needs. For the work of this thesis, this family of components consists of wideband, through-line coaxial components, coaxially fed resonator devices, and coaxial filters and diplexer devices. Some advantages of the coaxial line basis for this technology include wideband single mode operation, low loss and dispersion, and the possibility of dense line packing. Additively manufactured coaxial lines are not unknown in the literature, however, work on their designs has primarily focused on designs featuring split block construction [37, 45, 46], or design for hollow cavities filled with liquid metal [47, 48]. Only a small number of designs in the literature deal with a self-supported line similar to that described in this chapter [49, 50], and those that do are relatively low in frequency, and operate over a narrower bandwidth than that proposed here.

SLA manufactured cavity devices in the literature are significantly more prevalent, one of the more naturally monolithically printable structures, spherical resonator designs, are particularly common. [37, 39, 40]. As a great deal of work has been done with micromachining to characterize the behavior of rectangular cavities, [132, 138] the focus on the design of a rectangular cavity in this chapter will be primarily on comparing the differences between SLA manufactured and DMLS manufactured rectangular resonators, and the adaptation of a monolithic feed system to the larger minimum feature sizes required by AM.

AM filter and diplexer devices in the literature primarily focus on waveguide and cavity technologies [15, 38-40, 42-45]. Publications examining self-supporting coaxial AM topologies are more limited [49-51], and none examine diplexer devices. Looking at the existing body of work as a whole, the designs are largely narrowband, and for diplexers, concerned with non-contiguous operation. From this, we can see there is a need for solutions featuring wide pass bands with contiguous spectrum coverage. In addition, little has been attempted in the way of fully utilizing 3D printing to make compact designs. Those that do, like [42], utilize '2.5-D' strategies, like meandering lines in a single plane. The work put forward in this chapter examines in depth the construction of high frequency, wideband coaxial lines designed for monolithic DMLS fabrication, the compared behavior of DMLS and SLA fabrications through the perspective of resonator design, and the design and fabrication of monolithic filter devices and diplexers covering wide contiguous bandwidths. This work advances the state of the art for AM of coaxial components.

In this chapter, multiple devices are demonstrated. In section 6.2 a wideband coaxial line covering 10-30 GHz in DMLS fabrication, with designs for further bandwidth as the DMLS technology continues to mature. Second, section 6.3 presents the design and fabrication of a rectangular resonator in both DMLS and SLA technologies, and a comparison of the measured performance of the devices. Following this in sections 6.4, the design and fabrication of two filters is presented, operating over 4-7.8 and 7.8-15 GHz, respectively. Finally, section 6.5 examines the design of a monolithic contiguous diplexer integrating similar filters, in both a standard planar configuration, and two compact topologies fully utilizing the 3D printing capability to route lines. The major devices discussed in this chapter can be seen in Fig. 6.1.

6.2 Additive Manufacturing of Coaxial Components

6.2.1 Design Information for Ka-Band Coaxial Line

To design a monolithic, additively manufactured coaxial component, it is essential to first understand the boundaries posed by the manufacturing technology in use. DMLS and SLA technologies are relatively young manufacturing technologies, and the current tolerances they achieve, and the minimum feature sizes they allow, are comparatively large when compared with traditional manufacturing. The minimum feature sizes typically realizable in both technologies, and other relevant parameters, are presented in Table 6.1 [139, 140].

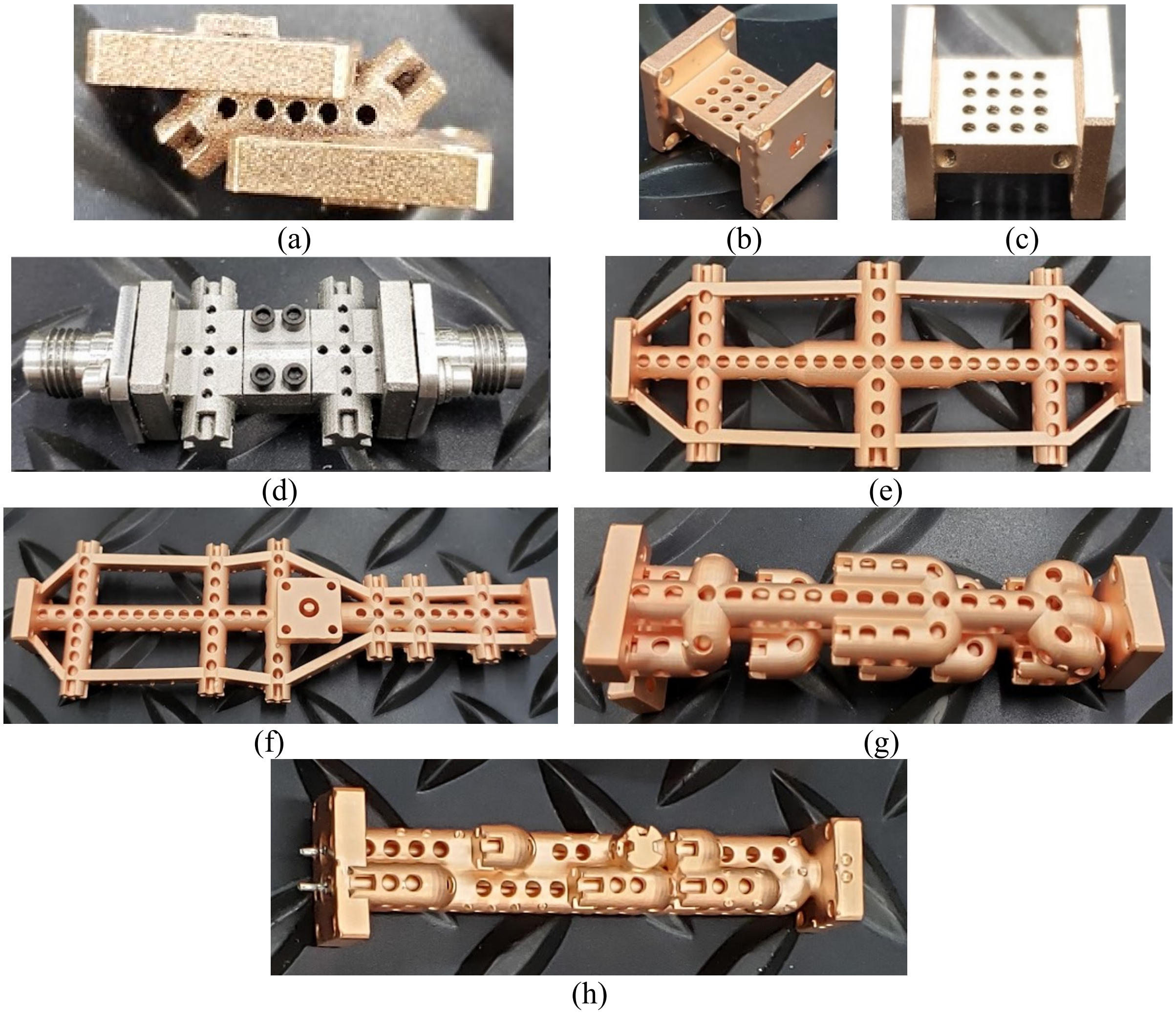

(a) (b) (c)

(d) (e)

(f) (g)

(h)

Fig. 6.1. (a) ‘Y-junction’ DMLS fabricated coaxial line, (b) rectangular resonator in SLA fabrication, (c) rectangular resonator in DMLS fabrication, (d) ‘High-band’ two-stub filter in DMLS fabrication, (e) ‘Low-band’ three-stub filter in SLA fabrication, (f) ‘Flat’ configuration of monolithic diplexer structure in SLA fabrication, (g) ‘Packed’ configuration of monolithic diplexer, with lines routed to maintain 13.5 x 9.8mm columnar area, and (h) ’20Ω Packed’ diplexer, redesigned for smaller footprint from the original ‘Packed’ configuration.

In addition to taking into account the minimum feature sizes, the physical process involved must be understood. Specifically, DMLS involves layer by layer sintering of a bed of metal powder. As successive layers of powder are added, and the particular layer is sintered in place, a large quantity of unsintered powder is left in place around the device; similarly, in SLA, a photopolymer resin is cured in place onto a part by a laser, leaving large amounts of uncured resin

TABLE 6.1. ADDITIVE MANUFACTURING TECHNOLOGY DESIGN GUIDELINES

DMLS Printing Parameters	
Tolerance	± 0.076 mm
Layer Thickness	30 um
Typical Minimum Positive Feature Size	0.75 mm
Typical Minimum Negative Feature Size	0.5 mm
Material	Copper Alloy CuNi2SiCr
SLA Printing Parameters	
Tolerance	± 0.05 mm
Layer Thickness	25 um
Typical Minimum Positive Feature Size	0.254 mm
Typical Minium Negative Feature Size	0.5 mm

stuck to the part. In each case, excess material must be removed both from the exterior and interior of the printed part. Designs for AM in each technology must have release holes placed throughout the part to enable the removal of unsintered or uncured material from the part through compressed air cleaning or other cleaning methods. These release holes, unless treated carefully, have a substantial impact on part performance that must be accounted for. Taking these design limitations into account, basic designs like those seen in Fig. 6.2 are arrived at, showing relevant design features on two variations of the basic monolithic coax, the 'T-junction' design, and the 'Y-junction' design. These designs both consist of a central line supported by two quarter wave shorted stub lines. The design is symmetric about the center, featuring two unit sections of quarter wave shorted stubs with quarter wave transformer sections to either side. The basic circuit configuration is shown in Fig. 6.3. In Fig. 6.2, these become the λ/4 'Input Transformers' and the λ/2 'Center Transformer.' This is done to extend the bandwidth beyond that available without the quarter wave transformer sections [17], [52]. In [141], the bandwidth of this system is shown to be extended by either continued addition of unit sections, or by the addition in each unit section of

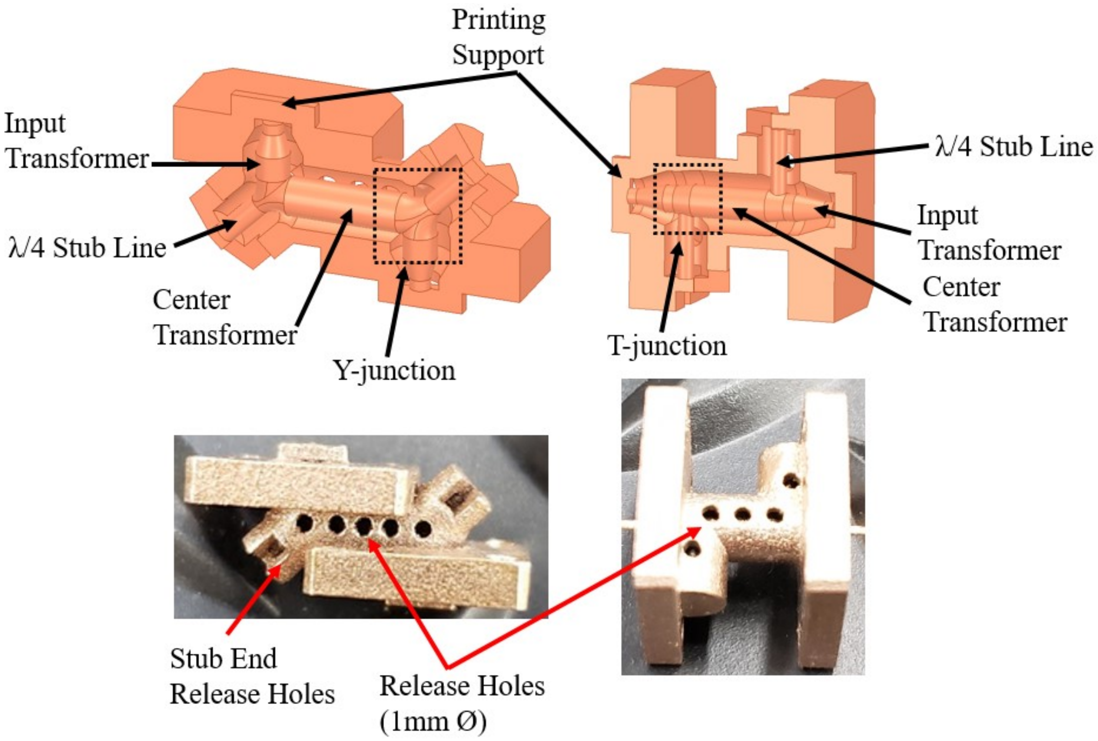

Fig. 6.2. Diagram showing important features of printed coaxial line designs, two critical design alternatives are shown, 'Y-junction' (left) and 'T-junction' (right).

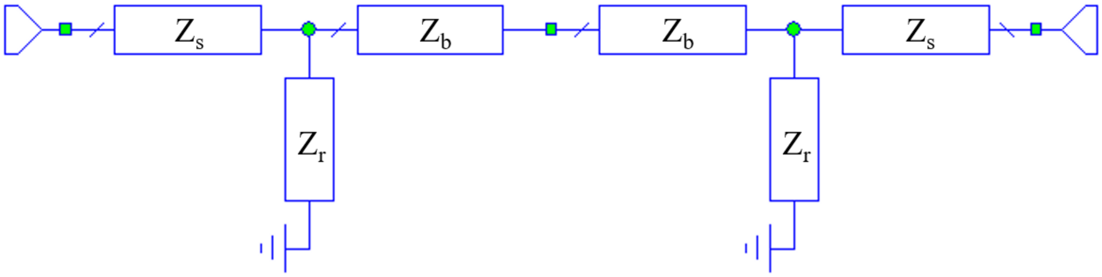

Fig. 6.3. Basic circuit model for the two stub coaxial line [141], each line section is a λ/4 transformer section. The model is symmetric, with 'Input Transformer' Z_S, 'Center Transformer' Z_B and Stub line Z_R.

additional quarter wave transformer sections. Further, the available fractional bandwidth is shown to be increasing for higher impedances of Z_R. For the purposes of this work, the original desired band of interest was to achieve greater than 20-40 GHz bandwidth (66% BW), with a goal of 10-40 GHz (120% BW), while maintaining the small form factor provided by the two-stub line, minimal IL, and RL >20dB. The work in [141] suggests that with $Z_R = 2Z_0$, a fractional bandwidth in the vicinity of 130% can be theoretically achieved. However, for the purposes of this work, this will be shown to be infeasible at this time over the frequencies of interest.

To obtain both low loss, and wideband operation, it is essential to first examine the available line geometries, as limited by high frequency second mode turn-on, and our minimum feature sizes from Table 6.1. Fig. 6.4(a) shows the second mode turn-on frequencies plotted against characteristic impedance, for varying coaxial outer diameter (OD). Colored areas of plotted lines show realizable geometries, and black dashed areas of plotted lines denote either that the inner conductor is smaller than the minimum positive feature size, or that the gap between the inner and outer conductors – hereafter 'air gap' – is smaller than the minimum negative feature size. Fig. 6.4(b) shows the expexted losses in dB/cm over the space of characteristic impedance and outer diameter. The triangular region represents all areas which satisfy a 45 GHz second mode turn-on, and are physically realizable, with unshaded regions to the upper left caused by the inner conductor size limits, unshaded regions to the lower left caused by the air gap size limits, and unshaded regions to the right caused by the minimum allowed second mode turn-on. From this information, it can be seen that expected ideal loss for a line which will operate with low loss in the upper Ka band ranges from 0.012 dB/cm to 0.022 dB/cm, with lowest loss arranged along the right hand side of the triangular region, as expected due to that edge having the widest coaxial lines.

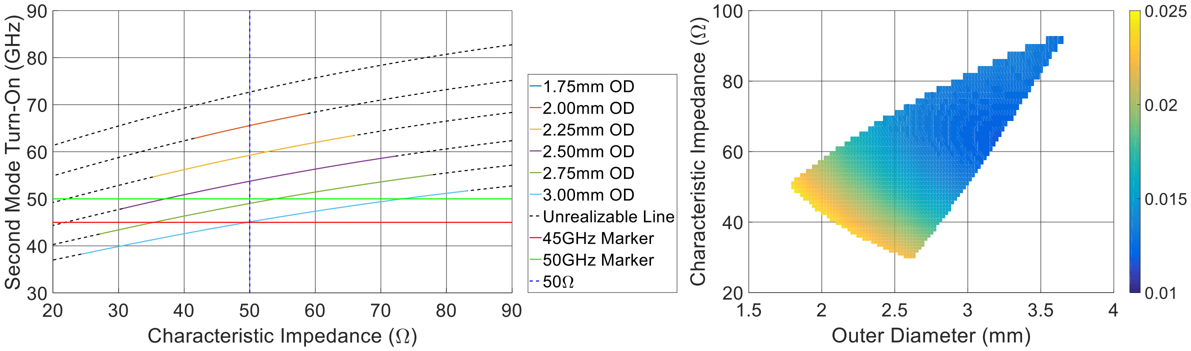

(a) (b)

Fig. 6.4. Basic design information for circular coax. (a) plots of second mode turn-on vs usable characteristic impedance for varying outer diameter lines. Dashed black lines denote unrealizable geometries. (b) expected loss in dB/cm for varying characteristic impedance and outer diameter. Blank areas denote unrealizable geometries or below 45GHz second mode cutoff

Additionally, this gives absolute bounds of what impedances can be utilized in the construction of coaxial filters operating up to near 40 GHz as approximately 32-86Ω.

According to the theory put forward in [141], this suggests that the maximum available operating bandwidth, using 86Ω for the stub impedance, for this topology would be 124.9% BW, with Z_S = 38.8Ω and Z_B = 36Ω. However, the wide OD required for an 86Ω line, due to the minimum inner conductor width, results in substantially poorer circuit performance, characterized by increased reactive loading in the junction areas. As can be seen in Fig. 6.5 (a), even for minimum diameter, higher loss stub lines, the higher impedance stub lines (which must be wider to account for minimum line width) result in increasing disagreement with circuit simulation. While good match below -20dB can still be obtained for models with up to 60Ω impedance by altering transformer impedances and line lengths, the superior agreement with circuit models demonstrated by the 50Ω stub line is selected as the model to be manufactured. As a result, maximum achievable bandwidth is narrowed to 11-40.1 GHz (113.9% BW). Also worth noting is that all full-wave simulations for these devices are carried out with modelled 2.4mm connectors. As a result of needing to mate to 2.4mm connectors, the input and output of the devices are tapered to a narrower OD of 1.77 mm, with an air gap of only 0.4mm.

Release holes for the wideband coaxial anchor are designed primarily with DMLS fabrication in mind. Studies performed on an early coax model of the appropriate sizing of release

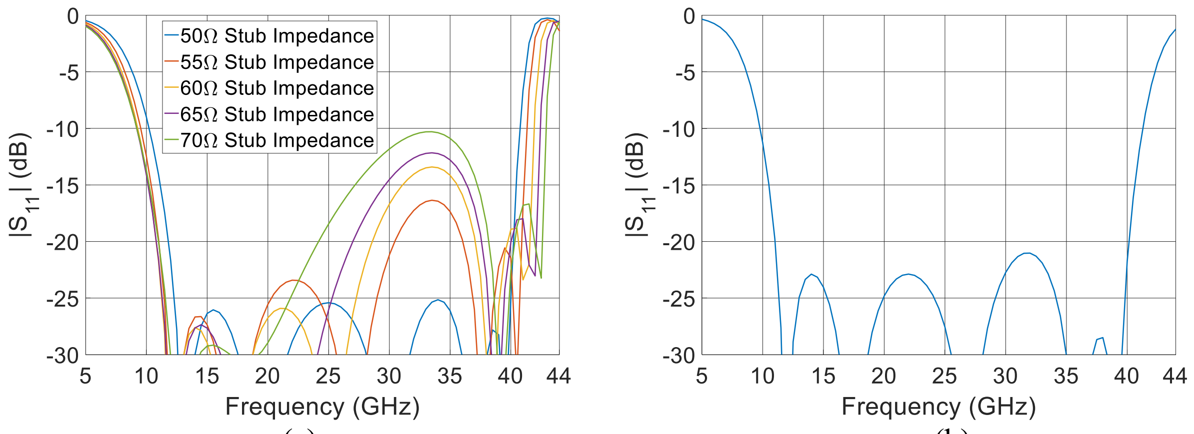

(a) (b)

Fig. 6.5. Results of wider OD, higher impedance coax structures on coax match (a), and (b) circuit model performance of 50Ω stub optimized circuit.

holes for high frequency operation indicate that release holes should be narrower than 1.25mm diameter to avoid substantial impact on $|S_{11}|$ (maintaining $|S_{11}|$ matched below -20dB), and maintain low radiation below -30dB relative to incident power. These results can be seen plotted in Fig. 6.6.

Performance of three designs can be seen in Fig. 6.7, consisting of one T-junction device with 0.5mm air gap, one Y-junction device with 0.5mm air gap, and one Y-junction device with 0.65mm air gap. As can be seen, the T-junction device shows expected bandwidth with RL > 20 dB of 11.5-40.1 GHz. The 0.5mm air gap Y-junction device has expected bandwidth of 11.5-39.7 GHz with RL > 18dB, and the 0.65mm air gap Y-junction device has expected bandwidth of 10.2-35.4 GHz with RL > 17.3dB.

6.2.2 Manufacture and Measurements of Ka-Band Coaxial Lines

As the reliability of the minimum air-gap manufacturable in DMLS and SLA fabrication for this device is not known, numerous devices are manufactured to evaluate performance. Designs shown in Fig. 6.2 are built assuming DMLS and SLA fabrication can reliably manufacture a 0.5mm air gap on the interior of the coaxial part. Wide bandwidths of 11-40 GHz for models shown in Fig. 6.2 rely on narrow line diameters to achieve sufficient performance. Wider air-gap models have greater reactive loading present at junctions which reduce available bandwidth.

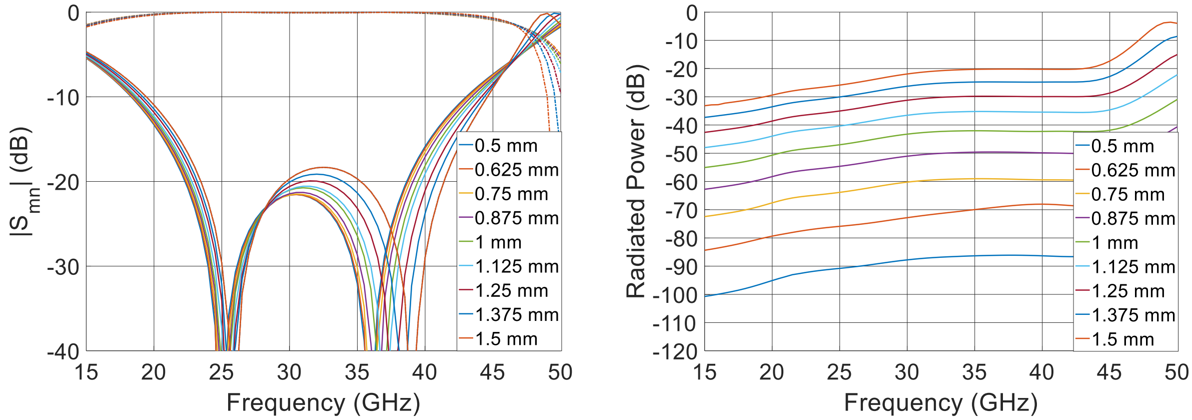

(a) (b)

Fig. 6.6. Impact of release holes in early coax model showing (a) S parameter behavior, and (b) radiated power relative to incident power.

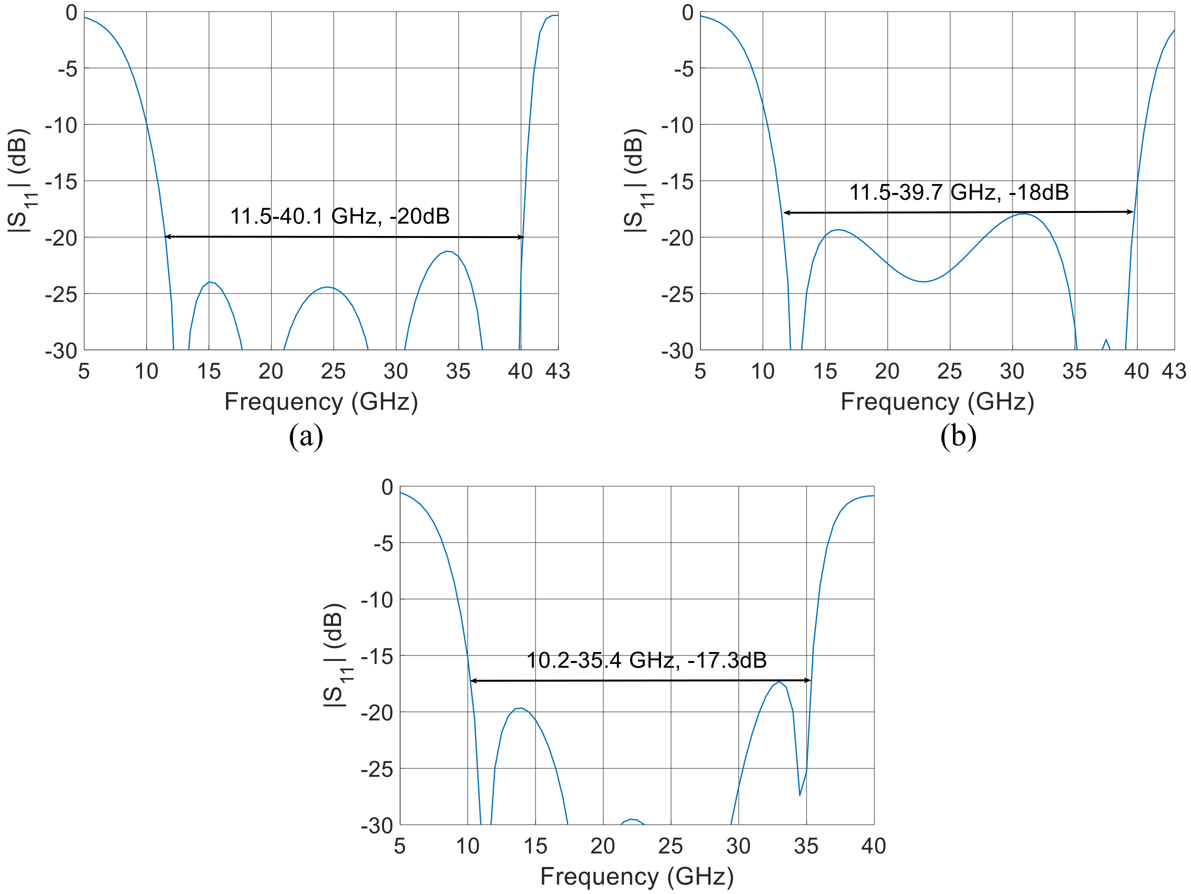

(a)

(b)

(c)

Fig. 6.7. Simulated performance of (a) 0.5mm air gap T-junction device, (b) 0.5mm air gap Y-junction device, and (c), 0.65mm air gap Y-junction device.

For SLA fabrication, only 0.5mm air gap models are fabricated. 0.5mm air-gap models are fabricated on a Formlabs 3 printer in Formlabs Tough v5 resin. Destructive testing of printed pieces prior to copper plating demonstrates successful SLA printing, however post plating destructive testing demonstrates shorting near the narrow port areas, and large unplated areas on the interior of the structure. The required fluid flow for SLA fabrication is not provided by the narrow port diameters and release holes.

For DMLS fabrication, multiple devices are built as 0.5mm air gap T and Y-junction strucutres, The results indicate that 0.5mm air gap is not reliably achievable at this time for the T-junction device, and shows varying degrees shorting or blockage in all cases. Multiple 0.5mm air gap Y-junction pieces manufactured show superior performance and are matched to better than

10dB RL, however show substantial disagreement with simulation consistent with changes to stub length. One Y-junction 0.65mm air gap device is manufactured in DMLS, and shows reasonable agreement with expectation. Shown in Fig. 6.8 is the measured performance of the best performing 0.65mm air-gap Y-junction model, manufactured in DMLS copper alloy. Wideband operation is obtained over 10-30 GHz with RL > 15dB. While this performance is not as close to original simulations as desired, it does show good agreement with closely modelled results. In-band IL remains less than 0.7dB, with a mean value of 0.31dB. Poorer agreement with simulation is due to the DMLS caused imperfections, which have a substantial impact on the realized dimensions. Tolerance analysis with up to 100µm diameter and 250µm length variations show good agreement with measured performance, specifically showing error sources being a mismatch in the lengths of the shorted stubs, and a lengthening of the 'Input transformer' sections. This is not entirely suprising, as the stub lines are likely printed in a vertical orientation, and the uppermost printed stub appears longer than expected by ~150µm, as typical of 3D printing processes, the first few thin layers of a vertical overhang may not fully solidify. Additionally, the input transformers and flanges have additional length added onto the model for printing, to allow a greater amount of

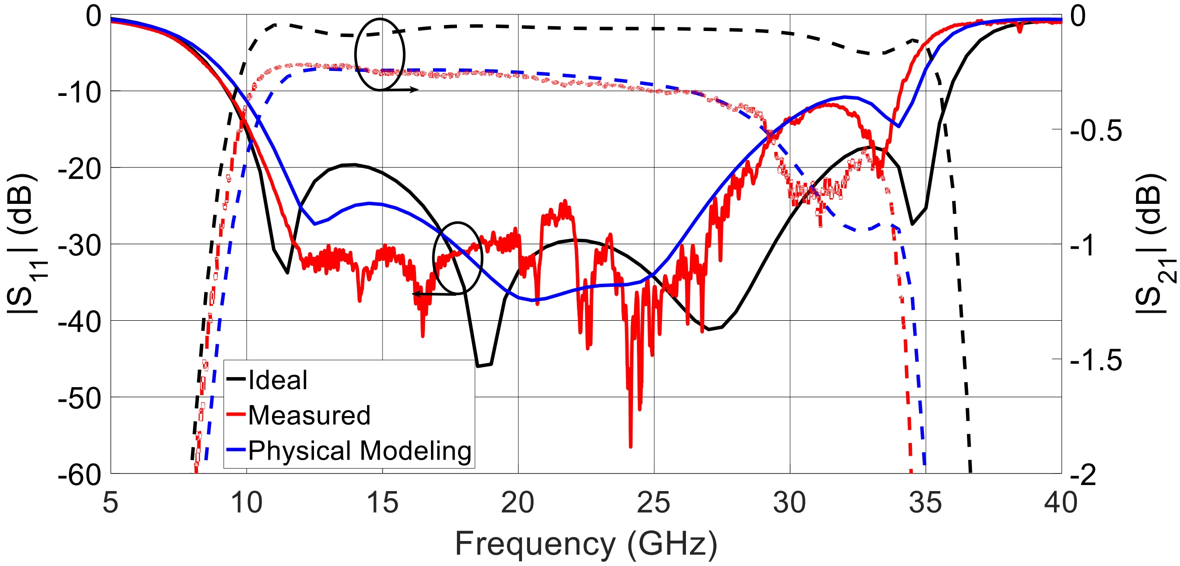

Fig. 6.8. Ideal simulation (black), measurement (red), and simulation with closely modeled dimensional changes and reduced conductivity (blue), showing good agreement between closely modelled performance and measurement.

material to be milled away to ensure connector flatness. This likely results in additional length of ~250µm. Changes to impedance are located primarily asymmetrically in the outermost transformer segments, on the order of ~1Ω, and in the stubs, with variation of ~3.5-4.5Ω. Based on measured maximum surface deviation of 52um, these changes are well within the expected range of printed dimensions. In addition, DMLS roughness contributes to higher losses. In this case, modelling with an equivalent conductivity of $\sigma \approx 5 \cdot 10^5\ S/m$ demonstrates good agreement with measured insertion loss. This conductivity is a substantial reduction in conductivity from the copper alloy nominal of $\sigma = 23 \cdot 10^6\ S/m$, This behavior is not captured effectively by existing surface roughness purpurbation models from Groiss [142], Hammerstad [143], or the equation put forward in [144].

The results of the manufactured Y-junction model with 0.65mm air gap indicate that reliable manufacturing can be obtained for systems achieving up to 3:1 bandwidth, however that 3.5:1 and 4:1 bandwidths may be slightly beyond the current capabilities of DMLS fabrication due to current DMLS tolerances, and the tight manufacturing tolerances required to achieve higher bandwidths. Designs with less stringent goals than 3.5:1 and 4:1 operation can be made to have greater leeway in tolerancing.

6.3 Performance Comparison of DMLS and SLA Resonators

6.3.1 Design of a High Q Coaxially-Fed 3D Printed Resonator

Of primary importance to the design of resonators are the limitations placed on its construction by the fabrication process. The initial design for this device is focused on the rapid prototyping capabilities of current DMLS and SLA processes, keeping in mind the dimensional limits of both methods. The printing material for DMLS remains the same as the previous section, CuNi2SiCr copper alloy ($\sigma = 2.3 \cdot 10^7$ S/m), in a 30µm layer thickness, with 0.75mm typical minimum positive feature size. With a desired resonance of 30GHz, an ideal square cavity with x and z dimensions of 7.07mm ensures single mode resonance when air-loaded [145]. To keep a relatively low height, while still ensuring enough room for inclusion of a DMLS coaxial feed, the height (y-) is set at 2mm. The selected values ensure a TE101 cavity mode with a Q_0 of 3395, or an expectation of 1691 when 10μm Groisse roughness model is used in standard copper. As noted in the previous section, the roughness models do not adequately capture system performance, as will be explored further here.

A small half-loop feed is often used to excite the cavity resonators [132], and is therefore considered here. A cylindrical coaxial feed with the inner conductor of the coaxial feed protruding into the cavity and shorting to ground as a loop is considered first. With the minimum diameter of the printable inner conductor diameter of 0.75mm this feature is a significant disruption to the overall cavity mode structure. To reduce the cavity loading from the inserted loop, it is rebuilt as a rectangular coaxial line with a right-angle bend shorting to the ground. A good balance between coupling and low cavity loading are found by positioning the end of the feed flush with the wall of the cavity.

Fig. 6.9 and Table 6.2 show critical resonator dimensions. Additionally, the corner elliptical release holes have 1mm minor axis diameter, 2mm major axis diameter (flush with cavity floor and ceiling). The cavity dimensions were altered from their original 7.07mm square to bring the actual resonant behavior of the cavity with the feed loading back to 30GHz. As a result of the feed placement, the loaded TE101 mode has some small field differences to the mode in the absence of the feed, though is largely similar. Primary differences from the unloaded TE101 mode are apparent in the E- and H-fields when not at their respective energy storage maximum, with an electric potential being generated between the center conductor and the cavity ceiling, when off of E-field maximum, and additional opposite circulating H-fields being generated about the shorted center conductors. Fig. 6.10 shows the cavity mode at 0° and 90° phase, for the E-field and H-field.

Release holes are chosen as an even symmetrical grid of 1mm diameter release holes in the ceiling and floor of the cavity. The even placement maintains solid conductive paths along the principle cavity planes, where current flow is concentrated, and maintains a solid conductor

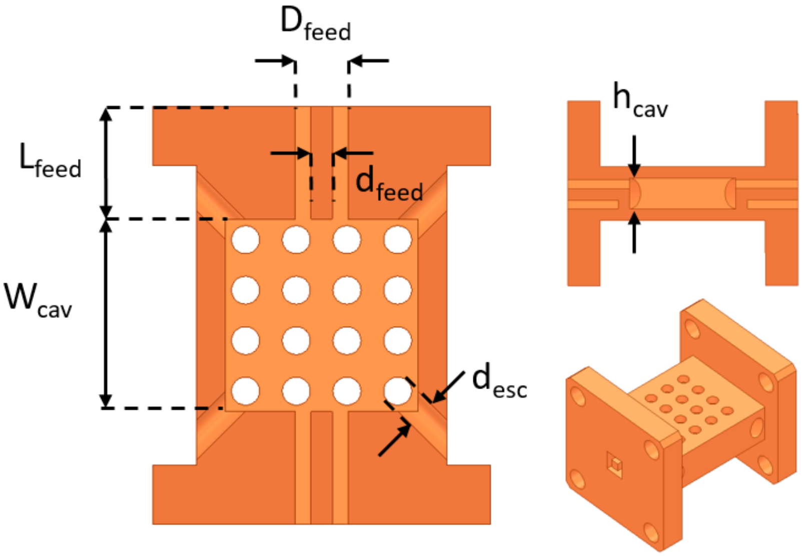

Fig. 6.9. Resonator model detail views, showing critical dimensions.

TABLE 6.2. CRICAL RESONATOR DIMENSIONS

$\mathbf{W_{cav}}$	$\mathbf{h_{cav}}$	$\mathbf{D_{feed}}$	$\mathbf{d_{feed}}$	$\mathbf{L_{feed}}$	$\mathbf{d_{esc}}$
6.87mm	2mm	1.87mm	0.75mm	4mm	1mm

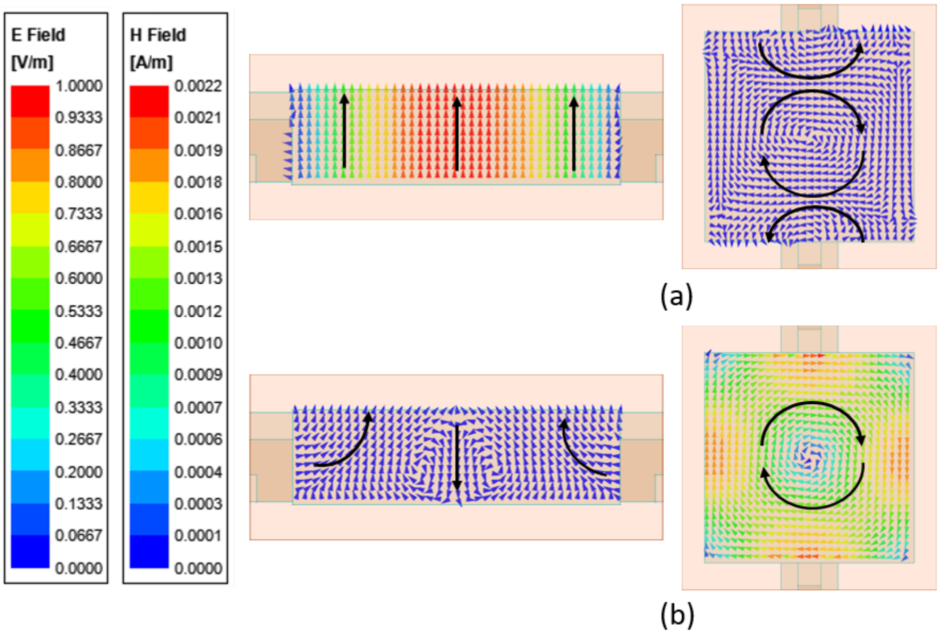

Fig. 6.10. Cavity mode detail. (a) 0° phase (b) 90° phase. Fields normalized to E-field maximum of 1V/m. Side view plots (left) show E-field, topview plots (right) show H-field

centred at the highest charge density. Larger than 1mm diameter holes permit too much radiation at 30GHz. A 4×4 hole grid (as opposed to 2×2) is chosen to maximize the number of release holes while keeping the radiation loss to be small (<-35dB relative to input power). Additional elliptical release holes are added to prevent any material build up in the cavity corners, cutting the corners away entirely. The release holes (without changing cavity dimensions) effect a slight drop in center frequency. Without the release holes, the compensated cavity size of 6.87mm resonates at 30.25GHz, whereas it resonates at 30GHz with the release holes included. Resulting Q_0 is 1353, assuming the material in use is smooth copper alloy. The total radiated power at resonance is simulated as -37.5 dB relative to the input power at one port indicating a very low level of radiation.

Note that the considered processes allow for resonator miniaturization using principles of evanescent mode filters and therefore capacitive loads. The impact of a loading stub is investigated using an eigenmode analysis with 5µm Groisse approximated surface roughness of pure copper walls. Placing a printable capacitive post in the cavity interior of up to 3.5mm diameter, with a capacitive gap as narrow as 0.25mm allows for a miniaturization factor of up to 55% as measured by the change in turn-on frequency. This corresponds to an accompanying drop in Q_0 from 1689 to 990. The results of this analysis are seen in Fig. 6.11.

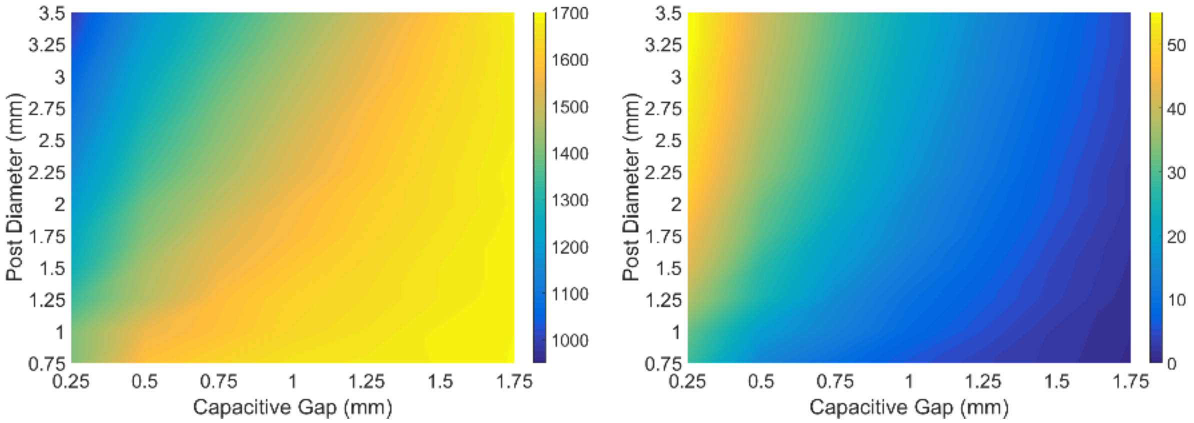

Fig. 6.11. (a) Q_0 in eigenmode analysis with corresponding capacitive post size. (b) Size reduction (%) with corresponding capacitive post size.

6.3.2 DMLS and SLA Fabrication of a Rectangular Resonator

The DMLS resonator is manufactured with a commercial company, whereas the SLA resonator is fabricated in-house with the FormLabs 3 printer. Each SLA model built was given four cycles of ultrasonic washing in alcohol, with uncured material blown off with compressed air between washings, followed by 1 hour of UV curing at 60ºC. The SLA models were then electroplated in copper by the outside commercial company. Two post processing steps of the DMLS resonators are performed. Specifically, the step 1 is sanding off an additional support added on the flange face to support the center conductor, whereas the step 2 is sanding the flange flat to ensure good mating to the 2.4mm connectors. Similar post processing steps are performed with the SLA fabricated device prior to copper plating.

To compensate for the chemical etching and copper plating process expected to result in additional material build-up while keeping in mind fabrication tolerances, a 100µm of material thickness is removed from the internal resonator surfaces. No compensation is performed for the DMLS manufacturing. Manufactured resonators are shown in Fig. 6.1(b) and (c).

The inspection of the fabricated DMLS resonator shows significant issues which can be primarily traced to surface quality of the DMLS print. The center frequency is shifted from 30GHz to 29.73GHz and is accompanied by a drop in Q_0 to 317 from an expected 1259. The insertion loss, |S21|, at resonance also reduced to -2dB from an expected -0.5dB obtained with the theoretical model with 10µm Groisse roughness approximation and copper alloy. These behaviours can be seen in Fig. 6.12(a).

To further examine the manufactured DMLS device, visual inspection of the interior with borescope and roughness measurement of the interior are carried out. The profilometry of the interior shows significant differences between inner and outer surface quality. Specifically, the outside surfaces have RMS roughness of 2.6-2.9µm, with maximum surface deviation of 10.9-13.2µm. However, the interior surfaces are printed with RMS roughness of 12.5-14.2 µm and maximum surface deviation of 47.1-53.2µm. Measurements of the RMS roughness on the exterior

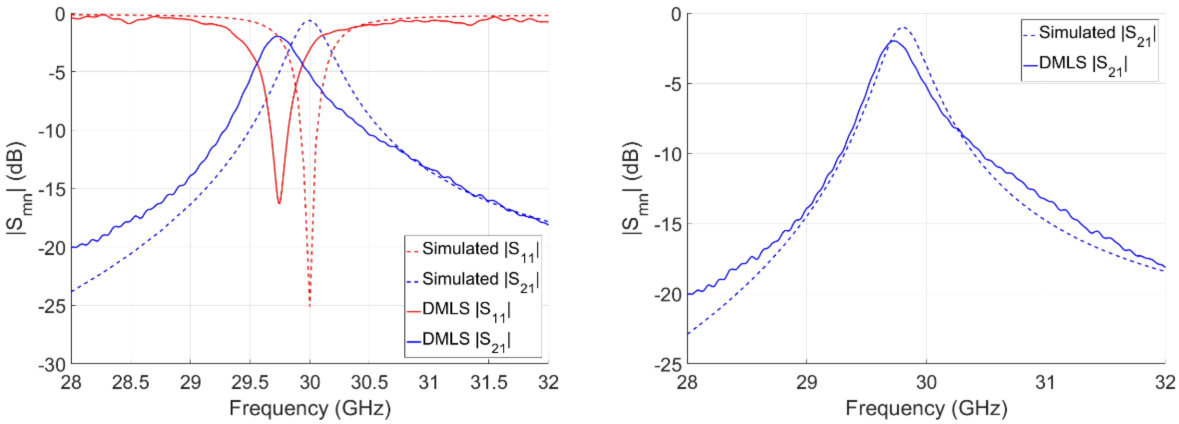

(a) (b)

Fig. 6.12. (a) Comparison between simulated and measured S-parameters of DMLS built resonator. (b) Measured and simulated insertion loss of the resonator with the adjusted model parameters to indicate device as fabricated.

were taken along orthogonal edges of the flange, and interior measurements were taken in two directions, perpendicular about the center of the resonator ceiling. The cutaway view of the resonator interior can be seen in Fig. 6.13, with the two measurement directions along the resonator ceiling highlighted with red and blue boxes.

Simulations of 12-14µm Groisse roughness approximations fail to fully capture the significant impact of these deviations. Close modelling of the measured DMLS interior of W_{cav} = 6.91mm, and h_{cav} = 1.98mm with the expected surface roughness provide a match to only within

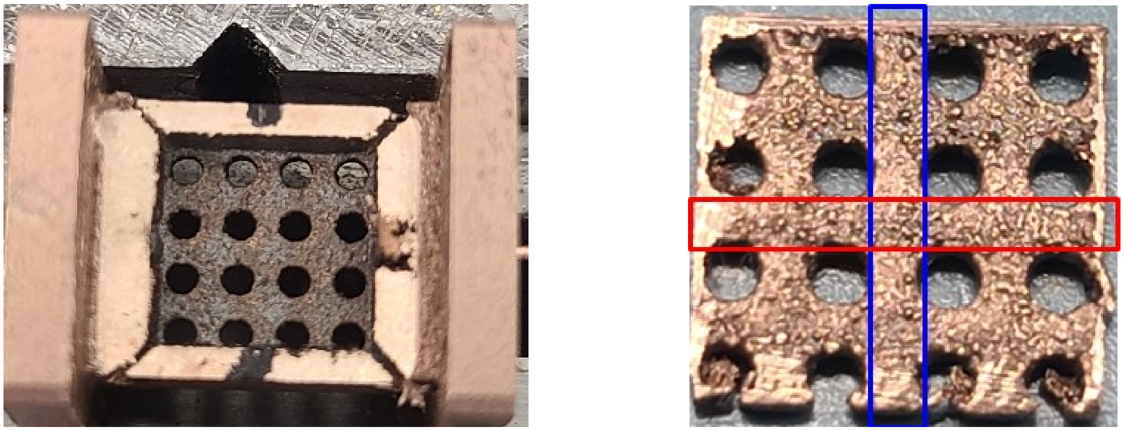

(a) (b)

Fig. 6.13. View of (a) resonator interior after removing its ceiling, and (b) ceiling surface with indicated two roughness measurement regions.

-15dB error, as seen in Fig. 6.12(b). From this we can see that the large impact of the DMLS roughness cannot be fully captured by standard roughness modelling effecting a change in conductivity. But rather that the surface deviation is severe enough to significantly change the geometry of the solution, making accurate modelling extremely challenging. For rapid, low-run prototyping desiring high accuracy, this is undesirable, however further iteration and use of DMLS printers on a design may yield better surface accuracy.

Three SLA fabricated and copper plated resonators all have relatively similar performance as shown in Fig. 6.14(a). The applied model compensation for copper plating (by removing 100µm of material) was too stringent, as center frequencies of the three pieces are at 29.72, 29.55, and 29.83 GHz. Corresponding Q_0 values are measured as 2370, 1672, and 3407, respectively.

Interior measurements are also performed on "SLA 2" of the three fabricated SLA models and 3.75µm RMS roughness is measured. Destructive testing and internal surface of coated SLA piece can be seen in Fig. 6.15. Utilizing the Groisse roughness approximation with the measured roughness, and simulating measurements of hcav = 2.29mm and Wcav = 7mm, provides excellent agreement with simulation to better than -22dB error, as can be seen in Fig. 6.14(b). From this, we can see that the etching process removed more material from the cavity interior than was electroplated onto the surfaces, however, the overall surface quality is very good, allowing for good approximation with standard roughness modelling tools, and production of high Q_0

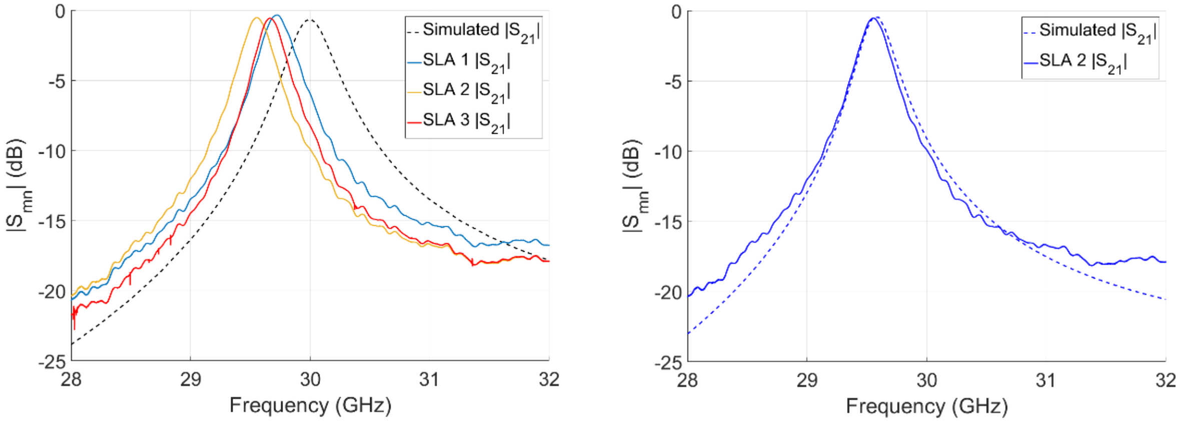

(a) (b)

Fig. 6.14. (a) Measured SLA resonators vs simulation with 10um RMS roughness. (b) Comparison between simulation and measurement of "SLA 2."

Fig. 6.15. Interior view of SLA coated piece after destructive test.

resonators. These results with SLA resonators confirm feasibility of building well performing resonators (and by extension corresponding filters) at Ka-band and higher frequencies comparable to the state-of-art process, such as PolyStrata [132]. All these at a much lower cost and development time, particularly important for rapid prototyping.

6.4 Design of Coaxial Filters for Monolithic Additive Manufacturing

6.4.1 Design of Coaxial Stub-Supported Filters

As mentioned in section 6.1, it is desired to expand the family of 3D printed components to include two filter designs. One from 4-7.8 GHz, and one from 7.8-15 GHz. The design of coaxial filters in this technology can be undertaken in many ways. However, the simplest method is to utilize the same techniques developed to create a standard coaxial line. The use of this technique to create ultra wideband filters in microstrip was explored in [141], which looks at both broadening the bandwidth of a single stub by surrounding it with successive quarter wave transformer sections, and cascading stub and transformer sections to act as a broadband filter. Similar to [49], this design utilizes cascaded sections consisting of a quarter wave shorted stub with quarter wave transformer elements placed in series to either side. A basic symmetric 2-segment model of this circuit can be seen in Fig. 6.3, showing three relevant impedances, again to be referred to as Z_S, Z_R, and Z_B [141]. A variety of more standard filter designs following a Chebyshev filter prototype and realized either with more typical quarter wave shunt stubs separated by single quarter wave sections, or as capacitively coupled shunt stub resonators are considered, and rejected for use here [145]. The wide line diameter in use results in a relatively low second-mode turn on, and strong parasitic loading at T and cross junctions. This produces spurious transmission through the filter halfway through the first upper side stop band, when the line lengths are close to half a wavelength. The design in use here alleviates this issue and has the added benefit of greater flexibility of miniaturization line-packing, due to the absence of an additional stub. The capacitively coupled shunt sections are rejected for use due to both manufacturing sensitivity, and difficulty in line packing, as the stubs would be extremely close together. As mentioned, these designs use a relatively wide line diameter. The coax outer diameter is set to 3.5mm. 3.5mm is a good balance between ensuring the second coaxial mode turn on remains past 30GHz, even for low-impedance lines, and being large enough to sustain a wide range of printable impedances, namely ~20Ω - 105Ω, as dictated by the narrowest reliable air gap of 500um, and the narrowest reliably manufacturable line width of approximately 600um. In [141], the intent is to create a wideband structure. To that end the characteristic impedance of the stubs is investigated up to 100Ω, with wider bandwidths achievable through higher impedance stub elements. For the purposes of this section, a high degree of attenuation is desired out of band. To achieve this, the opposite behavior is found to be beneficial, with Z_R reduced as low as 10Ω if possible. The small air gap required to realize this informs the choice to modify the basic design, similar to those presented for the coaxial line of section 6.2, to utilize two parallel 20Ω stubs to realize a lower impedance, and similarly utilizing parallel stubs for the 3-stub low band filter, Fig. 6.1 (e), and subsequent diplexer design. Table 6.3 shows the filter impedances as designed, for the filters in Fig. 6.1 (d) and (e). Note that the Z_R values listed in Table 6.3 are for the parallel stubs, and thus are represented in the original non-parallel circuit with half their listed impedance. Also note that the high-band filter in Fig. 6.1(d) consists of two identical filter sections, as shown in Fig. 6.3, and the single segment impedances are shown in Table 6.3 labeled as Z_{S1}, Z_{R1} ,and Z_{B1}. The low-band filter of Fig. 6.1(e) consists of three three filter sections. The outer two sections are the the same impedances, and are

TABLE 6.3. FILTER IMPEDANCES

	Z_{S1}	Z_{R1}	Z_{B1}	Z_{S2}	Z_{R2}
High Band	39.75	20	56.6	-	-
Low-Band	37.25	21	55	84.25	43

labeled as Z_{S1}, Z_{R1}, and Z_{B1}; The third, center section consists of the same transformer impedance to either side, labeled as Z_{S2}, and the stub impedance Z_{R2}.

With initial circuit configuration in mind, the next most critical element is the design of the coaxial cross junctions. Due to the high parasitic loading in the junction areas, a plainly constructed cross junction injects a difficult to compensate reactive loading into the circuit. This results in spurious transmission halfway through the upper stop-band of a filter. Resolving this spurious transmission necessitates either reducing coax outer diameter, bringing the overall structure closer to ideal operation, or altering the junction geometry to resolve parasitic reactance. Taking inspiration from the mitering of microstrip T and cross junctions [146] this work proposes the mitering of a coaxial line cross junction. The basic geometry of the 'compensated' coaxial cross junction can be seen in Fig. 6.16. The topology consists of tapering at a 45° angle from each nominal inner diameter entering the junction down to a common 'Junction Diameter.' The point at which each line begins tapering is at a set distance from the center of the junction, the 'Junction

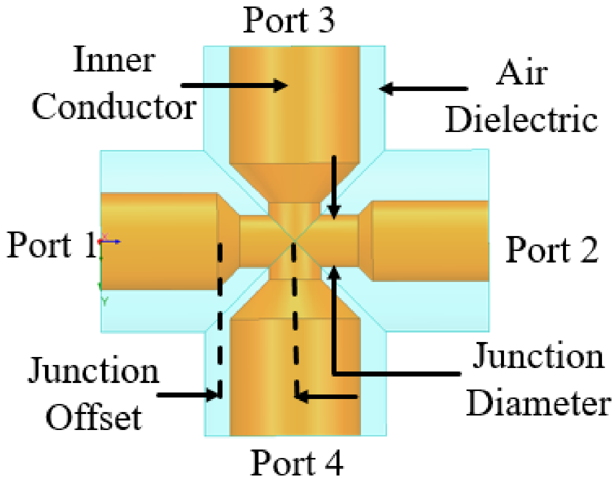

Fig. 6.16. Diagram of mitered coaxial cross-junction. The upper and lower lines (Port 3 and Port 4) are the same impedance, with left and right lines as unique impedances. All lines taper to a constant 'Junction Diameter', starting from a set distance from the junction center, the 'Junction Offset.' Ports are labeled to clarify S-parameters from Fig. 6.17.

Offset'. Through parametric minimization, best agreement is found (though dependent on the specific impedances of the junction) for a low junction offset, near 1.1-1.3mm, and a junction diameter near 1.3-1.5mm. With the junctions tuned individually, their scattering parameters can be compared against idealized circuit junctions of the same impedances. The error between any compared S-parameters in this manner is typically below -30dB. One example can be seen in Fig. 6.17(a), which shows the full-wave simulated and ideal transmission line cross junction S-parameters, which are difficult to visually distinguish due to very close overlap. Fig. 6.17(b) shows the error between the two sets of S-parameters, being less than -35dB out to 16 GHz. This result clearly shows a good agreement between initial circuit designs and the physical realization. Fig. 6.18 shows the parametric plots for the 6 different cross junctions in the diplexer design, showing maximum error between ideal circuit junctions and full-wave simulated junctions, amongst S_{11}, S_{21}, S_{31}, and S_{32} at 16 GHz plotted against junction diameter and junction offset.

6.4.2 Manufacturing and Measurement of Additively Manufactured Filters

The two manufacturing methods for these filters impose a separate set of requirements and limitations on their use. For the DMLS manufacture, as used in the high-band filter shown in Fig.

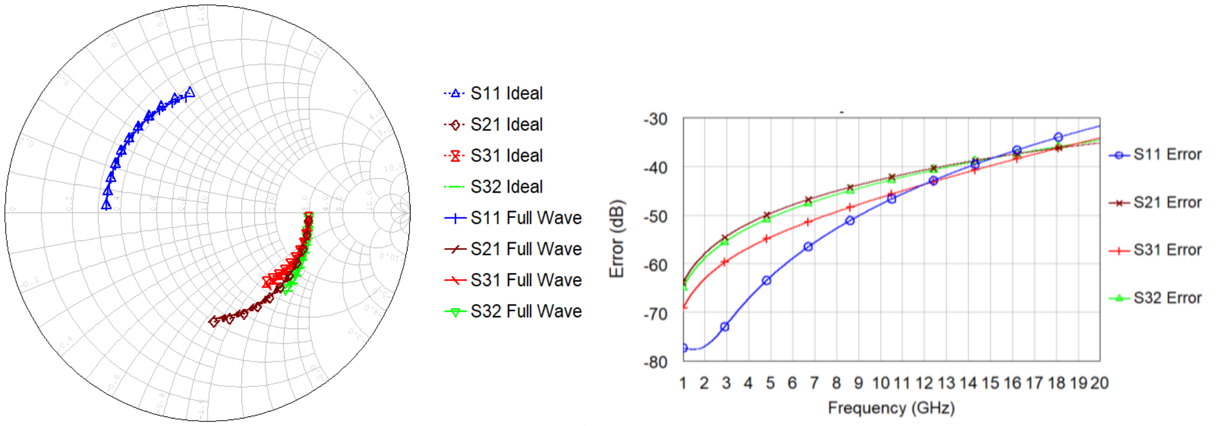

(a) (b)

Fig. 6.17. (a) S parameters and (b) error between ideal junction and full-wave simulated junction for diplexer low-band Stub 2. $Z_S = 55\Omega$, $Z_R = 30\Omega$, $Z_B = 34\Omega$. Junction offset 1.1mm, junction diameter 1mm. Full wave simulated S parameters and ideal junction S parameters are nearly indistinguishable.

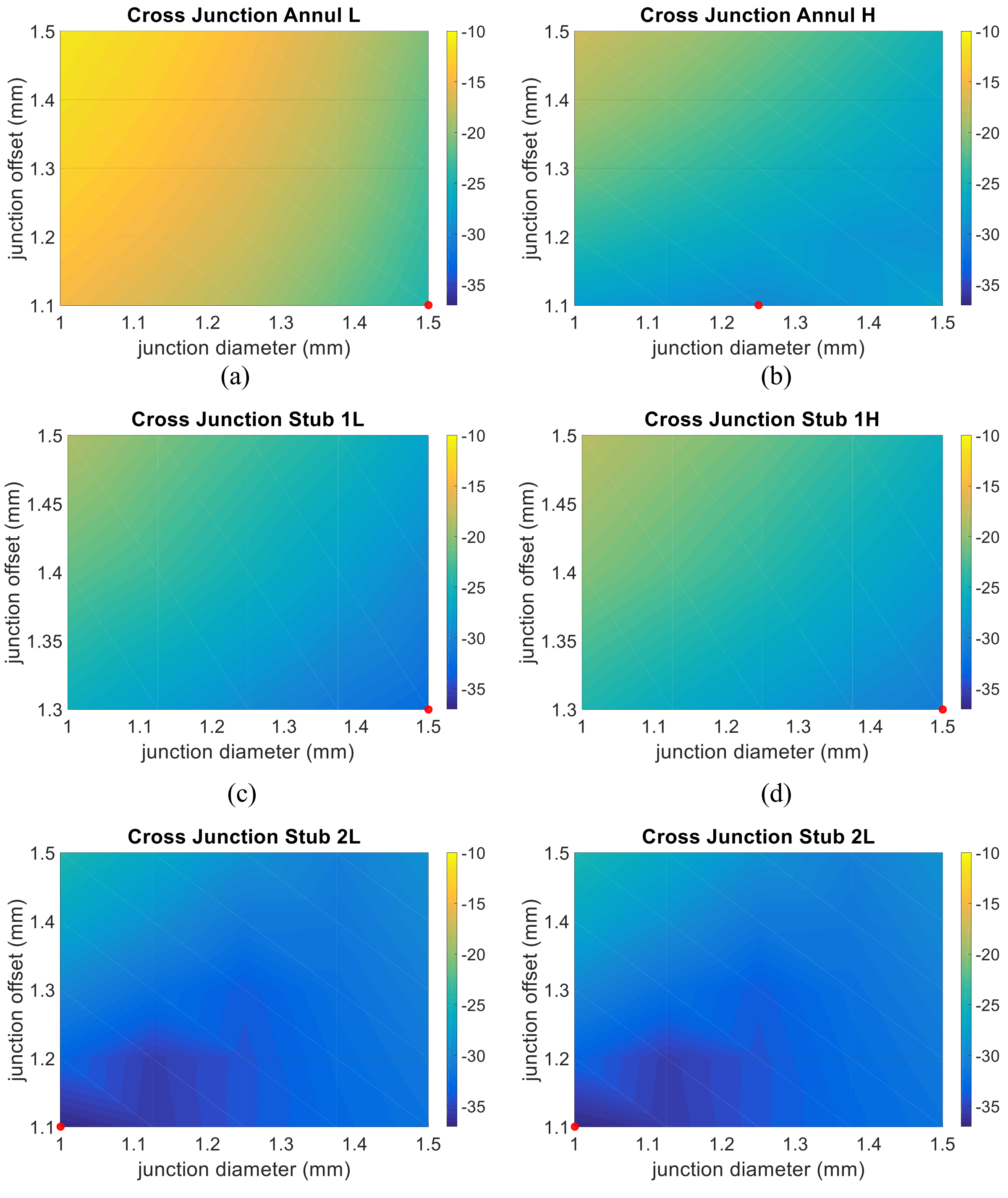

(a) (b)

(c) (d)

(e) (f)

Fig. 6.18. Plots of maximum S parameter error at 16 GHz for diplexer cross junctions. Colormap showd dB difference between ideal junction and full wave geometry S parameters, from -10 to -35 dB. Note that junction offset values for (c) and (d) do not extend down to 1.1mm due to geometry limitations for those junctions.

6.1(d), the surface roughness inherent to the process, and the addition of release holes to allow unsintered material to be removed are critical. Use of 1mm release holes allows for material to be removed, while keeping radiative losses below -45dB. The surface roughness from typical commercial DMLS processes in Inconel is found to be in the range of 15um RMS. Modeling this roughness in the larger structure of the high-band filter – as compared to the narrow dimensions of the coax of section 6.2 – is found to give relatively good agreement between measured and simulated performance for a DMLS manufactured filter consisting of 2 stubs. Due to process limitations with inner conductor aspect ratio, this model is printed with an inner support at the center. This is machined away, and the surrounding area is covered with a separately printed cover piece secured by screws. Comparison of ideal circuit simulation, circuit simulation with junction reactances, full wave simulation, and measurement can be seen in Fig. 6.19. Some disagreement between the original circuit simulations, and either the circuit simulations with junction reactances, or the full wave simulations, can be seen. Unfortuantely, this is primarily due to this design being constructed prior to later refinement of the correct junction offset and junction diameter. Close physical modeling of as-built dimensions brings the measurements, full-wave simulations, and

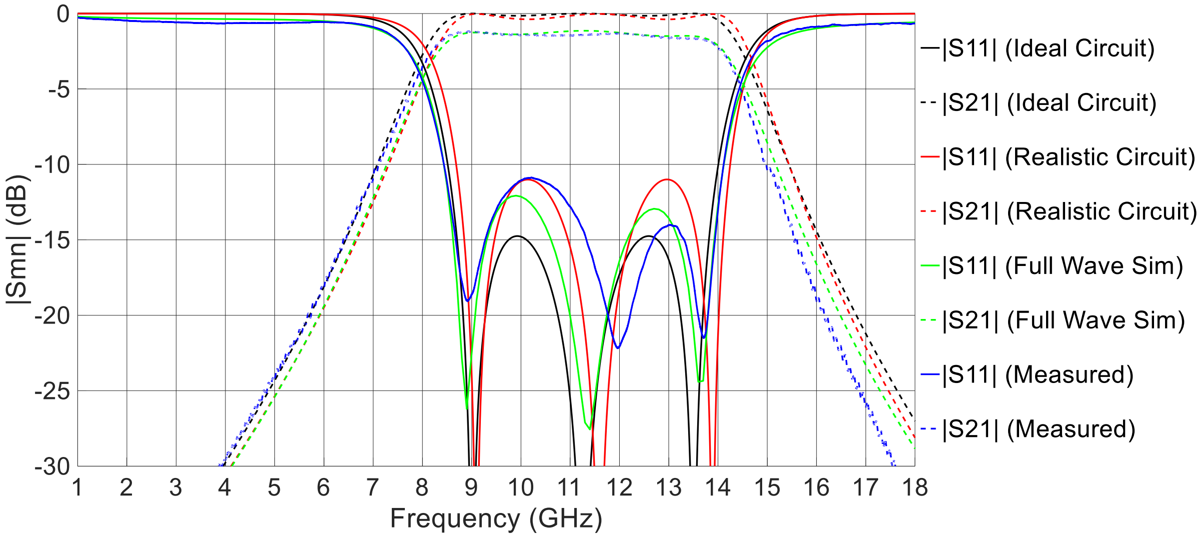

Fig. 6.19. Plot of simulated and measured high-band filter performance. Black lines show ideal circuit performance, red lines show circuit simulations with cross-junction reactances, green lines show full-wave simulated performance accounting for expected roughness and Inconel losses, and blue lines show measured filter performance.

junction reactance circuit simulations into close agreement.

For the SLA process, measured results of the printed device seen in Fig. 6.1(e) are seen in Fig. 6.20. Design iterations on the coated SLA process show that the narrow required dimensions for sharp filter band-edge performance make plating of monolithic devices challenging due to fluid flow and gas exchange in the plating process. This and later devices, like the monolithic diplexers seen in Fig. 6.1(f) and 6.1(g) feature larger release holes than the DMLS process, to better facilitate copper plating. Overall performance is in close agreement.

6.5 Design and Miniaturization of Coaxial Diplexers for Additive Manufacturing

6.5.1 Design of a Coaxial Diplexer

The design of a monolithic diplexer integrates two, 2-stub filter designs similar to that seen in Fig. 6.3, with an impedance annulling network reducing interaction between high and low-band circuits out of band. The basic architecture of the diplexer circuit can be seen in Fig. 6.21. The lines and stubs of the low-band filter are λ/4 at 11.59 GHz, and the lines and stubs of the high-band filter are λ/4 at 5.84 GHz. The annulling network features an asymmetric pair of stubs acting

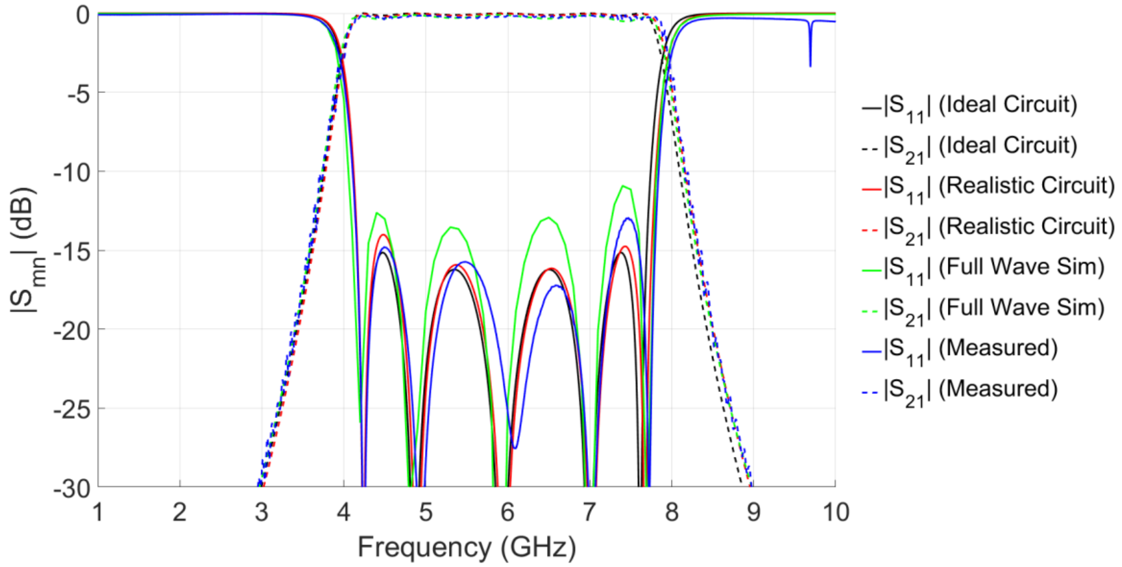

Fig. 6.20. Plot of simulated and measured low-band filter performance. Black lines show ideal circuit performance, red lines show circuit simulations with cross-junction reactances, green lines

show full wave simulated performance with release holes and blue lines show measured filter performance.

as impedance tuners, with the low-band side consisting of a series line, λ/4 at high band, followed by a shorted stub that is λ/4 at low band; The high-band side consists of a series line, λ/4 at low-band, followed by a shorted stub that is λ/4 at high band. The impedances for the system are optimized in Cadence AWR [147], and can be seen in Table 6.4. Impedances listed Table 6.4 for stub impedances follow the same convention of being the impedances used for the stubs as realized, which are with two stubs in parallel. Effective impedance of the stubs for the circuit model in Fig. 6.21 are half that shown in Table 6.4.

Additionally, what cannot be neglected in the final design is the impact of efforts to miniaturize and plate the structure. In particular, the impacts on performance from line packing, as in Fig. 6.1(g) and 6.1(h), and the large release holes used to facilitate copper plating. The 90°

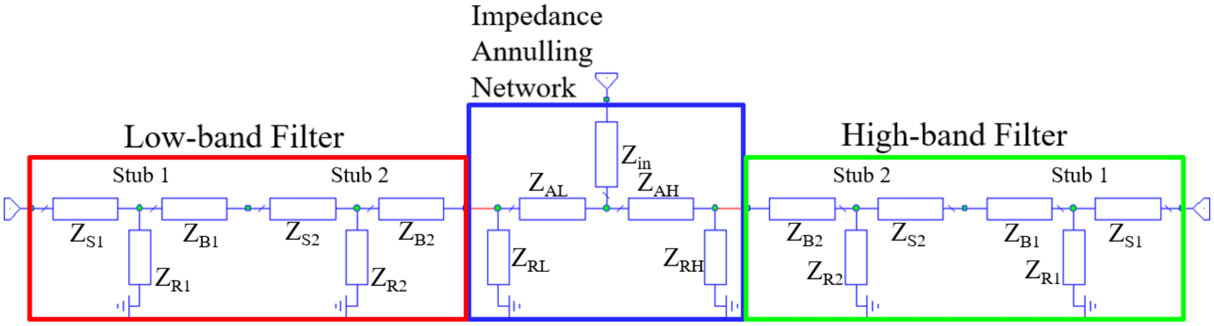

Fig. 6.21. Basic diagram of diplexer architecture, consisting of two 2-stub filters constructed from λ/4 segments at the low-band and high-band center frequencies. The annulling network in the center consists of two asymmetrical lines and stubs, with Z_{AH} and Z_{RL} being λ/4 at low-band, and Z_{AL} and Z_{RH} being λ/4 at high band.

TABLE 6.4. DIPLEXER IMPEDANCE VALUES

	Z_{S1}	Z_{R1}	Z_{B1}	Z_{S2}	Z_{R2}	Z_{B2}
High-Band	33	20	50	64	28	38
Low-Band	33	20	43	55	30	34
	Z_{A}	Z_{R}				
High-band Annulling	73	30				
Low-band Annulling	48	56				

stub bends utilized creating the ‘Packed’ and ’20Ω Packed’ designs have a substantial impact, altering the reactive load by reducing in-line inductance and adding additional capacitance in the bend area. For the low-band stubs, the impact is primarily inductive, and is easily compensated by reducing stub length. However, in the high band, the impact is more capacitive, and cannot be easily compensated for with length adjustment due to the short distances involved. Examination of possible mitering schemes is undertaken but does not provide improved performance in the high-band filter. Fig. 6.22 shows the change in performance from an intermediate design – with input junction altered aligning filter outputs, but without sroved performance in the high-band filter. Fig. 6.22 shows the change in performance from an intermediate design – with input junction altered aligning filter outputs, but without stub bends – to the diplexer design seen in Fig. 6.1(g).

The stub bends have the more significant impact, however the release hole sizing and placement is also important to the overall system performance. Simulations and construction of the high-band filter design of Fig. 6.1(d) show minimal impact due to 1mm release holes utilized for DMLS construction, and these small release holes allow for sufficient movement of unsintered material out of small structures. However for SLA constructed pieces, the facilitation of copper

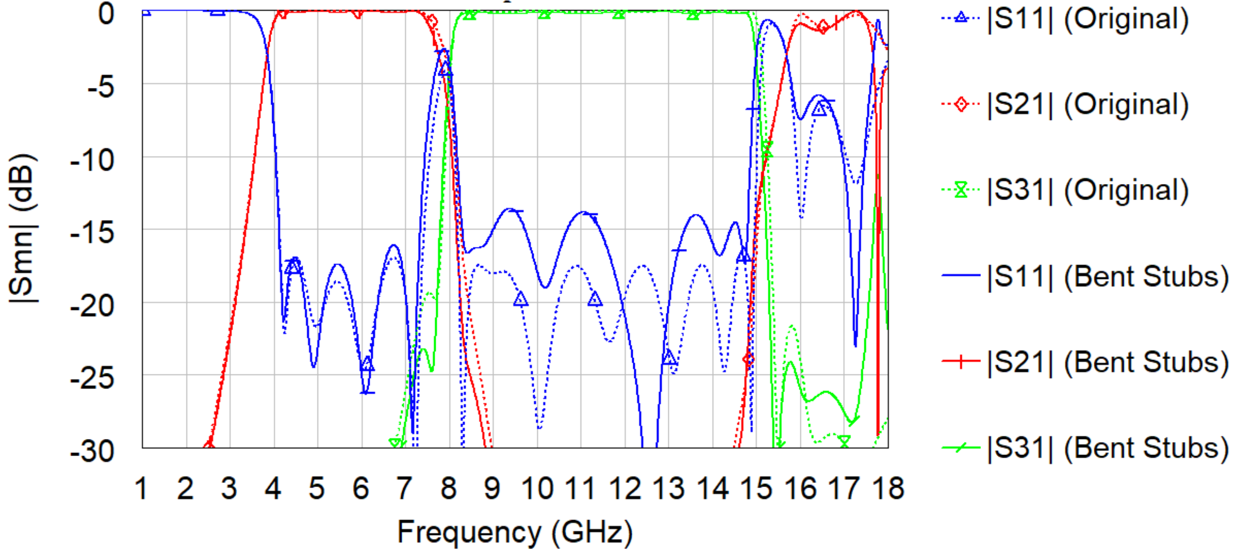

Fig. 6.22. Plot of simulated performance of compact diplexer with (solid lines) and without (dashed lines) bent stub lines. Primary impact is seen throughout the high-band, but low-band performance is also affected.

plating through the release holes is essential. For this, the 1mm release holes are too narrow. Widened release holes of 2mm diameter demonstrates good performance for plating, however the performance impact is more substantial. Comparison of Performance with and without release hole addition can be seen in Fig. 6.23, again on the 'Packed' diplexer design of Fig. 6.1(g). As the added release holes effect a local drop in characteristic impedance, the impacts of widening the inner line to compensate for release hole presence is also investigated. The addition of four symmetric release holes to a region of coaxial line substantially increases both inductance and capacitance in a way that cannot be compensated for with only inner conductor diameter variation. Tolerable local match can be obtained through diameter compensation, however overall phase behavior is substantially altered.

Due to narrow desired packing of <1 mm square columnar footprint. Another design is manufactured with different circuit parameters. This design is seen in Fig. 6.1(h). Stub lines are limited to a minimum impedance of 20Ω to ensure manufacturability and eliminate the need for parallel stub lines. The circuit parameters for this design can be seen in Table 6.5 This design trades reduced overall footprint for reduced RL above 13 GHz, and slower out of band attenuation.

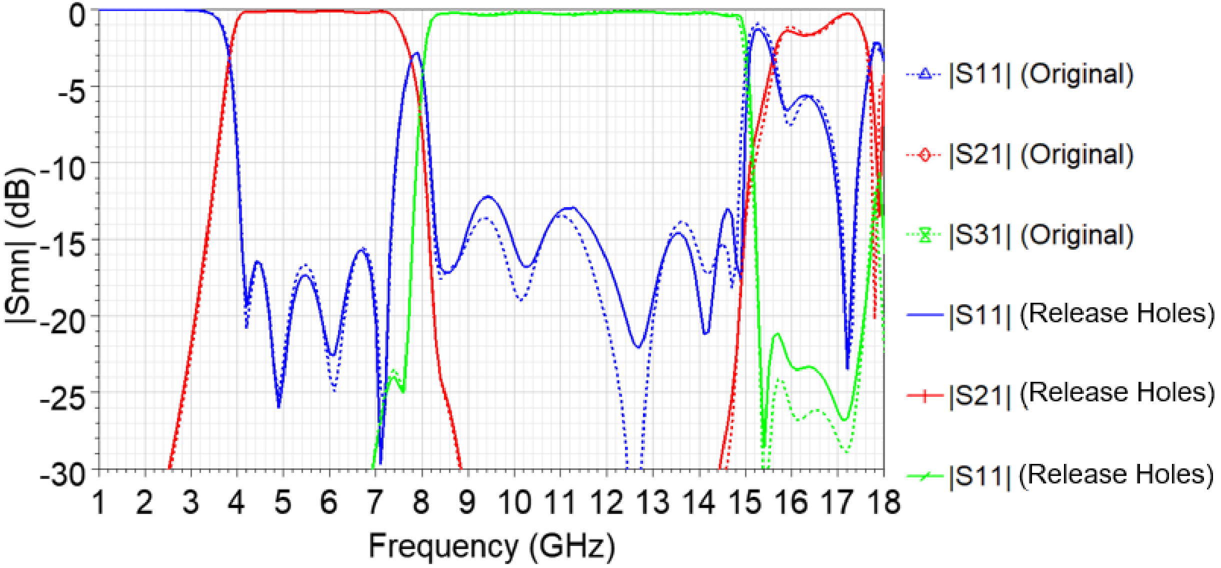

Fig. 6.23. Plot of simulated performance of compact diplexer with (solid lines) and without (dashed lines) added release holes. Primary impact is seen throughout the high-band, but low-band performance is also affected.

TABLE 6.5. SMALL PROFILE DIPLEXER IMPEDANCE VALUES

	Z_{S1}	Z_{R1}	Z_{B1}	Z_{S2}	Z_{R2}	Z_{B2}
High-Band	41	20	67	81	20	50
Low-Band	44	20	64	71	20	35

	Z_A	Z_R
High-band Annulling	81	20
Low-band Annulling	44	20

Performance of the two designs compared can be seen in Fig. 6.24.

6.5.2 Manufacturing and Measurements of Additively Manufactured Diplexers

Three different diplexer devices are presented here: a ‘flat’ configuration seen in Fig. 6.1(f) utilizing parallel stubs to effect circuit model stub impedances below 20Ω, a ‘packed’ configuration seen in Fig. 6.1(g) using the same circuit model as the ‘flat’ configuration, but with routed lines to effect a 9.8x13mm packing scheme, and a ‘20Ω’ configuration seen in Fig. 6.1(h) using a different circuit model to achieve a more compact 9.8x9.8mm packing scheme, but with slightly deteriorated performance in terms of out of band attenuation.

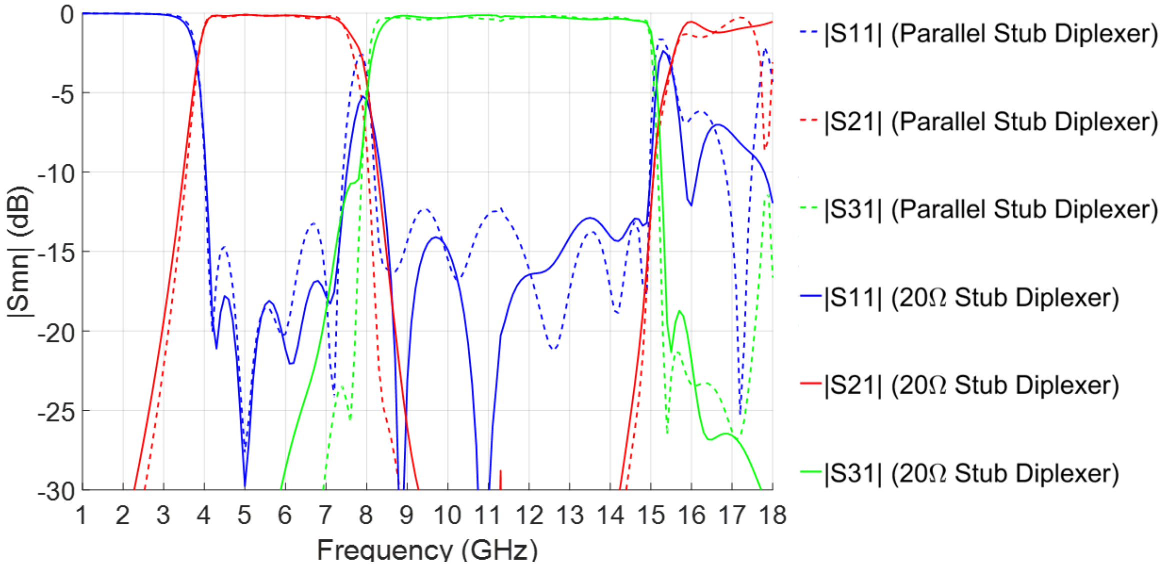

Fig. 6.24. Comparison of models showing difference in ideal performance of packed parallel stub diplexer and packed single stub ‘20Ω’ diplexer

Fig. 6.25 shows measured 'flat' configuration diplexer. Measured performance shows a bandwidth with RL> 15dB in the low band from 4.17-7.43 GHz, with mean IL of 0.16dB, and minimum IL in areas of good match of 0.1dB. The high band exhibits some performance deterioration, however demonstrates RL > 12.26dB over 8.32-13.36 dB, with mean IL of 0.26dB and minimum IL of 0.07dB. Overall agreement with simulation is good.

Measured performance of the 'packed' configuration diplexer can be seen in Fig. 6.26. Low band operates with RL > 14.02dB from 4.16-7.36 GHz, with mean IL of 0.19dB, and minimum IL of 0.09dB. High band operates from 8.36 – 15.14 GHz, with mean IL 0.47dB and minimum IL 0.14 dB. Overall agreement with simulation remains tolerable, with band edges well placed and mostly good return loss. Borescoping of this device shows a large number of non-shorting copper filaments present on the device interior in unreachable areas. These filaments are created during the plating process, likely due to transient high field strength on the device interior, and are the most common failure point of these devices. Fillaments can be created either fully bridging between inner and outer conductors, or forming a nonshorting 'spike' like those seen in this device. An example of such failure points can be seen in Fig. 6.27. Regardless, good operation

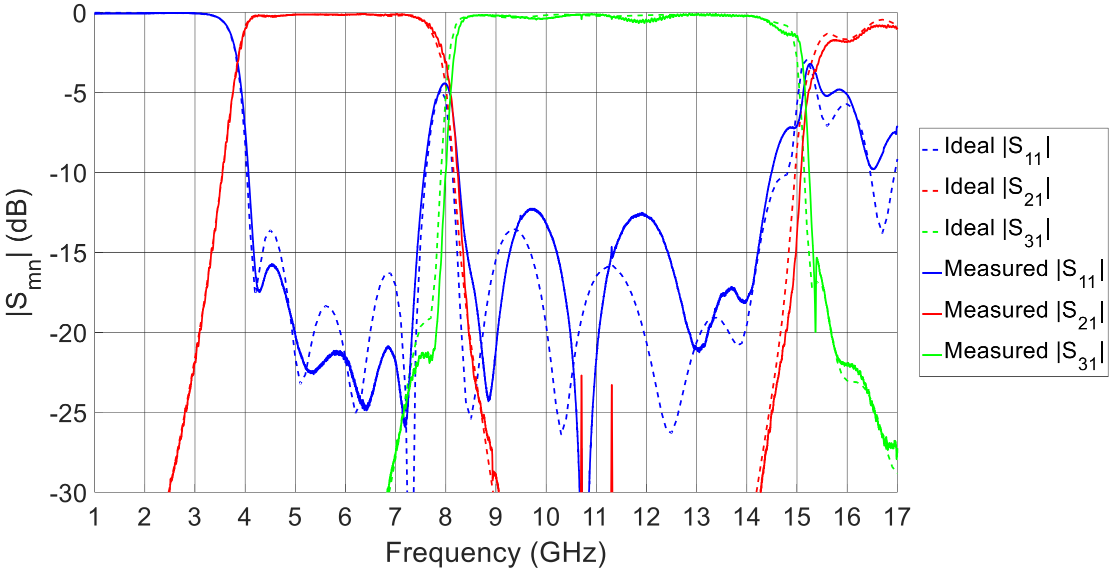

Fig. 6.25. Comparison of measured (solid lines) and simulated (dashed lines) performance for 'flat' configuration diplexer.

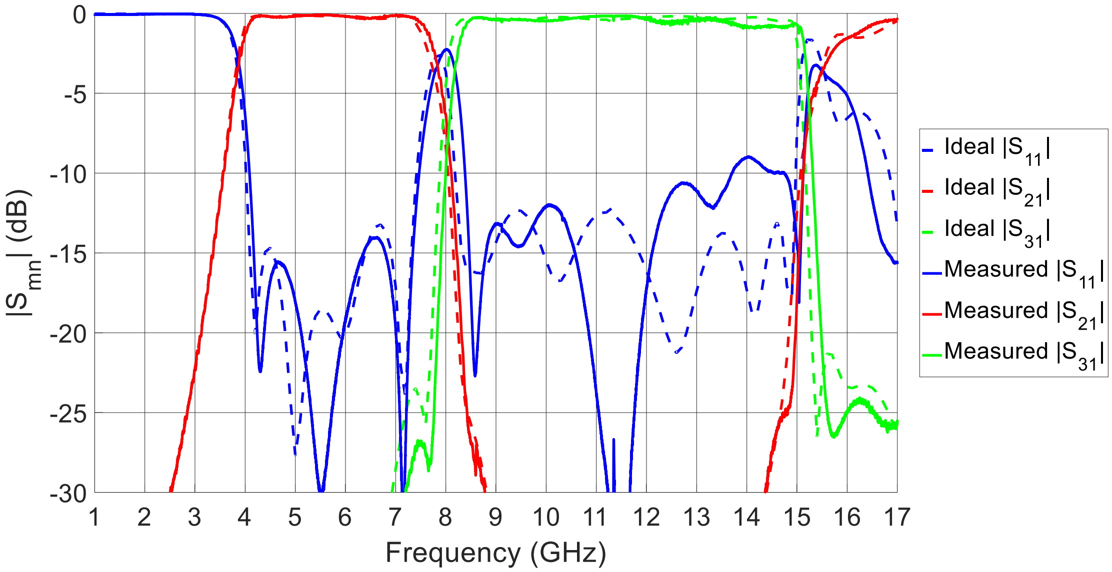

Fig. 6.26. Comparison of measured (solid lines) and simulated (dashed lines) performance for ‘packed’ configuration diplexer.

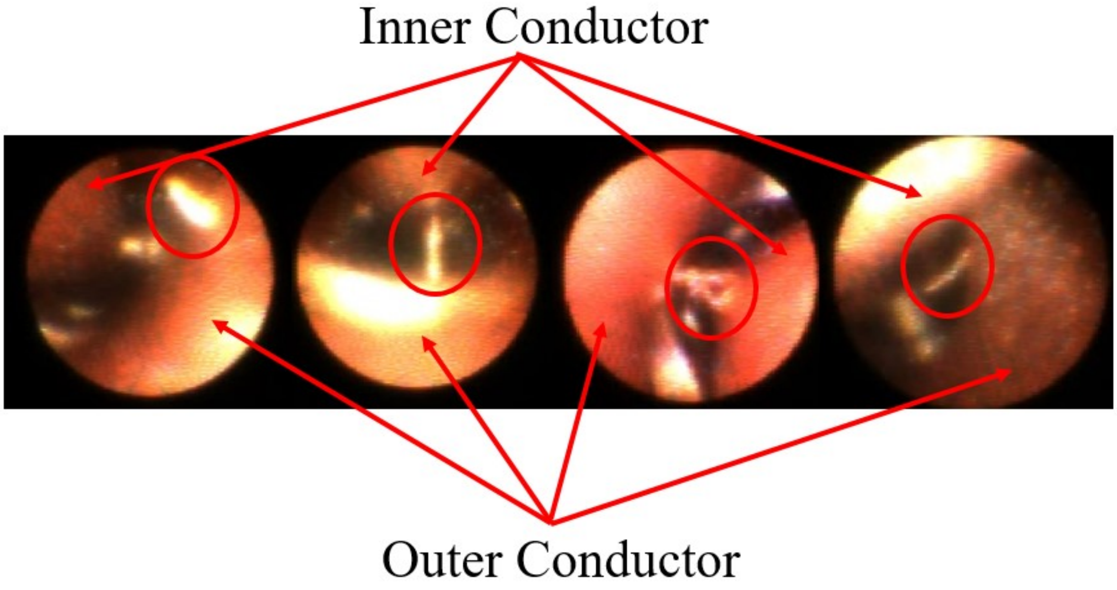

Fig. 6.27. Borescope images of interior copper filaments formed during copper plating. Inner and outer conductors are indicated. Circled features show a selected prominent shorting filaments.

in the presence of additional, randomly placed reactive loads demonstrates good robustness of the design.

Finally, measured performance of the ’20Ω packed’ diplexer configuration is plotted in Fig. 6.28. Low band performance show RL > 15dB from 4.2-7.34 GHz, with mean IL of 0.17dB,

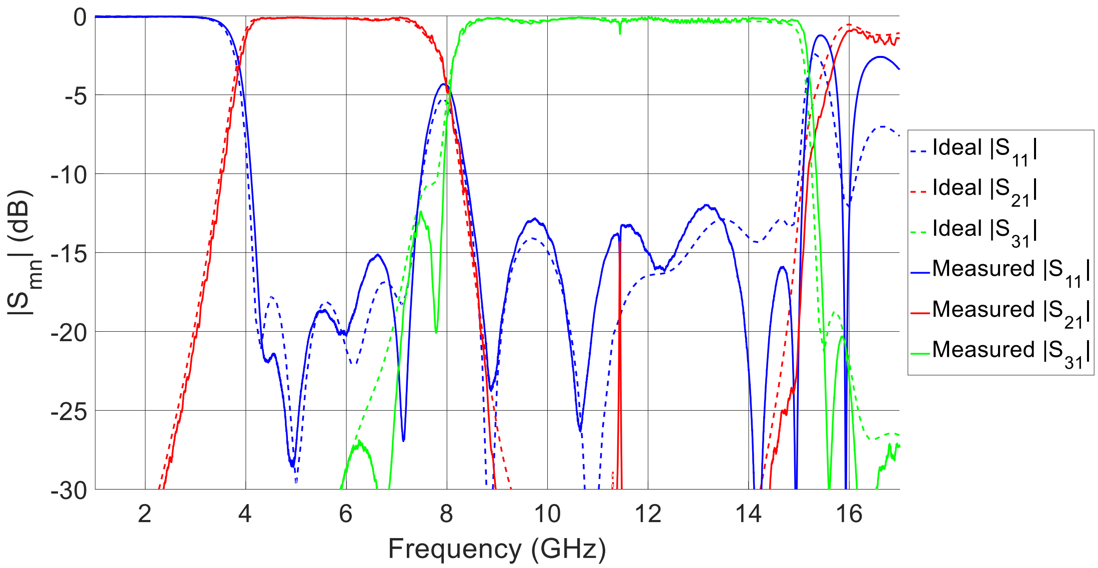

Fig. 6.28. Comparison of measured (solid lines) and simulated (dashed lines) performance for '20Ω packed' configuration diplexer.

minimum IL of 0.1dB, and maximum IL of 0.39dB. High band performance shows RL > 12dB from 8.47-15 GHz, with mean IL of 0.26dB, minimum IL of 0.08dB, and maximum IL of 0.5 dB, excluding the small spike at 11.44GHz. overall agreement remains good, particularly looking at transmission characteristics. This device shows relatively few internal defects that cause deteriorated performance. The primary defect as seen here is present in the spike near 11.44 GHz. This is a diplexer behavior caused by slight shortening of the low band annulling stub, on the order of 100-200um. This is likely caused either during the printing process, with material curing in place inside the end of the stub, or during the plating process. Fig. 6.29 shows the measured $|S_{22}|$ and $|S_{33}|$ for the '20Ω packed' diplexer configuration. As can be seen, this agrees well with measured $|S_{11}|$ performance, showing little to no transmission to the opposing channel.

6.6 Performance Comparison

The existing work in the literature, presented in Table 6.6, that is similar to the designs presented here is limited. The primary competing broadband 3D transmission line devices are those in [48], which consists of liquid metal suspended in a dielectric structure to form the

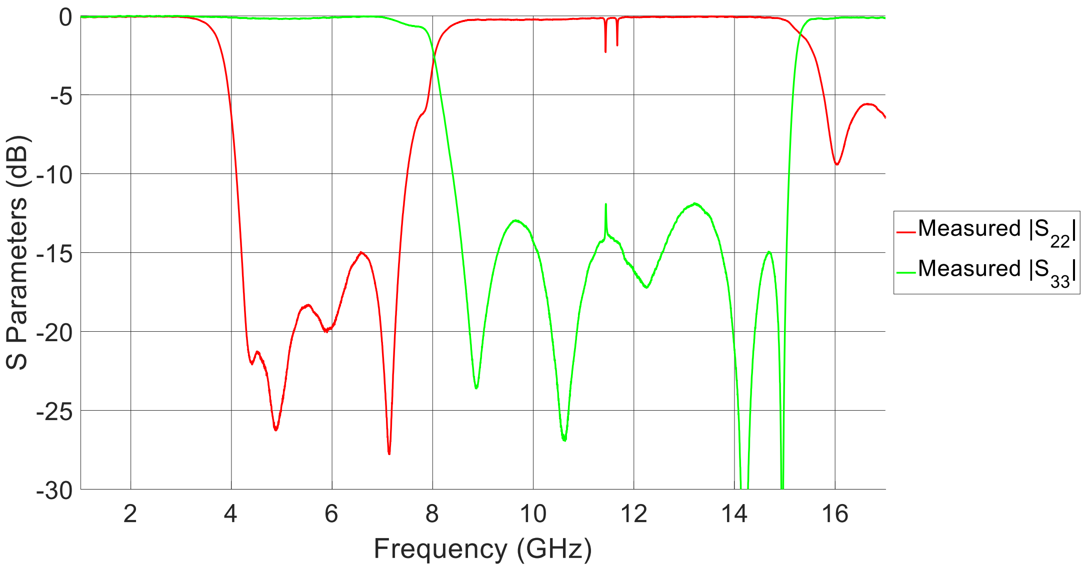

Fig. 6.29. Measured values for $|S_{22}|$ and $|S_{33}|$ for '20Ω packed' configuration diplexer.

conductors. This device does achieve DC operation, however shows substantially greater integration challenges. Resonator devices in literature are the broadest category, comparable 3D printed devices, however, in [38, 42] are much lower in frequency. [38] is fed with inserted prefabricated coaxial cables, and [42] is waveguide fed. Achieved Q_0 is comparable to existing work, and integrates monolithic coaxial feeding. Filter devices are a sparser category in the literature for 3D printed devices, with the majority being waveguide or resonator devices of substantially narrow band like [38, 42]. Coaxial devices like [45, 49] are more narrowband than the designs presented here, with greater losses. The closest design to this work is [49], which does not achieve good fabrication, is narrower in bandwidth, and utilizes a more standard chebyshev 3-stub filter design. Additionally, internal complexity in [49] is kept to a minimum, with straight line rectangular coax utilized throughout. The only 3D printed diplexer devices found in the literature were [44], which is not monolithic or miniaturized, features waveguide technology, and demonstrates poor IL and extremely narrow bandwidths, and [15], which is monolithic, but is also not miniaturized and features waveguide technology. [15] does however achieve good IL and RL, however over narrow, noncontiguous bandwidths. The work presented here, by contrast, achieves

TABLE 6.6. COMPARISON TO EXISTING LITERATURE

Source	Device Type	BW (GHz)	IL (dB)	RL (dB)	Q_0
[38]	Resonators	$f_0 \in [2.1\text{-}9.5]$	-	-	1638-3520
[38]	Bandpass filter	4.9-5.6	<0.35*	>15*	-
[48]	Tx line	0-12	<0.3 dB/cm	>10	-
[49]	Bandpass filter	8-12.4	<1.1	>8	-
[45]	Bandpass filter	2.97-3.02	<1.25	>20	-
[42]	Bandpass filter	9.85-10.15	<0.25	>20	-
[44]	Diplexer low	11.67-11.93	<2.12	>17.8	-
[44]	Diplexer high	12.04-12.29	<2.62	>23.9	-
[15]	Diplexer low	11.95-12.55	<0.4	>20	-
[15]	Diplexer high	13.95-14.55	<0.4	>20	-
This work	Tx line	10-30	<0.7 dB/cm	>15	-
This work	Resonator	$f_0 = 30$	0.53	21.8	3407
This work	Bandpass filter	8.4-13	<2.1	>10	-
This work	Bandpass filter	4.1-7.8	<0.4	>12	-
This work	Diplexer low	4.2-7.3	<0.4	>15	-
This work	Diplexer high	8.4-15	<0.5	>12	-

very wide bandwidths, good IL and RL, a high degree of miniaturization, and takes full advantage of the internal complexities achievable with 3D printing.

6.7 Conclusion

This chapter discusses the design and fabrication of many devices, forming a family of fully monolithic, additively manufactured coaxial components. These devices consist of coaxial ‘anchor’ devices, with the intent of feeding a larger 3D printed device or antenna with wideband operation, rectangular cavities which can be leveraged for further development of filters or other applications, in-line bandpass filters with low loss, and fully monolithic additively manufactured diplexers. These devices each extend the state of the art individually, and together form a fully formed contribution demonstrating the utility of additive manufacturing to manufacture high quality parts as the techniques and technologies develop further. DMLS 3D printed anchor devices are demonstrated achieving a 10-30 GHz bandwidth with better than 15dB return loss, showing the feasibility of high frequency device manufacture. DMLS and SLA 3D printed resonators show the compared performance of the two additive manufacturing techniques, and inform the selection of techniques based on expected loss characteristics and physical measurements. Fully monolithic filters demonstrate wider bandwidths and higher frequency operation than existing competing devices, operating over octave bandwidths from 4-7.8 GHz and 7.8-15 GHz with good robustness of manufacturing. Finally, fully monolithic, additively manufactured diplexer devices, taking full advantage of the capabilities of 3D printing to perform device miniaturization and realize complicated internal structures are constructed, and demonstrated to achieve good performance even with low-order filtering stages. Similar designs or performance are not seen in the literature. The combination of these things demonstrate that DMLS and SLA technologies are sufficiently mature to be used for high performance wideband design and fabrication well into K band, and as high as Ka band operation. Further work in this area can examine in greater detail the work of compensating for manufacturing error and nonideal elements in these devices, and further efforts at miniaturization and compact multi-device integration.

CHAPTER 7

CONCLUSIONS

7.1 Summary

This thesis has presented a comprehensive examination of systems to advance the understanding of AODF. This has been accomplished through the analysis of generalized functions modelling common radiation patterns, and drawing conclusions about the ideal case DF behavior. The framework developed for the analysis of DF antennas and system level goals provides insights into the limitations of all AODF systems, linking the antenna beam shape, and in particular the beamwidth, to the antenna mechanical squint, the detection FOV, the minimum system gain, and the noise tolerance as expressed through the DFF slope. The three system goals are found to be inversely correlated, with improvements to any one category diminishing the others. Using this model, and with knowledge of the expected beamwidths of a family of antennas, it is possible to determine precisely whether direction finding can be achieved with an antenna, what system performance can be expected, and what beamwidth and gain to design for to achieve good DF operation.

Utilizing this framework a family of curved aperture horn antennas have been designed for wide absolute bandwidth covering >75-110 GHz, high gain, high DFF slope operation, achieving better than 0.5dB/degree slope and better than 0dBi minimum gain across a FOV of 40°. The antennas are designed for tight H-plane pattern control, and achieve <3.8° 10dB beamwidth variation over 75-110 GHz. Multiple configurations of the curved aperture horn are manufactured by numerous techniques, and good agreement with simulation is obtained. This work also provides design data for the construction of future curved aperture horns, which has been absent from the literature.

The TEM horn antenna has been extended to a dual polarized configuration, and miniaturized through the spherical modes engineering technique. This technique has been extended through the addition of new current paths to the TEM horn antenna, improving modal behaviors and removing narrowband resonant behaviors from the structure. This structure has been integrated with a cavity to improve pattern behaviors for DF operation, and wide FOV coverage is obtained in simulation and measurement. A novel balun structure transitioning from two coax inputs to a four-wire line has been developed, enabling wideband feeding and removing the need for expensive beamforming components. Measured radiation patterns validate the design, showing excellent agreement with expected pattern shape.

Finally, a family of 3D printed coaxial components has been developed working from C-Ka band. Manufactured devices show low loss, good internal formation, and achieve geometry that cannot be constructed by traditional subtractive machining. The novel compensated coaxial cross junction enables future designs to avoid challenges associated with wide coaxial line diameter. Manufactured diplexers with wide, contiguous bands are demonstrated, achieving both good electrical performance, and tight mechanical integration requirements, being narrower than 9.8mm x 9.8mm to act as a wideband array feeding device. These devices advance the state of the art for the additive manufacture of wideband coaxial components, and provide a low cost means of rapidly prototyping and manufacturing high quality components.

7.2 Contributions

The contributions of this work are summarized as follows:

- The novel analytical framework linking receiver and system requirements to AODF capable beam shapes has been presented and validated.
- The analytical framework has been demonstrated for the design of multiple antennas.
- The impact of imperfect radiation patterns and wideband operation has been explained.
- The curved aperture horn antenna has been adapted to the challenges of mm-wave fabrication.

- Guidelines for the future design of the curved aperture horn have been presented in the form of parametric plots.
- Achieved rigorous AODF requirements over a >30GHz bandwidth at mm-wave frequencies.
- Designed the TEM horn to work as a dual polarized antenna.
- Demonstrated >5:1 bandwidth dual polarized DF operation with >60% efficiency in simulation, and 47-75% measured efficiency.
- Developed a novel integrated balun to feed dual-linear four-wire transmission line.
- Advanced the spherical mode miniaturization technique by eliminating spurious resonances in the combined Tem horn/Loop antenna
- Developed >3:1 bandwidth coaxial ‘Anchor’ lines, implementing in-line quarter wave transformer sections
- Developed accurately construced, high Q, coaxial-fed resonators at 30GHz, well above competing works in literature
- Produced monolithic, low loss, wideband bandpass filters in self-supporting air-filled coaxial technology.
- Developed miniaturized, monolithic, contiguous, wideband diplexers with low loss in self supporting air-filled coaxial technology
- Developed novel coaxial cross junction geometry to optimize for parasitics present in wide 3D printed coaxial line junctions.

7.3 Future Work

Future work in this are should focus on a number of topics. To advance the theory of AODF operation further, additional functional terms should be added to the cosine, sinc, and gaussian beam to obtain superior modelling of two effects, the ‘pattern ripple’ caused by near field interactions and poorly controlled modes radiating from large antennas, and the impact of realistic backlobes or noise floor behaviors. Pattern rippling can rapidly degrade the quality (i.e. reduce the FOV and DFF slope) for direction finding systems. Additional terms may be added to the standard beam models to create modelled rippling, such that the impact of rippling 'spacial frequency' and ripple amplitude can be investigated further to determine limits on acceptable pattern ripple. Such a term could be as in (7.1), below, treating B as some amplitude, and m as some frequency scaling term such that $B \ll A$ and $m \gg k$.

$$F(\theta) = Acos^{n}(k\theta) + Bcos(m\theta) \tag{7.1}$$

For realistic antennas, the backlobe is nonzero in many cases, and may be modelable with another secondary term scaled and added to the primary beam function. The correct selection and usage of an additional term may allow for the more accurate modelling of the nonidealities currently explained through the pattern concavity beamwidth.

Further work for the curved aperture horn could continue to examine the ways that the consistent beamwidth of this antenna archetype can be extended through deliberate multimode excitation, as well as to examine the accurate analytical modelling of this structure, as it is not adequately explained by the theory put forward in [68] (see appendix).

Additional improvements to the TEM horn must focus on improving a variety of factors. First developing a new mechanical design with superior mechanical stabilization and centering. Second the TEM horn should be examined with additional, more accurately known absorber models to determine superior choices of absorber material to achieve high efficiency without sacrificing low frequency match. Simulations suggest that absorbers such as the ECCOSORB LS series may permit higher than 70% efficiency across the band, however the match below 2GHz is degraded in simulations examined thus far. Additional tuning of the device, and examinations of further ways to improve mode structure are also worth examining, such as constructing the loop and shorting posts for the device from spherical surfaces rather than rectilinear surfaces and posts. Last, further modelling of the modal structure over the course of the balun transition is called for, $|S_{11}|$ simulations demonstrate good match and low coupling to the opposing polarization, however the design process involved selecting for TE_{11} impedance at one end of the transition and TEM impedance at the opposing end of the transition. Intermediate behavior involves a shift in field structure between the two modes that occurs over a short distance, and the impedance tapering is not well captured by TEM modeling of the ‘shielded’ four wire line.

The next most challenging step in the design of highly compact 3D printed components is to compensate for two effects: the impact of the large release holes utilized to achieve good plating, and the 90^{o} bends necessary to achieve tight line routing. Efforts to compensate for these impacts through simple geometric compensation are not thus far successful and results have been omitted. Widening inner conductor diameter below release holes to effect a continuous impedance, and mitering coaxial bends to reduce bend capacitance do not result in correct compensation.

BIBLIOGRAPHY

[1] S. E. Lipsky, Microwave Passive Direction Finding. Raleigh, NC: SciTech Publishing, 2004.

[2] F. Adcock, “Improvement in Means for Determining the Direction of a Distant Source of Electromagnetic Radiation,” British Patent 130490, 1919.

[3] W. Hong et al., "The Role of Millimeter-Wave Technologies in 5G/6G Wireless Communications," in IEEE Journal of Microwaves, vol. 1, no. 1, pp. 101-122, Jan. 2021.

[4] G. Lasser, J. Cazden and D. Filipovic, "A Spiral Antenna for Amplitude-Only Direction Finding," in 2017 IEEE International Symposium on Antennas and Propagation & USNC/URSI National Radio Science Meeting, 2017, pp. 927-928.

[5] J. Cazden and D. Filipovic, "Wideband Amplitude-Only Direction Finding Subsystem with Conical Spirals," in 2017 IEEE International Symposium on Antennas and Propagation & USNC/URSI National Radio Science Meeting, 2017, pp. 1103-1104.

[6] L. G. Bullock, G. R. Oeh and J. J. Sparagna, "An Analysis of Wide-Band Microwave Monopulse Direction-Finding Techniques," in IEEE Transactions on Aerospace and Electronic Systems, vol. AES-7, no. 1, pp. 188-203, Jan. 1971.

[7] M. Elmansouri, D. Filipovic and P. Hoover, "Performance of Multi-Arm Sinuous Antenna in Analog and Digital Angle of Arrival Estimation," in 2019 IEEE International Symposium on Antennas and Propagation and USNC/URSI Radio Science Meeting, 2019, pp. 1913-1914.

[8] M. A. Al-Tarifi and D. S. Filipovic, "Amplitude-only Direction Finding Using Squinted Stabilized-Pattern Horn Antennas in W-Band," in 2016 IEEE International Symposium on Antennas and Propagation and USNC/URSI National Radio Science Meeting, 2016, pp. 1183-1184.

[9] D. G. Lopez, M. A. Al-Tarifi, G. Lasser and D. S. Filipovic, "Wideband Antenna Systems for Millimeter-Wave Amplitude-Only Direction Finding," in IEEE Trans. Antennas and Propagation, vol. 66, no. 6, pp. 3122-3129, June 2018.

[10] R. Schmidt, "Multiple Emitter Location and Signal Parameter Estimation," in IEEE Trans. Antennas and Propagation, vol. 34, no. 3, pp. 276-280, March 1986.

[11] A. J. Barabell et al., “Performance Comparison of Superresolution Array Processing Algorithms,” Lincoln Laboratory, Lexington, MA, Report TST-72, 9 May 1984.

[12] T. Do-Hong and P. Russer, "Wideband Direction-of-Arrival Estimation and Beamforming for Smart Antennas System," in 2003 Radio and Wireless Conference, Boston, MA, 2003, pp. 127-130.

[13] G. R. Friedrichs, M. A. Elmansouri and D. S. Filipovic, "A Machine Learning Enhanced Small Circular Array for Amplitude Only Direction Finding," in 2021 IEEE International Symposium on Antennas and Propagation and USNC/URSI Radio Science Meeting, 2021, pp. 1479-1480.

[14] K. D. Merkel et al., "Extreme Bandwidth Spectrum Analysis," in 2016 IEEE Photonics Conference (IPC), 2016, pp. 487-488.

[15] E. Menargues et al., "3D Printed Feed-Chain and Antenna Components," in 2017 IEEE International Symposium on Antennas and Propagation & USNC/URSI National Radio Science Meeting, 2017, pp. 1-2.

[16] V. Gjokaj, P. Chahal, J. Papapolymerou and J. D. Albrecht, "A Novel 3D Printed Vivaldi Antenna Utilizing a Substrate Integrated Waveguide Transition," in 2017 IEEE International Symposium on Antennas and Propagation and USNC/URSI National Radio Science Meeting, 2017, pp. 1253-1254.

[17] L. Boskovic, I. Pisani, J. Cazden, and D. Filipovic, “Design and Characterization of a 3D Printed Helical Antenna Monolithically Integrated and Fed by and Air-Loaded Coaxial Line," in 2021 45th Allerton Antenna Applications Symposium (AAS), 2021.

[18] T. Isenlik, K. Yegin and D. E. Barkana, "Near-Constant Beamwidth Quadruple Bandwidth Double-Ridged Horn Antenna Design," in IET Microwaves, Antennas & Propagation, vol. 13, no. 12, pp. 2102-2109, Oct. 2019.

[19] B. M. Leiner, "An Analysis and Comparison of Energy Direction Finding Systems," in IEEE Trans. Aerospace and Electronic Systems, vol. AES-15, no. 6, pp. 861-873, Nov. 1979.

[20] R. S. Andrews, "Antenna and Other Systematic Effects on Amplitude Comparison Monopulse Systems," in IEE Journal on Electronic Circuits and Systems, vol. 3, no. 3, pp. 103-108, May 1979.

[21] D. G. Lopez and D. S. Filipovic, "On the Design of Milimeter-Wave Antennas for Amplitude-Only Direction Finding," in 2016 IEEE International Symposium on Phased Array Systems and Technology (PAST), 2016, pp. 1-8.

[22] P. Hajiani, H. Habibi, M. Hakkak and F. Mazlumi, "Accuracy in Wideband Direction of Arrival System," in 2007 International Symposium on Electromagnetic Compatibility, 2007, pp. 394-397.

[23] J. Mruk, Z. Hongyu, M. Uhm, Y. Saito and D. Filipovic, "Wideband mm-Wave Log-Periodic Antennas," in 2009 3rd European Conference on Antennas and Propagation, 2009, pp. 2584-2587.

[24] H. Zhou, N. A. Sutton and D. S. Filipovic, "W-band Endfire Log Periodic Dipole Array," in 2011 IEEE International Symposium on Antennas and Propagation (APSURSI), 2011, pp. 1233-1236.

[25] J. R. Mruk, Y. Saito, K. Kim, M. Radway and D. Filipovic, "A Directly Fed Ku- to W-Band 2-Arm Archimedean Spiral antenna," in 2011 41st European Microwave Conference, 2011, pp. 539-542.

[26] M. Abbasi and D. S. Ricketts, "W-Band Corrugated and Non-Corrugated Conical Horn Antennas Using Stereolithography 3D-Printing Technology," in 2016 Asia-Pacific Microwave Conference (APMC), 2016, pp. 1-3.

[27] M. Abbas-Azimi, F. Mazlumi and F. Behnia, "Design of Broadband Constant-Beamwidth Conical Corrugated-Horn Antennas [Antenna Designer's Notebook] ," in IEEE Antennas and Propagation Magazine, vol. 51, no. 5, pp. 109-114, Oct. 2009.

[28] S. Manafi, M. Al-Tarifi and D. S. Filipovic, "45–110 GHz Quad-Ridge Horn With Stable Gain and Symmetric Beam," in IEEE Transactions on Antennas and Propagation, vol. 65, no. 9, pp. 4858-4863, Sept. 2017.

[29] J. Thornton and K. C. Huang, "Polyrod Antennas," in Modern Lens Antennas for Communications Engineering , IEEE, 2012, pp.77-112.

[30] C. Parker and R. Anderson, "Constant Beamwidth Broadband Antennas," in 1958 IRE International Convention Record, 1957, pp. 87-98.

[31] D. V. Lioubtchenko, S. N. Dudorov, J. A. Mallat and A. V. Raisanen, "Dielectric Rod Waveguide Antenna for W Band with Good Input Match," in IEEE Microwave and Wireless Components Letters, vol. 15, no. 1, pp. 4-6, Jan. 2005.

[32] M. A. Al-Tarifi and D. S. Filipovic, "On the assessment of antenna patterns for wideband amplitude-only direction finding," IEEE Antennas and Wireless Propagation Letters, vol. 17, no. 3, pp. 385-388, March 2018.

[33] W. N. Kefauver, T. P. Cencich and D. S. Filipovic, "On the Frequency-Independent Modes of a Four-Arm Modulated Arm Width Spiral," in IEEE Transactions on Antennas and Propagation, vol. 61, no. 9, pp. 4467-4475, Sept. 2013.

[34] H. S. Zhang, K. Xiao, L. Qiu and S. L. Chai, "Four-Arm Sinuous Antenna for Direction Finding System," in 2014 IEEE International Wireless Symposium (IWS 2014), X'ian, 2014, pp. 1-4.

[35] A. Akgiray, S. Weinreb, W. A. Imbriale and C. Beaudoin, "Circular Quadruple-Ridged Flared Horn Achieving Near-Constant Beamwidth Over Multioctave Bandwidth: Design and Measurements," in IEEE Transactions on Antennas and Propagation, vol. 61, no. 3, pp. 1099-1108, March 2013.

[36] A. Giacomini, A. Potenza, R. Morbidini and L. Foged, "Quad-ridge Dual Polarized Antenna for Use in the 2–32GHz Band," in 2012 6th European Conference on Antennas and Propagation (EUCAP), 2012, pp. 769-772.

[37] Y. He, E. Drew, P. Chahal, J. Z. Zhang and J. Papapolymerou, "3D Printed Spherical Cavity Resonator With Fine Tuning Using Nanomagnetic Thin Film," in 2020 50th European Microwave Conference (EuMC), 2021, pp. 388-391.

[38] K. Zhao and D. Psychogiou, "Monolithic SLA-Based Capacitively-loaded High-Q Coaxial Resonators and Bandpass Filters," in 2020 50th European Microwave Conference (EuMC), 2021, pp. 471-474.

[39] J. Li, C. Guo, L. Mao, J. Xiang, G. Huang and T. Yuan, "Monolithically 3-D Printed Hemispherical Resonator Waveguide Filters With Improved Out-of-Band Rejections," in IEEE Access, vol. 6, pp. 57030-57048, 2018.

[40] J. Li, G. Huang and T. Yuan, "Monolithic 3-D Printed Spherical-Resonator-Based Olympic-Topology Bandpass Filters," 2018 IEEE International Symposium on Antennas and Propagation and USNC/URSI National Radio Science Meeting, 2018, pp. 1441-1442.

[41] C. Guo, X. Shang, J. Li, M. J. Lancaster and J. Xu, "3-D Printed Lightweight Microwave Waveguide Devices," in 2016 IEEE 5th Asia-Pacific Conference on Antennas and Propagation (APCAP), 2016, pp. 47-48.

[42] C. Guo, X. Shang, J. Li, F. Zhang, M. J. Lancaster and J. Xu, "A Lightweight 3-D Printed X-Band Bandpass Filter Based on Spherical Dual-Mode Resonators," in IEEE Microwave and Wireless Components Letters, vol. 26, no. 8, pp. 568-570, Aug. 2016.

[43] Y. Zhang et al., "A 3-D Printed Ka-band Twisted Waveguide Filter with Filtering and Polarization Rotation," in 2019 IEEE International Symposium on Antennas and Propagation and USNC/URSI Radio Science Meeting, 2019, pp. 1701-1702.

[44] E. Laplanche et al., "A Ku-Band Diplexer Based on 3dB Directional Couplers Made by Plastic Additive Manufacturing," in 2017 47th European Microwave Conference (EuMC), 2017, pp. 428-431.

[45] G. Venanzoni, M. Dionigi, C. Tomassoni and R. Sorrentino, "Design of a Compact 3D Printed Coaxial Filter," in 2018 48th European Microwave Conference (EuMC), 2018, pp. 280-283.

[46] C. Tomassoni, G. Venanzoni, M. Dionigi and R. Sorrentino, "Compact Doublet Structure for Quasi-Elliptical Filters Using Stereolitographic 3D Printing," in 2017 47th European Microwave Conference (EuMC), 2017, pp. 993-996.

[47] V. Palazzi et al., "Microfluidics-Based 3D-Printed 4 × 4 Butler Matrix in Coaxial Technology for Applications up to K Band," in IEEE MTT-S International Microwave Symposium (IMS), 2019, pp. 1371-1374.

[48] J. Shen, D. P. Parekh, M. D. Dickey, and D. S. Ricketts, "3D Printed Coaxial Transmission Line Using Low Loss Dielectric and Liquid Metal Conductor," in IEEE MTT-S International Microwave Symposium, 2018, pp. 59-62.

[49] Y. Yu et al., "A Connectorized X-Band 3-D Printed Air-Filled Self-Suspended Rectangular Coaxial Transmission Line," in 2019 49th European Microwave Conference (EuMC), 2019, pp. 690-693.

[50] C. Guo et al., "A 3-D Printed E-Plane Waveguide Magic-T Using Air-Filled Coax-to-Waveguide Transitions," in IEEE Transactions on Microwave Theory and Techniques, vol. 67, no. 12, pp. 4984-4994, Dec. 2019.

[51] G. Venanzoni et al., "Design and Fabrication of 3-D Printed Inline Coaxial Filters with Improved Stopband," in IEEE Transactions on Microwave Theory and Techniques, vol. 68, no. 7, pp. 2633-2643, July 2020.

[52] L. Boskovic, J. Cazden, and D. Filipovic, “Design and Characterization of an All-Metal 3D Printed Air-Dielectric Coaxial Line” to be published in Microwave Components Letters.

[53] O. A. Abd El-Alim, E. E. Agrama and M. E. Ezz-El-Arab, "Second-Order Discriminant Function for Amplitude Comparison Monopulse Antenna Systems (EW Antenna Array)," in IEEE Transactions Instrumentation and Measurement, vol. 40, no. 3, pp. 596-600, June 1991.

[54] K. D. Merkel et al., “20 GHz Instantaneous Bandwidth RF Spectrum Analyzer Measurements with High Sensitivity and Spur Free Dynamic Range,” in 2014 GOMACTech, Charleston, SC, 2014.

[55] R. K. Mohan et al., “Ultra-Wideband Spectral Analysis Using S2 Technology,” in Journal of Luminescence, Vol 127, No. 1, pp 116-128, March 2007.

[56] Y. Kol, and N. Herscovici, “Analysis and Design of Wideband Constant Beamwidth Sectoral Horns,” in Journal of Electromagnetic Waves and Applications, vol. 4, no. 7, pp. 673-682, 1990.

[57] C. Viswanadham, "A Practical Approach for Controlling the Shape of the Radiation Pattern of a Microwave Log-Periodic Antenna for Wideband Applications" in IEEE Antennas and Propagation Magazine, vol. 56, no. 5, pp. 304-314, Oct. 2014.

[58] G. Morris, "A Broad-Band Constant Beamwidth Corrugated Rectangular Horn," in IEEE Transactions on Antennas and Propagation, vol. 30, no. 5, pp. 966-974, September 1982.

[59] P. J. Massey, "Improvements in Constant Beamwidth Horns," in 1988 18th European Microwave Conference, Stockholm, Sweden, 1988, pp. 124-129.

[60] C. Balanis, Antenna Theory: Analysis and Design, 4th Ed. Hoboken, NJ: John Wiley & Sons, 2016.

[61] R. J. Dewey and R. Hill, "Wideband Constant Beamwidth Horn Antenna," in 1981 11th European Microwave Conference, Amsterdam, Netherlands, 1981, pp. 745-750.

[62] M. A. Al-Tarifi and D. S. Filipovic, "On the Design and Fabrication of W-Band Stabilized-Pattern Dual-Polarized Horn Antennas with DMLS and CNC," in IET Microwaves, Antennas & Propagation, vol. 11, no. 14, pp. 1930-1935, 19 11 2017.

[63] J. Cazden, M. Al-Tarifi, L. Boskovic and D. Filipovic, "A W-band Curved Aperture Horn Antenna with Consistent Radiation Patterns," in 2018 IEEE International Symposium on Antennas and Propagation and USNC/URSI National Radio Science Meeting, Boston, MA, 2018, pp. 593-594.

[64] R. K. Mohan, C. Harrington, T. Sharpe, Z. W. Barber, and W. R. Babbitt, “Broadband Multi-Emitter Signal Analysis and Direction Finding Using a Dual-Port Interferometric Photonic Spectrum Analyzer Based on Spatial-Spectral Materials,” in International Topical Meeting on Microwaves and Photonics (MWP), Oct. 2013, pp. 241—244.

[65] P. Berger et al., "RF Spectrum Analyzer for Pulsed Signals: Ultra-Wide Instantaneous Bandwidth, High Sensitivity, and High Time-Resolution," in Journal of Lightwave Technology, vol. 34, no. 20, pp. 4658-4663, 15 Oct.15, 2016.

[66] P. Berger et al., "20 GHz Instantaneous Bandwidth RF Spectrum Analyzer with High Time-resolution," in International Topical meeting on Microwaves and Photonics (MWP), 2014, pp. 331-334.

[67] R. J. Dewey, “Horn Antenna with Wide Flare Angle,” United States Patent 4630062, Dec 16, 1986.

[68] M. Singh and G. Sanyal, “Directional Properties of Nonplanar Aperture-Type Antennas,” in IEEE Transactions on Antennas and Propagation, Vol 26, no. 6, pp. 867-870, November 1978.

[69] D. Filipovic, and T. Cencich, “Frequency Independent Antennas”, Ch. 13 in the Antenna Engineering Handbook, 4th Edition, McGraw Hill, 2007.

[70] R. H. DuHamel, “Dual Polarized Sinuous Antenna”, US Patent 4658262, 1987.

[71] K. Chung, S. Pyun, and J. Choi, “Design of an Ultrawide-Band TEM Horn Antenna with a Microstrip-Type Balun,” in IEEE Transactions on Antennas and Propagation, vol. 53, no. 10, pp. 3410-3413, Oct. 2005.

[72] W. N. Kefauver, T. P. Cencich and D. S. Filipovic, "Modulated Arm Width (MAW) Spiral: Theory, Modeling, Design and Measurements," in IEEE Transactions on Antennas and Propagation, vol. 58, no. 11, pp. 3515-3523, Nov. 2010.

[73] E. Mehboodi, M. Movahhedi, and A. Heidari, "Wideband Dual-Polarised SAW Spiral Antenna for Monopulse System", in Microwaves Antennas & Propagation IET, vol. 12, no. 4, pp. 607-611, 2018.

[74] R. Pack and D. S. Filipovic, "Design of MAW Spiral Antennas for Direction-of-Arrival Sensing Using the Cramér-Rao Bound", in 2017 International Symposium on Antennas and Propagation and USNC/URSI National Radio Science Meeting, pp. 925-926, 2017.

[75] R. Pack, G. Lasser, and D. S. Filipovic, "Performance Characterization of Four-Arm MAW Spiral Antennas for Digital Direction-of-Arrival Sensing", in IEEE Transactions on Antennas and Propagation, vol. 66, no. 6, pp. 2761-2769, 2018.

[76] D. Kim, C. Y. Park, Y. Kim, H. Kim and Y. J. Yoon, "Four-Arm Sinuous Antenna With Low Input Impedance for Wide Gain Bandwidth," in IEEE Access, vol. 10, pp. 35265-35272, 2022.

[77] R. Sammeta and D. S. Filipovic, "Improved Efficiency Lens-Loaded Cavity-Backed Transmit Sinuous Antenna," in IEEE Transactions on Antennas and Propagation, vol. 62, no. 12, pp. 6000-6009, Dec. 2014.

[78] K. A. Abdalmalak, G. Santamaría Botello, S. L. Romano, L. E. García Muñoz and D. S. Vargas, "An Updated Version of the Dyson Conical Quad-Spiral Array (DYQSA) Feed System for VGOS Applications," in 2017 IEEE International Symposium on Antennas and Propagation and USNC/URSI National Radio Science Meeting, 2017, pp. 1539-1540.

[79] G. R. Friedrichs, J. A. Cazden and D. S. Filipovic, "Design of Dual-Polarized Pyramidal Log-Periodic Antenna with Integrated Feed for Additive Manufacturing," 2020 International Applied Computational Electromagnetics Society Symposium (ACES), 2020, pp. 1-2.

[80] L. L. Tsai, W. T. Hudson and G. Brown, "Transient Fields Radiated by TEM Horns," in 1975 IEEE International Symposium on Electromagnetic Compatibility, 1975, pp. 1-5.

[81] S. Evans et al., "TEM Horn Antenna: Input Reflection Characteristics in Transmission," in IEE Proceedings H - Microwaves, Optics and Antennas, vol. 130, no. 6, pp. 403-409, October 1983.

[82] N. Rojhani, M. Pieraccini and S. S. Golazari, "A Compact TEM Horn Antenna for Ground Penetrating Radar," in 2018 International Conference on Advances in Computing, Communications and Informatics (ICACCI), 2018, pp. 1641-1645.

[83] M. A. Elmansouri and D. S. Filipovic, "TEM Horn Inspired Wideband Antennas for Diverse Applications," in 2019 IEEE-APS Topical Conference on Antennas and Propagation in Wireless Communications (APWC), 2019, pp. 1-5.

[84] R. T. Lee and G. S. Smith, "A Design Study for the Basic TEM Horn Antenna," in IEEE Antennas and Propagation Magazine, vol. 46, no. 1, pp. 86-92, Feb. 2004.

[85] C. H. Baum, “Low-Frequency-Compensated TEM Horn,” in Sensor and Simulation Note 377, 1995.

[86] M. H. Vogel, “Design of the Low-Frequency Compensation of an Extreme-Bandwidth TEM Horn and Lens IRA,” Ch. 13 in Ultra-Wideband Short-Pulse Electromagnetics 3, Springer, Boston, MA, 1997.

[87] C. H. Baum, “Combined Electric and Magnetic Dipoles for Mesoband Radiation” in Proceedings of the 2009 International Conference on Electromagnetics in Advanced Applications, ICEAA 09, 2009, pp 1-7.

[88] X. Liu, G. Wang and W. Wang, "Design and Performance of TEM Horn Antenna with Low-Frequency Compensation," in Asia-Pacific Conference on Environmental Electromagnetics, 2003. CEEM 2003. Proceedings., 2003, pp. 306-309.

[89] H. Park, J. Kim, J. Ryu, J. Choi and Y. Yoon, "Modified Low-Frequency Compensated TEM (LFCTEM) Horn Antenna to Improve the Radiation Performance," in 2013 Asia-Pacific Microwave Conference Proceedings (APMC), 2013, pp. 1163-1165.

[90] V. I. Koshelev, Y. I. Buyanov, Y. A. Andreev, V. V. Plisko and K. N. Sukhushin, "Ultrawideband Radiators of High-Power Pulses," in 28th IEEE International Conference on Plasma Science and 13th IEEE International Pulsed Power Conference, 2001, vol. 2, pp. 1661-1664.

[91] M. Elmansouri and D. S. Filipovic, “Design of Combined-Antennas Using Spherical Modes,” in Antenna Applications Symposium, Monticello, IL, USA, Sep. 2014, pp. 167–187.

[92] M. A. Elmansouri and D. S. Filipovic, “Miniaturization of TEM Horn Using Spherical Modes Engineering,” in IEEE Transactions on Antennas and Propagation, vol. 64, no. 12, pp. 5064-5073, Dec. 2016.

[93] G. Strauss and K. Breitsameter, "A Circular Polarized TEM Horn Antenna Array with Large Scanning Angle," in 2011 IEEE Radio and Wireless Symposium, Phoenix, AZ, 2011, pp. 98-101.

[94] S. Ghosh, B. K. Sarkar and S. V. Pandey, "TEM Horn Antenna using Improved UWB Feeding Mechanism," in 2008 38th European Microwave Conference, Amsterdam, 2008, pp. 1398-1401.

[95] A. R. Mallahzadeh and F. Karshenas, "Modified TEM Horn Antenna for Broadband Applications," in Progress In Electromagnetics Research, Vol. 90, 105-119, 2009.

[96] R. T. Lee and G. S. Smith, “A Design Study for the Basic TEM Horn Antenna,” in 2003 IEEE International Symposium on Antennas and Propagation and USNC/URSI National Radio Science Meeting, 2003, vol. 1, pp. 225-228.

[97] M. A. Elmansouri and D. S. Filipovic, “Reduced-Size TEM Horn for Short-Pulse High-Power Electromagnetic Systems,” in 2014 IEEE International Symposium on Antennas and Propagation and USNC/URSI National Radio Science Meeting, 2014, pp. 828-829.

[98] H. A. Wheeler, “Transmission-Line Properties of Parallel Strips Separated by a Dielectric Sheet,” in IEEE Transactions on Microwave Theory and Techniques, vol. 13, no. 2, pp. 172-185, Mar. 1965.

[99] M. Ignatenko and D. S. Filipovic, "4–40 GHz Conical Spiral Antenna Recessed in a Cavity," in 2017 IEEE International Symposium on Antennas and Propagation and USNC/URSI National Radio Science Meeting, 2017, pp. 1537-1538.

[100] D. G. Lopez and D. S. Filipovic, "Flush Mountable K/Ka Band Amplitude Only Direction Finding System," in 2016 IEEE International Symposium on Antennas and Propagation and USNC/URSI National Radio Science Meeting, 2016, pp. 507-508.

[101] D. E. Bockelman and W. R. Eisenstadt, “Combined Differential and Common-Mode Scattering Parameters: Theory and Simulation,” in IEEE Transactions on Microwave Theory and Techniques, Vol 43, pp. 1530-1539, 1995.

[102] W. Sun and C. A. Balanis, "Analysis and Design of Quadruple-Ridged Waveguides," in IEEE Transactions on Microwave Theory and Techniques, vol. 42, no. 12, pp. 2201-2207, Dec. 1994.

[103] A. Jafargholi and M. Kamyab, “A New Approach for Feeding Sinuous Antenna,” in AEU International Journal of Electronics and Communications, vol. 65, no. 4, pp. 312-319, 2011.

[104] J. H. Cloete and T. Sickel, "The Planar Dual-Polarized Cavity Backed Sinuous Antenna - a Design Summary," in 2012 IEEE-APS Topical Conference on Antennas and Propagation in Wireless Communications (APWC), 2012, pp. 1169-1172.

[105] N. Lorho et al., "Miniaturization of an UWB Dual-Polarized Antenna," in 2015 IEEE International Conference on Ubiquitous Wireless Broadband (ICUWB), 2015, pp. 1-5

[106] H. Shirinabadi, M. Ahmadi-Boroujeni, E. Arbabi and K. Mohammadpour-Aghdam, "Design of a Printed Non-Planar Dual-Polarised Log-Periodic Dipole Array," in IET Microwaves, Antennas & Propagation, vol. 11, no. 4, pp. 490-494, 18 3 2017.

[107] J. Cazden, L. Boskovic, and D. Filipovic, “Design and Performance of Log Periodic Dipole Arrays with Integrated Impedance Transforming Feeds,” in 2019 Antenna Applications Symposium, 2019, pp. 201-223.

[108] S. Zheng et al., "A Broadband Dual Circularly Polarized Conical Four-Arm Sinuous Antenna," in IEEE Transactions on Antennas and Propagation, vol. 66, no. 1, pp. 71-80, Jan. 2018

[109] R.L. Carrel, “Analysis and Design of the Log Periodic Dipole Antenna,” Antenna Lab, University of Illinois, 1961.

[110] R. DuHamel and F. Ore, "Logarithmically Periodic Antenna Designs," in 1958 IRE International Convention Record, New York, NY, USA, 1958, pp. 139-151.

[111] R. DuHamel and D. Isbell, "Broadband Logarithmically Periodic Antenna Structures," in 1958 IRE International Convention Record, New York, NY, USA, 1957, pp. 119-128.

[112] A. N. Plastikov, V. A. Vasiliev and S. E. Chadov, "Dual-Band Dual-Polarized Log-Periodic Feed for Reflector Antenna," in 2013 IX Internatioal Conference on Antenna Theory and Techniques, Odessa, 2013, pp. 455-457.

[113] ETS-Lindgren, “ETS-Lindgren Public Website Antennas,” [Online]. Available: http://www.ets-lindgren.com/products/antennas/log-periodic-dipole-array [Accessed: July 1, 2019]

[114] I. Afifi, M. M. M. Ali and A. Sebak, "Wideband Printed Ridge Gap Semi-Log Periodic Structure Antenna for Millimeter Wave Applications," in 2018 18th International Symposium on Antenna Technology and Applied Electromagnetics (ANTEM), Waterloo, ON, 2018, pp. 1-2.

[115] X. Ding, B. Wang and R. Zang, "Design and Realization of a Printed Microstrip Log-Periodic Antenna," in 2012 IEEE International Workshop on Electromagnetics: Applications and Student Innovation Competition, Chengdu, Sichuan, 2012, pp. 1-3.

[116] G. Zhai, "Gain Enhancement of Printed Log-Periodic Dipole Array Antenna Using an Elliptical Patch," in 2015 IEEE 4th Asia-Pacific Conference on Antennas and Propagation (APCAP), Kuta, 2015, pp. 54-55.

[117] Q. Sun, J. Wang, J. Cui, J. Fu, C. Zhou and E. Wang, "A Compact Printed Log-Periodic Antenna with Loaded Stub," in 2014 3rd Asia-Pacific Conference on Antennas and Propagation, Harbin, 2014, pp. 593-595.

[118] T. Jiang, W. Hong and Z. Kuai, "Compact Ultra-Wideband Directional Printed Antenna with Notched Band," in 2011 China-Japan Joint Microwave Conference, Hangzhou, 2011, pp. 1-4.

[119] L. Chang, S. He, J. Q. Zhang and D. Li, "A Compact Dielectric-Loaded Log-Periodic Dipole Array (LPDA) Antenna," in IEEE Antennas and Wireless Propagation Letters, vol. 16, pp. 2759-2762, 2017.

[120] G. A. Casula, P. Maxia and G. Montisci, "Design of a Printed Wide Band Log-Periodic Antenna Dipole Array with a New Feeding Technique," in 2012 6th European Conference on Antennas and Propagation (EUCAP), Prague, 2012, pp. 1882-1884.

[121] N. Srisoontorn, C. Mahatthanajatuphat and P. Akkaraekthalin, "A Printed Log Periodic Dipole Antenna with 3/2 Curve Fractal Elements," 2016 13th International Conference on Electrical Engineering/Electronics, Computer, Telecommunications and Information Technology (ECTI-CON), Chiang Mai, 2016, pp. 1-4.

[122] G. A. Casula, P. Maxia and G. Mazzarella, "A Printed LPDA with UWB Capability," 2010 International Workshop on Antenna Technology (iWAT), Lisbon, 2010, pp. 1-4.

[123] D. E. Anagnostou, J. Papapolymerou, M. M. Tentzeris and C. G. Christodoulou, "A Printed Log-Periodic Koch-Dipole Array (LPKDA)," in IEEE Antennas and Wireless Propagation Letters, vol. 7, pp. 456-460, 2008.

[124] G. H. Zhai, W. Hong, K. Wu and Z. Q. Kuai, "Wideband Substrate Integrated Printed Log-Periodic Dipole Array Antenna," in IET Microwaves, Antennas & Propagation, vol. 4, no. 7, pp. 899-905, July 2010.

[125] C. Yu et al., "Ultrawideband Printed Log-Periodic Dipole Antenna With Multiple Notched Bands," in IEEE Transactions on Antennas and Propagation, vol. 59, no. 3, pp. 725-732, March 2011.

[126] G. Bozdag and A. Kustepeli, "Subsectional Tapered Fed Printed LPDA Antenna With a Feeding Point Patch," in IEEE Antennas and Wireless Propagation Letters, vol. 15, pp. 437-440, 2016.

[127] F. Zengin, E. Akkaya, F. Güneş and F. N. Ecevit, "Printed Log-Periodic Trapezoidal Dipole Array Antenna with a Balun-Feed for Ultra-Wideband Applications," in IET Microwaves, Antennas & Propagation, vol. 12, no. 9, pp. 1570-1574, 25 7 2018.

[128] K. Anim and Y. Jung, "Shortened Log-Periodic Dipole Antenna Using Printed Dual-Band Dipole Elements," in IEEE Transactions on Antennas and Propagation, vol. 66, no. 12, pp. 6762-6771, Dec. 2018.

[129] P. I. Dankov, "Characterization of Dielectric Properties, Resultant Isotropy and Anisotropy of 3D Printed Dielectrics," in 2018 48th European Microwave Conference (EuMC), Madrid, 2018, pp. 823-826.

[130] ANSYS Electromagnetics Suite. Canonsburg, PA: ANSYS, Inc., 2022.

[131] D. S. Filipovic et al., “Modeling, Design, Fabrication and Performance of Rectangular Micro-Coaxial Lines and Components”, in IEEE MTT-S International Microwave Symposium (IMS), 2006, pp. 1393-1396.

[132] K. J. Vanhille, D. L. Fontaine, C. Nichols, Z. Popovic and D. S. Filipovic, "Ka-Band Miniaturized Quasi-Planar High-Q Resonators," in IEEE Transactions on Microwave Theory and Techniques, vol. 55, no. 6, pp. 1272-1279, June 2007

[133] Y. Qin, “Integrated, Multidisciplinary Approaches for Micro-Manufacturing Research, and New Opportunities and Challenges to Micro-Manufacturing,” in Journal of Nanomaterials, Nanoengineering and Nanosystems. vol. 232, no. 1, pp. 5-21, Nov. 2017.

[134] S. Manafi, M. Al-Tarifi, and D. Filipovic, “Millimeter-Wave Double-Ridge Waveguide and Components,” in IEEE Transactions on Microwave Theory and Techniques, vol. 66, no. 11, pp. 4726-4736, August 2018.

[135] S. Manafi, M. Al-Tarifi, and D. Filipovic, “Isolation Improvement Techniques for Wideband Millimeter-Wave Repeaters,” in IEEE Antennas and Wireless Propagation Letters, vol. 17, no. 2, pp. 355-358, January 2018.

[136] L. Periasamy and A. J. Gasiewski, "Antenna Design and Prelaunch Performance of a Low-Cost 118.75 GHz Temperature Sounding CubeSat Radiometer With 3-D-Printed Corrugated Feed and Offset Reflector Optics," in IEEE Transactions on Antennas and Propagation, vol. 68, no. 6, pp. 4881-4893, June 2020

[137] Formlabs, “Form 3+: Industrial-Quality Desktop SLA 3D Printer” formlabs.com, 2022. Available: https://formlabs.com/3d-printers/form-3/. [Accessed: Jan. 4, 2022].

[138] A. Margomenos et al., "K and Ka-Band Silicon Micromachined Evanescent Mode Resonators," 2007 European Microwave Conference, 2007, pp. 446-449

[139] (2020) Protolabs 3D printing guidelines. [Online]. Available: https://www.protolabs.com/services/3d-printing/direct-metal-laser-sintering/#design-guidelines

[140] (2020) Protolabs 3D printing guidelines. [Online]. Available: https://www.protolabs.com/services/3d-printing/stereolithography/#design-guidelines

[141] M. Uhm, K. Kim and D. S. Filipovic, "Ultra-Wideband Bandpass Filters Using Quarter-Wave Short-Circuited Shunt Stubs and Quarter-Wave Series Transformers," in IEEE Microwave and Wireless Components Letters, vol. 18, no. 10, pp. 668-670, Oct. 2008

[142] S. Groiss, I. Bardi, O. Biro, K. Preis, and K. Richter, “Parameters of lossy cavity resonators calculated by the finite element method,” IEEE Transactions on Magnetics, vol. 32, no. 3, pp. 894–897, May 1996.

[143] E. Hammerstad and O. Jensen, “Accurate Models for Microstrip Computer-Aided Design,” in IEEE MTT-S Int. Microw. Symp. Dig., Washington, DC, May 1980, pp. 407–409.

[144] M. V. Lukic and D. S. Filipovic, "Modeling of 3-D Surface Roughness Effects with Application to μ-Coaxial Lines," in IEEE Transactions on Microwave Theory and Techniques, vol. 55, no. 3, pp. 518-525, March 2007.

[145] D. M. Pozar, Microwave Engineering, 4th ed., Hoboken, NJ: John Wiley, 2012.

[146] R. Garg, I. Bahl, and M. Bozzi, Microstrip Lines and Slotlines, 3rd Ed. Boston, MA: Artech House, 2013.

[147] Cadence AWR Microwave Office. San Jose, CA: Cadence Design Systems, Inc., 2022

APPENDIX

Appendix A: Disagreement of Curved Aperture Horn Theory and Simulation

The theory of nonplanar aperture type antennas is put forward in [106], which discusses the curved aperture horn generalized to any parabolic or cylindrical face. It reports the analytical aperture fields and far fields under the following assumptions: That the horn is only flared in one direction, either the E or H plane, that the propagating mode inside the horn is only the fundamental mode, that there is no reflection from the aperture, and that the normal vector to the aperture surface of parabolic apertures is equivalent to the normal vector for the circular case as a function of angle about the origin. Ignoring the normal vector approximation, which is trivially true for our circular profile apertures. The primary issue with these assumptions lies in the assumption of only the fundamental mode propagating. As will be briefly investigated below, this leads to results that are seemingly accurate to simulation in the case of narrow angular width horns, on the order of 60-80°, however for wide angular width horns the calculation for the far field breaks down, producing extraneous sidelobes that do not exist in simulated results. (A.1)-(A.3) shows the reproduced equations for the H-plane curved aperture sectoral horn, with notation adapted to match the style of this thesis, and excluding the term which cancels due to a circular only aperture, and (A.4)-(A.5) show the equations of the calculated far fields in the E and H-plane respectively. Θ represents the theta postion of the observation point in the far field, while θ is the angle describing the position on the horn aperture. The expressions provided appear to show good agreement with simulation for the horn described in chapter 3. As seen in Fig. A.1, below.

$$E_y = cos\left(\frac{\pi}{W_{ang}}\theta\right)H^{(2)}_{\frac{\pi}{W_{ang}}}(kL_{horn})e^{j\omega t} \tag{A.1}$$

$$H_r = \frac{\pi}{j\omega\mu W_{ang}}\frac{sin\left(\frac{\pi}{W_{ang}}\theta\right)}{L_{horn}}H^{(2)}_{\frac{\pi}{W_{ang}}}(kL_{horn})e^{j\omega t} \tag{A.2}$$

$$H_\theta = \frac{k}{j\omega\mu}cos\left(\frac{\pi}{W_{ang}}\theta\right)H^{(2)\prime}_{\frac{\pi}{W_{ang}}}(kL_{horn})e^{j\omega t} \tag{A.3}$$

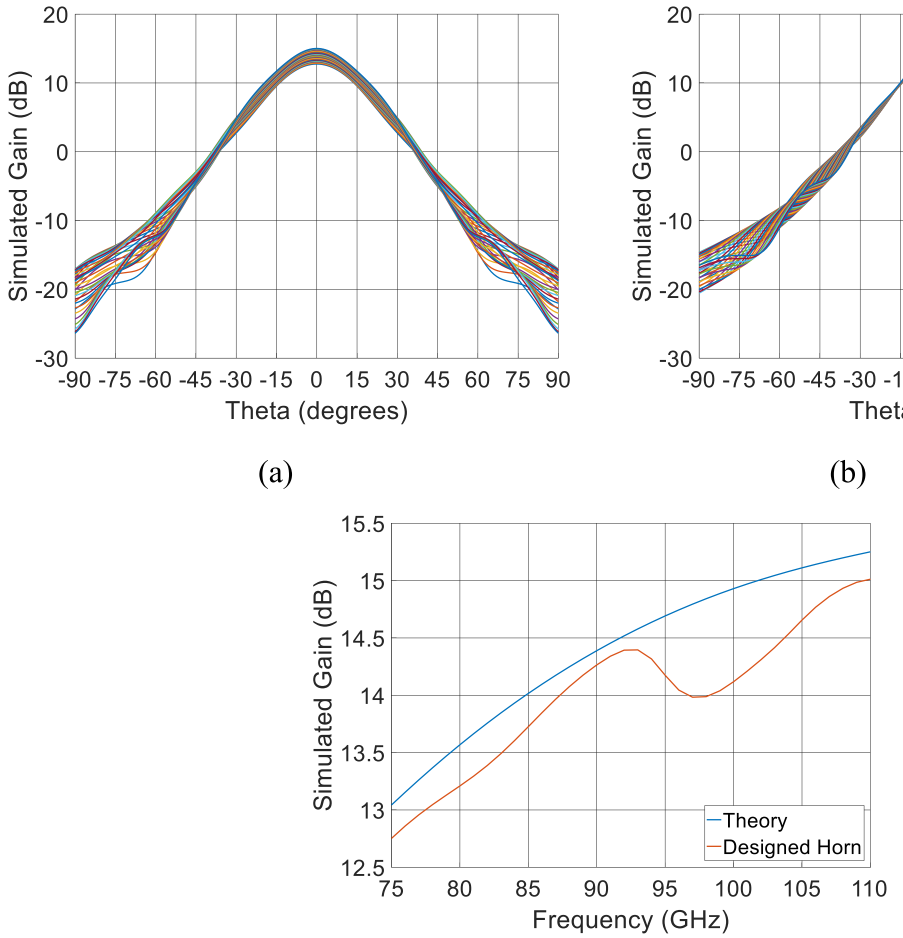

(a) (b)

Fig. A.1. (a) simulated H-plane radiation pattern of designed horn from chapter 3. (b) theoretical H-plane radiation pattern of sectoral horn of b=3.8mm, L_{horn} = 9.2mm and W_{ang} = 70°. (c) Boresight gain for the theory and the horn as designed.

$$F_{HE}(\Theta) = \left| \frac{sin\left(\frac{b_{ap}\pi}{\lambda} sin(\Theta)\right)}{\frac{b_{ap}\pi}{\lambda} sin(\Theta)} \right| *$$

$$\left| \int_{-\frac{W_{ang}}{2}}^{\frac{W_{ang}}{2}} \left[\frac{3j}{kL_{horn}} cos(\Theta) - (cos(\theta) + cos(\Theta)) \right] cos(3\theta)\, e^{jkL_{horn}(cos(\Theta)\,cos(\theta)-1)} \sqrt{L_{horn}} \partial\theta \right| \quad (A.4)$$

$$F_{HH}(\Theta) = \left| \int_{-\frac{W_{ang}}{2}}^{\frac{W_{ang}}{2}} \left[\frac{3j}{kL_{horn}} - cos(\Theta - \theta) - 1 \right] cos(3\theta)\, e^{jkL_{horn}(cos(\Theta-\theta)-1)} \sqrt{L_{horn}} \partial\theta \right| \quad (A.5)$$

As can be seen, the theory shows reasonable agreement with simulated performance, both in shape, and in relatively close agreement in boresight gain. Obviously, there will be differences associated with the non-sectoral nature of the designed horn introducing phase error in the E-plane, as well as due to the presence of higher order modes generated by the waveguide to horn transition, as described by dewey [61]. However, when this calculation is applied to wide angular width horns, the pattern shape sharply disagrees with simulation. The likely cause of this is the generation of multiple modes in the wider horn. Fig. A.2, shows the H-plane radiation pattern of increasing angular width horns with similar dimensions to the horn designed in chapter 3, and Fig. A.3 shows simulated H-plane radiation patterns of horns with the same dimensions as those described in Fig. A.2. As can be seen, there is quite rapidly substantial disagreement between theoretical and simulated patterns. Future work in this area could reexamine the theoretical predictions put forward, and expand the number of modes utilized in calculating the radiation patterns.

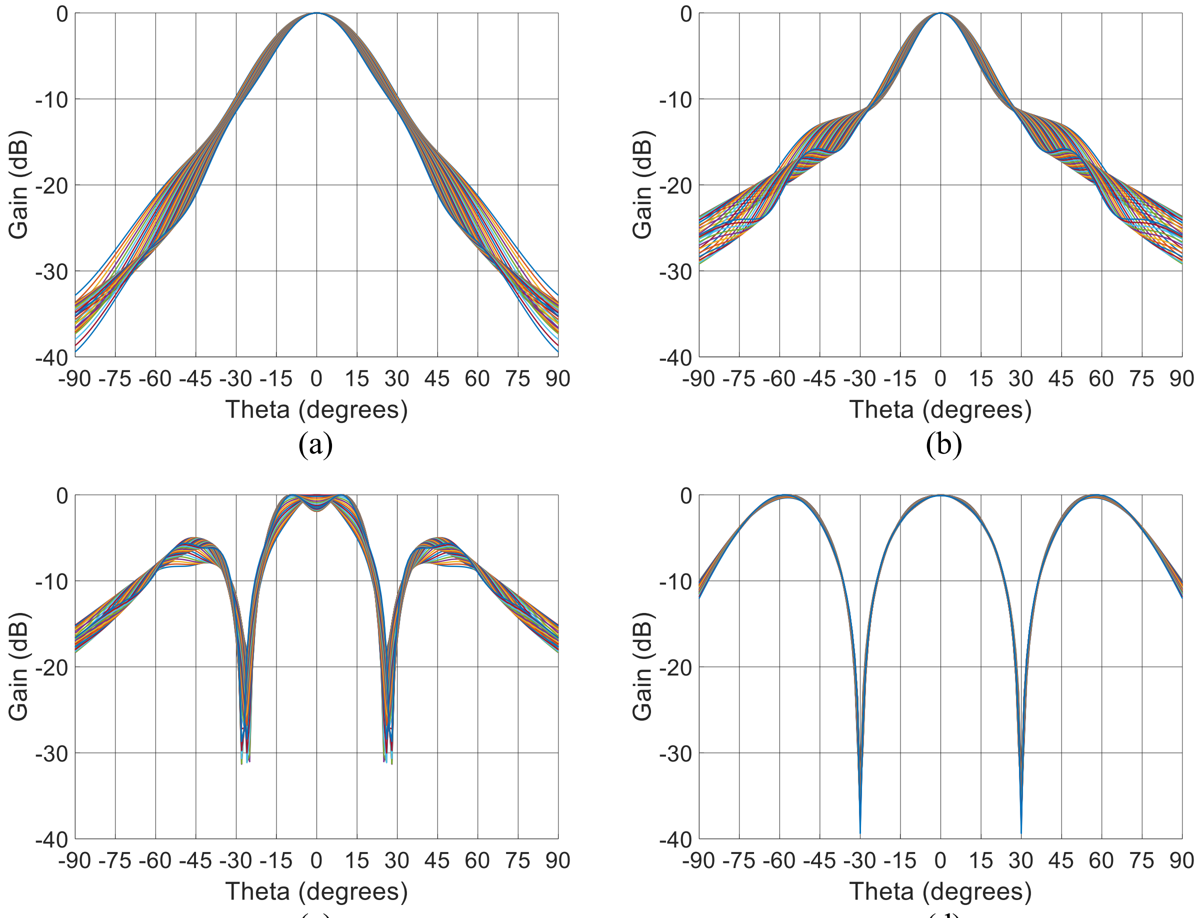

(a) (b)

(c) (d)

Fig. A.2. H-plane patterns according to theory, for L_{horn} = 9mm, b_{ap} = 4mm, and W_{ang} = 60° (a), 80° (b), 110° (c), and 180° (d).

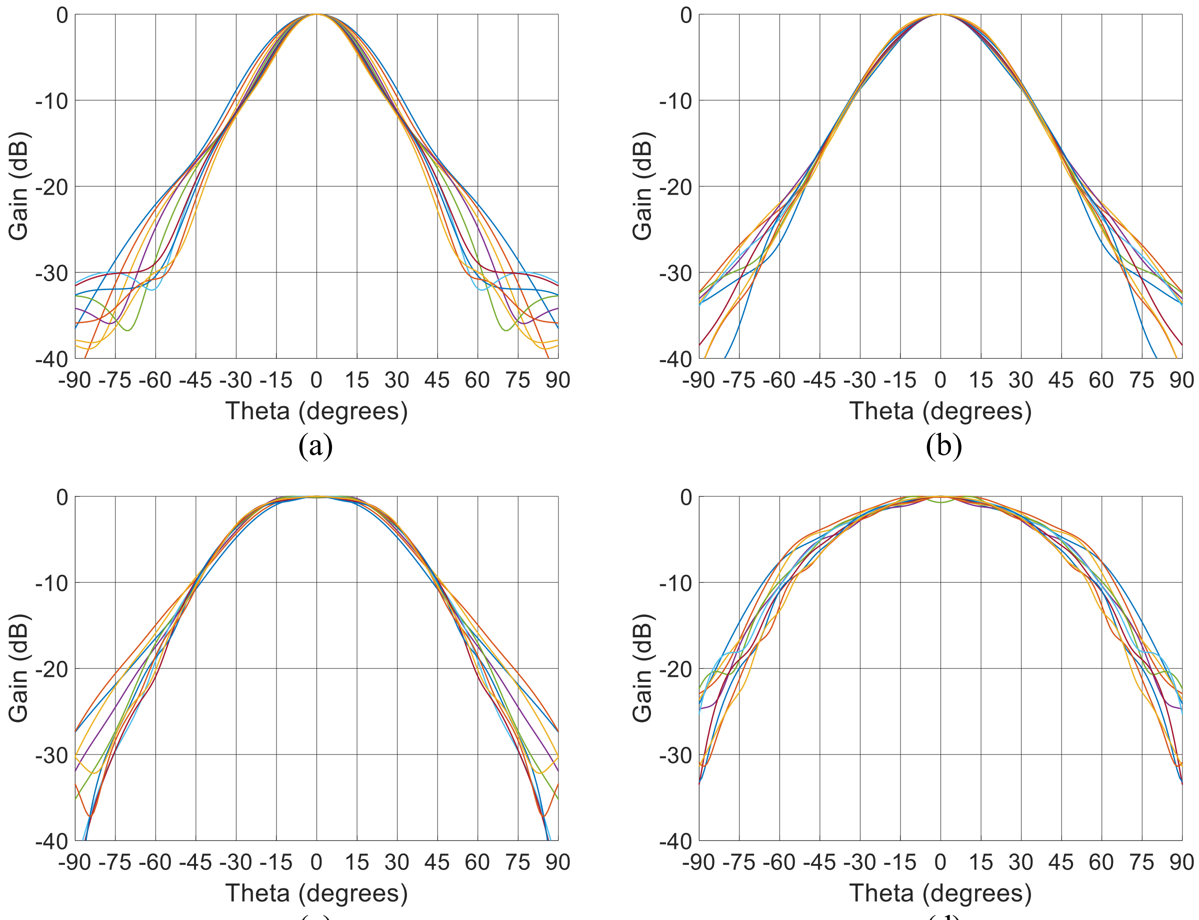

(a) (b) (c) (d)

Fig. A.3. H-plane patterns according to simulation, for L_{horn} = 9mm, b_{ap} = 4mm, and W_{ang} = 60° (a), 80° (b), 110° (c), and 180° (d).

Appendix B: TEM Horn Modal Content

This appendix collects the change in modal behavior as the design of the TEM horn is progressed from a basic 60mm width, 60mm length horn, Fig. B.1, to the final design. As can be seen, the initial TEM horn has primarily power radiated in TM spherical modes, with minimal TE mode power over frequency. Addition of a rear loop, Fig. B.2 brings substantially more power into the TE_{11} and TE_{12} modes, with power still existing in the TM_{12} and TM_{13} modes. The phase behavior is poor, however, with phase difference between TM_{11} and TE_{11} dropping to 0 just before 3GHz. this corresponds to rear fire radiation of the freespace device. Phase between the TM modes is also poor, drifting away from 0^{o} from 1-2.5 GHz. Addition of the phasing capacitive slot improves behavior substantially in Fig. B.3. The TE_{12} mode is now excitecd, with primary power entering that mode through fields across the capacitive gap. Phase is substantially improved, with near 0^{o} phase between TE_{11}, TE_{12} and TE_{13}, near 0^{o} phase between $TM_{11,}$ TM_{12}, and TM_{13}, and 150-180^{o} phase between the collected TE and TM modes. Further modifications to the structure, namely adding the bowtie sections, changes the mode behavior radically. In Fig. B.4, the turn-on region is seen to be extended up to near 3.5 GHz. More power is directed to lower order modes over a greater stretch of the bandwidth, and phase between the modes is further improved. Fig. B.5 shows similar, but somewhat degraded modal performance from Fig. B.4, and is the modal behavior of the TEM horn structure with realistic material thickness of 1mm, whereas Fig. B.1 to Fig. B.4 show antennas constructed from thin sheets. The design up until Fig. B.5 is intended, at least in part, to act as a standalone antenna, and higher gain is pursued with a smaller turn-on region and a larger TEM horn. Fig. B.6 shows the radiating element modes, after being reduced in size following cavity integration. This includes the reduction in size of the TEM horn, reduction and reshaping of the TEM horn loop, and the substitution of linear capacitive slots, which direct less power towards TE_{13}. These changes show the TEM horn in it's turn-on region for a greater bandwidth, extending from approximately 1.67 to near 4.5 GHz. fewer modes are excited by this structure, and with superior phasing. Finally, Fig. B.7 shows the behavior with the addition of the shorting posts. In this design, fewer modes retain substantial power, with most power going into the TM modes, and the TE$_{11}$ mode excited with reasonably even power across the band. Phase between TE and TM modes is now very linear near 150°. Fig. B.8 shows the match and gain performance of the isolated TEM horn radiating body with and without the shorting posts.

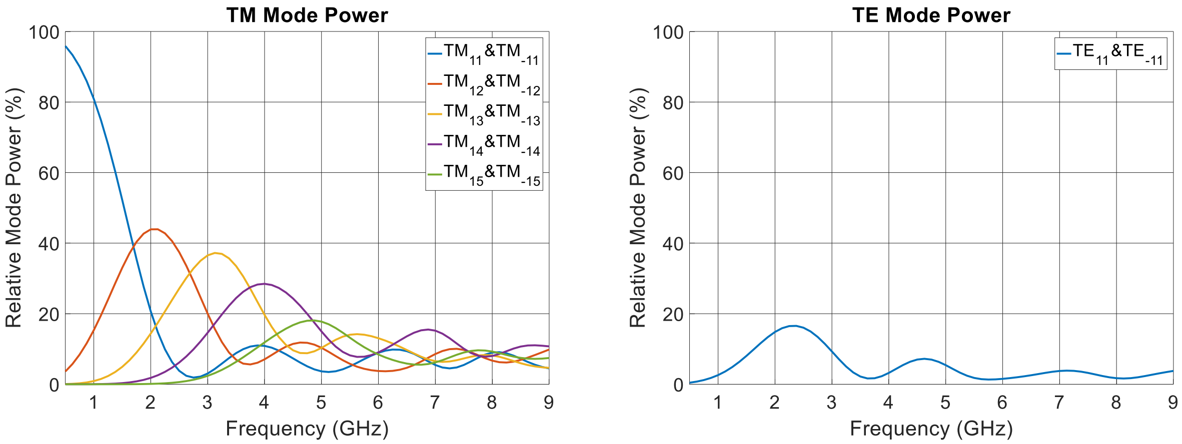

Fig. B.1 Radiated relative mode power from a standard dual polarized TEM horn with aperture width and horn length 60mm. curves are limited to all modes that show greater than 15% power

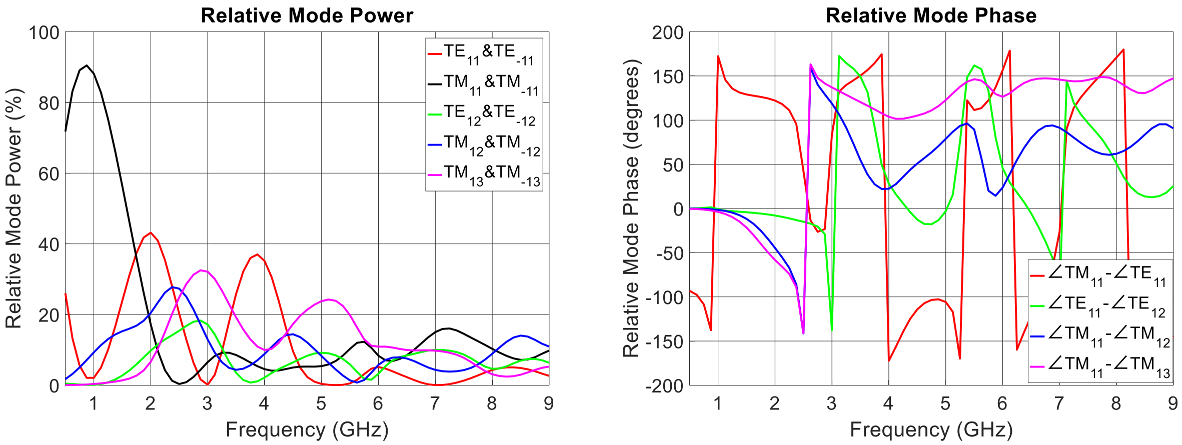

Fig. B.2 Thin material TEM horn with only attached loop section. Radiated modes with power >15% and mode relative phase.

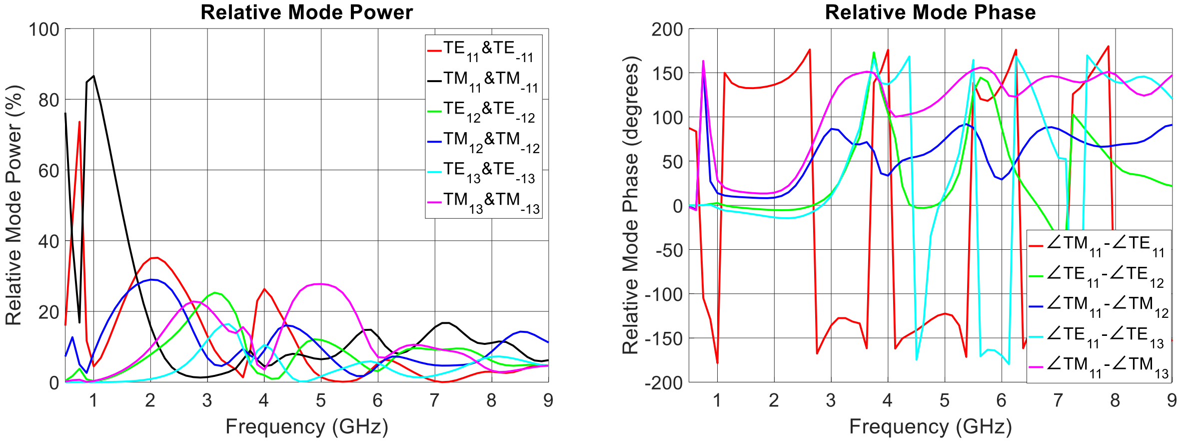

Fig. B.3. Thin material TEM horn with attached loop section and capacitive gaps. Radiated modes with power >15% and mode relative phase.

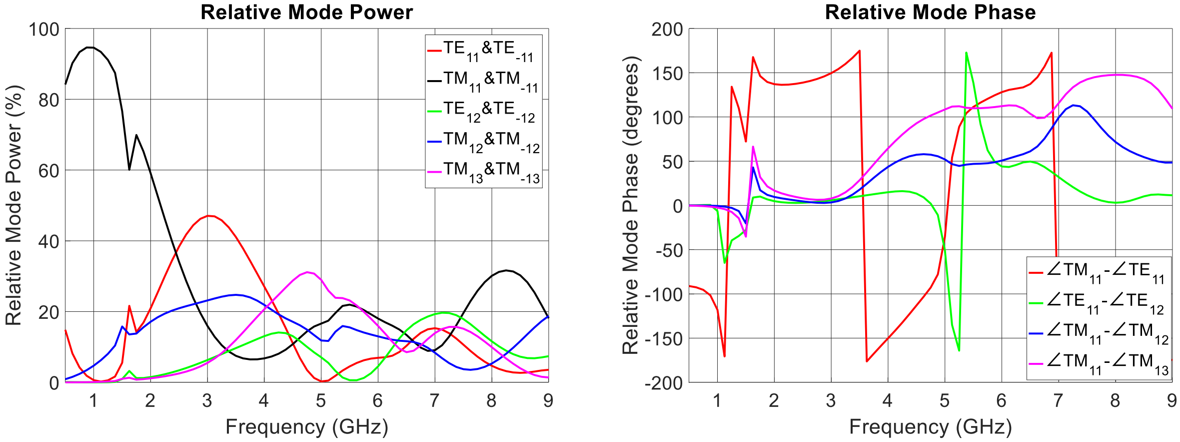

Fig. B.4 Thin material TEM horn with attached loop section, capacitive gap, and bowtie plates. Radiated modes with power >15% and mode relative phase.

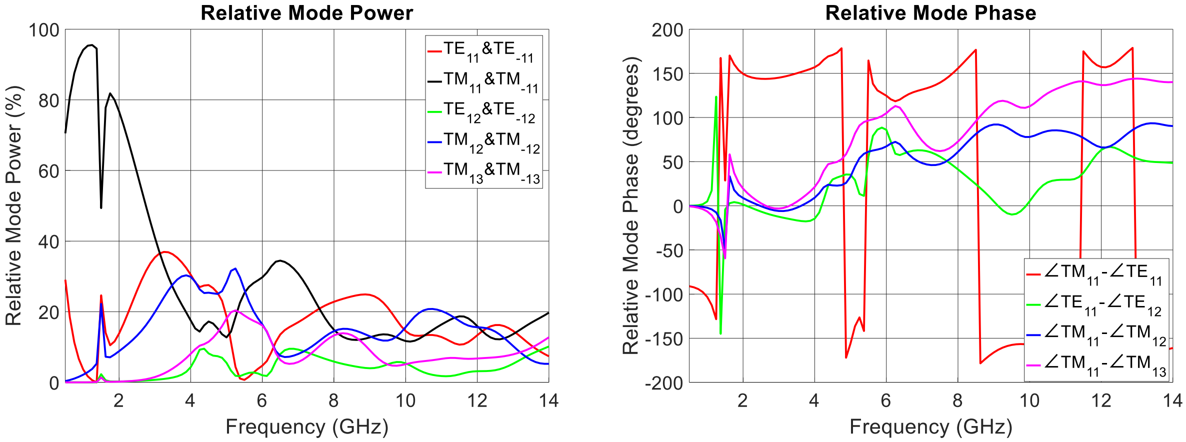

Fig. B.5 Thick material TEM horn, as in Fig. 4.1(b), standalone freespace antenna prior to cavity integration. Radiated modes with power >15% and mode relative phase

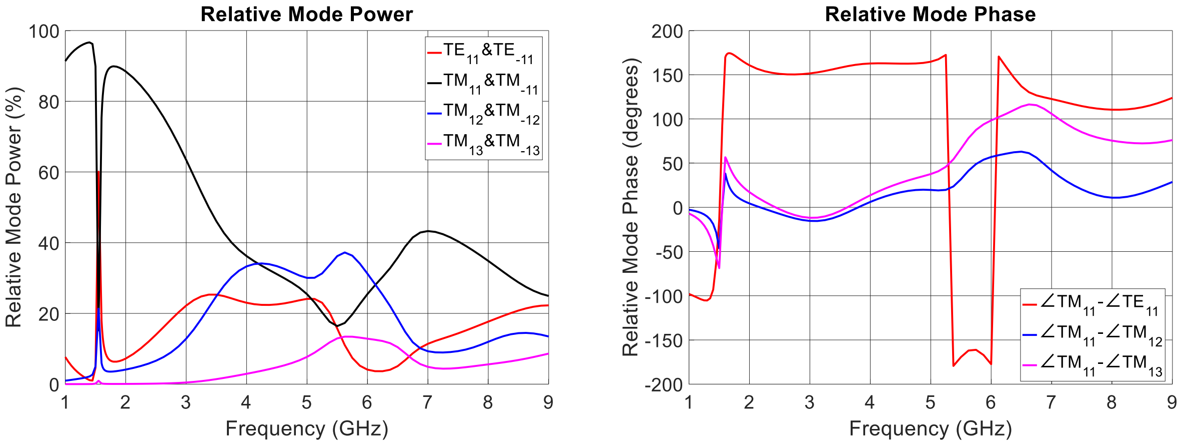

Fig. B.6 Modes of radiating element for cavity integration, with size reduction and linear slots, without shorting posts. Radiated modes with power >10% and mode relative phase

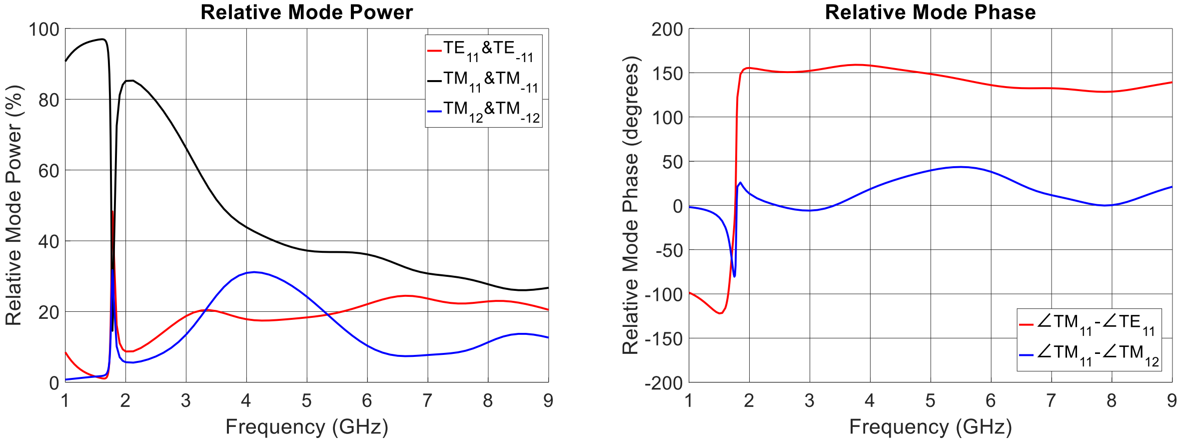

Fig. B.7. Modes of radiating element for cavity integration, with all final features. Radiated modes with power >10% and mode relative phase

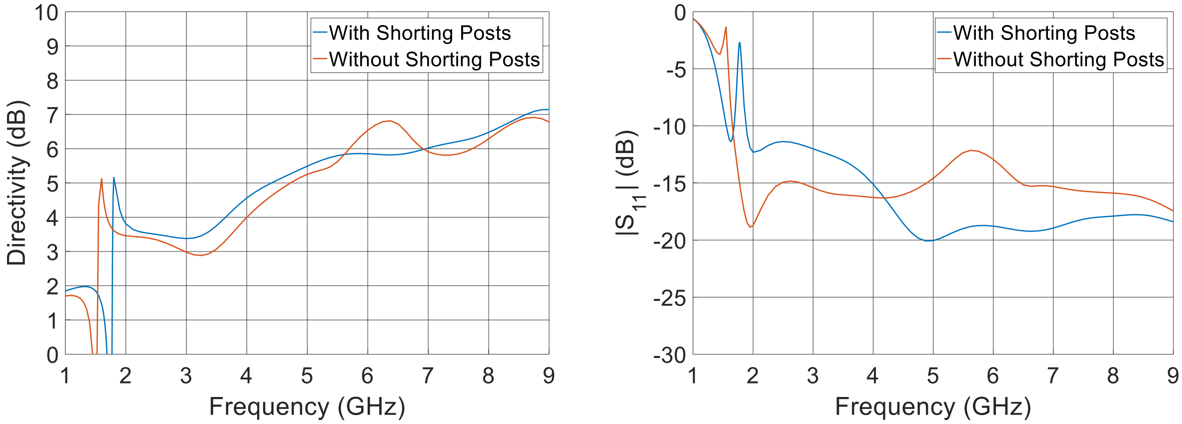

Fig. B.8 Boresight gain and $|S_{11}|$ for cavity integration element in freespace, with and without shorting posts.

Appendix C: TEM Horn Operation Compared With Sinuous

In comparing the behaviors of the TEM horn proposed in chapter 4 and an appropriate sinuous antenna, it is possible to examine in depth the behaviors of a sinuous antenna designed for the same frequencies of interest, with a similar absorber lined cavity backing. The two antennas can be seen in Fig. C.1. First, the match behavior of the two designs can be compared, with the match behavior of the TEM horn and sinuous antennas compared with similar coaxial bundle feeds of 50Ω cable. As can be seen in Fig. C.2, the TEM horn is more appropriately matched with 50Ω cabling, however good match can be obtained for the sinuous antenna with 90Ω bundle feeding. Looking next into the broadside gain and efficiency in Fig. C.3, the improvement in both categories for the TEM horn over the sinuous antenna can be seen. This is to be expected, as the TEM horn is acting as a naturally unidirectional antenna with backlobe reduced by absorber and pattern shape improved by recession into a cavity, meanwhile for the sinuous antenna, the use of the cavity is primarily to prevent an entire hemisphere of the radiation from being emitted, as well as to try to constructively phase whatever power is not absorbed. Fig. C.4 shows one respect in which the sinuous antenna is likely a superior archetype, in that sinuous antenna can achieve much wider direction finding FOV, as the pattern shape is well approximated by cosine beam shapes. However, as a receive antenna, it can be seen that the TEM horn has significant benefits. Fig. C.5 plots the group delay of the antennas, and Fig. C.6 demonstrates the impact of the group delay on a transmitted pulse through each system. The sinuous antenna behaves in a significantly more dispersive manner, degrading signal integrity, while group delay is nearly flat across the band for the TEM horn, enabling much higher fidelity of transmitted signals.

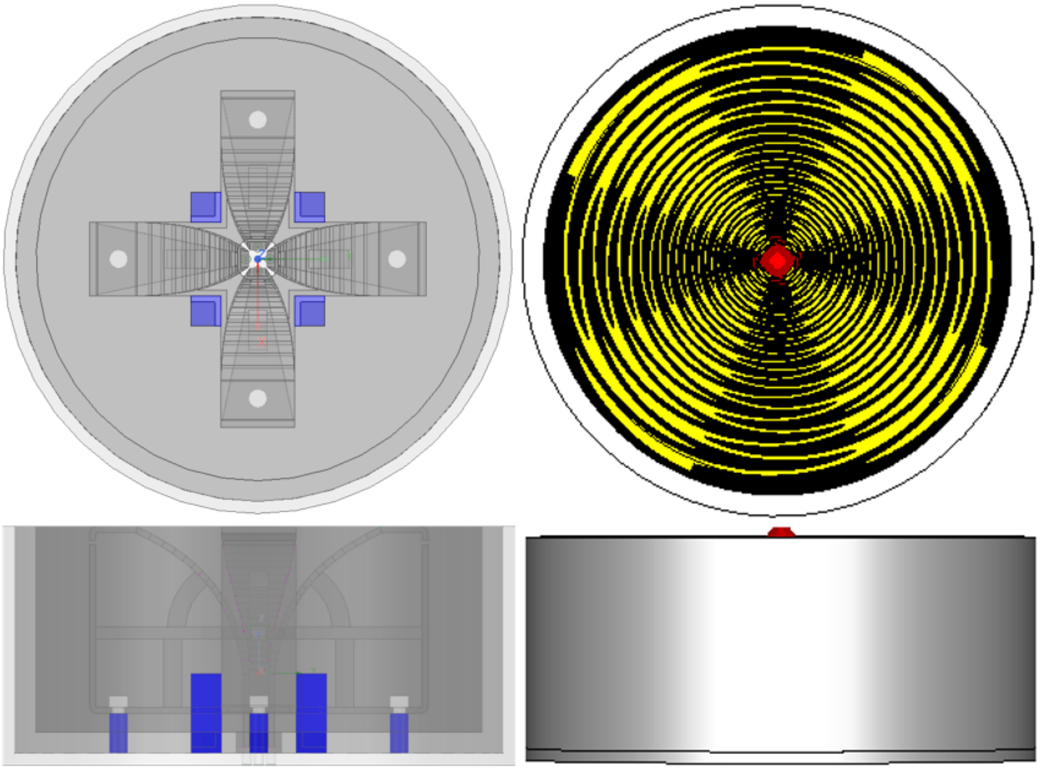

Fig. C.1. Geometry of TEM horn and equivalently sized sinuous antenna.

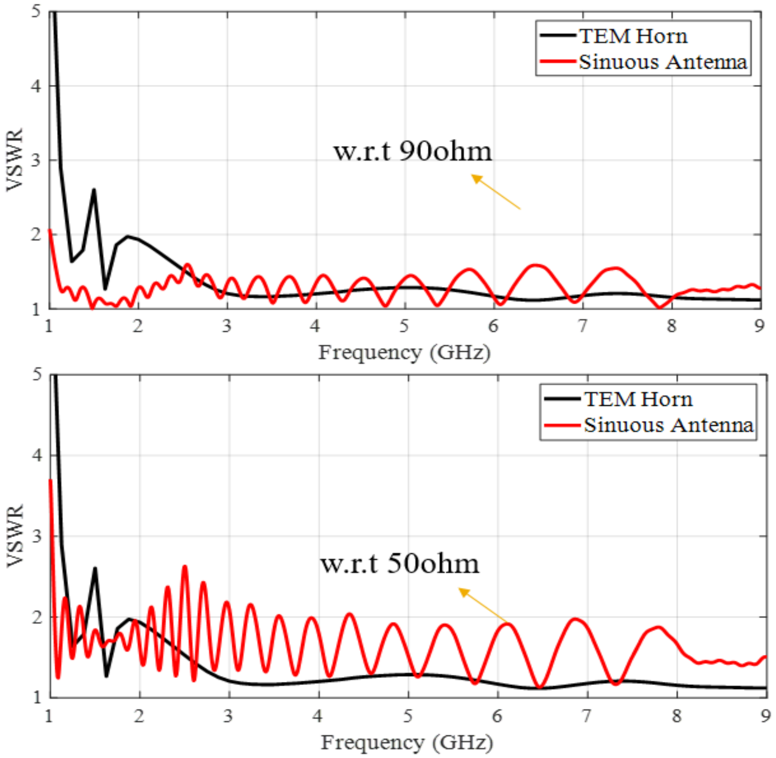

Fig. C.2 VSWR of TEM horn and Sinuous antenna

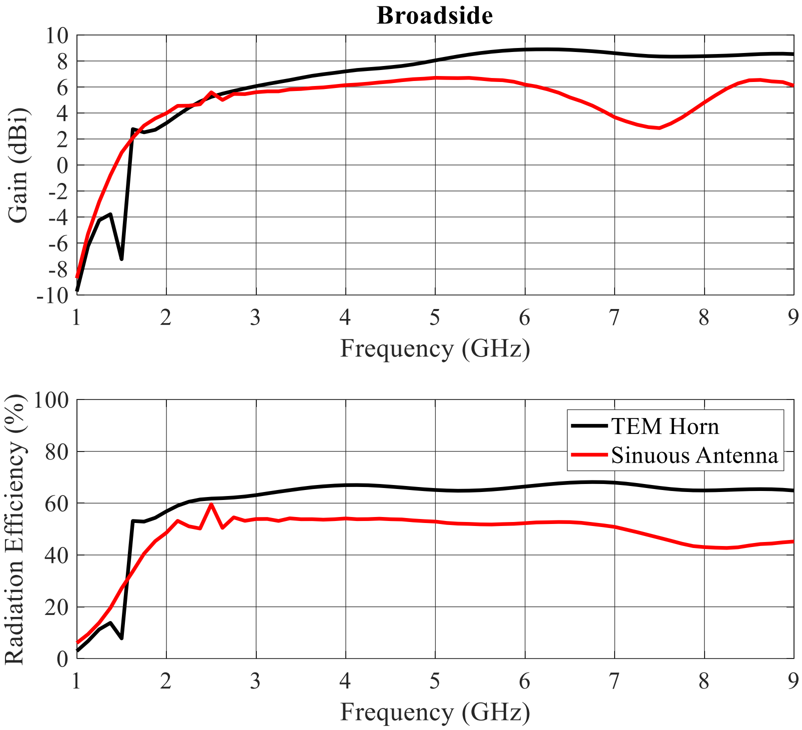

Fig. C.3. Gain and radiation efficiency from TEM horn antenna and sinuous antenna

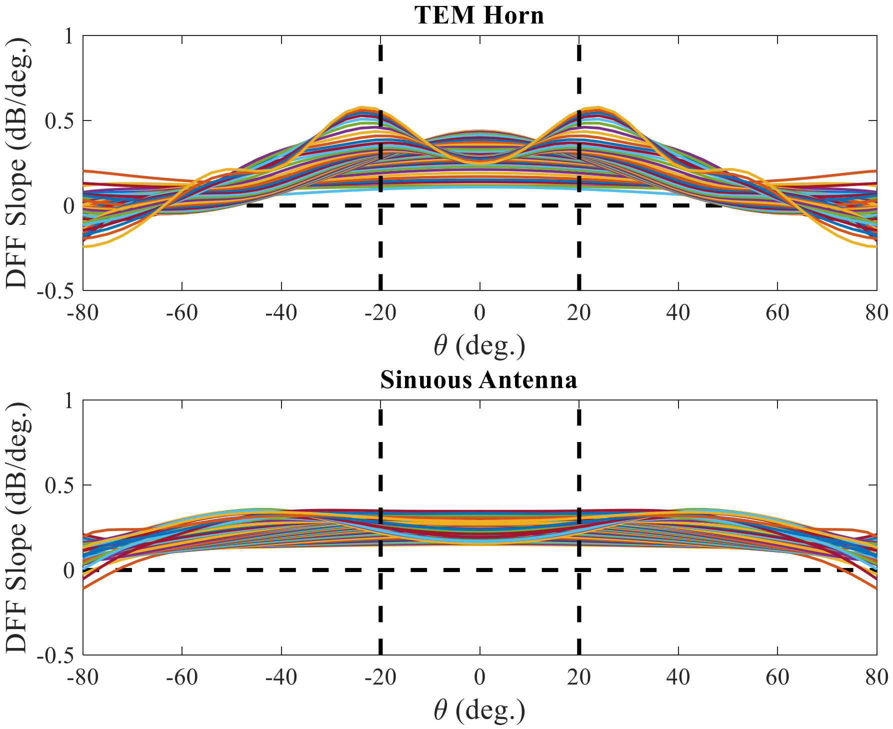

Fig. C.4. DFF Slope for TEM horn and sinuous antenna in H-plane

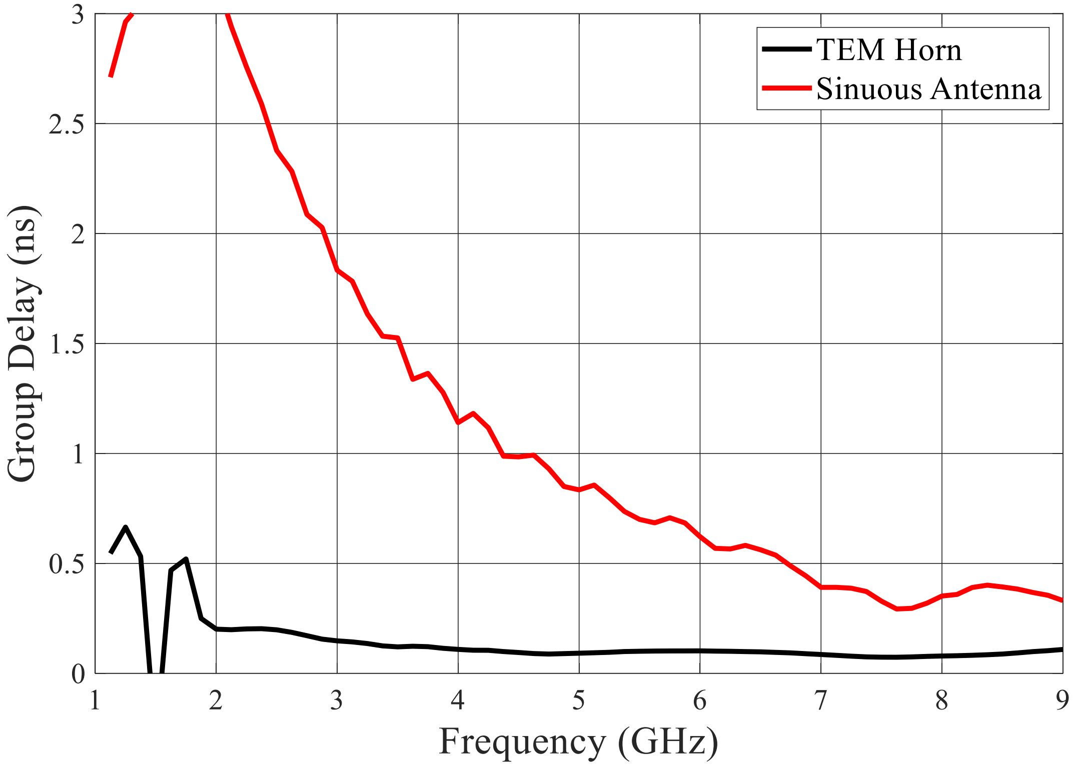

Fig. C.5. Group delay for TEM horn and sinuous antenna

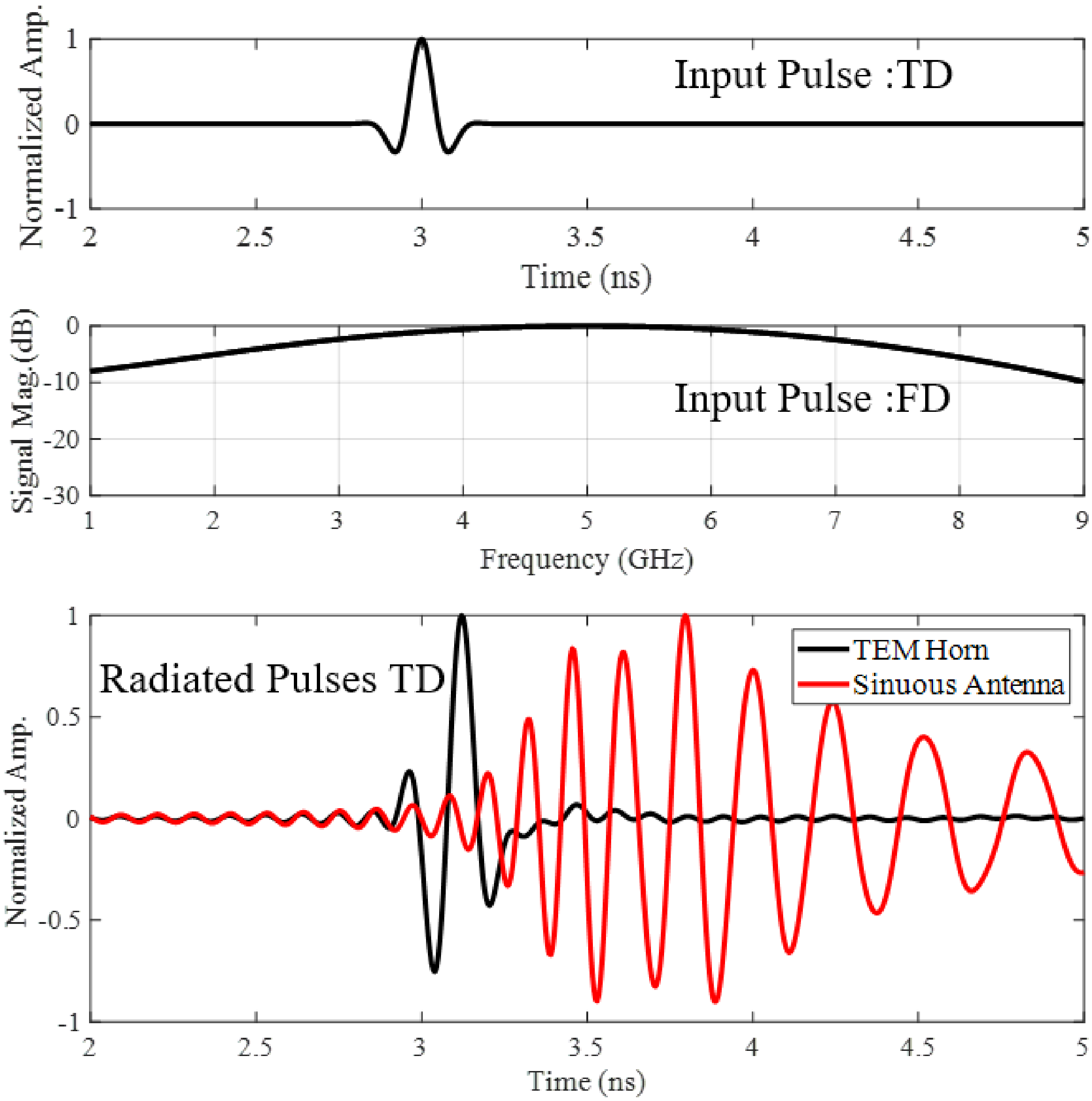

Fig. C.6. Time domain view of radiated pulse from TEM horn and sinuous antenna.